A FULL ELECTROMAGNETIC ANALYSIS OF FRESNEL ZONE PLATE ANTENNAS AND THE APPLICATION TO A FREE-SPACE FOCUSED-BEAM MEASUREMENT SYSTEM

A Thesis
Presented to
The Academic Faculty

by

David R. Reid

In Partial Fulfillment
of the Requirements for the Degree
Doctor of Philosophy in the
School of Electrical and Computer Engineering

Georgia Institute of Technology
December 2008

A FULL ELECTROMAGNETIC ANALYSIS OF FRESNEL ZONE PLATE ANTENNAS AND THE APPLICATION TO A FREE-SPACE FOCUSED-BEAM MEASUREMENT SYSTEM

Approved by:

Glenn S. Smith, Advisor
School of Electrical and Computer Engineering
Georgia Institute of Technology

Waymond R. Scott, Jr.
School of Electrical and Computer Engineering
Georgia Institute of Technology

Andrew F. Peterson
School of Electrical and Computer Engineering
Georgia Institute of Technology

Gregory D. Durgin
School of Electrical and Computer Engineering
Georgia Institute of Technology

John W. Schultz
Signature Technology Laboratory
Georgia Tech Research Institute

Date Approved: November 7 2008

To my wife, Sara,

to my parents,

and to my brother, Benji.

ACKNOWLEDGEMENTS

This dissertation would not have been possible without the help and support of many individuals. I would like to express my gratitude to those who have assisted me with this work.

First, I would like to thank my thesis advisor, Dr. Glenn Smith. Working with Dr. Smith has been a tremendous opportunity, and over the past five years I have learned so much from him. Through his advice, his patient teaching, and his careful evaluation of my work, Dr. Smith has shown me what it takes to do good research. Dr. Smith's relentless pursuit of excellence is inspiring. I am grateful for the John Pippin Chair in Electromagnetics, which partially funded my work.

I would like to thank my thesis committee for reviewing this work. My committee consists of Dr. Smith, Dr. Waymond Scott, Dr. Andrew Peterson, Dr. Greg Durgin, and Dr. John Schultz. I would especially like to thank Dr. Scott for his help with many aspects of this work and for sharing the computational resources required for this work.

I would also like to thank all of those at the Signature Technology Laboratory of the Georgia Tech Research Institute who helped to support this project. My work was funded in part by a Shackelford Fellowship from GTRI. Individually, I would like to thank Paul Friederich, Lon Pringle, and John Meadors for making this possible. Dr. Schultz played a huge role in this research. His discussions about the focused-beam system and his expertise were invaluable. I would like to thank James Fraley for helping me to get the zone plate fabricated and for teaching me how to use SolidWorks. Thanks to Stephen Blalock for his help with the measurement systems and to Brian Cieszynski, Matt Habib and all of the coops for their assistance with the experimental portions of this work. Thanks also to Jim Maloney, Jim Acree, and Brian Shirley for their feedback and advice.

I would like to acknowledge the help of Dr. James Wiltse, who was responsible for much of the early research on Fresnel zone plates and is one of the world's experts on the topic.

Dr. Wiltse generously shared his time with me, offering advice, proofreading my papers, sharing ideas, and supporting my research efforts. It has been an honor to have Dr. Wiltse involved with this work.

Kurt Wiesmayer of Wiesmann Tool, Inc., did an exceptional job fabricating the zone plate. I appreciate the time he took with me to explain the fabrication process and his patience with me as I stumbled through the process of preparing the zone plate design.

My friends have been hugely supportive throughout my time in graduate school, helping to keep me smiling and having fun. I'm particularly grateful for the friendship of Billy, Jenny, Curtis, Brian, Sabrina, Brad, Spencer, Phill, Natalie, Ana, and Brandon. Thanks to my fellow grad students for their help and for their interesting discussions, particularly Ilker Capoglu, Mike McFadden, Pelham Norville, Tegan Counts, Ricardo Lopez, Mu-Hsin Wei, and Benny Venkatesan. I am especially grateful for Todd Lee, who took me under his wing and helped me learn how to be a graduate student. Todd taught me the nuances of FDTD and C++ and spent countless hours assisting me along the way. Thanks to Todd and Mike for their all of their hard work developing and maintaining the computer cluster.

Without the support of my family, I would not be where I am today. My parents, Pam and Rich, and my brother Benji have shaped me into the person that I am today. They have unfailingly supported me every step of the way and have always encouraged me to follow my dreams. Thanks also to my Grandparents for their enthusiastic support of all of my endeavors! I have also been blessed with supportive in-laws: Phil, Robin, Mark, Alex, and Sheri, who have welcomed me into their family and been wonderful.

Special thanks go to my wife, Sara. None of this would have been possible without her. In the periods of excitement and in the periods of frustration, Sara was by my side. This thesis, therefore, is as much a testament to her hard work and sacrifice as it is to mine. Constantly reassuring me, patiently supporting me, and steadily loving me, Sara has kept me going. Her presence in my life has made every day so much fun. You are the best friend that I could ask for!

And finally, praise be to God, from whom all blessings flow.

TABLE OF CONTENTS

LIST OF TABLES

LIST OF FIGURES

SUMMARY

In this research, Fresnel zone plates were studied using an accurate, full-electromagnetic simulator based on the body-of-revolution finite-difference time-domain (BOR-FDTD) method. This method offers an advantage over many of the simpler methods that are used to analyze zone plates. These simpler methods cannot correctly account for many of the factors that influence the focusing ability of a zone plate, particularly for microwave and millimeter-wave applications. The BOR-FDTD simulator overcomes this deficiency and allows a more complete analysis of the focusing by zone plates. This tool was used to investigate zone plates for two different applications: zone plates used as antennas in communications systems and zone plates used as focusing elements in free-space, focused-beam measurement systems. Through detailed studies of zone plates for these applications, a number of general characteristics of the zone plate were given a more in-depth look than they have been given in the past. Some of the conclusions from these studies are applicable for the design of any zone plate, especially for use in microwave and millimeter-wave applications.

For the first application, parametric design studies were performed for Soret, folded, and grooved-dielectric, phase-correcting zone plates for antenna applications. These studies were used to generate new design graphs. From the design graphs, general observations are made about the effect of varying different physical parameters on the focusing ability of a zone plate. For the grooved-dielectric, phase-correcting zone plate, these studies show that focal length, the base thickness, and the number of phase corrections per zone affect the focusing ability in ways that are unexpected, based on many of the simple techniques typically used to analyze zone plates. The effect of each of these parameters on the focusing ability of a zone plate is evaluated individually.

For the second application, a zone plate was designed to be used as a focusing element in a free-space, focused-beam measurement system, which is used to measure the electrical

properties of sheets of material. The design was based on new equations and BOR-FDTD simulations. Using simulation results, the performance of this zone plate is compared to the performance of a doubly-hyperbolic lens in an existing focused-beam system. In order for the zone plate to be used in this system, the field focused by the zone plate must have certain characteristics. These include a specific amplitude taper, phase uniformity, and linear polarization. These characteristics are compared to the corresponding characteristics of the lens. Additionally, the bandwidth of the zone plate was studied, and a technique for increasing the usable bandwidth of a zone plate in a focused-beam system was proposed and evaluated.

This zone plate was built and its focusing ability compared to that of the doubly-hyperbolic lens by measuring all three components of the electric field in a volume surrounding the focal point of both devices. Next, a complete focused-beam system, using two zone plates as focusing elements, was used to measure the permittivity of three materials. These measurements are compared to results for a system that uses the lenses as focusing elements and to published values. The proposed technique for expanding the bandwidth of the zone plate was tested and is shown to have promise to improve the permittivity measurements.

As a natural follow-up to this work (a topic for future research), it would be interesting to know if the design of the zone plate could be improved by using a non-traditional design methodology: something other than the traditional optical (ray-tracing) methods. The question is posed: Using the BOR-FDTD method, can a roughly similar volume of material be shaped in a way that results in improved focusing performance compared to a traditional zone plate? Of course, this is a rather open-ended question. However, some insight can be gained by examining the following approach. A genetic algorithm was used to optimize a zone plate. This concept was tested by optimizing two zone plates: one for antenna applications and the other for use in the focused-beam system. This study shows that an optimization routine can improve the performance of a zone plate incrementally. The value of this improvement, however, depends on the particular application for which it will be used.

CHAPTER I

INTRODUCTION

In this work, Fresnel zone plates are investigated using the body-of-revolution finite-difference time-domain method. Detailed design graphs are presented for microwave and millimeter-wave antennas that use Soret zone plates, folded zone plates, and grooved-dielectric, phase-correcting zone plates as focusing elements. The focusing mechanism of these zone plates is studied and factors influencing their focusing ability are examined in detail. The feasibility of using a zone plate as a focusing element in a free-space, focused-beam system for measuring the electromagnetic properties of dielectrics is evaluated both with simulations and with measurements, and the tradeoffs of using a zone plate for this application are discussed. A topic for future research, non-traditional zone plate design, is introduced, and a preliminary analysis of the optimization of zone plates with a genetic algorithm is presented.

1.1 Historical Overview

The origin of the zone plate can be traced to Augustin-Jean Fresnel. Pictured in Fig. 1.1, Fresnel (1788-1827) made significant contributions to the wave theory of light, including the experimental proof that light is a transverse wave. Fresnel, as part of his pioneering work in the field of optics, introduced the zone method: By segmenting an aperture into a number of *zones* and accounting for the effects of each zone at the point of observation, many diffractive phenomena can be explained [1].

This idea is illustrated in Fig. 1.2. In this figure, a plane wave is propagating in free space. Huygens' principle states that the field at a point F can be described by the superposition of an infinite number of spherically-radiating point sources in the plane α [2]. For example, there is a specific contribution at F from a source at point A. For any other point along the plane, the distance to F is longer than the distance AF, which means that the phase of the contribution is different. The phase of the contribution from point B, for example, is shifted by some amount from the contribution from point A. The

Figure 1.1: Augustin-Jean Fresnel. Image credit: Wikipedia.org

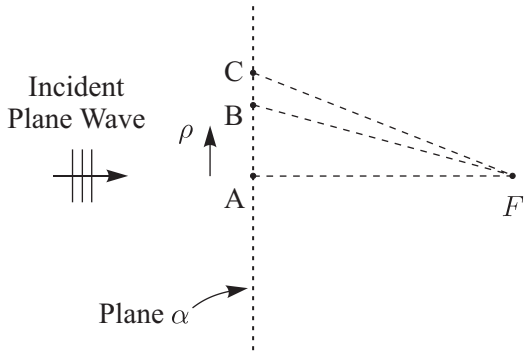

Figure 1.2: Geometry used to illustrate Fresnel's zoning concept.

distance between A and B can chosen such that, at a particular frequency, the phase of the contributions from the two points differs by π radians. The contributions to the field at F from A and B are then exactly out of phase and destructively interfere. Likewise, a point C can be chosen such that the contributions from A and C are in phase (differ by 2π radians) and add constructively at F. This feature repeats: There are points on the plane α, further from A, which have contributions that have phase shifts that are integer multiples of 2π radians. Each of these points marks the boundary of a full-wave Fresnel zone. This means that, in Fig. 1.2, every point between A and C is in the same full-wave zone. The loci of points that mark the boundaries of each full-wave zone are, of course, circles on the plane α.

Every point on the plane α has a corresponding point within the same full-wave zone at which the contribution is exactly out of phase. For instance, each point between A and B has a corresponding, out-of-phase point between B and C. Jacques-Louis Soret noted that if these out-of-phase contributions could be eliminated, the remaining contributions would add constructively at the point F. By making alternating sections of each zone on the plane α opaque and transparent to electromagnetic radiation, a *zone plate* could be constructed that had lens-like focusing properties [3]. These regions are called half-wave zones, because their boundaries mark the points at which the phase of the contribution to the field at F is shifted by π radians (a half-wavelength in length). Therefore, there are two half-wave zones in every full-wave zone. It is interesting that entries in Lord Rayleigh's notebook indicate that he had developed this idea four years earlier than Soret [4]. Rayleigh never published the idea, however, so it is Soret who gets historical credit for the original zone plate.

Lord Rayleigh does get credit, however, for the introduction of the phase-correcting zone plate, which is a method that improves the focusing ability of a Soret zone plate [5]. Instead of blocking the incident field in alternating half-wave zones as Soret did, Rayleigh suggested reversing the phase of the incident field in these half-wave zones. For example, if the phase of the contribution from every point between B and C in Fig. 1.2 could be shifted by π radians, these contributions would add constructively with those from points between A and B. The phase-correcting technique allows the entirety of each full-wave Fresnel zone

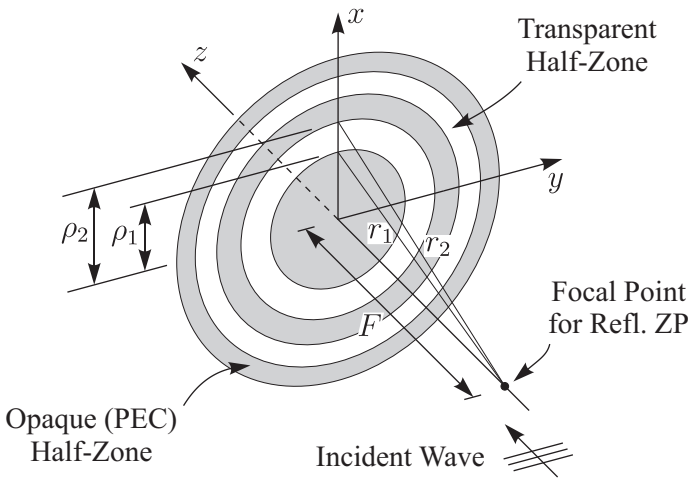

Figure 1.3: Geometry of the Soret zone plate.

to contribute to the focusing, rather than only half of each zone, as is the case for the Soret zone plate. Extending this idea, the focusing ability of a zone plate should be improved by subdividing the Fresnel zones to correct the phase in finer increments [6]. Zones smaller than half-wave zones can be defined, and the phase of their contributions can be made to add constructively by shifting the phase by the appropriate amount (less than π radians).

Using these relatively simple concepts, a number of different devices have been developed. The following sections of this introduction will look in detail at the two primary classes of zone plates and at specific examples of zone plates found in the literature.

1.2 Soret and Folded Zone Plates

The simplest and oldest type of zone plate, the *Soret zone plate*, is made of annuli of perfect electrical conductors (PEC) that block every other half-wave zone, as Soret proposed. This zone plate is illustrated in Fig. 1.3. Studying Fig. 1.3, it can be seen that a portion of the incident field will be reflected by the opaque half-wave zones, while the remainder will be transmitted through the transparent half-zones. The half-wave zones are designed such that only the portions of field that will constructively interfere at the distance F in front of the zone plate are reflected by the opaque part of the zone plate. A similar constructive interference will also occur for the transmitted field at the distance F behind the zone plate. Therefore, there are two focal points associated with this structure, and it can be

used either as a *reflection zone plate* if the feed is on the same side of the zone plate as the incident wave, or a *transmission zone plate* if the feed is located on the opposite side of the zone plate.

To ensure constructive interference, the radii of the zones are computed based on the requirement that the distance from the focal point to the edge of a zone be a half wavelength longer than the distance from the focal point to the edge of the previous zone, as discussed in Sec. 1.1. In Fig. 1.3, ρ_1 and ρ_2 are chosen so that $r_2 = r_1 + \lambda/2$. Applying this requirement to each subsequent zone leads to the well-known design formula for Soret zone plates. If each of these half-wave zones is numbered consecutively starting at the center of the zone plate, the outer radius of the n^{th} half-wave zone is

$$\rho_n = \sqrt{\left(\frac{n\lambda}{2}\right)^2 + n\lambda F}\,, \tag{1.1}$$

in which λ is the design wavelength in free space. The total number of half-wave zones is N_{Soret}, and this number includes both the opaque and the transparent zones.

In determining the radii that define each half-wave zone, it is never specified whether the odd numbered zones or the even numbered zones should be made opaque. Based on Fresnel's zoning principle, these complementary configurations work equally well. The choice of which zones to make opaque depends primarily on the mode of operation of the zone plate. Typically, even numbered zones are opaque for transmission zone plates. In this case, the total number of half-wave zones N_{Soret} is even. Odd numbered zones are opaque for reflection zone plates, like that in Fig. 1.3, and N_{Soret} is odd. Describing the number of zones in terms of N_{Soret} ensures the outer zone is always opaque so that there is no confusion about the location of the edge of the zone plate. The diameter of the zone plate is then $D = 2\rho_{N_{\text{Soret}}}$.

This work will address reflection zone plates for which the odd numbered zones are opaque and the total number of half-wave zones N_{Soret} is odd. This is done without sacrificing generality, however, because the concepts discussed pertain equally well to transmission zone plates.

The obvious problem with the Soret zone plate is that its ability to focus power is

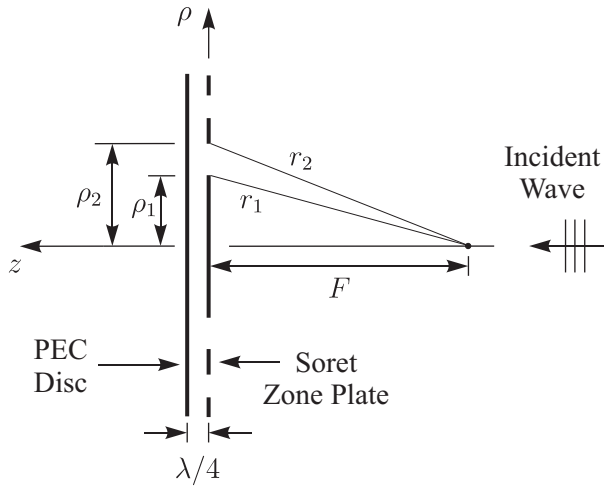

Figure 1.4: Geometry of the folded zone plate.

inherently limited. The presence of both a transmission focal point and a reflection focal point means that only half of the incident energy is focused to each of the focal points. The *folded zone plate* is a variant of the Soret zone plate designed to address this problem. This zone plate is shown in cross section in Fig. 1.4 and is created by placing a PEC disc at the distance $\lambda/4$ behind a Soret zone plate. The distance to the PEC disc imparts an additional round-trip phase change of π radians on the portion of the incident field that is transmitted through the zone plate and reflected by the disc [7]. The term 'folded' arises from the fact that this zone plate is essentially folding, or imaging, the transmission focal point to the location of the reflection focal point. The field reflected by the disc adds constructively with the field reflected by the opaque zones at the focal point. This configuration, therefore, roughly doubles the magnitude of the electromagnetic field at the focal point compared to the Soret zone plate.

1.3 Phase-Correcting Zone Plates

The phase correction proposed by Rayleigh as a way of improving the performance of Soret zone plates has been implemented successfully using a number of different techniques. A few of the most common methods for achieving the desired phase correction are shown in cross section in Fig. 1.5. The folded zone plate that has already been discussed is, in fact, a rudimentary phase-correcting zone plate. For comparison, this zone plate is shown again

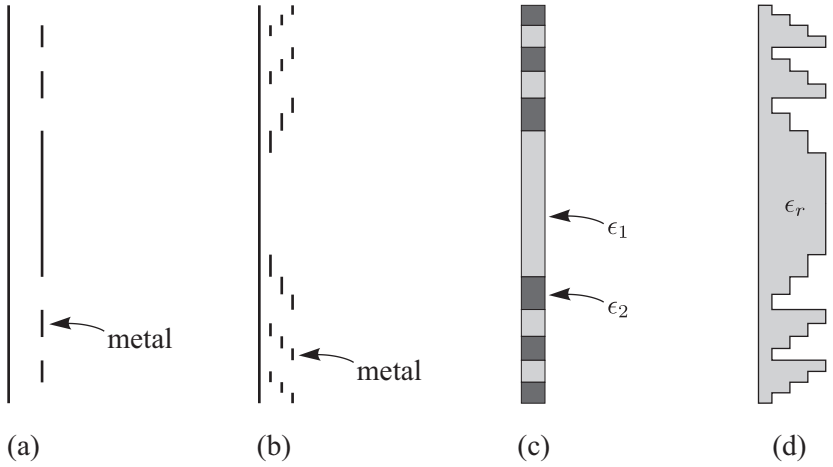

Figure 1.5: Geometry of various phase-correcting zone plates: (a) the folded zone plate, (b) the multilayer zone plate, (c) the planar lens, and (d) the grooved-dielectric, phase-correcting zone plate

in Fig. 1.5(a). As discussed, this zone plate imparts a phase shift by forcing parts of the incident field to travel an additional distance. The multilayer Fresnel zone plate, shown in Fig. 1.5(b), extends this idea further. Opaque annuli are placed at a number of different distances (three in the figure) away from the reflecting disc [8]. Each level of annuli imparts a different phase shift on a different portion of the incident field to correct the phase in finer increments than a folded zone plate. Fig. 1.5(c) shows a planar lens [9]. This zone plate, used in the transmission mode, incorporates two or more dielectrics to impart different phase shifts on the incident field. The zone plate in the figure is made from two dielectrics, and if the permittivities of the dielectrics, ϵ_1 and ϵ_2, are chosen correctly, this zone plate can have two planar interfaces. This feature is beneficial because it allows the zone plate to be mounted flush with a surface, such as a wall or the exterior of a ship or aircraft. One of the most commonly used methods to achieve phase correction is to cut circular grooves into a single dielectric slab, as shown in Fig. 1.5(d). It is this zone plate, the grooved-dielectric, phase-correcting zone plate, that will be considered in this work.

A grooved-dielectric, phase-correcting zone plate works by forcing the incident wave to travel through different amounts of the dielectric. The difference in travel time through the grooves adjusts the phase at the output plane of the zone plate. The axially symmetric geometry of this zone plate is shown in detail in Fig. 1.6. This type of zone plate is relatively

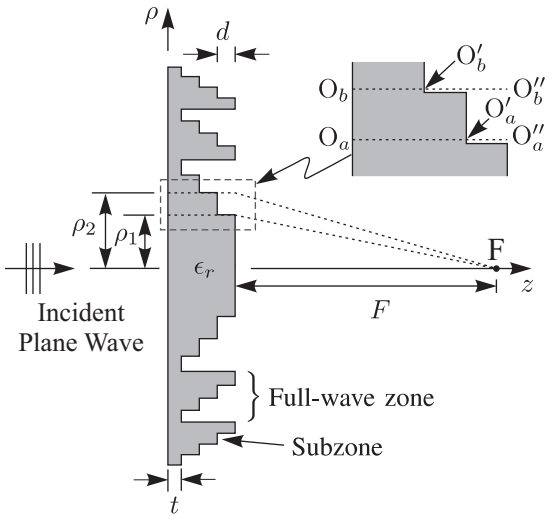

Figure 1.6: Cross section of the grooved-dielectric, phase-correcting zone plate.

simple to manufacture and does not require a dielectric with any particular permittivity.

When working with Soret and folded zone plates, it is a convenient to think about dividing the zone plate into N_{Soret} half-wave zones. For phase-correcting zone plates, however, the idea of fractional zones is not as useful; therefore, slightly different terminology is used. Instead of N_{Soret} half-wave zones, a phase-correcting zone plate is divided into N full-wave Fresnel zones. For a zone plate with N_{Soret} even, a phase-correcting zone plate with the same diameter has $N = N_{\text{Soret}}/2$ full-wave zones.

The zone plate shown in Fig. 1.6 has $N = 3$ full-wave zones. The focal length of the zone plate is F, and the diameter of the zone plate, D, is twice the radius of the outermost full-wave zone. In Sec. 1.1, a full-wave Fresnel zone was defined by the requirement that the distance from the focal point to the edge of a zone be a wavelength longer than the distance from the focal point to the edge of the previous zone. This requirement gives rise to the standard design formula for zone plates. The outer radius of the m^{th} full-wave zone is [10]

$$\Pi_m = \sqrt{(m\lambda)^2 + 2mF\lambda}, \quad m = 1, 2, ..., N. \tag{1.2}$$

Each of the full-wave zones is subdivided into P subzones ($P = 4$ are shown in the Fig. 1.6), defined such that the distance from the focal point to the edge of a subzone is λ/P longer than the distance from the focal point to the edge of the previous subzone. When

the subzones are numbered consecutively starting at the center of the zone plate, there are NP subzones. The outer radius of the n^{th} subzone is

$$\rho_n = \sqrt{\left(\frac{n\lambda}{P}\right)^2 + \frac{2nF\lambda}{P}}, \quad n = 1, 2, ..., NP. \tag{1.3}$$

When $P = 2$, Eq. (1.3) reduces to Eq. (1.1), as expected.

Because of the path length difference of λ/P established by Eq. (1.3), the phase of the contribution at F from each subzone lags the phase from the previous subzone by $2\pi/P$ radians. The phase is corrected to compensate for this by adjusting the thickness of the dielectric in each subzone. The velocity of an electromagnetic wave traveling through a dielectric is less than the velocity in free space, a fact that can be used to impart the opposite phase shift on the subzones closer to the focal point. For consecutive subzones, the thickness decreases by the distance d:

$$d = \frac{\lambda}{P\left(\sqrt{\epsilon_r} - 1\right)}, \tag{1.4}$$

in which ϵ_r is the relative permittivity of the dielectric.

An example is presented to illustrate the theory behind this design process. Consider the second and third subzones of the first full-wave zone shown in the inset in Fig. 1.6. The phases of the horizontal rays traveling through the zone plate at the inner radii of these zones are related by

$$2\pi\left[\left(\mathrm{O}_b\mathrm{O}'_b\right)\sqrt{\epsilon_r} + \left(\mathrm{O}'_b\mathrm{O}''_b\right)\right]/\lambda = 2\pi\left[\left(\mathrm{O}_a\mathrm{O}'_a\right)\sqrt{\epsilon_r} + \left(\mathrm{O}'_a\mathrm{O}''_a\right)\right]/\lambda - 2\pi/P. \tag{1.5}$$

This result together with Eq. (1.3) means that the rays travelling through these points and arriving at the focal point, F, are in phase:

$$2\pi\left[\left(\mathrm{O}_a\mathrm{O}'_a\right)\sqrt{\epsilon_r} + \left(\mathrm{O}'_a\mathrm{O}''_a\right) + \mathrm{O}''_a\mathrm{F}\right]/\lambda = 2\pi\left[\left(\mathrm{O}_b\mathrm{O}'_b\right)\sqrt{\epsilon_r} + \left(\mathrm{O}'_b\mathrm{O}''_b\right) + \mathrm{O}''_b\mathrm{F}\right]/\lambda. \tag{1.6}$$

Examining Eqs. (1.2), (1.3), and (1.4), it can be seen that the phase correction can be made smoother by increasing P. Figure 1.7 shows the effect on the profile of a zone plate of varying P. The figure shows profiles for zone plates with $P = 2$, $P = 4$, and $P = 8$, as well as the profile in the limit as $P \to \infty$.

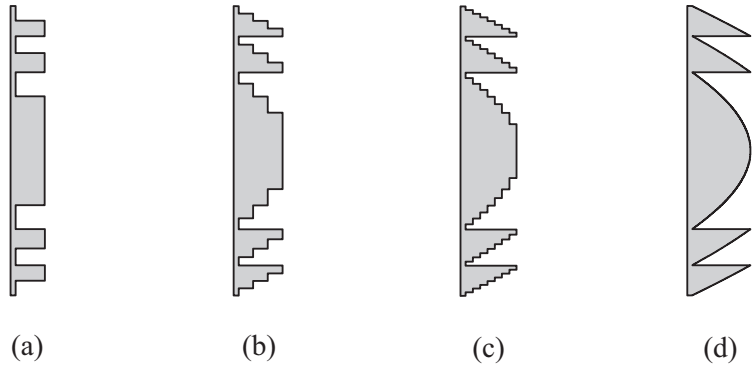

Figure 1.7: Cross sections of zone plates with (a) $P = 2$, (b) $P = 4$, (c) $P = 8$, and (d) $P \to \infty$.

When the design procedure described above is followed, the thickness of the outermost subzone in each full-wave zone is zero. While this produces the proper phase shift in these subzones, it presents a manufacturing problem, requiring concentric rings of dielectric to be suspended without support. The solution to this problem is to add a base of thickness t to each of the subzones. This base can be seen in Fig. 1.6. The base thickness is chosen for mechanical reasons, but it will be shown that it also affects the electromagnetic properties of the zone plate.

1.4 Applications of Zone Plates

Fresnel zone plates trace their history to the field of optics. It is not surprising, therefore, that most of the early zone plates were used as optical devices. One of the earliest applications of the zone plate was as an objective lens for an optical telescope built by Robert Wood. Using a gramophone needle to cut grooves in a wax-coated piece of glass, Wood created the first phase-correcting zone plate [4]. Because of this contribution, phase-correcting zone plates are frequently referred to as Wood-type zone plates [10]. Optical lenses are typically not very large, so the benefits of zone plates (reduced weight and thickness) are not needed for many applications. For this reason, the zone plate was considered an experimental curiosity for years.

Though scattered references appear in the literature after Wood's telescope [11], it was not until the middle of the twentieth century that researchers 'rediscovered' zone plates and began to widely utilize them in a variety of lower-frequency applications. A period

of experimental work served as the basis for the renewed interest in zone plates. Hull constructed a Soret zone plate with zones that could be individually removed to study the effect of the number of zones on the focusing ability [12], and Van Buskirk and Hendrix experimented with folded zone plates at X-band frequencies (8.2-12.4 GHz) [7]. Sanyal and Singh constructed both Soret and phase-correcting zone plates to perform a comparison, although they made a significant error in the calculation of the groove depth for the latter, which affected their conclusions [13].

Around this time, researchers began to use zone plates in communication systems. Sobel, Wentworth, and Wiltse developed a phase-correcting zone plate for millimeter-wave transmission systems [6]. Weibel and Dressel also used a phase-correcting zone plate receiver in millimeter-wave link experiments [14]. Zone plates are still being used in communications systems, especially for applications for which form-factor requirements exclude the use of other technologies. Curvilinear zone plates have been designed for radomes and other conformal antenna applications [15–17]. Wall- or roof-mounted zone plates have been commercialized for indoor communications [18, 19], and a zone plate integrated into a solar sail has been proposed as a light-weight option for space vehicle communications [20]. Cylindrical zone plates produce a beam that is omnidirectional in the azimuth plane and is ideal for wireless LAN coverage [21]. Zone plates with multiple focal points have been developed for satellite communications, allowing signals to be received from multiple satellites simultaneously [22].

Zone plates can also be adapted to different fabrication techniques. Integrated-circuit zone plate antennas have been developed as replacements for patch antennas at millimeter-wave frequencies [23, 24], while folded zone plates [25] and multilayered phase-correcting zone plates [8] have been fabricated directly on dielectric substrates.

Today, with improved manufacturing technology and the advent fiber-optics for high-bandwidth communications, the application of zone plates has returned full-circle to optics. Zone plates are used as collimating lenses for optical systems [26, 27] and as optical signal processing filters [28]. Other applications have arisen that require lenses to be as light as possible. Space-based telescopes for detecting extra-solar planets have been proposed,

requiring large apertures but minimal weight to reduce the cost of delivering the telescope to orbit [29, 30]. Zone plates are even used for photography. High-end camera lenses use zone plate-like focusing elements to correct for chromatic abberation without adding much weight [31, 32]. Soret zone plates, by themselves, are sometimes used as camera lenses because of the artistically desirable, soft-focus effect they produce [33].

Recent research has extended the use of zone plates to even higher frequencies, such as X-rays. At these frequencies, it is difficult to find a material with a refractive index that is appropriate for fabricating focusing elements. Soret and folded zone plates are particularly useful for the focusing these signals because they do not rely on refraction for focusing. Applications include zone plates for high resolution X-ray and Gamma-ray astronomy [34]. Some commercially available X-ray imaging systems also incorporate zone plates [35].

This section is not intended to present an exhaustive list of the applications for zone plates. Instead, the goal of this section is to convey a few examples that represent some of the diversity of what has historically been done and what is currently being done in the field of Fresnel zone plates. A number of other applications of zone plates are summarized in the books by Hristov [10], Minin and Minin [36, 37], and Guo and Barton [38].

1.5 Application to Free-Space, Focused-Beam Measurement Systems

A practical application that will be specifically addressed in this work is the use of zone plates as focusing elements in a free-space, focused-beam measurement system. The focused-beam system, as it will be referred to in the remainder of the document, is used to characterize the electromagnetic properties (complex permittivity and permeability) of a material. A typical focused-beam system, like the one shown in Fig. 1.8, consists of two horn antennas and two focusing elements. The field radiated by the transmit horn is converted by a lens into a Gaussian beam with the waist at the point where the sample of material is placed. Another lens focuses the field that is transmitted through the sample to the receive horn, where it is measured. In addition, the transmit horn is used to measure the field reflected from the sample. At the waist of a Gaussian beam, where the sample is placed, the phase is uniform and the amplitude has a Gaussian taper [39]. For a sample that is large enough

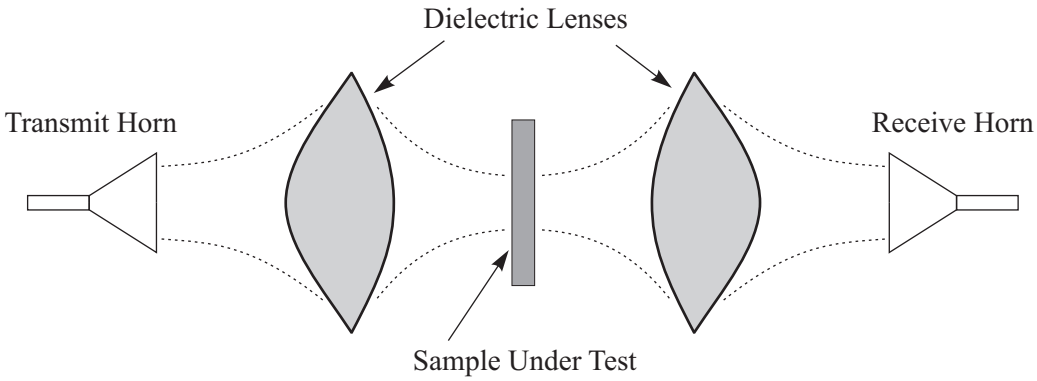

Figure 1.8: Schematic diagram of a focused-beam measurement system.

that the field of the beam is insignificant at its edges, the beam can be approximated as a plane wave normally incident on an infinite piece of the sample. Using this assumption, plane wave theory can be used to model the measurement system. The measured values of the reflection and transmission coefficients can then be used to calculate the complex permittivity and permeability of the sample [40–43].

The sizes of the components of a focused-beam system scale with the inverse of the frequency. For measurements at low frequencies, the size, weight, and cost of the dielectric lenses can become extreme. For example, the lenses in a system designed to make measurements for frequencies as low as 800 MHz, shown in Fig. 1.9, have a diameter of 6 feet and weigh thousands of pounds each. In addition to being difficult to manipulate, these lenses present manufacturing challenges: It is difficult to find a thick enough slab of material from which to machine the lenses, while molding the lenses also presents issues, including the presence of air bubbles in the completed lenses.

In this work, a zone plate will be evaluated as a replacement for the doubly-hyperbolic lens in a focused-beam system. A system that uses zone plates, like that seen in Fig. 1.10 offers a few distinct advantages. Zone plates are lighter and thinner than traditional lenses and could make a focused-beam system for low frequencies easier to setup and reconfigure. Additionally, zone plates could mitigate many of the manufacturing problems associated with lenses. A reduction in cost is another advantage of zone plates compared to lenses. For example, one common material used to make dielectric lenses and zone plates for microwave

Figure 1.9: Photograph of a focused-beam system designed to make material measurements for frequencies as low as 800 MHz. Image credit: Dr. John Schultz and STL/GTRI.

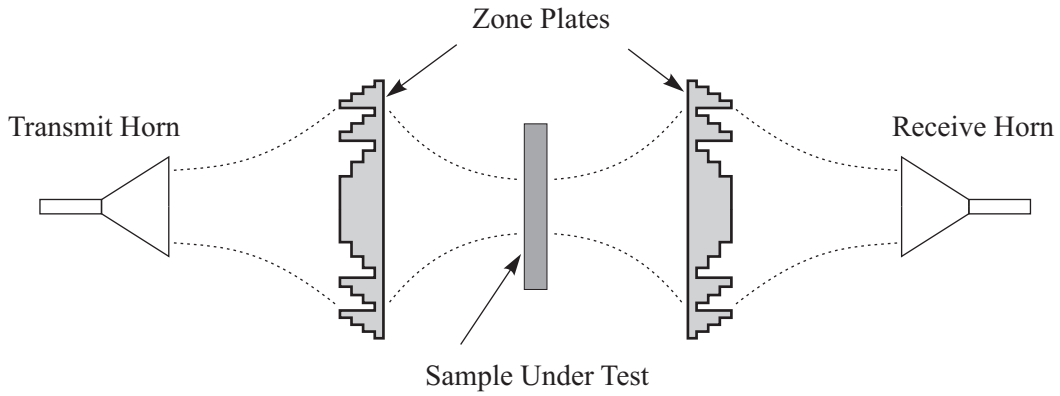

Figure 1.10: Schematic diagram of a focused-beam measurement system using zone plates.

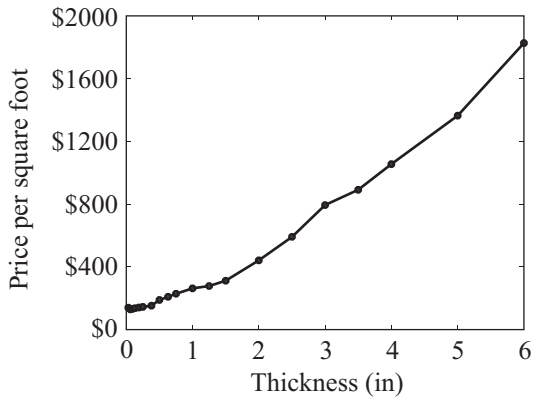

Figure 1.11: Cost per square foot of Rexolite (August 2008) [44].

and millimeter-wave frequencies is Rexolite. The cost of Rexolite increases nonlinearly with thickness, as can be seen in Fig. 1.11 [44]. The reduction in thickness of the zone plate therefore translates into an even larger reduction in cost. Because of the advantages in weight, thickness, and cost, zone plates may allow the operating frequency of a focused-beam system to be lowered further, to regions where lenses are prohibitively large.

Zone plates are not without their drawbacks, however. The most well-documented of these is their limited bandwidth [45]. Zone plates are diffractive devices and are designed to work at one particular frequency. This is evident from the presence of the wavelength-dependent terms in Eqs. (1.1)-(1.4). Away from the design frequency, the performance of the zone plate degrades. In addition, the field at the sample in a focused-beam system must have phase uniformity and a specified amplitude taper, as discussed above. The profile of a zone plate is discontinuous, and there is concern about how this will affect both of these qualities.

Hristov indicates indicate that Brandt, Pashin, and Petelin attempted to use zone plates for free-space measurement systems in 1958 (Figure 5.30 and reference #66 in [10]). Hristov's reference, which is in Russian, has not been found by this author.

1.6 A Discussion of Fresnel Lenses and Fresnel Zone Plates

In 1822, during his tenure as French Commissioner of Lighthouses, Fresnel developed a ground-breaking lighthouses lens. The visible range of a lighthouse beam is limited by the

optics used to collimate the light from the source, which was historically an oil lamp. In the early nineteenth century, the state of the art lighthouse optics were metal reflectors that were placed behind the source. These reflectors were inefficient, but lenses, which would be an improvement, were too heavy to be supported and rotated at the top of a lighthouse. Fresnel developed a much lighter lens by sectioning the lens and removing much of the glass from each section. The result is a lens, now called the Fresnel Lens, that *looks* similar to a phase-correcting Fresnel zone plate, specifically when $P \to \infty$. Because of this similarity in appearance and in name, it is easy to confuse the two devices. This section will briefly examine the theory behind the Fresnel lens to draw a distinction between it and the zone plate.

Figure 1.12 is a photograph of the author and a Fresnel lens from the lighthouse at Point Loma in San Diego, CA. The lens pictured is the original lens for the new Point Loma lighthouse, purchased in 1891 from Henry Le Paute of Paris, France for approximately $4,000. With the exception of a brief period of blackout during World War II, the lens was used continuously until 1997, when it was decommissioned [46]. A simplified schematic drawing of this Fresnel lens is given in Fig. 1.13. The lines emanating from the source show how the lens refracts rays of light.

Though Fresnel lenses resemble phase-correcting zone plates, they are fundamentally different devices. Zone plates are designed to work for a monochromatic source or incident plane wave. Their focusing is coherent: Through diffraction (and sometimes refraction), the phase of the field from each zone adds constructively at the focal point. Fresnel lenses, however, must collimate radiation from an incoherent source containing frequencies over the whole visible range. Fresnel lenses can achieve this because they are much larger with respect to the wavelength than the zone plates studied in this work. The center-most section of the lens in Fig. 1.12 is hundreds of thousands of wavelengths across at optical frequencies! The dimensions of the lens, therefore, do not need to be held to optical tolerances. Instead of the strict zoning described by Eq. (1.3), a Fresnel lens is designed by choosing a desired thickness for the lens and then ensuring that the profile in each section satisfies Snell's law of refraction. This refraction does not take the phase of the focused field into account, but

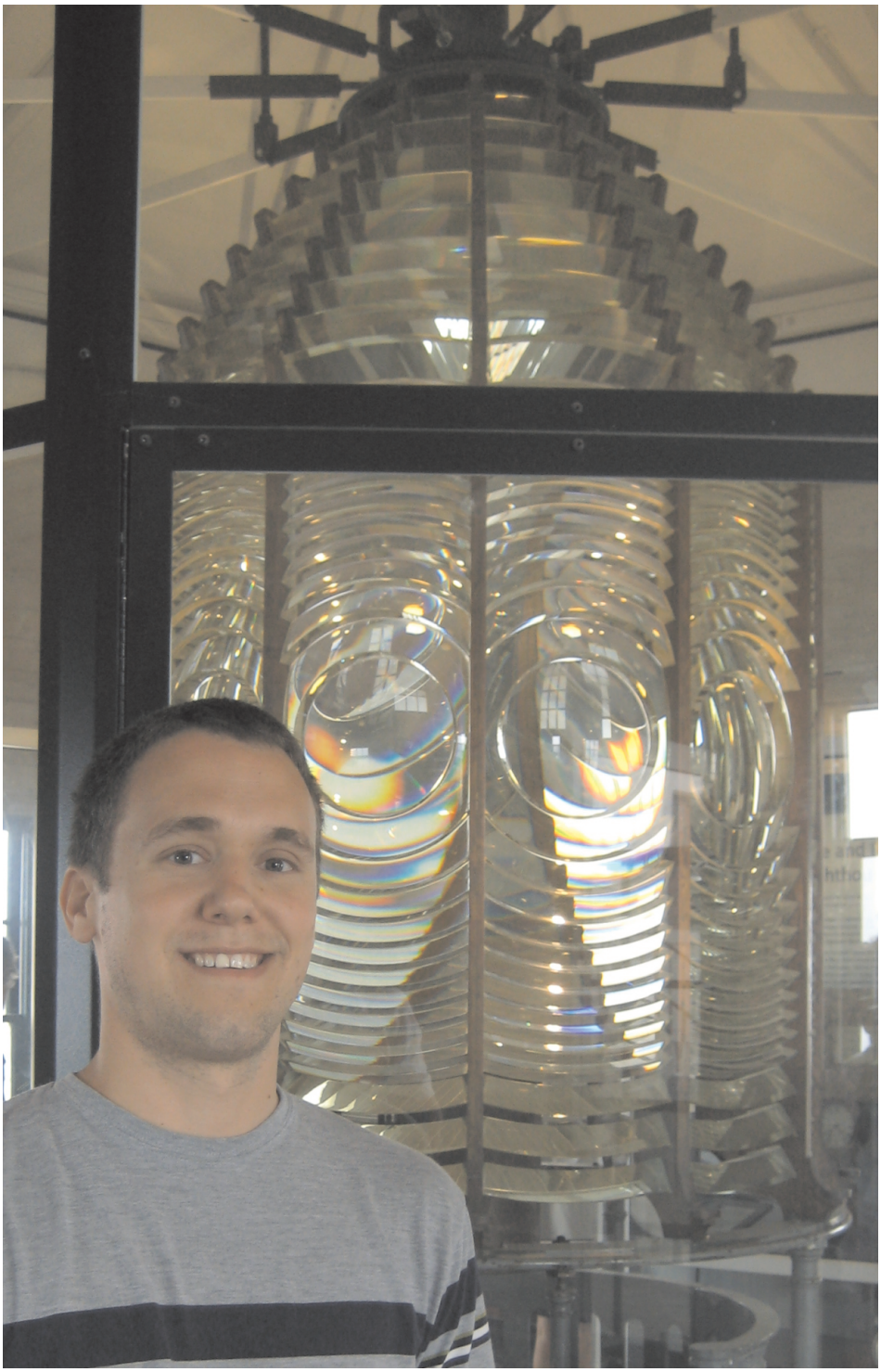

Figure 1.12: The author with a Fresnel lens at the Point Loma lighthouse in San Diego, CA.

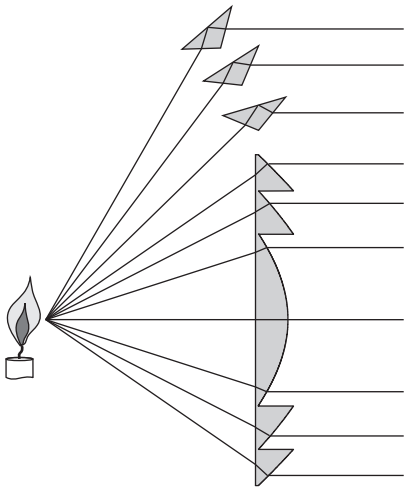

Figure 1.13: Schematic drawing of a Fresnel lens.

instead incoherently sums the power at the focal point. Unlike zone plates, Fresnel lenses use additional prisms to redirect the light radiated upwards by the source. These prisms can be seen in both Fig. 1.12 (in the conical-shaped section at the top of the lens) and in Fig. 1.13. Following the rays that are incident on these prisms in Fig. 1.13 shows that the prisms use both refraction and internal reflection to correct the ray's path. Historically, each ring and prism of the lens was fabricated by polishing a separate piece of glass. Fresnel lenses were not only a breakthrough for nautical safety and navigation, but also beautiful hand-crafted pieces of art.

1.7 Contribution of Research

This chapter has described the long history of the Fresnel zone plate. Despite all of the work that has been done, there are many aspects of zone plates that have never been addressed using a rigorous, full-electromagnetic analysis. It will be shown in this work that an accurate, full-electromagnetic method allows us to consider effects that are not accounted for using the simpler theories that are frequently applied to the analysis of zone plates. This is particularly important for microwave and millimeter-wave applications, where these effects can be significant.

A body-of-revolution finite-difference time-domain (BOR-FDTD) simulator was developed to address this shortcoming. This computer program allows zone plates to be examined

in more detail than they have in the past, and accounts for all of the factors that influence the focusing by a zone plate. This powerful modeling tool is applied to the study of two particular microwave/millimeter-wave applications of zone plates: zone plates used as antennas in communications applications and zone plates used as focusing elements in free-space, focused-beam measurement systems. Both of these applications allow distinct aspects of the zone plate to be examined. These studies examine a number of characteristics of zone plates in greater detail than has been done before. Results that are specific to these two applications, such as design graphs and system-level performance studies are an important contribution of this work. Many of the conclusions drawn are relevant to applications for zone plates in addition to the two discussed in this work.

This work is organized around these two applications. Within the context of these applications, individual topics of interest are addressed. A brief overview and an explanation of the contributions of each part of the dissertation follows.

The first zone plates examined are those used as antennas in communications applications. For these applications, the zone plate must either collimate radiation from a point source in the transmit mode, or focus an incident plane wave in the receive mode. The challenge when designing many antennas for communications systems is to collect (or transmit) as much power as possible. Parametric studies are performed for Soret, folded, and grooved-dielectric zone plate antennas to examine the effects of various parameters on the ability of the zone plates to collect or transmit power. The results of these studies are used to generate new design graphs for each type of zone plate. These design graphs will help engineers to choose the appropriate parameters to meet specific performance requirements and to evaluate tradeoffs made in the design process. In addition, the design graphs are used to make general statements about the effect of the configuration and the physical properties of the zone plate on its focusing ability.

When designing a grooved-dielectric, phase-correcting zone plate, a number of different parameters must be specified. Historically, these parameters have been chosen based on arguments derived using geometrical (ray-tracing) techniques, but it will be shown that these techniques are unable to account for many of the factors that influence the focusing.

In this work, the more accurate BOR-FDTD method is used to give new insight into the effect of these parameters. In particular, a few design choices are examined in detail; these include:

- the focal length of the zone plate
- the base thickness of the zone plate
- the effect of a matching layer
- the number of phase corrections per zone.

The resulting observations are used to develop general rules of thumb for designing zone plates.

A second, more novel application of zone plates is also studied. In this application, zone plates are used as focusing elements in a free-space, focused-beam system used to measure the electrical properties of sheets of material. In a focused-beam system, unlike most communications systems, both the source and the focal point are near the zone plate. The zone plate must, therefore, replace the functionality of a doubly-hyperbolic lens. The advantages of a zone plate over a lens for this application include a reduction in the weight and the amount of material needed to manufacture the device. These advantages allow the zone plate to be scaled for use at lower frequencies.

In this work, a zone plate is designed to replace a particular doubly-hyperbolic lens: the lens used in GTRI's existing focused-beam system. To this end, new design equations are developed for a zone plate that has one planar side (to simplify manufacturing). These design equations are used in conjunction with BOR-FDTD simulations to develop a novel zone plate that incorporates knowledge that was developed in the earlier stages of this work.

The use of this zone plate in a focused-beam system is studied both experimentally and with FDTD simulations. In a focused-beam system, the field at the beam waist (the sample location) is approximated as a plane wave. The feasibility of using a zone plate in this system therefore depends on the nature of the field in the focal region of the zone plate. In particular, one would like answers to the following questions:

- Is the amplitude taper of the field at the beam waist sufficient?
- Is the phase of the field at the beam waist sufficiently uniform?
- Is the field at the beam waist linearly polarized?
- Is the bandwidth of the zone plate large enough to warrant its use?

Measurements and simulations of the field focused by the existing lens are used as a baseline against which the performance of the zone plate is compared. The answer to these questions is important for this particular application, but the findings can be applied to zone plates in any focusing system.

As a final test, the complete focused-beam system, with the new zone plates as focusing elements, is used to measure the permittivity of dielectric sheets. To evaluate the accuracy of these measurements, the results obtained are compared to results for a system that uses the traditional lenses and to published values. A new technique for extending the bandwidth over which the zone plate can be used is proposed and tested. The results presented will allow designers to make an informed decision about whether the weight and cost savings offered by using a zone plate overshadow its disadvantages, principally reduced bandwidth.

The zone plates studied throughout this work are traditional designs which are based on optical, ray-tracing methods. With the power of full-wave simulators, such as the BOR-FDTD method, available, a natural question arises: If we were given a block of material of the same volume, could we use these methods to develop a focusing element that is better than the traditional zone plate? To start answering this question, the topic of non-traditional zone plate design is addressed. A preliminary analysis of one particular non-traditional design method is presented: Two zone plates, one for antenna applications and the other for focused-beam applications, are designed and optimized using a genetic algorithm. These zone plates are compared with traditionally-designed zone plates and with lenses and are shown to have improved performance. However, the value of these improvements depends on the requirements of a particular application.

1.8 Outline

In this section, an outline of this dissertation is presented. Figure 1.14 is a graphical representation of this outline and the organizational structure of this work. In this chapter, Chapter 1, the basic operation of a zone plate was described and their applications discussed. The particular application of zone plates to a free-space, focused-beam measurement system was introduced. In Chapter 2, the methods that are typically used to analyze zone plates are described, and the need for a rigorous, full-electromagnetic analysis is explained. The technique chosen for this research, the BOR-FDTD method, is applied to the zone plate. The computational tool that results is used throughout the remainder of this work.

The first application of zone plates studied is in antennas for communications systems, as discussed in Sec. 1.4. In Chapter 3, a visualization of the Poynting vector near a zone plate is used to discuss the focusing mechanism of the Soret zone plate. Metrics for evaluating zone plate antennas are defined, and parametric studies for Soret and folded zone plates are used to generate design graphs based on these metrics. These design graphs are used to make general observations about the effect of various design parameters on the focusing ability of zone plates. Existing measurements for integrated-circuit zone plate antennas are used to validate the BOR-FDTD simulations for Soret zone plates.

In Chapter 4, a similar study to that in Chapter 3 is performed for grooved-dielectric, phase-correcting zone plates. Design graphs are presented for this type of zone plate as well. Individual design choices, including the focal length, the base thickness, the use of a matching layer, and the number of phase corrections per subzone are evaluated using BOR-FDTD simulations. Existing measurements for the field focused by a doubly-hyperbolic lens and the far-field pattern of a grooved-dielectric zone plate are used to validate the BOR-FDTD simulations for these devices.

Starting with Chapter 5, research done on the second application is presented. The lens used for GTRI's standard focused-beam system is discussed, and design equations for a single-sided zone plate to replace this lens are derived. BOR-FDTD simulations are used to compare the focusing ability of a single lens with a single zone plate. The application of the zone plate to a focused-beam system is then studied using simulation results, and a

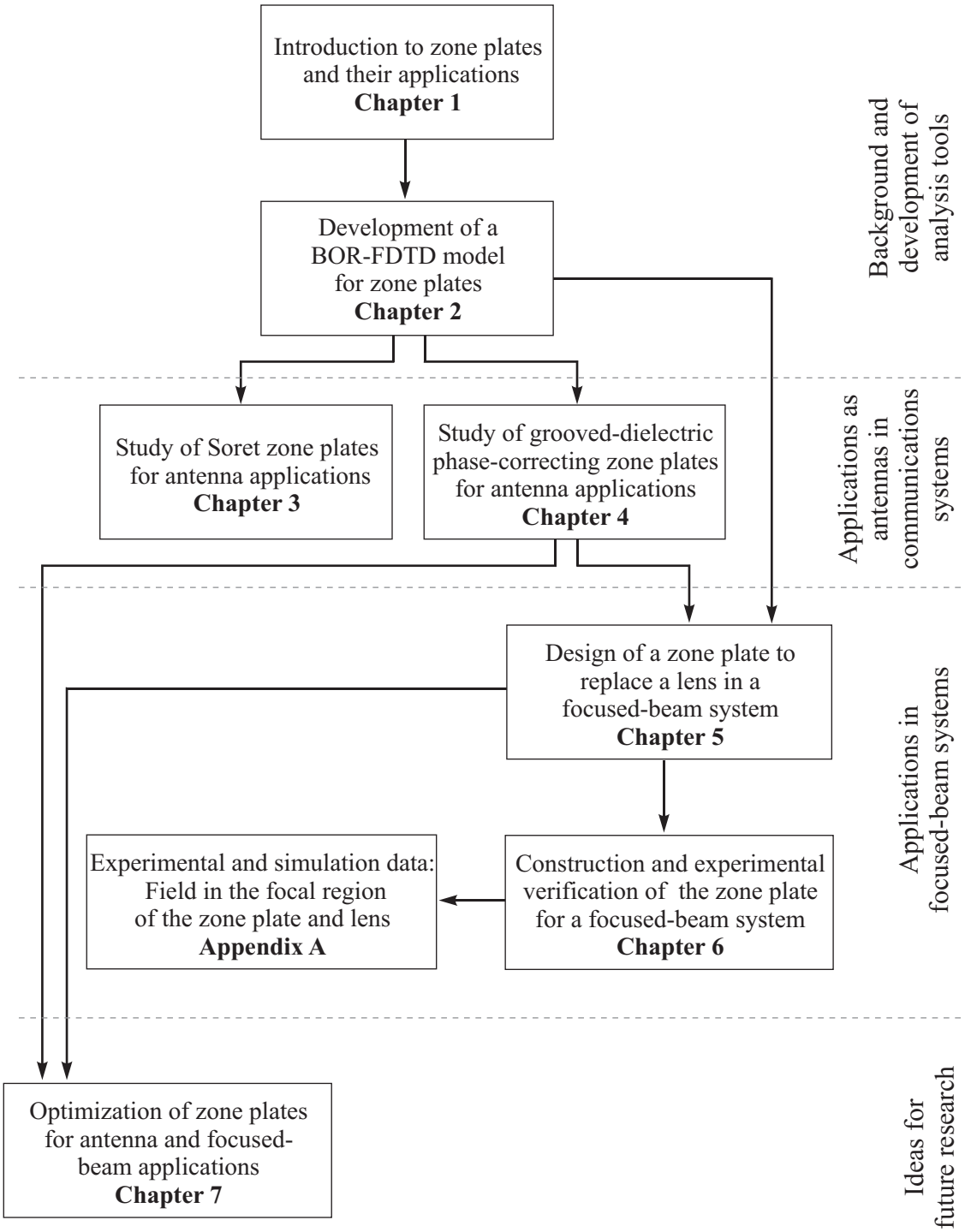

Figure 1.14: Outline of research.

proposal for improving the usable bandwidth of the zone plate is presented.

In Chapter 6, this zone plate is studied both with simulations and with measurements. The fabrication procedure for the zone plate is discussed, as is the measurement system used to probe the field focused by the zone plate. The questions expressed earlier about the field focused by the zone plate are individually addressed. Finally, a full focused-beam system with zone plates as focusing elements is tested. To evaluate the accuracy of the system, permittivity measurements for three different materials are presented and compared to measurements from a system that uses lenses and to published values.

Chapter 7 is concerned with the improvement of zone plate performance using non-traditional methods in the design process. This idea is only briefly explored; it is mainly presented as a topic for future research. The particular example of zone plates designed with a genetic algorithm (GA) is presented. A brief overview of the GA is given, followed by a discussion of the formulation of the zone plate optimization problem. A zone plate for antenna applications is designed using the GA and is compared with a lens and a traditionally-designed zone plate. The same process is repeated for a zone plate for focused-beam applications. The value of the improvement achieved with the optimization is discussed.

CHAPTER II

BOR-FDTD ANALYSIS OF ZONE PLATES

The synthesis of a zone plate, based on the simple but powerful principles discussed in the introduction, is straightforward. The accurate analysis of such a device, however, is far more difficult. In this chapter, an overview of the techniques that are typically used to analyze zone plates is presented. The merits and accuracy of these techniques are discussed. The primary analysis technique used in this work, the body-of-revolution, finite-difference time-domain (BOR-FDTD) method, is presented, and the implementation of this technique for the analysis of zone plates is described.

2.1 Overview of Techniques for the Analysis of Zone Plates

A number of different techniques have been used to analyze Fresnel zone plates. These techniques vary in complexity, depending on the accuracy required and the geometrical properties of the zone plate. The simplest and earliest methods are based on geometrical optics principles, which follow the same reasoning that Soret, Rayleigh, and Wood used in the development of zone plates [7, 10]. These methods rely on the assumption that $(F/D)^2 \gg 1$, and therefore the contribution of every zone to the field at the focus is approximately the same. For optical zone plates, this is a decent approximation, and since most early zone plates were for optical applications, these methods were sufficient.

As zone plates began to be used outside of optics, different techniques were applied to their analysis. Kirchhoff diffraction theory is one method that is frequently used to analyze zone plates. The scalar Kirchhoff diffraction integral has been applied to the analysis of zone plates with general feeds [13, 47], while zone plates for which the polarization of the feed is important have been treated with the vectorial Kirchhoff diffraction integral [48]. Using this technique, the solution of the wave equation at a point in space is expressed in terms of the solution of the wave equation and its derivative at all points on a closed surface surrounding the point [49]. This closed surface is typically chosen to be a hemisphere

of large radius. The aperture of the zone plate is contained in the planar section of the hemisphere. The electromagnetic field is assumed to be uniform over each open subzone of a Soret zone plate and an integration is performed over each of these subzones. The field and its derivative are assumed to be zero over each blocked subzone and on the spherical section of the hemisphere, far from the zone plate. In a phase-correcting zone plate, the phase shift of the field is assumed to be perfect, and an integration is performed over the entire zone plate.

The assumption that the electromagnetic field is uniform over each subzone is not necessarily good, however. For this assumption to be valid, the widths of the subzones ($\Delta\rho_n$) must be large compared to the wavelength; certainly $\Delta\rho_n/\lambda > 1$. When the condition $NP \gg 1$ is satisfied, which is true for many practical zone plates, the minimum width for a subzone (the outer one, $n = NP$) is

$$\left(\frac{\Delta\rho_n}{\lambda}\right)_{\min} = \left(\frac{\Delta\rho_{NP}}{\lambda}\right) \approx \frac{1}{P}\sqrt{1 + 4\left(\frac{F}{D}\right)^2}\,. \tag{2.1}$$

Upon solving Eq. (2.1) for F/D, we have

$$\frac{F}{D} \approx \frac{1}{2}\sqrt{P^2\left(\frac{\Delta\rho_n}{\lambda}\right)^2_{\min} - 1}\,. \tag{2.2}$$

A typical value for the number of subzones per full-wave zone in a phase-correcting zone plate is $P = 4$, and for the inequality $\Delta\rho_n/\lambda > 1$ to be satisfied, we should at least have $(\Delta\rho_n/\lambda)_{\min} = 2$. Upon substituting these numerical values into Eq. (2.2), we find that F/D must be greater than four. This is a condition usually satisfied for zone plates used at optical frequencies but not for those used at microwave and millimeter-wave frequencies [11].

In addition to the Kirchhoff diffraction integral, more advanced diffraction techniques have been applied to the analysis of zone plates. These methods rely on modifying the Kirchhoff solution to include combinations of the geometric theory of diffraction, uniform asymptotic theory, and edge current corrections, among other techniques [23, 24, 50–52]. The drawback of these diffraction techniques is that they are not valid for zone plates of all sizes or for determining the radiation patterns in all directions. To use these methods,

the results from different techniques must be stitched together to form a meaningful design graph over a large range of design parameters [51].

An additional difficulty imposed on the analysis of phase-correcting zone plates, which is not present in the case of the Soret zone plates, is the need to model reflections and other physical effects of the dielectric. A method has been presented that addresses this issue by incorporating plane-wave reflection and transmission coefficients into the model [53]. Each subzone is first treated as an infinite slab of dielectric, and the coefficients for the infinite series of internal reflections are computed. These coefficients are then incorporated into the field calculations. This method is an improvement over methods that treat each subzone as an ideal phase shifter, but it still relies on the assumption that the reflections can be treated as independent plane-wave reflections.

In light of the issues mentioned above, the way to ensure that microwave and millimeter-wave zone plates are modeled accurately over a wide range of parameters is to use a full-electromagnetic technique. In the past, researchers have done this by applying rigorous numerical techniques to the analysis of zone plates, including integral equation methods [27, 54] and finite-difference time-domain (FDTD) methods [55, 56]. A good FDTD analysis for phase-correcting zone plates used as optical microlenses has been reported, in which design graphs are presented that demonstrate the effect of the f-number (the ratio of the focal length to the diameter, F/D) on the focusing ability of the microlenses [57].

2.2 The BOR-FDTD Method

The full-electromagnetic technique used in this work is the body-of-revolution finite-difference time-domain (BOR-FDTD) method. The BOR-FDTD algorithm exploits the rotational symmetry of Fresnel zone plates and is therefore a natural choice for modeling the devices. For the most part, the standard implementation of BOR-FDTD is used. In this section, the basics of the method will be explained, without dwelling on the details that can be found in the literature [58, 59]. This discussion will provide the background necessary to understand the specific adaptations that are made to the algorithm to model zone plates.

Using BOR-FDTD, the computational cost of modeling zone plate antennas is reduced

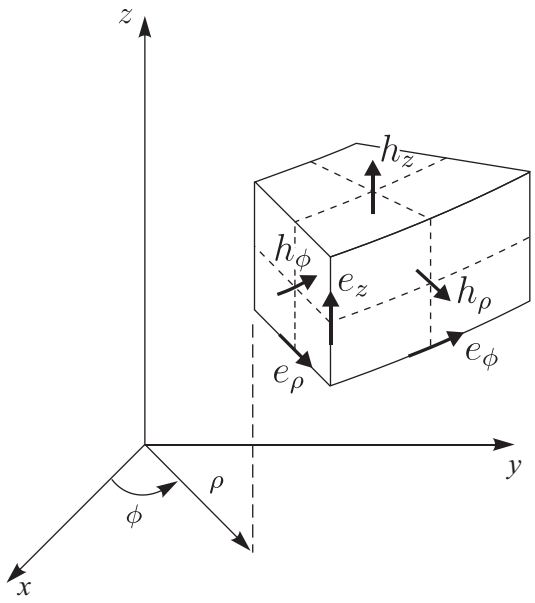

Figure 2.1: Three-dimensional layout of field components for FDTD in cylindrical coordinates.

by decomposing the electromagnetic field into a Fourier series of rotationally symmetric modes:

$$\begin{aligned}\vec{E}(\rho,\phi,z,t) &= \sum_{m=0}^{\infty} \vec{e}_u(\rho,z,t,m)\cos m\phi + \vec{e}_v(\rho,z,t,m)\sin m\phi \\ \vec{H}(\rho,\phi,z,t) &= \sum_{m=0}^{\infty} \vec{h}_u(\rho,z,t,m)\cos m\phi + \vec{h}_v(\rho,z,t,m)\sin m\phi\,, \end{aligned} \tag{2.3}$$

in which the Fourier coefficients ($\vec{e}_u$, $\vec{e}_v$, $\vec{h}_u$, and $\vec{h}_v$) represent the electric and magnetic field and are unknown, the Fourier mode is represented by m, and the subscripts u and v indicate fields with cosinusoidal and sinusoidal dependence, respectively.

When the Fourier-series representation of the field, Eq. (2.3), is substituted into Maxwell's equations, a time-stepping algorithm can be developed to find values of the Fourier-series coefficients at a future time from those at the present time using a computer. To do this, a volume of space is discretized and the differential equations are approximated as difference equations using the central difference approximation. A cylindrical volume of space can be discretized in a manner similar to the Yee method for a rectangular lattice [60], with spatially-staggered field components that can be seen in Fig. 2.1. Rearranging the difference equations results in FDTD update equations in cylindrical coordinates. The field

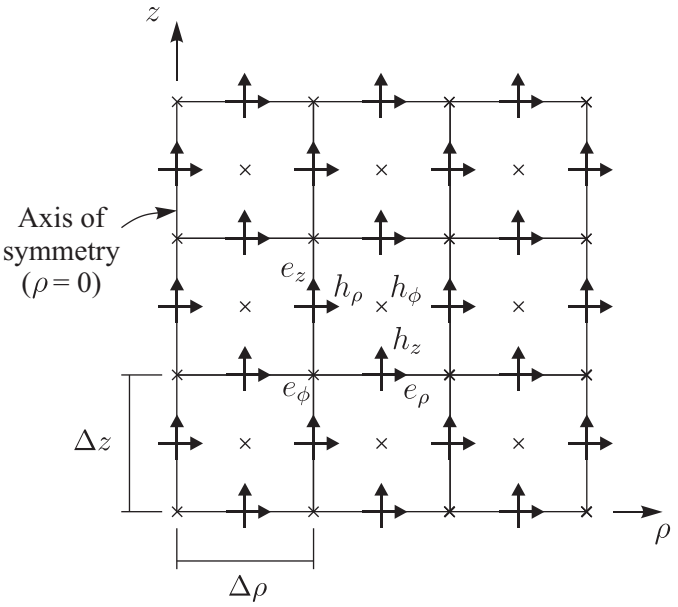

Figure 2.2: Two-dimensional layout of field components for BOR-FDTD.

values are computed in a leap-frogging fashion: The values of the magnetic field components are computed from the neighboring electric field components, the time is advanced by a half time step ($\Delta t/2$), and the electric field components are computed from the neighboring magnetic field components. This process, referred to as *updating* the field components, is then repeated until a specified number of time steps have been completed.

The computational advantage of the BOR-FDTD method comes from the fact that the azimuthal (ϕ) dependence can be removed from these equations and calculated analytically. This reduces the computational space to one with two dimensions, while preserving knowledge of the solution in three dimensions. The two-dimensional grid that is used for BOR-FDTD simulations is shown in Fig. 2.2. The spacing between a field component and the nearest occurrence of the same component is $\Delta\rho$ in the ρ-direction and by Δz in the z-direction. Notice that there are now co-located field components (e_z and h_ρ, h_z and e_ρ), which differs from the standard Yee method. A position within this grid with the coordinates (ρ, z) is represented by the indices $i = \rho/\Delta\rho$ and $k = z/\Delta z$. The magnetic field components are computed for integer time steps, $n = t/\Delta t$, and the electric field components are computed for a time that is a half-time step later, $n + 1/2$. It is important to note that, for a given mode m, Eq. (2.3) can be decomposed into two sets of fields which

are independent for isotropic materials :

$$\begin{aligned}
\vec{E}(\rho,\phi,z,t,m) &= \sum_{m=0}^{\infty}\vec{E}_A(\rho,\phi,z,t,m)+\sum_{m=0}^{\infty}\vec{E}_B(\rho,\phi,z,t,m)\\
\vec{H}(\rho,\phi,z,t,m) &= \sum_{m=0}^{\infty}\vec{H}_A(\rho,\phi,z,t,m)+\sum_{m=0}^{\infty}\vec{H}_B(\rho,\phi,z,t,m)\,.
\end{aligned}\tag{2.4}$$

In these equations

$$\begin{aligned}
\vec{E}_A(\rho,\phi,z,t,m) &= e_\rho\cos(m\phi)\hat{\rho}+e_\phi\sin(m\phi)\hat{\phi}+e_z\cos(m\phi)\hat{z}\\
\vec{H}_A(\rho,\phi,z,t,m) &= h_\rho\sin(m\phi)\hat{\rho}+h_\phi\cos(m\phi)\hat{\phi}+h_z\sin(m\phi)\hat{z}\,,
\end{aligned}\tag{2.5}$$

$$\begin{aligned}
\vec{E}_B(\rho,\phi,z,t,m) &= e_\rho\sin(m\phi)\hat{\rho}+e_\phi\cos(m\phi)\hat{\phi}+e_z\sin(m\phi)\hat{z}\\
\vec{H}_B(\rho,\phi,z,t,m) &= h_\rho\cos(m\phi)\hat{\rho}+h_\phi\sin(m\phi)\hat{\phi}+h_z\cos(m\phi)\hat{z}\,,
\end{aligned}\tag{2.6}$$

and the space-time-mode dependence of the Fourier coefficients $(e_*(\rho,z,t,m)\,,\ h_*(\rho,z,t,m))$ has been suppressed for clarity. The BOR-FDTD update equations for the fields with the azimuthal dependence of Eq. (2.5) are:

$$\begin{aligned}
e_\rho|^{n+1/2}_{i+1/2,\,k} &= e_\rho|^{n-1/2}_{i+1/2,\,k}+\frac{\Delta t}{\epsilon\Delta z}\left(h_\phi|^{n}_{i+1/2,\,k-1/2}-h_\phi|^{n}_{i+1/2,\,k+1/2}\right)\\
&+ \frac{m\Delta t}{\epsilon(i+1/2)\Delta\rho}h_z|^{n}_{i+1/2,\,k}\\
e_\phi|^{n+1/2}_{i,\,k} &= e_\phi|^{n-1/2}_{i,\,k}+\frac{\Delta t}{\epsilon\Delta\rho}\left(h_z|^{n}_{i-1/2,\,k}-h_z|^{n}_{i+1/2,\,k}\right)\\
&+ \frac{\Delta t}{\epsilon\Delta z}\left(h_\rho|^{n}_{i,\,k+1/2}-h_\rho|^{n}_{i,\,k-1/2}\right)\\
e_z|^{n+1/2}_{i,\,k+1/2} &= e_z|^{n-1/2}_{i,\,k+1/2}-\frac{m\Delta t}{\epsilon i\Delta\rho}h_\rho|^{n}_{i,\,k+1/2}\\
&+ \frac{(i+1/2)\Delta t}{\epsilon i\Delta\rho}h_\phi|^{n}_{i+1/2,\,k+1/2}-\frac{(i-1/2)\Delta t}{\epsilon i\Delta\rho}h_\phi|^{n}_{i-1/2,\,k+1/2}\\
h_\rho|^{n+1}_{i,\,k+1/2} &= h_\rho|^{n}_{i,\,k+1/2}+\frac{\Delta t}{\mu\Delta z}\left(e_\phi|^{n+1/2}_{i,\,k+1}-e_\phi|^{n+1/2}_{i,\,k}\right)\\
&+ \frac{m\Delta t}{\mu i\Delta\rho}e_z|^{n+1/2}_{i,\,k+1/2}\\
h_\phi|^{n+1}_{i+1/2,\,k+1/2} &= h_\phi|^{n}_{i+1/2,\,k+1/2}+\frac{\Delta t}{\mu\Delta\rho}\left(e_z|^{n+1/2}_{i+1,\,k+1/2}-e_z|^{n+1/2}_{i,\,k+1/2}\right)\\
&+ \frac{\Delta t}{\mu\Delta z}\left(e_\rho|^{n+1/2}_{i+1/2,\,k}-e_\rho|^{n+1/2}_{i,\,k+1}\right)\\
h_z|^{n+1}_{i+1/2,\,k} &= h_z|^{n}_{i+1/2,\,k}+\frac{\Delta t}{(i+1/2)\mu\Delta\rho}\left(ie_\phi|^{n+1/2}_{i,\,k}-(i+1)e_\phi|^{n+1/2}_{i+1,\,k}\right)\\
&- \frac{m\Delta t}{(i+1/2)\mu\Delta\rho}e_\rho|^{n+1/2}_{i+1/2,\,k}\,.
\end{aligned}\tag{2.7}$$

For these equations, the ϕ-dependence of the field has been removed and the co-located field components have been accounted for.

Figure 2.2 also shows that there are field components located along the z-axis (e_ϕ, e_z, and h_ρ). These components require special boundary conditions, and therefore special update equations. The e_z component is zero for any mode $m > 0$. Additionally, e_ϕ and h_ρ are zero for any mode $m \neq 1$ [58]. The update equations for the on-axis components are:

$$
\begin{aligned}
e_z|_{0,\,k+1/2}^{n+1/2} &= \begin{cases} e_z|_{0,\,k+1/2}^{n-1/2} + \frac{4\Delta t}{\epsilon \Delta \rho} h_\phi|_{1/2,\,k+1/2}^{n} & m = 0 \\ 0 & m > 0 \end{cases} \\
e_\phi|_{0,\,k}^{n+1/2} &= \begin{cases} e_\phi|_{0,\,k}^{n-1/2} - \frac{2\Delta t}{\epsilon \Delta \rho} h_z|_{1/2,\,k}^{n} \\ \quad + \frac{\Delta t}{\epsilon \Delta z}\left(h_\rho|_{0,\,k+1/2}^{n} - h_\rho|_{0,\,k-1/2}^{n} \right) & m = 1 \\ 0 & m \neq 1 \end{cases} \\
h_\rho|_{0,\,k+1/2}^{n+1} &= \begin{cases} h_\rho|_{0,\,k+1/2}^{n} + \frac{\Delta t}{\mu \Delta \rho} e_z|_{1,\,k+1/2}^{n+1/2} \\ \quad + \frac{\Delta t}{\mu \Delta z}\left(e_\phi|_{0,\,k+1}^{n+1/2} - e_\phi|_{0,\,k}^{n+1/2} \right) & m = 1 \\ 0 & m \neq 1\,. \end{cases}
\end{aligned}
\tag{2.8}
$$

The field components that are solved for in Eqs. (2.7) and (2.8) can be substituted into Eq. (2.5) to reconstruct the full three-dimensional field.

The update equations given in Eqs. (2.7) and (2.8) are only for fields with the azimuthal dependence described by Eq. (2.5). For many problems, these equations are sufficient to describe the field. In general, however, the solution to a problem is wholly or partially comprised of fields with the azimuthal dependence described by Eq. (2.6). In this case, a relationship between Eq. (2.5) and Eq. (2.6) can be exploited so that the update equations for Eq. (2.6) do need to be implemented. If all of the field components in Eq. (2.6) are rotated by $\phi_r = 90^\circ$ about the axis of symmetry, the resulting field has the azimuthal dependence of Eq. (2.5). Therefore, to simulate fields with the azimuthal dependence of Eq. (2.6), the fields of the source can be transformed (rotated by $\phi_r = 90^\circ$), the simulations can be run using the update equations given in Eqs. (2.7) and (2.8), and the results can be transformed back. For $m = 0$, the update equations simplify to the same form, so no transformations are necessary.

Additionally, the Fourier modes represented by m in Eq. (2.3) are orthogonal. This means that a separate BOR-FDTD simulation can be run for each mode, and the results from all modes can be superimposed to obtain the complete field. The number of modes (and therefore independent simulations) required depends on the nature of the problem. Problems with a rotationally symmetric electromagnetic field, such as a monopole oriented along the axis of symmetry, can be represented using only the $m = 0$ mode [61]. Other problems, such as those with linearly polarized fields propagating along the axis of symmetry, can also be represented with a single mode, the $m = 1$ mode. In general, however, some number of modes greater than one will be necessary to represent the electromagnetic field. As more modes are added, the numerical stability condition changes. An empirically-determined representation of the stability condition is given in [58]:

$$\Delta t \leq \Delta x / sc \,, \tag{2.9}$$

in which Δx is the cell size ($\Delta\rho$ or Δz), c is the speed of light in free space, $s \approx m + 1$ for $m > 0$, and $s = \sqrt{2}$ for $m = 0$. This means that, for a fixed cell size, the number of time steps necessary to represent the same amount of actual time increases with m. Therefore, much of the benefit of the BOR-FDTD method is lost as the number of modes (m) needed grows. This is not a concern for this work, however, because all of the problems addressed here can be represented by the $m = 1$ mode.

2.3 BOR-FDTD Modeling of Zone Plates

The goal of this section to illustrate how the BOR-FDTD method is used to model zone plates. Details about the method, including the simulation setup, simulation parameters, and the source conditions will be discussed. The parallelization of the method will be explained. Special attention will be given to methodologies that are not a standard part of the BOR-FDTD algorithm, including a technique for modeling the field from a pyramidal horn.

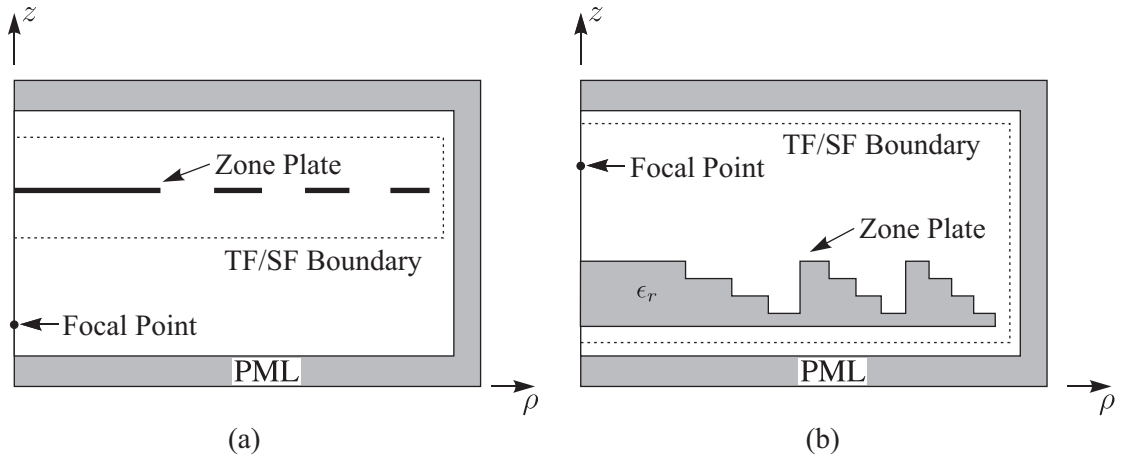

Figure 2.3: Geometry for the BOR-FDTD simulation of (a) a Soret zone plate antenna and (b) a phase-correcting zone plate antenna.

2.3.1 Simulation Parameters

The representation of the physical region modeled by the BOR-FDTD method is called the simulation space. The simulation space includes the zone plate and the free space that surrounds it and is shown in Fig. 2.3 for two problems that are typical of those encountered in this work. The opaque zones that make up a Soret zone plate, shown in Fig. 2.3(a), are constructed from PEC annuli and are incorporated into a simulation by setting the tangential components of the electric field to zero along the surface of the BOR-FDTD cells that coincide with the annuli. In the case of the folded zone plate (not shown in Fig. 2.3), the reflector is modeled as a PEC disc with a diameter equal to the diameter of the outermost closed zone, D. A phase-correcting zone plate, shown in Fig. 2.3(b) is modeled as a collection of annular rings of dielectric with the relative permittivity ϵ_r.

The numerical representation of an electromagnetic wave accumulates error as it propagates through a discretized space. These errors, called numerical dispersion, are due to small errors in the velocity of propagation of an electromagnetic wave in the FDTD grid and increase as the path traveled by the wave gets longer. This is particularly troublesome because the zone plates simulated in this work are electrically-large structures (up to 75 wavelengths in diameter). The error due to numerical dispersion can be decreased by increasing the sampling density of the FDTD grid. Experimentation with the BOR-FDTD

model showed that sampling density of 100 cells per wavelength sufficiently reduced the error from dispersion. The simulation space is discretized into cells that are square ($\Delta\rho = \Delta z$ in Fig. 2.2). As an added benefit, the fine sampling density also ensures that the features of a zone plate are modeled in adequate detail.

As Fig. 2.3 shows, the geometries that are modeled for this work consist of a zone plate in free space. To accurately model such a structure, an absorbing boundary condition is necessary to prevent reflections at the edge of the simulation space. The absorbing boundary condition used is the uniaxial perfectly matched layer (PML). The uniaxial PML is a region of anisotropic material with parameters that are carefully chosen to absorb as much of the incident field as possible while reflecting as little as possible. Details of its implementation in cylindrical coordinates can be found in [58]. The PML can be seen surrounding the simulation space on three sides in Fig. 2.3.

2.3.2 Source Conditions

One of the advantages of the FDTD method is that it produces time-domain results, which can be Fourier transformed into the frequency domain. Therefore, a single time-domain simulation gives results over a broad range of frequencies. This range of frequencies can be controlled by the time-domain waveform. In this work, two different waveforms are used. The differentiated Gaussian pulse is used for modeling zone plate antennas:

$$E_{\mathrm{dg}}(t) = -E_{\mathrm{o}} \left(\frac{t}{\tau_p}\right) \exp\left\{-\left[(t/\tau_p)^2 - 1\right]/2\right\} , \tag{2.10}$$

in which $\tau_p = 1/\omega_p$ and ω_p is the center frequency in radians/sec. This waveform offers a broad range of frequencies without significant low-frequency content, which can be problematic for FDTD simulations [62]. The Fourier transform of Eq. (2.10) is

$$E_{\mathrm{dg}}(\omega) = j\omega\tau_p^2\sqrt{2\pi}E_{\mathrm{o}} \exp\left\{-\left[(\omega\tau_p)^2 - 1\right]/2\right\} . \tag{2.11}$$

For some applications, such as a focused-beam system, a pulse with a narrower bandwidth is desired. For these applications, a modulated Gaussian pulse is used:

$$E_{\mathrm{mg}}(t) = E_{\mathrm{o}} \exp\left[-(t/\tau_p)^2/2\right] \sin(\omega_{\mathrm{o}} t) . \tag{2.12}$$

The Fourier transform of Eq. (2.12) is

$$\begin{aligned} E_{\mathrm{mg}}(\omega) &= -\frac{j}{2}\tau_p\sqrt{2\pi}E_{\mathrm{o}}\exp\left\{-\left[(\omega-\omega_{\mathrm{o}})\,\tau_p\right]^2/2\right\} \\ &\quad +\frac{j}{2}\tau_p\sqrt{2\pi}E_{\mathrm{o}}\exp\left\{-\left[(\omega-\omega_{\mathrm{o}})\,\tau_p\right]^2/2\right\}\,. \end{aligned} \tag{2.13}$$

The frequency content of a modulated Gaussian pulse can be controlled by choosing ω_{o} and τ_p.

Three different types of source conditions are used in this study. The simplest of these is a model for an infinitesimal dipole, oriented along the ρ-axis for $\phi = 0$. The dipole is a 'hard source' implemented by setting the field to a particular value. For a specified location z, the e_ρ component closest to the axis is driven with a differentiated Gaussian pulse in time.

The remaining two sources are based on the total-field scattered-field (TF/SF) formulation. The idea behind the TF/SF formulation is that the total electromagnetic field can be decomposed into an incident component and a scattered component,

$$\begin{aligned} \vec{E}_{\mathrm{tot}} &= \vec{E}_{\mathrm{inc}} + \vec{E}_{\mathrm{scat}} \\ \vec{H}_{\mathrm{tot}} &= \vec{H}_{\mathrm{inc}} + \vec{H}_{\mathrm{scat}}\,, \end{aligned} \tag{2.14}$$

and these components can be treated separately throughout the simulation space. The 'inc' subscript refers to the incident field. This field is known and is determined by the type of source desired; it can be any solution to Maxwell's equations. The 'scat' subscript refers to the scattered field. This field is unknown and is the quantity that is solved for with the BOR-FDTD method. To implement a TF/SF source, a surface called the TF/SF boundary is placed around the section of the simulation space that contains a scatterer. In the case of the BOR-FDTD method, this surface has three sides, which constitutes a closed surface when revolved about the z-axis. The TF/SF boundary can be seen in Fig. 2.3. The update equations along the boundary of the box are then manipulated by adding or subtracting the incident field so the total field exists inside the box and only the scattered field exists outside the box. The details of these modifications to the update equations can be found in [60]. This process is frequently referred to as *injecting* the field of the source into the

simulation space, and the source itself is called an *injector*. These terms will be used in the remainder of this document.

Two different types of injectors are used in this work. A plane-wave injector is used to study zone plate antennas in the receive mode. An analytical representation of a plane wave propagating in the z-direction is needed for the TF/SF formulation. In rectangular coordinates the field for the plane wave is

$$\begin{aligned} \vec{E}_{\text{inc}}(x,y,z,t) &= E_{\text{dg}}(t)\hat{x} \\ \vec{H}_{\text{inc}}(x,y,z,t) &= \frac{1}{\eta_{\text{o}}} E_{\text{dg}}(t)\hat{y}\,, \end{aligned} \tag{2.15}$$

in which η_{o} is the impedance of free space, $\eta_{\text{o}} = \sqrt{\mu_{\text{o}}/\epsilon_{\text{o}}} \approx 377\,\Omega$. Rewriting this in cylindrical coordinates,

$$\begin{aligned} \vec{E}_{\text{inc}}(\rho,\phi,z,t) &= E_{\text{dg}}(t)\cos\phi\hat{\rho} - E_{\text{dg}}(t)\sin\phi\hat{\phi} \\ \vec{H}_{\text{inc}}(\rho,\phi,z,t) &= \frac{1}{\eta_{\text{o}}}\left(E_{\text{dg}}(t)\sin\phi\hat{\rho} + E_{\text{dg}}(t)\cos\phi\hat{\phi}\right)\,. \end{aligned} \tag{2.16}$$

Note that the field depends only on components with either a sine or cosine variance and therefore can be represented with a single Fourier mode, $m = 1$.

The second type of injector used in this work is a Gaussian beam injector. This injector is used to model the pyramidal horn antenna used in the focused-beam measurement system. The field from this horn antenna was measured and found to closely resemble the far-field of a Gaussian beam. The far-field of a Gaussian beam with an electric field polarized in the $\hat{x}$ direction can be written in spherical coordinates [63]:

$$\begin{aligned} \vec{E}_{\text{inc}}(r,\theta,\phi) &= \left[F_\theta(\theta,\phi)\hat{\theta} + F_\phi(\theta,\phi)\hat{\phi}\right] e^{-jk_{\text{o}}r}/r \\ F_\theta(\theta,\phi) &= \frac{2j}{k_{\text{o}}}\left(\frac{k_{\text{o}}w}{2}\right)^2 E_{\text{o}}\exp\left\{-[(k_{\text{o}}w_{\text{o}}/2)\sin\theta]^2\right\}\cos\phi \\ F_\phi(\theta,\phi) &= -\frac{2j}{k_{\text{o}}}\left(\frac{k_{\text{o}}w}{2}\right)^2 E_{\text{o}}\exp\left\{-[(k_{\text{o}}w_{\text{o}}/2)\sin\theta]^2\right\}\cos\theta\sin\phi\,, \end{aligned} \tag{2.17}$$

in which $k_{\text{o}} = 2\pi f/c$, f is the frequency, and c is the speed of light in free space. Rewriting

this in cylindrical coordinates,

$$\begin{aligned}\vec{E}_{\text{inc}}(\rho,\phi,z) &= C(\rho,z)\left[\frac{z-z_{\text{o}}}{r}\cos\phi\hat{\rho}-\frac{z-z_{\text{o}}}{r}\sin\phi\hat{\phi}-\frac{\rho}{r}\cos\phi\hat{z}\right]\\ \vec{H}_{\text{inc}}(\rho,\phi,z) &= \frac{C(\rho,z)}{\eta_{\text{o}}}\left[\left(\frac{z-z_{\text{o}}}{r}\right)^2\sin\phi\hat{\rho}+\cos\phi\hat{\phi}-\frac{\rho(z-z_{\text{o}})}{r^2}\sin\phi\hat{z}\right], \quad (2.18)\end{aligned}$$

in which

$$C(\rho,z)=\frac{2j}{rk_{\text{o}}}\left(k_{\text{o}}w_{\text{o}}/2\right)^2\exp\left\{-\left[k_{\text{o}}w_{\text{o}}\rho/(2r)\right]^2\right\}e^{-jk_{\text{o}}r}/r\,, \quad (2.19)$$

and $r=\sqrt{\rho^2+(z-z_{\text{o}})^2}$. To be injected into the BOR-FDTD simulation, the field must be written in the time-domain. In this work, the Gaussian beam injector is used to simulate the horn antenna for the focused-beam system for a single frequency at a time. Rather than taking the Fourier transform of Eq. (2.18) and convolving it with a modulated Gaussian envelope, the frequency-dependent terms in the real part of Eq. (2.18) can be treated as a constant and the spherical phase can be converted into time delay:

$$\begin{aligned}\vec{E}_{\text{inc}}(\rho,\phi,z,t) &= C(\rho,z)E_{\text{mg}}(t-r/c)\left[\frac{z-z_{\text{o}}}{r}\cos\phi\hat{\rho}-\frac{z-z_{\text{o}}}{r}\sin\phi\hat{\phi}-\frac{\rho}{r}\cos\phi\hat{z}\right]\\ \vec{H}_{\text{inc}}(\rho,\phi,z,t) &= \frac{C(\rho,z)}{\eta_{\text{o}}}E_{\text{mg}}(t-r/c)\left[\left(\frac{z-z_{\text{o}}}{r}\right)^2\sin\phi\hat{\rho}\right.\\ &+ \left.\cos\phi\hat{\phi}-\frac{\rho(z-z_{\text{o}})}{r^2}\sin\phi\hat{z}\right], \quad (2.20)\end{aligned}$$

in which

$$C(\rho,z)=\frac{2j}{rk_{\text{o}}}\left(k_{\text{o}}w_{\text{o}}/2\right)^2\exp\left\{-\left[k_{\text{o}}w_{\text{o}}\rho/(2r)\right]^2\right\}. \quad (2.21)$$

This representation of the Gaussian beam is meaningful only at a single frequency, but this is sufficient for its use in this work. Like the plane wave, the Gaussian beam injector can be represented with a single Fourier mode, $m=1$.

The parameters z_{o} and w_{o} in Eq. (2.18) describe the location and the radius of the beam waist. These parameters were used to build the model of the horn in the focused-beam system. The field of the isolated horn antenna was measured on a plane located 43.2 cm from the aperture of the antenna. Details about the measurement procedure can be found in Chapter 6. The parameters z_{o} and ω_{o} were then fit to the measurements on this plane by minimizing the root mean square (RMS) error of the model over the entire plane.

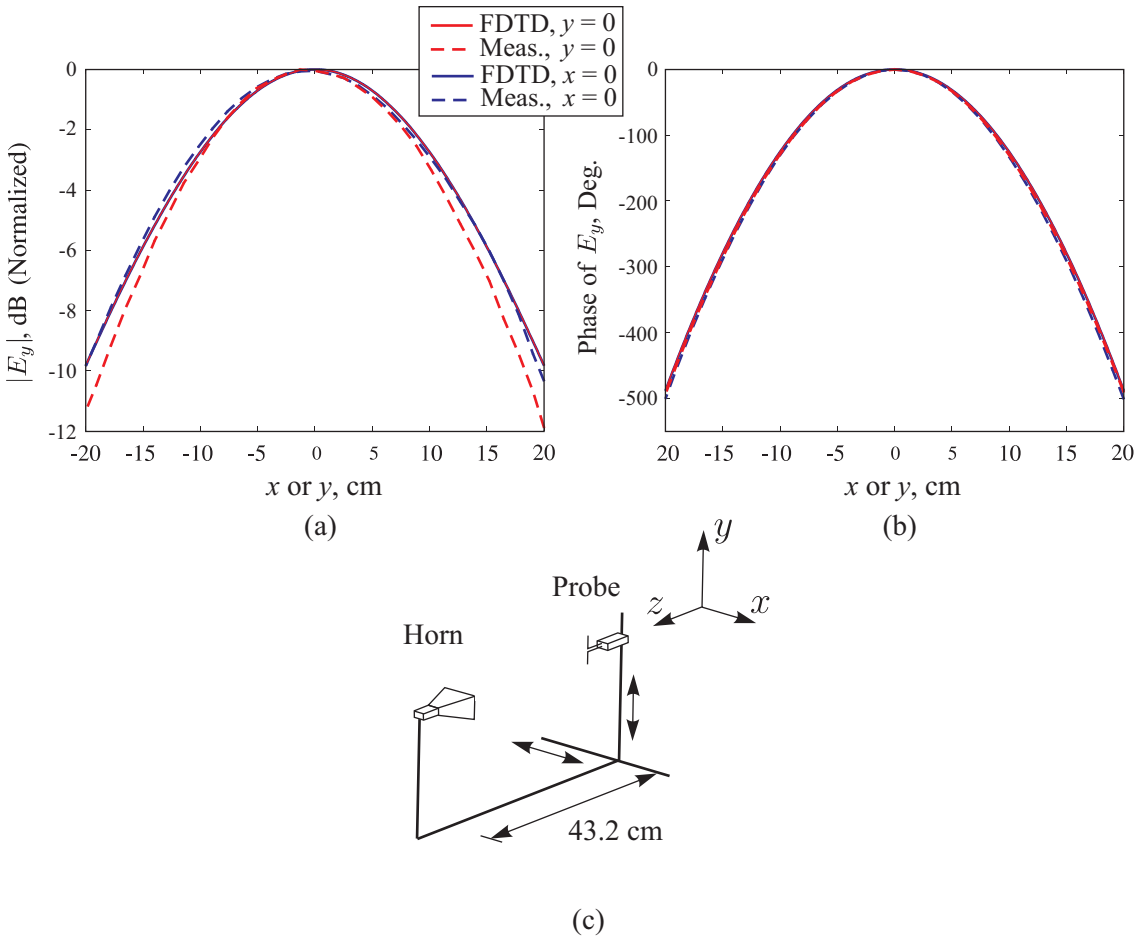

Figure 2.4: Measured and simulated (FDTD) results for the electric field E_y of the isolated horn antenna. (a) Magnitude and (b) phase for the horn at $f = 10\,\text{GHz}$. (c) Schematic diagram of the measurement setup.

A comparison of the resultant model for the horn at 10 GHz and the measurements can be seen in Fig. 2.4. Figure 2.4(a) shows the magnitude of the electric field, while Fig. 2.4(b) shows the phase, plotted for two cuts. The red lines are for horizontal cuts ($y = 0$), and the blue lines are for vertical cuts ($x = 0$). The solid lines are for the BOR-FDTD simulations and the dashed lines are for the measurements. For reference, the coordinate system used for the measurements is shown in Fig. 2.4(c). The figures show reasonable agreement between the simulations and the measurements. The asymmetry of the measured fields is one noticeable difference between the simulations and measurements, however. The magnitude of the measured field for the horizontal cut falls off faster than it does for the vertical cut. This is not true for the simulations, for which the two cuts are almost identical.

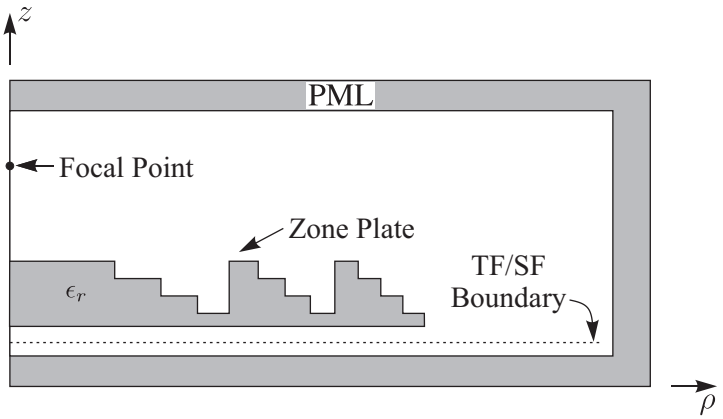

Figure 2.5: Geometry for the BOR-FDTD simulation of a zone plate with a Gaussian beam injector.

This is a restriction imposed by the BOR-FDTD method: The type of asymmetry seen in the measurement is difficult to decompose into a Fourier series, so a more symmetric model for the horn is used. Despite this difference, results presented in Chapter 6 show that good agreement between simulations and measurements of zone plates and lenses is still obtained.

For the focused-beam system simulations, we are interested in total field quantities for comparison with measurements. For this reason, the TF/SF method can be formulated in a slightly different manner. Instead of a three-sided, closed surface, the TF/SF boundary for the Gaussian beam injector is just a single surface, as shown in cross section in Fig. 2.5. The field for the Gaussian beam is added or subtracted along this surface so that the total field (incident Gaussian beam + scattered field) exists in the region above the injector surface and only the scattered field exists in the region below the surface. Truncating the TF/SF boundary at the edge of this surface, instead of surrounding the zone plate with a closed surface, creates a numerical error. For the Gaussian beam injector, however, the field has decayed so much by the point of truncation that the error introduced is negligible.

2.3.3 Parallelization

The BOR-FDTD method allows the zone plates studied in this work to be simulated as two-dimensional problems. Nevertheless, the electrically-large simulation space necessary to model a zone plate and its focal region means that simulations can take prohibitively long to complete on a single computer. One method used to speed the simulations up is

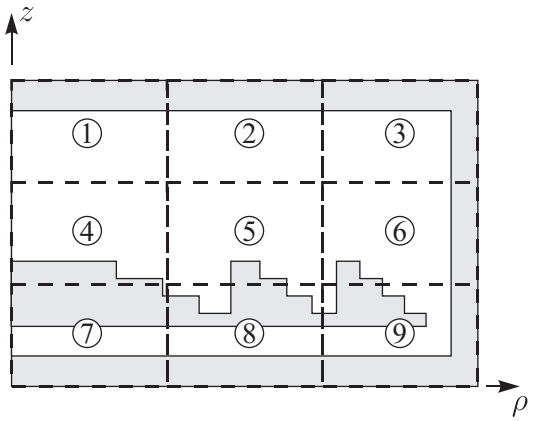

Figure 2.6: Geometry for the parallelized BOR-FDTD simulation of a phase-correcting zone plate antenna.

to *parallelize* the problem. This is done by splitting the simulation space into a number of different pieces, as is shown in Fig. 2.6. In this figure, for example, the dashed lines divide the simulation space into nine pieces. The update equations for each piece are computed on a separate computer processor (called a *node*). Recall from Sec. 2.2 that the update of a particular field component requires knowledge of the neighboring components. The field components at the edge of a node, therefore, require information about the field in an adjacent node. This is achieved by using the Message Passing Interface (MPI) protocol to synchronize the electromagnetic field at the boundary: After each time step, the magnetic field values along the boundary of each node are communicated to the node that computes the fields in the adjacent block. The update equations are then computed for the next time step, and the process is repeated. The overhead associated with this process is minimal, and the transfer of field data between adjacent nodes is the only additional computation necessary to run the simulation on many processors instead of one.

To perform the simulations in this work, a 'Beowulf-style' cluster of seventy-three desktop computers was used. These computers were networked using ethernet to allow the transfer of data between computers. In a cluster with this configuration, each node has access to only its own memory but can communicate with all of the other nodes. Each of the nodes features a dual-core AMD Athlon 64 X2 processor and two gigabytes of RAM.

One of the larger simulations performed for this work was for a focused-beam system

lens. On a single core (half of the computing power of a dual-core computer), this simulation took 13.5 hours. The same job, run on the entire cluster, took 15 minutes. This particular simulation required 1.92 GB of RAM, and therefore is essentially the biggest problem that can be run on a single machine. Run in parallel, this memory requirement is spread out over different computers.

The ability to run individual simulations of zone plates rapidly using this cluster allowed parametric studies to be performed and was essential to the generation of the design graphs that will be presented in the upcoming chapters.

CHAPTER III

DESIGN STUDY FOR SORET AND FOLDED ZONE PLATE ANTENNAS

In this chapter, a study of Soret and folded zone plate antennas using BOR-FDTD is presented. Visualizations of the electromagnetic field around a zone plate are used to discuss its focusing mechanism. Metrics for evaluating the focusing properties of zone plate antennas are defined, and parametric studies based on these are performed by varying the number of zones, the focal length, and the diameter of the zone plate. The results of the studies are used to generate design graphs. The design graphs are used to make general statements about the effect of these parameters on the focusing ability of the zone plates. Finally, the BOR-FDTD method is compared to other techniques typically used to analyze zone plates, and the simulation results are validated by comparison with existing measurements.

3.1 Visualizations

Some of the most interesting and instructive results of the BOR-FDTD simulations are the visualizations of the electromagnetic field and related quantities surrounding the zone plate antenna. A visualization of the magnitude of the time average of the Poynting vector $\left|\langle\vec{S}(t)\rangle\right|$ near the zone plate can provide insight into the focusing mechanism of the zone plate.

In Fig. 3.1, $\left|\langle\vec{S}(t)\rangle\right|$ is plotted in dB for a Soret zone plate and for a metal disc, with blue being the least intense and red being the most intense. The result on the left is for a PEC disc with diameter $D/\lambda = 40.3$, and the result on the right is for a Soret zone plate with the same diameter and $F/\lambda = 10$ ($N_{\text{Soret}} = 25$). The excitation is a normally incident plane wave with the electric field oriented in the x-direction. In both cases, the upper figure is a half cross section in the plane perpendicular to the electric field of the incident wave (the yz-plane), and the lower figure is a quarter cross section in the plane perpendicular to

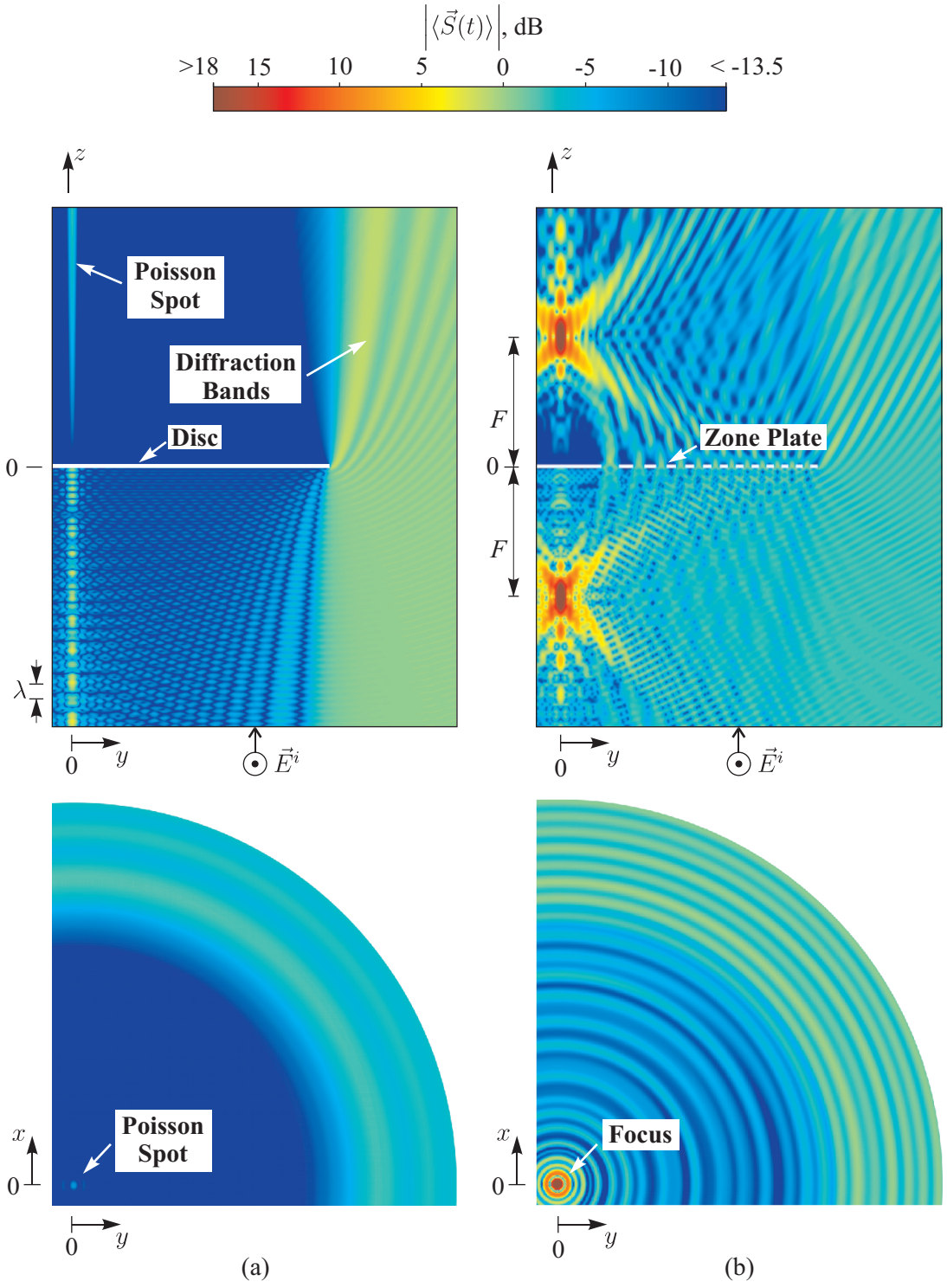

Figure 3.1: Magnitude of the time average of the Poynting vector $\left|\langle\vec{S}(t)\rangle\right|$ on two cross sections for (a) a PEC disc, for which the transverse cross section is for $z = 0.49D$ (z is twice the focal length of the zone plate) and (b) a Soret zone plate, for which the transverse cross section is for $z = F$. The zone plate has $N_{\text{Soret}} = 25$ zones and a focal length of $F/\lambda = 10$. Both the disc and the zone plate have a diameter of $D/\lambda = 40.3$. Because of the symmetry of the electromagnetic field, only a portion of each cross section is shown.

the direction of propagation of the incident wave (the xy-plane). In Fig. 3.1(a), the bottom figure is for $z = 2F = 0.49D$, whereas in Fig. 3.1(b), the bottom figure is for $z = F$. The data are normalized to the magnitude of the time average of the Poynting vector for the incident wave, $\left|\langle \vec{S}^i(t) \rangle\right|$ (0 dB on graph).

First, consider the results for the disc in Fig. 3.1(a). Directly behind the disc ($\rho < D/2$, $z > 0$) there is a shadow, except along and close to the axis ($\rho = 0$) where energy is being transported along the axis. This energy forms the famous Poisson spot or spot of Arago [64]. In front of the disc ($\rho < D/2$, $z < 0$), there is a distinct pattern that can be interpreted as the interference of the field scattered by the edge of the disc and the field of the standing wave due to direct reflection from the disc. To the right of the disc ($\rho > D/2$), the constant time-average power (0 dB) for the incident wave is seen for $z < 0$, and diffraction bands are evident for $z > 0$.

Now, consider the results for the Soret zone plate in Fig. 3.1(b). The two focal points (reflection and transmission) are clearly seen in the figure. Note that energy flows into these points and then out. Energy is clearly passing through the openings in the zone plate (compare this with the results for the disc), and this energy is being concentrated at the far focal point. Similarly, energy is being reflected by the structure of the zone plate and concentrated at the near focal point. Notice that the energy is spread out over regions surrounding the focal points. This spreading is particularly evident along the axis. As expected, the diffraction bands for the zone plate are more complex than those for the disc.

3.2 Metrics for Evaluating Zone Plate Antennas

Detailed studies of the effects of geometrical parameters on the focusing ability of zone plate antennas are one of the major contributions of this work. For these studies, metrics for quantifying the focusing ability must be defined. This is complicated by the fact that a zone plate antenna is composed of two major subsystems: One is the zone plate itself, and the other is the feed. Figure 3.2 is a schematic diagram of a zone plate antenna which shows these two components. Frequently, the feed is a dipole, an open-ended waveguide, or a horn antenna (as shown in Fig. 3.2) placed at the focal point of the zone plate. Because one of the

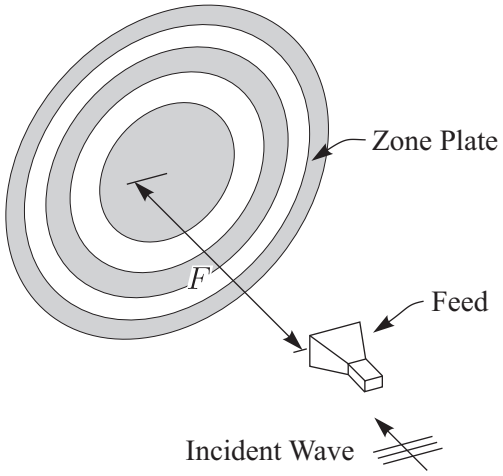

Figure 3.2: Schematic diagram showing the relationship between the zone plate and the feed in a Soret zone plate antenna.

purposes of this research is to look for trends in zone plate antenna performance, the feed for the zone plate has been made as simple as possible to allow the effects of the zone plate to be separated from the effects of the feed. For a specific zone plate antenna (zone plate and feed), the field pattern of the feed (a receiving antenna) could be incorporated into the model, if desired. This would account for any mismatch of the polarization characteristics of the zone plate and feed.

To quantify the focusing ability of a zone plate at the focal point, the focusing gain FG is introduced. This is the ratio of the magnitude of the axial component of the time-average Poynting vector at the focal point to the magnitude of the axial component of the time-average Poynting vector for the incident plane wave. The time-average Poynting vector $\langle \vec{S}(t) \rangle$ is the real part of the complex Poynting vector $\vec{S}_c$, so

$$FG = \frac{\left| \mathrm{Re}[\hat{z} \cdot \vec{S}_c^{\mathrm{scat}}] \right|}{\left| \mathrm{Re}[\hat{z} \cdot \vec{S}_c^{i}] \right|}, \tag{3.1}$$

in which the superscript 'scat' refers to the scattered field and the superscript i refers to the incident field. For the reflecting zone plates (Soret and folded), the feed is located between the zone plate and the source of the plane wave (see Fig. 3.2), so it effectively blocks the incident field from reaching the focal point; therefore, the scattered field (total field minus incident field) is used for the calculation of $\vec{S}_c^{\mathrm{scat}}$ in the numerator of Eq. (3.1). This is clear

in Fig. 2.3(a), which shows the focal point in the scattered-field region of the BOR-FDTD simulation space for the Soret zone plate antenna.

A more physically realistic method is also used to quantify the focusing ability of a zone plate. This method accounts for the finite size of a horn or waveguide feed by modeling the feed as an aperture of radius ρ_{disc} that receives all of the power normally incident upon it. The effective area A_e of a receiving zone plate antenna is calculated by integrating the axial component of the time-average Poynting vector over the area of the feed and dividing by the axial component of the time-average Poynting vector for the incident plane wave. The effective area for the antenna on reception can then be converted into a gain on transmission by multiplying by $4\pi/\lambda^2$:

$$G = \frac{4\pi}{\lambda^2} A_e = \frac{4\pi \left| \int_0^{2\pi} \int_0^{\rho_{\text{disc}}} \text{Re}[\hat{z} \cdot \vec{S}_c^{\text{scat}}] \rho \, \mathrm{d}\rho \, \mathrm{d}\phi \right|}{\lambda^2 \left| \text{Re}[\hat{z} \cdot \vec{S}_c^{i}] \right|}. \tag{3.2}$$

As in Eq. (3.1), the scattered field is used for the calculation of $\vec{S}_c^{\text{scat}}$ in the numerator of Eq. (3.2). This gain takes into account the spreading of the energy on the focal plane, whereas the focusing gain defined by Eq. (3.1) does not.

3.3 Parametric Studies and Design Graphs

For the parametric studies performed in this work, the values of the focal length F, the diameter D, and the number of half-wave zones N_{Soret} were varied over the ranges of values typically encountered in microwave and millimeter-wave applications. In the design graphs presented in this work, the focal lengths and diameters of the zone plates are given in terms of the design wavelength: F/λ and D/λ. This allows antenna designers to use these results for zone plates designed for any frequency. For reference, the geometries of the Soret and folded zone plates are repeated in Fig. 3.3.

3.3.1 Design Graphs Based on the Focusing Gain

A series of simulations was run for Soret zone plate antennas of varying F/λ and N_{Soret}. The focusing gain FG was calculated using Eq. (3.1) and is plotted in relief in Fig. 3.4 The dashed lines are for constant N_{Soret}, and the solid lines are for constant F/λ. This

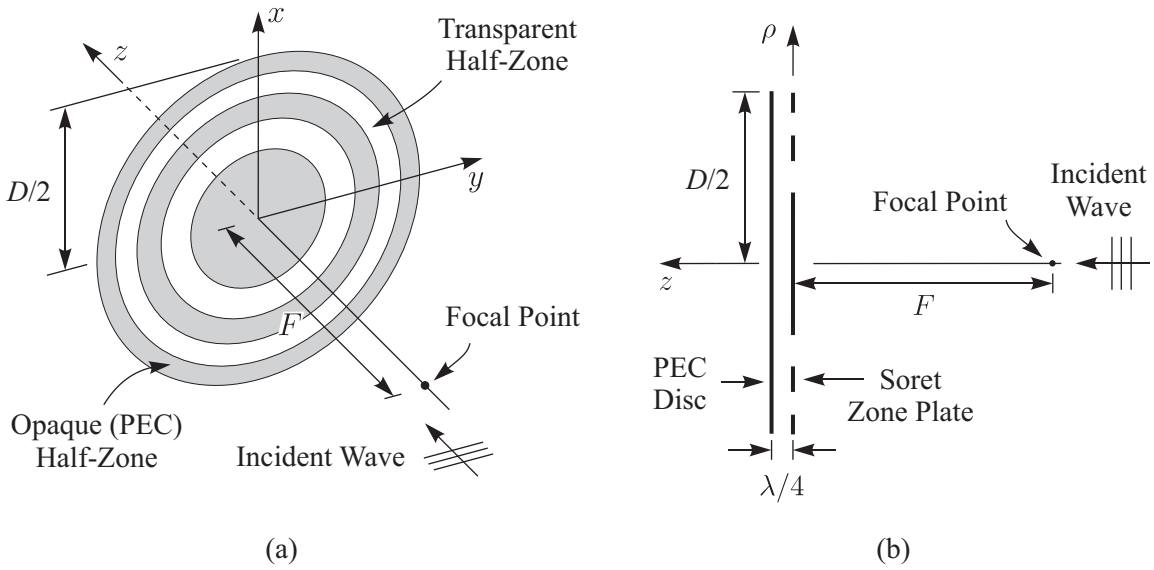

Figure 3.3: Geometry of (a) the Soret zone plate and (b) the folded zone plate.

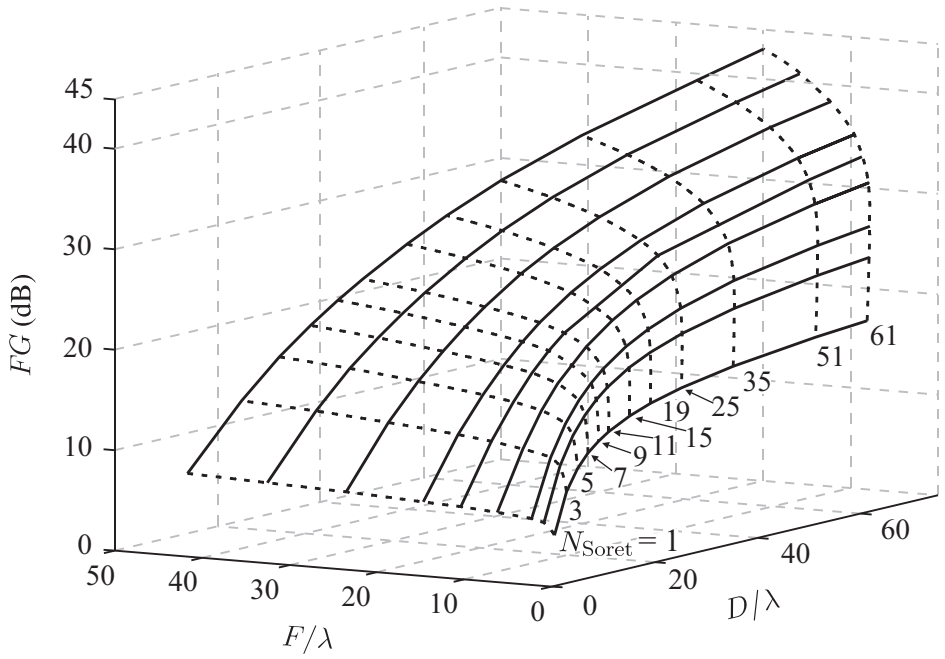

Figure 3.4: Focusing gain, FG, of the Soret zone plate antenna for various values of F/λ and D/λ. The dashed lines are for constant N_{Soret}, and the solid lines are for constant F/λ.

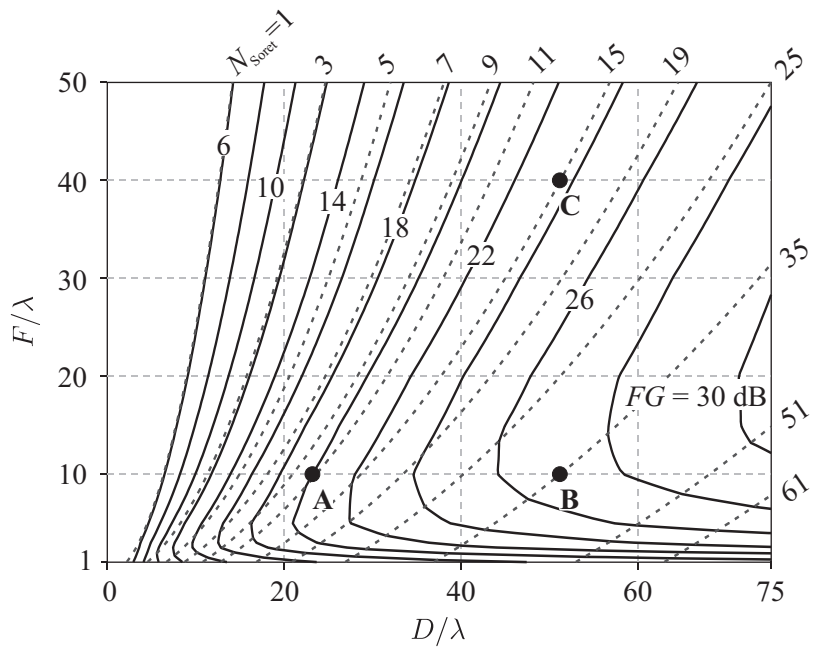

Figure 3.5: Design graph for the Soret zone plate antenna. The solid lines represent contours of constant focusing gain FG (in dB), while the dashed lines are for constant N_{Soret}.

representation of the data is useful for observing trends as the parameters are varied. In Fig. 3.5, these same data are presented in a form more suitable for designing zone plate antennas. The solid lines are contours of constant FG, spaced 2 dB apart, and the dashed lines are for constant N_{Soret}. These plots show the focusing gain as a function of the continuous variables, F/λ and D/λ. However, because N_{Soret} is restricted to integer values, only a finite number of points can be obtained for a given F/λ. These points lie along the lines of constant N_{Soret}. Note that not all of these lines of constant N_{Soret} are shown in Fig. 3.5.

Soret zone plate antennas are defined by the three primary design parameters F/λ, D/λ, and N_{Soret}, as well as the focusing gain FG. The parameters F/λ, D/λ, and N_{Soret} are related through (1.1), and therefore only two of the three can be independently chosen. Figure 3.5 can be used to design a zone plate antenna given any two of these four quantities. For example, given the desired focusing gain and F/λ, we can determine D/λ and N_{Soret}. In this case, Figure 3.5 is used to find the appropriate zone plate diameter, and then the closest geometry with an integer number of zones is found by solving Eq. (1.1) for N_{Soret}

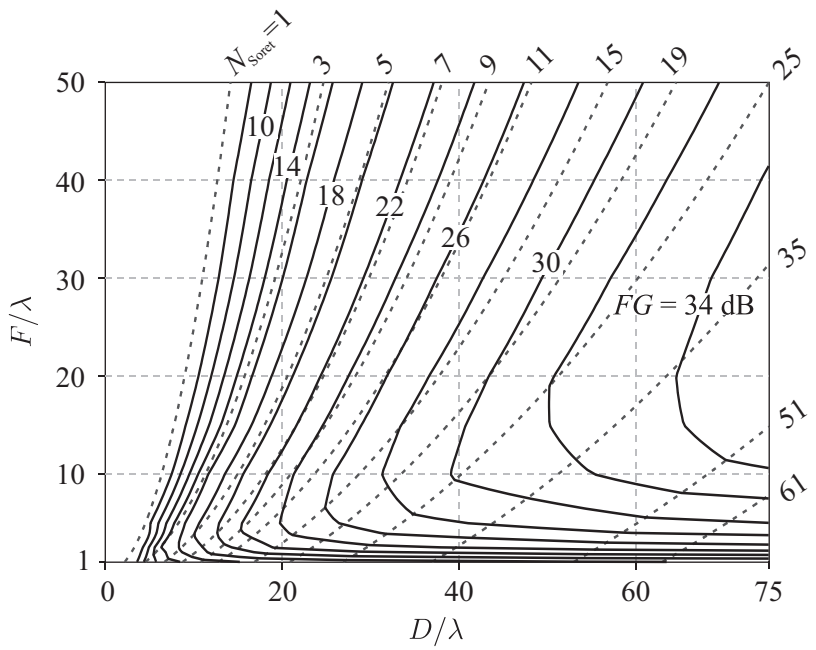

Figure 3.6: Design graph for the folded zone plate antenna. The solid lines represent contours of constant focusing gain FG (in dB), while the dashed lines are for constant N_{Soret}.

and rounding the result:

$$N_{\text{Soret}} = \text{round}\left[-2\,(F/\lambda) + 2\sqrt{(F/\lambda)^2 + \frac{1}{4}\,(D/\lambda)^2}\right]. \tag{3.3}$$

Figures 3.4 and 3.5 give the focusing gain FG for all points within the rectangular grid displayed, even though some areas near the edges of the grid may represent unrealistic designs.

Adding a reflecting disc of diameter D/λ at the distance $\lambda/4$ behind a Soret zone plate transforms it into a folded zone plate, as depicted in Fig. 3.3(b). The parametric study was repeated for the folded zone plate antenna. A contour plot of the focusing gain FG for this antenna is shown in Fig. 3.6.

3.3.2 General Observations From Design Graphs

In addition to being a useful tool for those wishing to design a zone plate antenna, these design graphs can be used to make general statements about the effect of the design parameters on the focusing ability of these zone plates. To this end, there are a few interesting trends that can be observed in Figs. 3.4, 3.5, and 3.6. When the focal length, F/λ, or

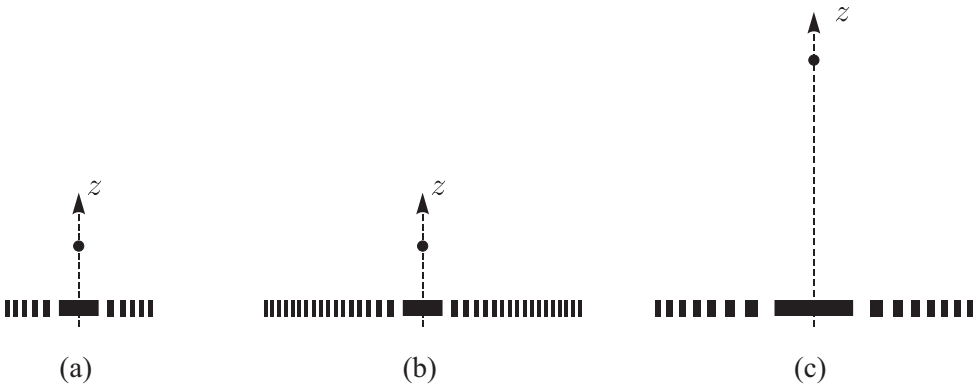

Figure 3.7: Cross sections of the three Soret zone plates marked by dots in Fig. 3.5. The parameters for the zone plates are (a) $F/\lambda = 10$, $N_{\text{Soret}} = 11$, and $D/\lambda = 23.7$, (b) $F/\lambda = 10$, $N_{\text{Soret}} = 35$, and $D/\lambda = 51.2$, and (c) $F/\lambda = 40$, $N_{\text{Soret}} = 15$, and $D/\lambda = 51.2$.

the number of zones, N_{Soret}, is held constant and the other quantity (N_{Soret} or F/λ) is increased, the focusing gain FG increases. Of course, the diameter, D/λ, also varies in both cases to accommodate the relationship in Eq. (1.1). The incremental increase in FG eventually tapers off, however. These trends can be at least partially explained by simple physical phenomena. Figure 3.7 will be used to help illustrate the causes of the trends. The figure shows cross-sectional profile of the three zone plates marked by dots in Fig. 3.5. The zone plate in Fig. 3.7(a) has a focal length $F/\lambda = 10$ and $N_{\text{Soret}} = 11$ half-wave zones. The diameter, therefore, is $D/\lambda = 23.7$. This profile corresponds to the zone plate marked by point **A**. The zone plates in Fig. 3.7(b) and (c) correspond to points **B** ($F/\lambda = 10$, $N_{\text{Soret}} = 35$, and $D/\lambda = 51.2$) and **C** ($F/\lambda = 40$, $N_{\text{Soret}} = 15$, and $D/\lambda = 51.2$), respectively. These profiles are drawn to scale, with the exception of the thickness of the metal annuli, which have been thickened so that they are more visible.

Examples of these two trends can be seen in Fig. 3.8. Figure 3.8(a) shows FG as a function of N_{Soret} for Soret zone plate antennas with $F/\lambda = 20$ and is generated by taking the focusing gain along a horizontal line in Fig. 3.5. As more zones are added to the zone plate (and D/λ increases), more of the incident energy can be focused and FG increases. However, as the diameter grows, each successive additional zone focuses the incident energy more obliquely (with a smaller angle between the outermost zone and the focal point) than the previous zone. This can be seen by comparing the angle from the outermost zone to the

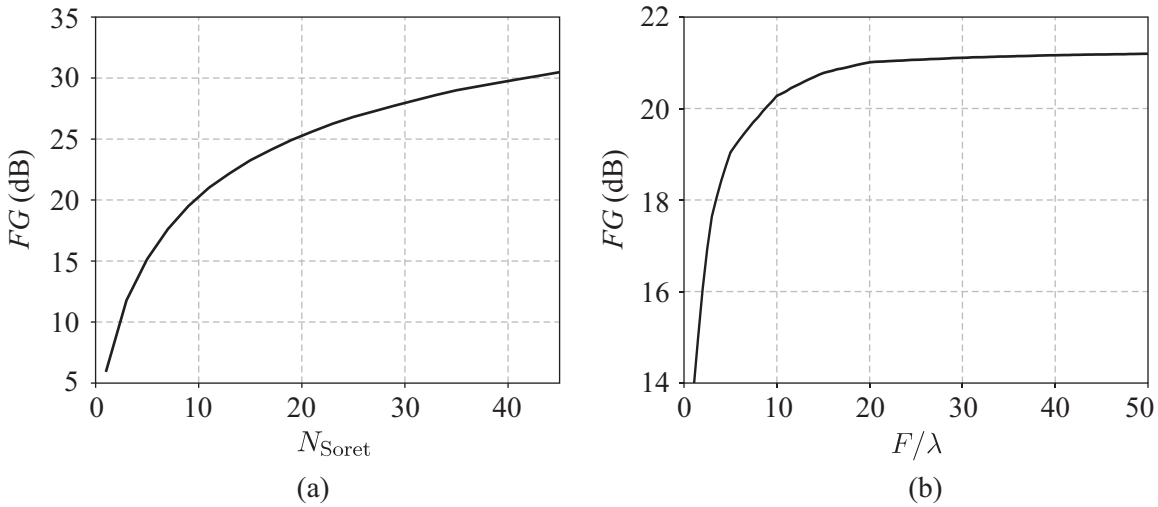

Figure 3.8: Focusing gain for zone plates with (a) $F/\lambda = 20$ and (b) $N_{\text{Soret}} = 11$.

focal point in the zone plate profiles in Fig. 3.7(a) and (b). This means that each additional zone contributes less to the focusing gain than the previous and results in the trend for FG that is seen in Fig. 3.8(a): FG is continuously increasing, but with a decreasing rate of change. It is not surprising that the gain does not grow without bound, as predicted by geometrical optics. As N_{Soret} is increased, the outermost zones decrease in width relative to the wavelength, according to Eq. (2.1), and the geometrical principles used to design the zone plate become less accurate.

Figure 3.8(b) shows FG as a function of F/λ for Soret zone plates with $N_{\text{Soret}} = 11$. This figure is generated by taking the focusing gain along a dashed line of constant N_{Soret} in Fig. 3.5. The trend in this figure is similar to that seen in Fig. 3.8(a): As F/λ is made larger, the rate of increase of FG decreases. In Fig. 3.8(b), in fact, there is almost no increase in FG for $F/\lambda \gtrsim 20$. The explanation for this trend is also similar: For very low F/λ, the outer zones must focus energy very obliquely (see Fig. 3.7(a)). As F/λ is increased, the focusing becomes less and less oblique (see Fig. 3.7(c)), and FG increases. Eventually, as changes in F/λ begins to affect smaller and smaller changes in the angle from the outmost zone to the focal point, and the rate of increase in FG decreases.

Another interesting trend is noticed when F/λ and N_{Soret} are adjusted simultaneously in a way that keeps the diameter of the zone plate constant. Initially, as F/λ is increased,

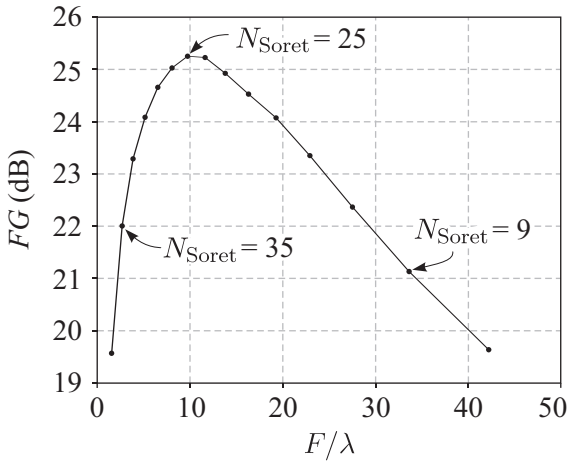

Figure 3.9: Focusing gain for zone plates with $D/\lambda = 40$.

FG increases because the focusing from the outer zones is less oblique. At the same time, however, as F/λ is increased, the number of zones in the zone plate must be reduced to satisfy Eq. (1.1). This causes a decreases in FG. Comparison of Figs. 3.7(b) and (c), which have the same diameter, illustrates these two ideas. For a certain F/λ, these competing factors balance out, and a maximum FG is reached. Beyond this point, FG decreases with increasing F/λ. As an example of this trend, Fig. 3.9 shows FG as a function of F/λ for Soret zone plate antennas with $D/\lambda = 40$. This line is generated by taking the focusing gain along a vertical line in Fig. 3.5. The maximum focusing gain ($FG_{\max} \approx 25.3\,\text{dB}$) occurs for $N_{\text{Soret}} = 25$ (marked in Fig. 3.9), when the focal length is $F/\lambda = 9.8$. N_{Soret} has been marked for a few additional points to reinforce that it decreases as F/λ increases.

The three trends illustrated in Figs. 3.8 and 3.9 are true for folded zone plate antennas as well. Using the information in Figs. 3.5 and 3.6, the maximum focusing gain for a zone plate antenna of any given diameter can be found. This was done for the range of diameters studied in this work, and the graph in Fig. 3.10 was constructed using this information. The values of F/λ and N_{Soret} at which the maximum focusing gain occurs are indicated for a few points on each curve.

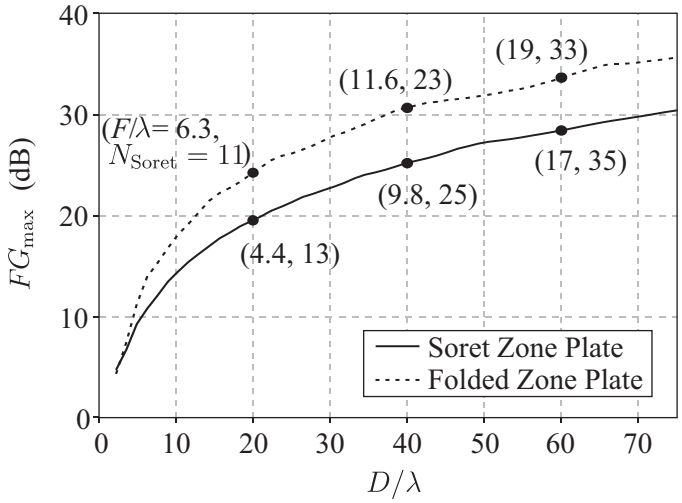

Figure 3.10: The maximum value of the focusing gain FG for a Soret or folded zone plate antenna with a fixed diameter D/λ.

3.3.3 Comparison of Soret and Folded Zone Plates

From a comparison of Figs. 3.5 and 3.6, it is evident that the focusing gain of the folded zone plate antenna is generally greater than that of the Soret zone plate antenna, as expected. In Sec. 1.2, based on a simple argument, it was stated that adding the reflecting disc should double the magnitude of the electromagnetic field at the focal point, thereby quadrupling the scattered power and increasing the focusing gain by 6 dB. Comparing Figs. 3.5 and 3.6, it can be seen that the increase in focusing gain is not 6 dB for all focal lengths and diameters. In Fig. 3.11, this idea is examined further by comparing the focusing gains for the two types of zone plate antennas when the number of zones is fixed at $N_{\text{Soret}} = 25$. The increase in focusing gain for the folded zone plate antenna is seen to be much less than 6 dB when F/λ is small, and to approach 6 dB as F/λ becomes large. The anticipated fourfold increase in power at the focal point is based on a simple analysis that ignores multiple diffraction and assumes that radiated energy passing through the clear portions of the zone plate will be perfectly reflected back through the same clear portions with a round-trip phase change of π. For zone plates with short focal lengths, these assumptions are not good, and the increase in focusing gain due to the addition of the reflector is small or non-existent.

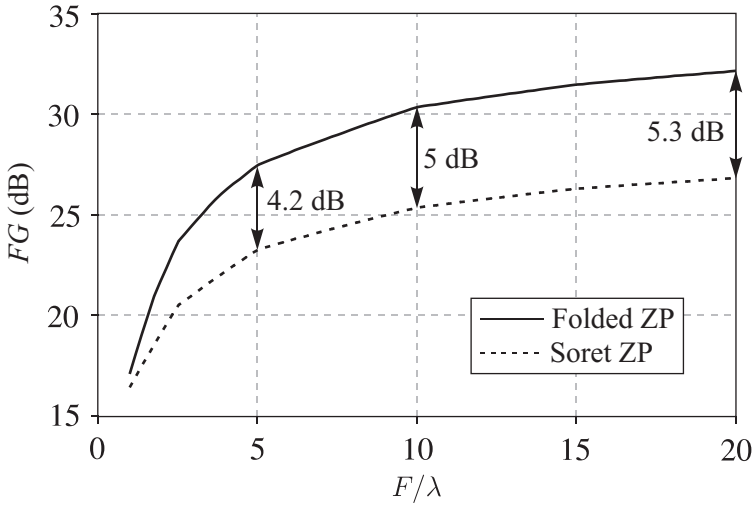

Figure 3.11: Comparison of FG for the Soret and folded zone plate antennas for a constant number of zones $N_{\text{Soret}} = 25$.

3.3.4 Design Graphs Based on the Gain

The same parametric studies for the Soret and folded zone plates were repeated using the gain G to quantify the focusing ability of the zone plate. The gain is calculated using Eq. (3.2), with radius of the disc of integration chosen to be $\rho_{\text{disc}} = \lambda/2$ to represent a typical feed. Figures 3.12 and 3.13 show the gain for Soret and folded zone plate antennas, respectively. The same overall trends evident in Figs. 3.5 and 3.6 are seen in Figs. 3.12 and 3.13. Increasing the radius of the 'feed aperture' ρ_{disc} in Eq. (3.2) generally increases G, although the amount of this increase depends on the distribution of power in the focal plane.

The maximum possible value of G can also be calculated for a zone plate with a given diameter. Figure 3.14 shows $G_{\max}$ as D/λ is varied over the range of diameters studied in this work. The gain for a uniformly illuminated aperture, $G = (\pi D/\lambda)^2$, is also shown in Fig. 3.14. A comparison of this gain with that for the zone plates illustrates the well-documented inefficiency of the Soret and folded zone plates as compared to a perfect focusing element [10, 38]. The comparison of the gain for a Soret and folded zone plate antenna with identical parameters is similar to the comparison of the focusing gain in Fig. 3.11: The expected 6 dB increase for the folded zone plate antenna is not seen, especially for antennas with short focal lengths.

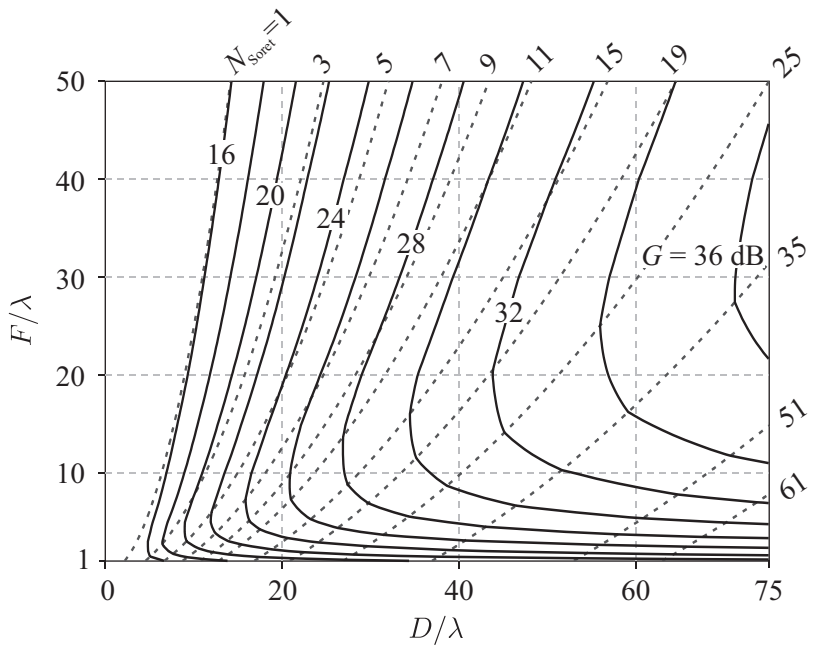

Figure 3.12: Design graph for the Soret zone plate antenna with $\rho_{\text{disc}} = \lambda/2$. The solid lines represent contours of constant gain G (in dB), while the dashed lines are for constant $N_{\text{Soret}} = 25$.

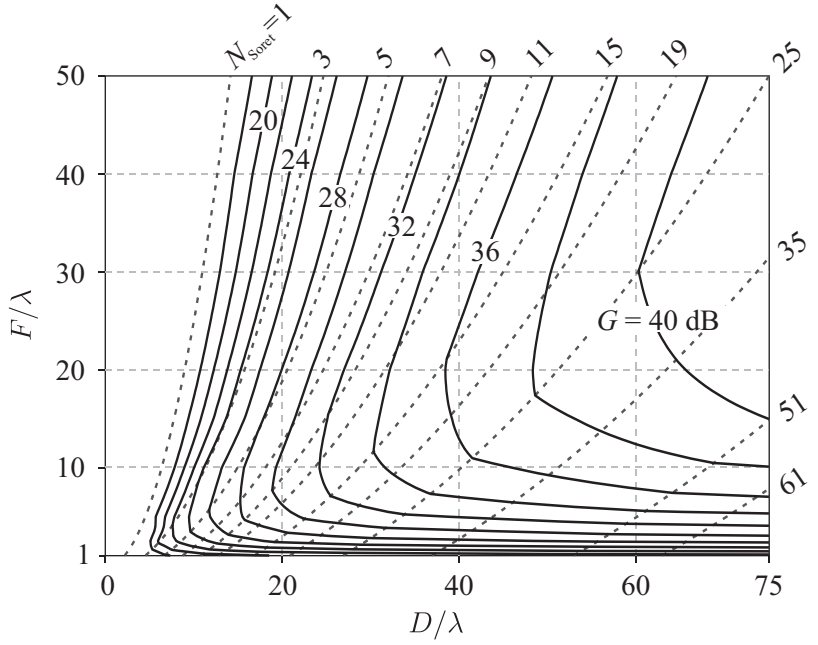

Figure 3.13: Design graph for the folded zone plate antenna with $\rho_{\text{disc}} = \lambda/2$. The solid lines represent contours of constant gain G (in dB), while the dashed lines are for constant $N_{\text{Soret}} = 25$.

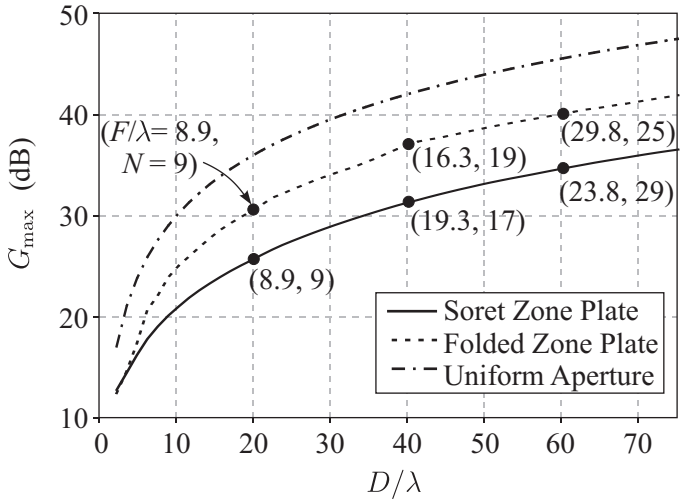

Figure 3.14: The maximum value of the gain G for a zone plate with a fixed diameter D/λ and with $\rho_{\text{disc}} = \lambda/2$. The gain of a uniformly illuminated aperture of the same diameter is also shown.

3.4 Comparison of the BOR-FDTD Method to Other Methods of Analysis

In Sec. 2.1, some of the methods that are frequently used to analyze zone plates were presented, and the reasoning behind the decision to use the BOR-FDTD method in this work was discussed. To support these arguments, a detailed comparison of the BOR-FDTD method with two other analysis techniques will be presented in this section for Soret zone plate antennas.

As discussed in Sec. 2.1, a simple geometric theory is sometimes used to analyze Fresnel zone plates when $(F/D)^2 >> 1$. Under this condition, the so-called *paraxial approximation* applies, and the area of each zone (and therefore the contribution from each zone to the focusing) is approximately the same [10]. Using Fresnel's zone theory, each successive pair of zones added to a Soret zone plate (one opaque and one transparent) increases the magnitude of the electric field at the focal point by an additive factor that is twice the magnitude of the incident electric field, E_{o}. For a Soret zone plate with odd opaque zones (i.e., the center zone is blocked) the focusing gain of the zone plate antenna at the focal point is

$$FG_{\text{Soret}} = \left| \frac{E_{\text{focal}}}{E_{\text{o}}} \right|^2 = \left| \frac{(N_{\text{Soret}} + 1)E_{\text{o}}}{E_{\text{o}}} \right|^2 = (N_{\text{Soret}} + 1)^2 \, . \tag{3.4}$$

When the reflecting plate is added to create a folded zone plate, each additional zone

(either opaque or transparent) adds another factor of $2E_{\mathrm{o}}$ to the field at the focal point. The focusing gain for a folded zone plate antenna is therefore

$$FG_{\mathrm{folded}} = \left| \frac{(2N_{\mathrm{Soret}})E_{\mathrm{o}}}{E_{\mathrm{o}}} \right|^2 = (2N_{\mathrm{Soret}})^2 \, . \tag{3.5}$$

Kirchhoff diffraction theory is also frequently used to analyze zone plates. Applied to a single annular aperture of the Soret zone plate in Fig. 3.3(a), the scalar Kirchhoff diffraction integral yields

$$E_n(z) = \frac{E_{\mathrm{o}} jk}{2} \int_{\rho_{n-1}}^{\rho_n} \frac{e^{-jkr}}{r} \left[1 + \frac{z}{r} \left(1 + \frac{1}{jkr} \right) \right] \rho \, \mathrm{d}\rho, \tag{3.6}$$

in which z is set equal to F to find the focusing gain at the focal point. To model a reflection zone plate with Eq. (3.6), the incident electromagnetic field is assumed to be perfectly reflected by the opaque zones. The phase shift associated with this reflection is uniform and can therefore be disregarded. The contribution to the field from the reflection from each opaque zone is summed to give the focusing gain

$$FG_{\mathrm{Soret}} = \left| \frac{1}{E_{\mathrm{o}}} \sum_{l=1}^{N_{\mathrm{Soret}}} E_l(z) \right|^2 \, , \tag{3.7}$$

in which only the odd zones are summed. The scalar diffraction analysis of a folded zone plate uses the assumption that the addition of the reflecting disc produces fields on fictitious zones, located in the transparent regions of the zone plate in Fig. 3.3(b), that differ in phase by exactly π from the fields incident on these zones. The focusing gain of the folded zone plate is then

$$FG_{\mathrm{folded}} = \left| \frac{1}{E_{\mathrm{o}}} \left(\sum_{l=1}^{N_{\mathrm{Soret}}} E_l(z) - \sum_{m=2}^{N_{\mathrm{Soret}}-1} E_m(z) \right) \right|^2 \, , \tag{3.8}$$

in which l is the index for the opaque zones (odd integers in the type of zone plates studied in this work) and m is the index for the fictitious zones (even integers).

Figure 3.15 compares the focusing gains FG for Soret zone plate antennas calculated using the BOR-FDTD method, the geometrical theory as defined in Eq. (3.4), and the scalar form of the Kirchhoff diffraction integral (KDI) in Eq. (3.7). The focal lengths used for these graphs, $F/\lambda = 3$ and $F/\lambda = 20$, were chosen to demonstrate the dependence of the accuracy of the different analysis methods on this parameter. It is clear from the figures

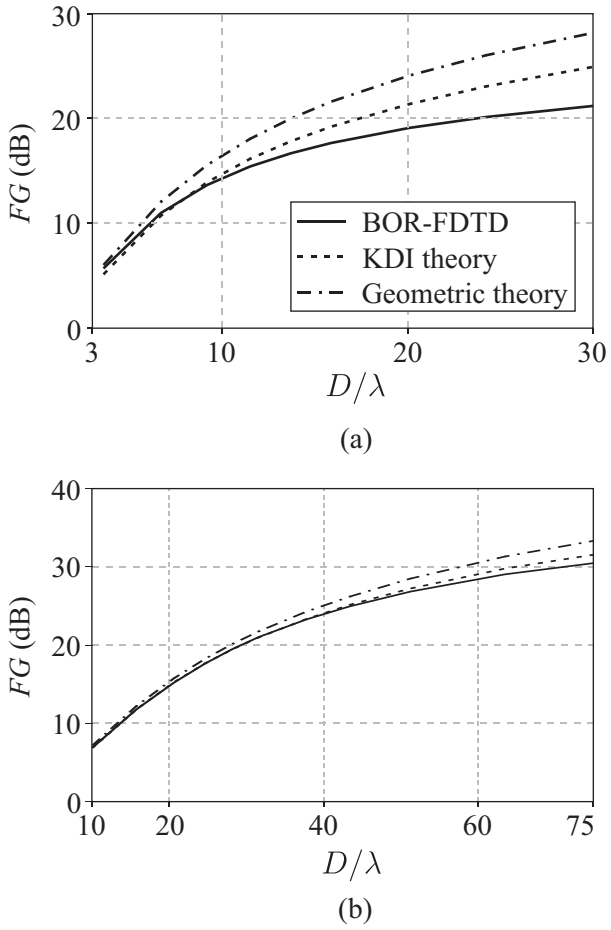

Figure 3.15: Comparison of focusing gains for Soret zone plate antennas computed with the BOR-FDTD method and two analytical techniques when (a) $F/\lambda = 3$ and (b) $F/\lambda = 20$.

that the analytical techniques diverge from the BOR-FDTD results as D/λ becomes large with respect to F/λ (as F/D becomes small) and that both the geometric theory and KDI theory overestimate the focusing gain. These results seem logical, because for small F/D, the paraxial approximation does not apply and the geometric theory is not accurate. In addition, when F/D is small, the width of the outer zones approaches the minimum value, $\lambda/2$. The Kirchhoff diffraction theory uses the assumption that the incident field is reflected unperturbed by the opaque zones, and as the zones become narrower, this assumption becomes inaccurate. These figures offer additional justification for using the BOR-FDTD method throughout this work, despite the fact that it requires more computational time and memory.

3.5 Comparison of BOR-FDTD with Measurements

Any method of analysis is best validated by comparison with measurements. However, accurate measurements for the type of zone plates antennas studied in this chapter, particularly the folded zone plate antenna, are not readily available. Measured far-field patterns for a similar zone plate antenna, the integrated-circuit (IC) zone plate antenna, are presented in [23] and in [24]. Comparison of the BOR-FDTD model with these measurements requires a few modifications to the BOR-FDTD analysis. These modifications will be discussed in this section, and then the comparison will be presented.

The IC zone plate antenna consists of a Soret zone plate mounted on a dielectric substrate and backed by a quarter wavelength thick dielectric substrate and a reflecting disc to form a folded zone plate. The geometry for the IC zone plate antenna is shown in Fig. 3.16. Mounted opposite the zone plate and reflector on the dielectric substrate is a dipole to feed the antenna. The substrate used for the measurements had a relative permittivity of $\epsilon_r = 3.86$ and an attenuation constant of $\alpha = 0.016\,\mathrm{Np\,/\,mm}$ at the frequency $f = 230\,\mathrm{GHz}$.

3.5.1 Near-Field to Far-Field Transformation Methodology

The presence of the finite dielectric substrate shown in Fig. 3.16 causes difficulties when measuring or computing far-field quantities. The issue of reflections from the edges of the

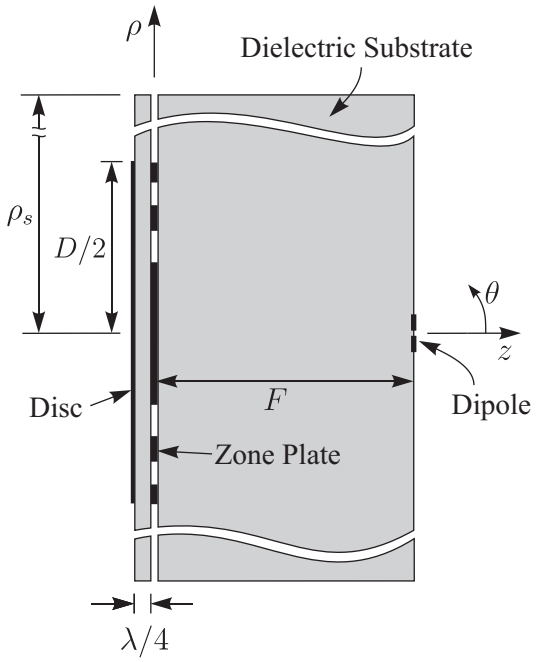

Figure 3.16: Geometry for the integrated-circuit zone plate antenna.

substrate during the measurement process was described as being "generally very troublesome" in [23]. To reduce the effects of these reflections in the measured data, an electrically-large substrate was used in conjunction with millimeter-wave absorbing material that was placed around the outer edges of the substrate.

A similar technique was implemented in the BOR-FDTD simulations. A cylindrical substrate with an electrically-large radius was terminated with PML. While this technique effectively models an infinite substrate, allowing no reflections from the outer edge, it presents problems for computing far-field quantities with the FDTD method. The traditional near-field to far-field transformation (NFFFT) technique used in the FDTD algorithm involves integrating the product of the free-space Green's function and the frequency-domain electromagnetic field over a closed surface in free space. This process is not suitable for problems involving an infinite substrate, because the free-space Green's function is not valid for surfaces passing through the substrate [60]. Methods for computing the NFFFT for antennas on layered dielectric slabs exist [65]. However, in this work, this problem was avoided in an easy-to-implement manner, using an approximation to the full NFFFT.

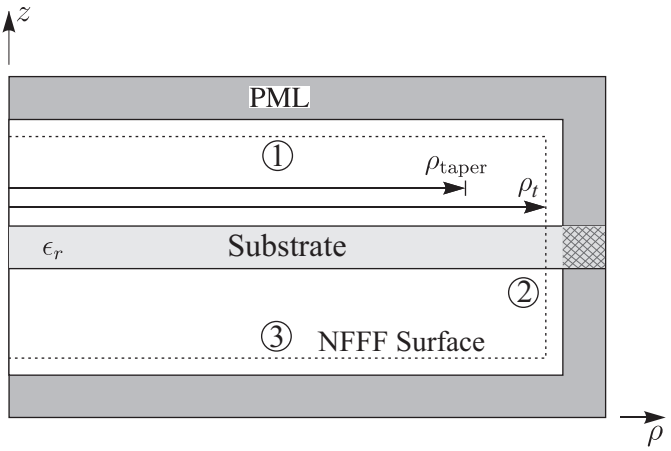

Figure 3.17: Diagram showing the relationship between the near-field to far-field transform surface and the dielectric substrate.

In this approximation, the standard NFFFT integrals are used; however, only the contribution from specific portions of the transform surface are included. The relevant geometry is shown in Fig. 3.17. The contribution of the NFFFT integral along the surface 2, where the free-space Green's function does not apply, is set to zero. The integral is then taken along surface 1 or surface 3, depending on the direction in which the far-field is being calculated. To mitigate the problems that arise when the integral is abruptly truncated, the electromagnetic field on the surface of interest (either surface 1 or 3) is spatially filtered before being integrated. The filter response is unity in the region between $\rho = 0$ and $\rho = \rho_{\text{taper}} > D/2$, leaving the field in this region unchanged. In the region between $\rho = \rho_{\text{taper}}$ and $\rho = \rho_t$, the filter response decreases linearly from unity to zero and smooths out the abrupt truncation.

This procedure introduces an error into the far-field patterns computed by the NFFFT. This error can be reduced by increasing the size of ρ_t. In the typical implementation of a NFFFT, the simulation space is confined to the region immediately surrounding the scatterer (e.g. out to the radius $D/2$ for a zone plate). The major drawback of this technique, therefore, is the need to simulate substrates with a radius ρ_t that is significantly larger than the radius of the zone plate. The size of ρ_t is dependant on the particular problem, as it should be made large enough that the frequency-domain electromagnetic field is sufficiently small along surface 2.

To validate the transformer and to demonstrate the effect of the radius of the substrate,

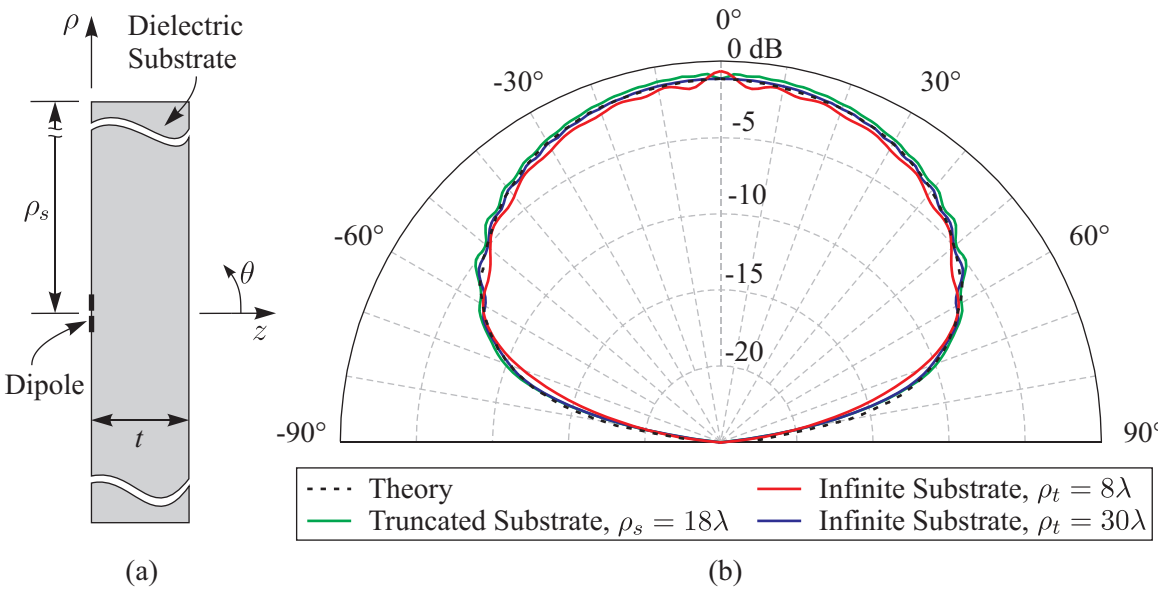

Figure 3.18: (a) Geometry of an infinitesimal dipole on a substrate. (b) Power patterns computed using different NFFFT techniques. Theoretical results from [23].

the far-field pattern of an infinitesimal dipole on a substrate is compared with theoretical results. The substrate is 0.3 mm thick with a permittivity of $\epsilon_r = 3.86$, and the geometry is shown in Fig. 3.18(a). The power patterns for the E-plane (xz-plane) computed by different NFFFT techniques are shown in Fig. 3.18(b). The dashed black line in Fig. 3.18(b) is the theoretical power pattern, computed in [23]. The green line is the power pattern for a dipole on a finite substrate with radius $\rho_s = 18\lambda$ calculated using the standard, free-space NFFFT. The red line is the power pattern calculated with the modified NFFFT presented in this section for an infinite substrate with $\rho_t = 8\lambda$. The ripples in this pattern are even worse than the pattern for the truncated substrate. For an infinite substrate with $\rho_t = 30\lambda$, however, there is a noticeable improvement in the agreement with the theoretical results.

For highly directive antennas, such as the IC zone plate antennas considered in [23] and [24], the error in the NFFFT is less of a concern. Most of the power is concentrated around $\theta = 0°$, so the contribution to the far-field from the areas where the NFFFT is truncated is much smaller. For the IC zone plate antennas in this work, a radius of ρ_t approximately five times as large as the radius of the zone plate was chosen to prevent the introduction of significant error.

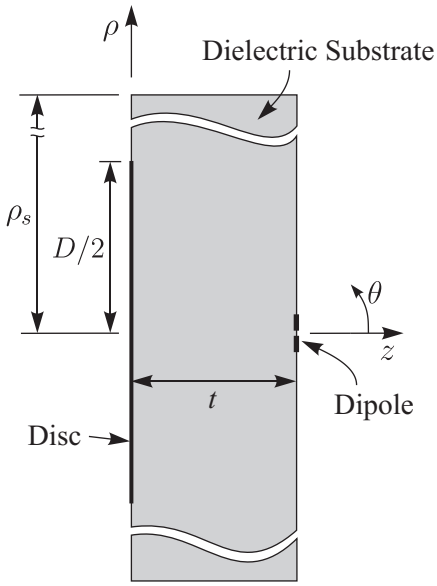

Figure 3.19: Geometry for a dipole on a substrate backed by a metal disc.

3.5.2 Comparison with Measurements

Initially, the BOR-FDTD results were compared to measurements of a dipole on a substrate backed by a metallic disc [23]. Figure 3.19 shows the geometry of a dipole on a substrate with thickness $t/\lambda_d = 3.77$, backed by a disc with diameter $D/\lambda_d = 8$, in which $\lambda_d = \lambda/\sqrt{\epsilon_r}$ is the wavelength in the substrate. The power pattern for this antenna is shown in Fig. 3.20. The power pattern is for the E-plane (xz-plane), and the agreement between the BOR-FDTD results and the measurements is reasonably good.

Next, a complete IC zone plate antenna (see Fig. 3.16) was modeled using the BOR-FDTD method. The parameters used in this simulation were $N_{\text{Soret}} = 18$, $F/\lambda_d = 9.04$ ($F = 6.0\,\text{mm}$), and $D/\lambda_d = 31.25$ ($D = 20.72\,\text{mm}$). The pattern in the E-plane for this IC zone plate antenna is plotted in Fig. 3.21. Considering that the high-frequency measurement technique in [23] makes obtaining highly accurate results difficult, the agreement between the computed and measured power patterns is also reasonably good. This is especially true in the region of the main lobe.

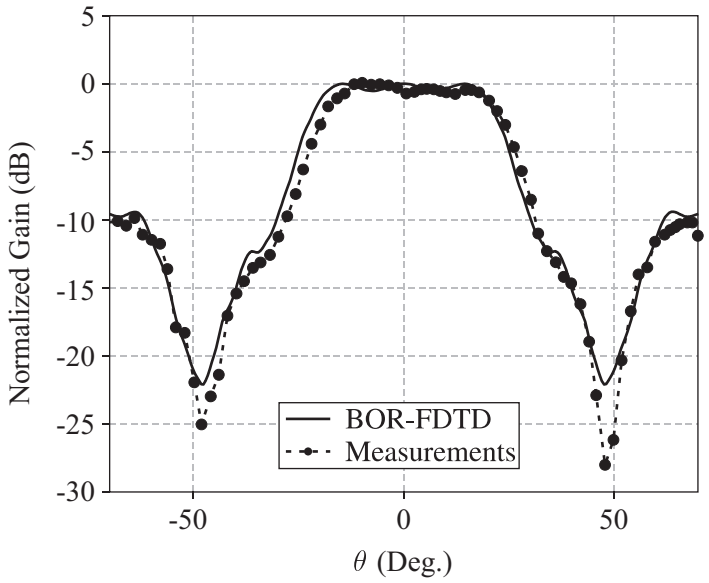

Figure 3.20: Power pattern in the E-plane for a dipole antenna on a substrate with thickness $t/\lambda_d = 3.77$, backed by a metallic disc with diameter $D/\lambda_d = 8$. Measured data from [23].

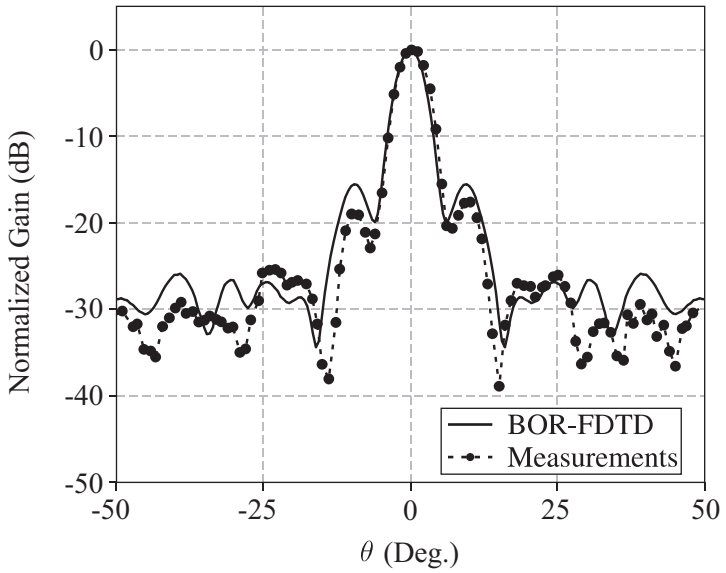

Figure 3.21: Power pattern in the E-plane for the IC zone-plate antenna with $f/\lambda_d = 9.04$. Measured data from [23].

CHAPTER IV

DESIGN STUDY FOR GROOVED-DIELECTRIC ZONE PLATE ANTENNAS

In this chapter, a study similar to that in Chapter 3 is performed for grooved-dielectric, phase-correcting zone plate antennas using the BOR-FDTD method. Visualizations of the electromagnetic field are used to discuss the focusing mechanism of this type of zone plate, and the results of a parametric study are used to generate design graphs. By taking advantage of the accuracy of the BOR-FDTD method, a number of factors that influence the focusing ability of a zone plate are examined in more detail than they have been before. These factors include the base thickness, the number of phase corrections per zone, the presence of a matching layer, and the tendency of the actual focal length to be shorter than the desired focal length. Design graphs are also given which show the weight and volume savings for zone plates compared to hyperbolic lenses. The performance metrics used for the design study are compared to metrics that commonly appear in the literature to clarify the terminology used throughout this work. Finally, the BOR-FDTD analysis is validated by comparison with previous measurements.

4.1 Visualizations

In Sec. 3.1, visualizations of the magnitude of the time average of the Poynting vector $\left|\langle\vec{S}(t)\rangle\right|$ were used to discuss the focusing mechanism of the Soret zone plate. In this section, similar figures are presented to give insight into the focusing mechanism of a grooved-dielectric, phase-correcting zone plate. $\left|\langle\vec{S}(t)\rangle\right|$ is plotted in cross section in Fig. 4.1 for a hyperbolic lens of diameter $D/\lambda = 39.8$ and focal length $F/\lambda = 30$ as well as for a phase-correcting zone plate of the same diameter and focal length ($N = 6$, $P = 4$). Both devices are for a dielectric with the relative permittivity $\epsilon_r = 2.53$, which is a typical value for Rexolite [66].

The excitation is a normally incident plane wave with the electric field oriented in the

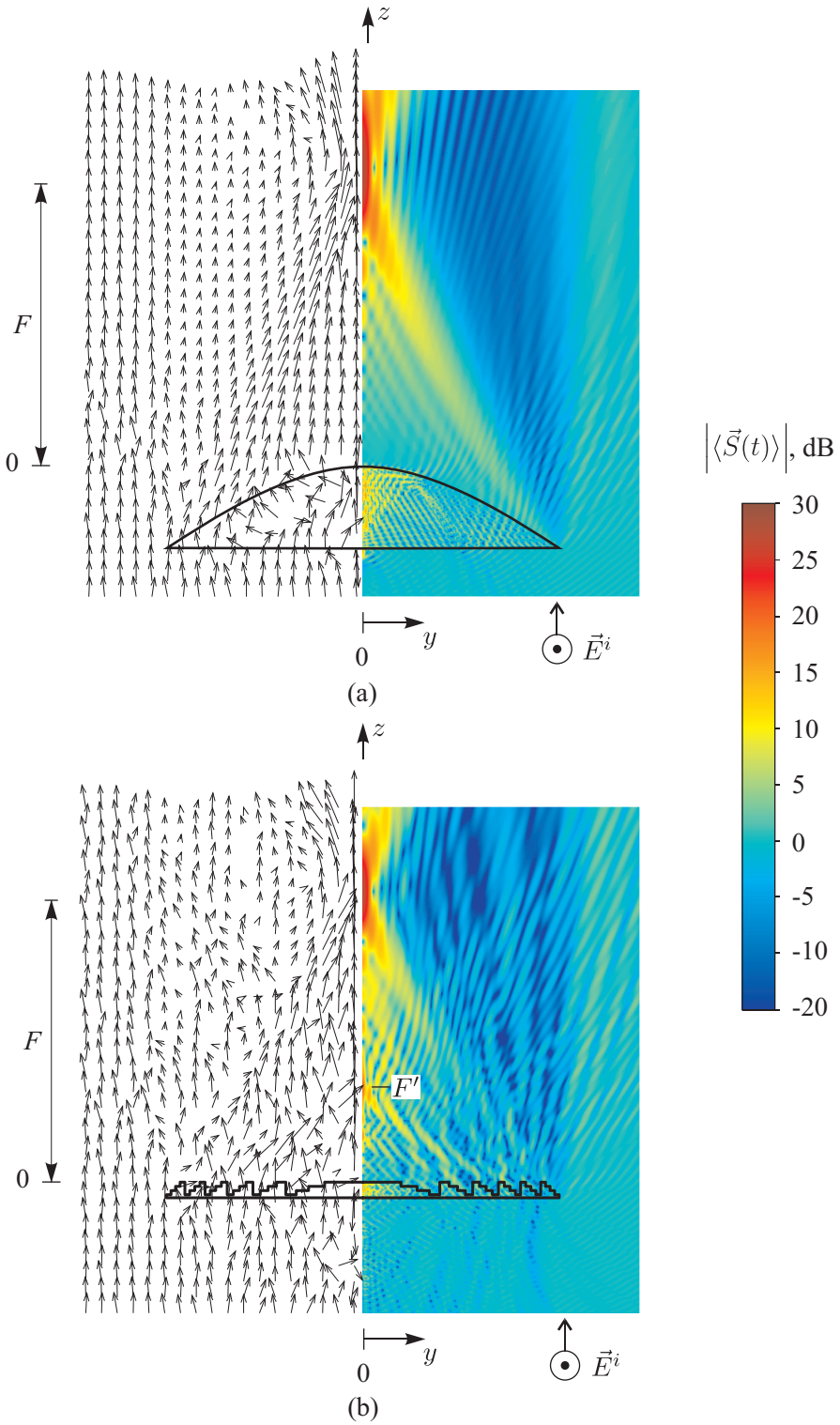

Figure 4.1: Magnitude and direction of the time average of the Poynting vector $\left|\langle\vec{S}(t)\rangle\right|$ for (a) a hyperbolic lens with a diameter of $D/\lambda = 39.8$ and a focal length of $F/\lambda = 30$ and (b) a grooved-dielectric, phase-correcting zone plate with a focal length of $F/\lambda = 30$, $N = 6$ zones ($D/\lambda = 39.8$), a base thickness of $t/\lambda = 0.1$, and four ($P = 4$) phase corrections per full-wave zone. Both devices are constructed from a dielectric with $\epsilon_r = 2.53$.

x-direction, and the cross sections shown are for the plane perpendicular to this incident electric field (the yz-plane). The left halves of Figs. 4.1(a) and 4.1(b) show arrows indicating the direction of the time-average Poynting vector. The length of each arrow is proportional to the logarithm of the magnitude of the time-average Poynting vector $\left|\langle\vec{S}(t)\rangle\right|$ at the point where the arrow originates. The right half of each of these figures shows $\left|\langle\vec{S}(t)\rangle\right|$ plotted in dB, with red representing the greatest intensity and blue representing the least intensity. Outlines for the hyperbolic lens and the phase-correcting zone plate are on the respective plots.

As expected, the spatial variation in the power is much smoother for the lens than for the phase-correcting zone plate. The interpretation of Fig. 4.1(a) is straightforward: Outside of the lens, the arrows in Fig. 4.1(a) look like the rays that one expects from a geometrical (ray-tracing) analysis. Inside of the lens, there is an interference pattern created by reflections from the surfaces of the lens. Such a simple interpretation is not readily possible for the zone plate in Fig. 4.1(b), for which the spatial variation in power is more complicated. Clearly, however, both devices focus energy at the distance F from the device. For the zone plate, there is a second maximum on the axis at $z = F' \approx F/3$. This secondary focal point is well-documented in the literature [67]. In the region beyond the lens and zone plate ($\rho > D/2$) the time-average Poynting vector for the incident plane wave (0 dB) can be seen, overlaid by diffraction bands. The cross sections in Fig. 4.1 clearly show the reduction in the volume of dielectric that can be achieved by replacing a lens with a zone plate. For this example, the volume, and hence the weight, is reduced by a factor of about six.

4.2 Parametric Study and Design Graphs

A parametric study was performed for the grooved-dielectric, phase-correcting zone plate antenna, in a manner similar to the studies for the Soret and folded zone plates in Sec. 3.3. For reference, the geometry of the grooved-dielectric, phase-correcting zone plate is shown in Fig. 4.2. The three primary geometrical parameters that describe a zone plate are the focal length, the diameter, and the number of zones. These parameters are interrelated

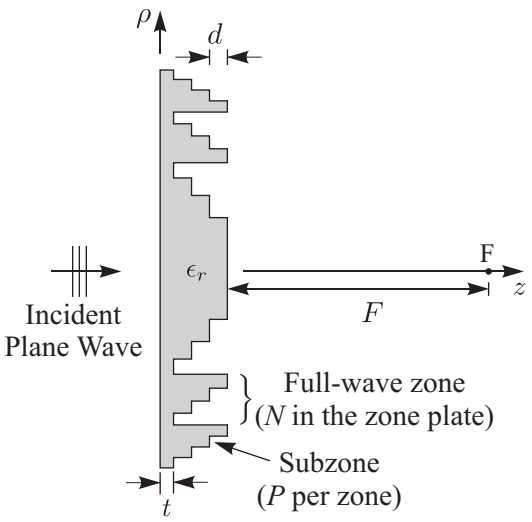

Figure 4.2: Geometry of the grooved-dielectric, phase-correcting zone plate.

through Eq. (1.2), $D/\lambda = 2\sqrt{N(N + 2F/\lambda)}$, and therefore only two of the three can be chosen independently.

In this study, like that for the Soret and folded zone plate antennas in Chapter 3, the focal length F is varied from 1 to 50 wavelengths, and the diameter D is varied from 3.5 to 75 wavelengths. The number of zones N, therefore, ranges from 1 to 37, and the ratio of the focal length to the diameter, or the f-number, covers cases up to approximately 2.5. These f-number values are typical of microwave or millimeter-wave zone plates [68]. Quarter-wave zone plates are used, meaning the phase is corrected in 90 degree increments ($P = 4$). The base thickness of the dielectric slab is $t/\lambda = 0.1$.

The dielectric used for the zone plates was assumed to be lossless and to have the relative permittivity of Rexolite, $\epsilon_r = 2.53$. There were two reasons for the omission of the loss: First, this reduced the number of parameters that had to be considered in the design study and allowed us to concentrate on the important geometrical parameters that mainly determine the focusing ability of the lenses. Second, calculations that were made using a loss typical of that for Rexolite showed that the effect of loss on the gain was generally less than the effect caused by other parameters, such as the base thickness, which is considered.

The same metrics introduced in Sec. 3.2 are used to quantify the focusing ability of these zone plate antennas as well. The focusing gain FG is defined for phase-correcting

zone plates in a manner similar to Eq. (3.1) for Soret and folded zone plates:

$$FG = \frac{\left|\mathrm{Re}[\hat{z} \cdot \vec{S}_c^{\,\mathrm{tot}}]\right|}{\left|\mathrm{Re}[\hat{z} \cdot \vec{S}_c^{\,i}]\right|}, \tag{4.1}$$

Likewise, the formula for the gain is similar to Eq. (3.2):

$$G = \frac{4\pi \left| \int_0^{2\pi} \int_0^{\rho_{\mathrm{disc}}} \mathrm{Re}[\hat{z} \cdot \vec{S}_c^{\,\mathrm{tot}}] \rho \, \mathrm{d}\rho \, \mathrm{d}\phi \right|}{\lambda^2 \left|\mathrm{Re}[\hat{z} \cdot \vec{S}_c^{\,i}]\right|}. \tag{4.2}$$

There is one important difference in the calculation of these metrics for grooved-dielectric, phase-correcting zone plate antennas: These antennas use zone plates in the transmission mode, and the incident field therefore makes an important contribution at the focal point. For this reason, the total field was used for the calculation of $\vec{S}_c^{\,\mathrm{tot}}$ in the numerators of Eqs. (4.1) and (4.2), unlike Eqs. (3.1) and (3.2), which use the scattered field. This distinction is clear in Fig. 2.3, which shows the focal point in the scattered-field region for the Soret zone plate and in the total-field region for the grooved-dielectric, phase-correcting zone plate.

4.2.1 Design Graphs Based on Focusing Gain

Figure 4.3 is a design graph for the focusing gain for the grooved-dielectric, phase-correcting zone plate antenna. The solid lines are contours of constant focusing gain FG (spaced 2 dB apart) while the dashed lines are for a constant number of full-wave zones N. Note that not all of the lines of constant N are shown. For convenience, the curves of constant FG are shown as continuous lines; of course, they have practical meaning only where they intersect a curve of constant N, which must be an integer. Results are given for all points in the grid, even though some regions near the edges represent unrealistic designs.

The trends in this plot are similar to the trends for the Soret and folded zone plates: Increasing the diameter D/λ while holding the focal length F constant results in an increase in the focusing gain FG. For larger values of D/λ, however, the effect lessens, as can be seen by the increase in the spacing between contours for any horizontal line though Fig. 4.3 as D/λ gets larger. Likewise, if the number of zones N is held constant and diameter and focal length are allowed to increase in a way that satisfies Eq. (1.2), the focusing gain also generally increases. Again, the increase eventually tapers off. Finally, note that when the

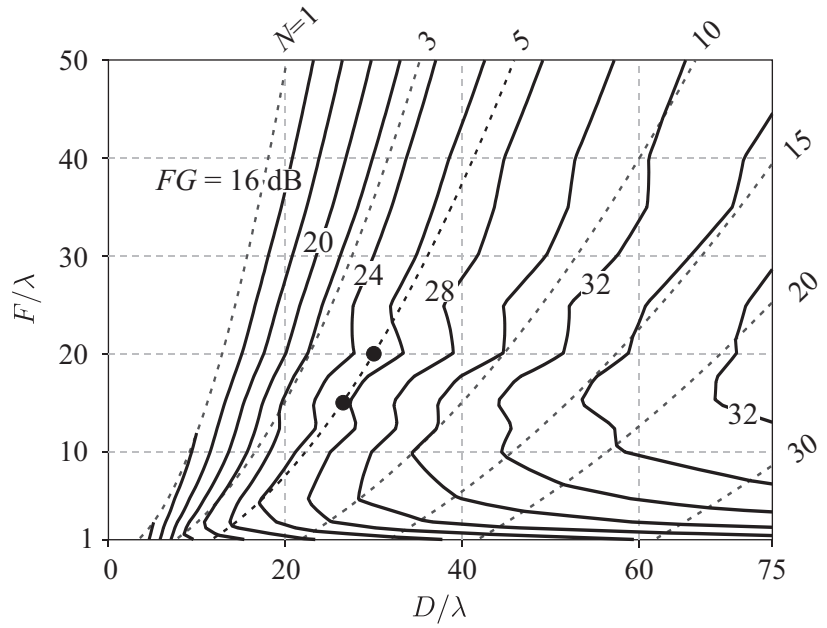

Figure 4.3: Design graph for the grooved-dielectric, phase-correcting zone plate antenna. The solid lines represent contours of constant focusing gain FG (in dB), while the dashed lines represent lines of constant number of full-wave zones N. $P = 4$, $\epsilon_r = 2.53$, and $t/\lambda = 0.1$.

diameter is held constant and N and F/λ are increased, the focusing gain initially increases. Eventually, FG reaches a maximum and begins to decrease. The maximum value for the focusing gain was found for a grooved-dielectric, phase-correcting zone plate as a function of diameter, as was done for Soret and folded zone plates in Fig. 3.10. The value of $FG_{\max}$ is plotted in Fig. 4.4. The values of N and F/λ that result in the zone plate with the highest FG are given for a few diameters in the figure. A more detailed discussion of all three of these general trends in terms of a few simple physical phenomena can be found in Chapter 3.

One major difference between the design graph for the grooved-dielectric, phase-correcting zone plate (Fig. 4.3) and the Soret and folded zone plates (Fig. 3.5), however, is the presence of the ripples that can be seen in the lines of constant FG in Fig. 4.3. In Sec. 4.2.3, it will be shown that these ripples are caused by multiple reflections within the dielectric and are related to the base thickness t of the zone plate.

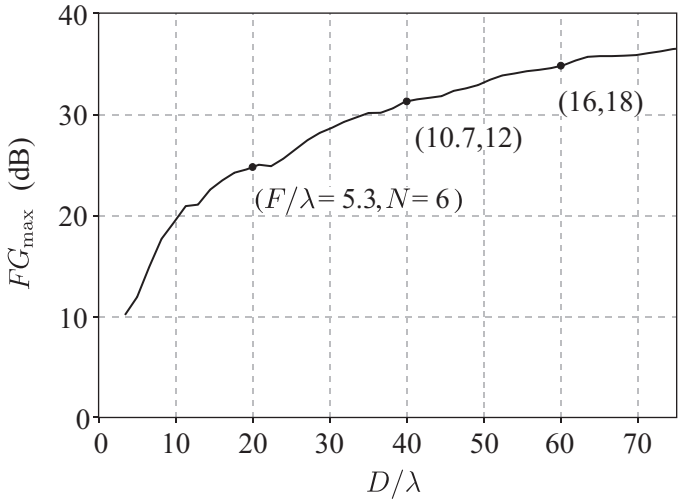

Figure 4.4: The maximum value of the focusing gain FG for a grooved-dielectric, phase-correcting zone plate antenna with a fixed diameter D/λ.

4.2.2 Design Graphs Based on the Gain

The gain, G, computed from Eq. (3.2) with $\rho_{\text{disc}} = \lambda/2$ is shown in Fig. 4.5 in the same manner that the focusing gain is presented in Fig. 4.3. The analysis of this design graph is very similar to the analysis of Fig. 4.3: as the diameter, focal length, and number of zones are varied, the gain is seen to follow the same trends as the focusing gain. An increase in the radius of the aperture, ρ_{disc}, beyond $\lambda/2$ would increase the value of G, though the amount of increase would depend on how the power is distributed in the focal plane of the zone plate. The maximum value of G for a zone plate antenna with a given diameter is plotted in Fig. 4.6. The values of N and F/λ that result in the zone plate with the highest G are given for a few diameters in the figure.

4.2.3 Effect of the Base Thickness on Focusing Ability

The design graphs for grooved-dielectric, phase-correcting zone plates (Figs. 4.3 and 4.5) show ripples in the lines of constant FG and G. To examine the effect of these ripples, we will compare the focusing gain of a zone plate with $F/\lambda = 20$ and $N = 5$ ($D/\lambda = 30$) to that of a zone plate with $F/\lambda = 15$ and $N = 5$ ($D/\lambda = 26.5$). The points that correspond to these designs are marked with dots in Fig. 4.3. Based on a simple geometric analysis, we would expect the focusing gain of the zone plate with $F/\lambda = 20$ to be slightly greater

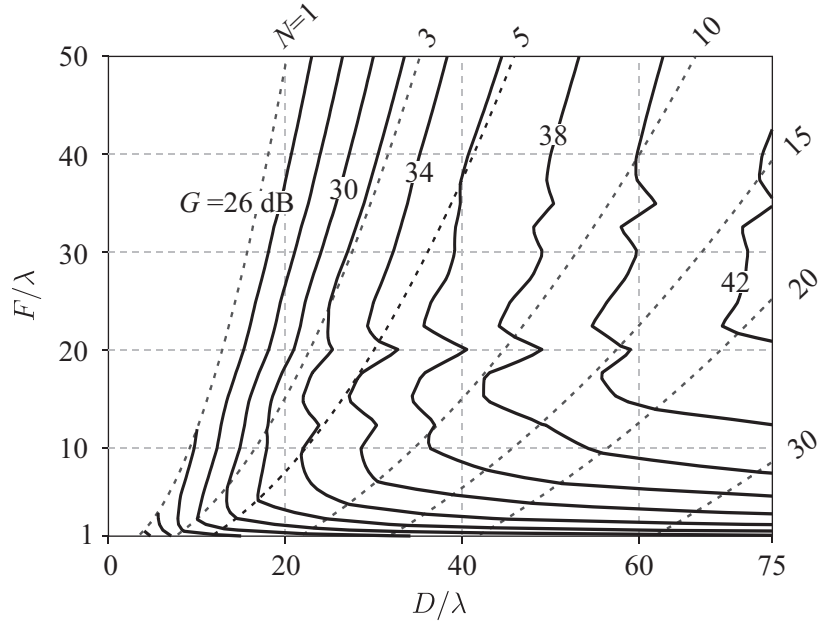

Figure 4.5: Design graph for the grooved-dielectric, phase-correcting zone plate antenna with $\rho_{\text{disc}} = \lambda/2$. The solid lines represent contours of constant gain G (in dB), while the dashed lines represent lines of constant number of full-wave zones N. $P = 4$, $\epsilon_r = 2.53$, and $t/\lambda = 0.1$.

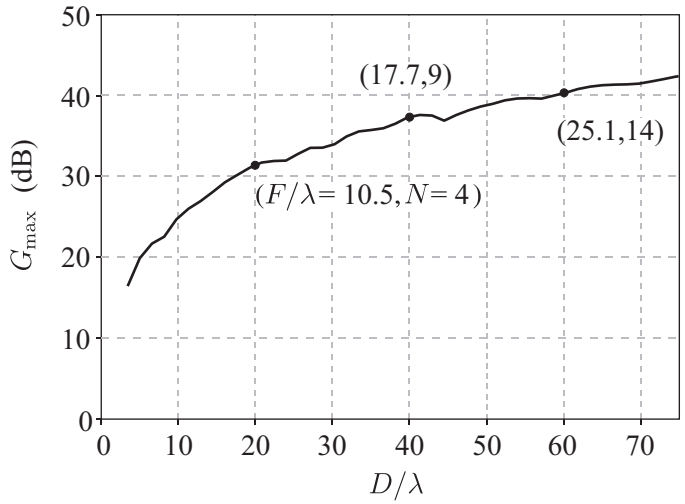

Figure 4.6: The maximum value of the focusing gain G for a grooved-dielectric, phase-correcting zone plate antenna with a fixed diameter D/λ.

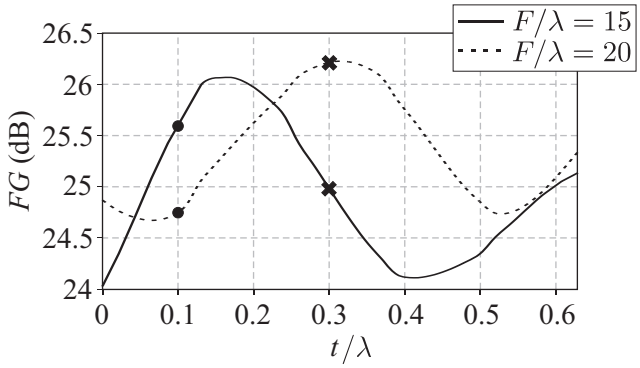

Figure 4.7: Focusing gain FG as the base thickness t/λ is varied for two similar zone plates. The solid line shows FG for a zone plate with $F/\lambda = 15$ ($D/\lambda = 26.5$), and the dashed line for a zone plate with $F/\lambda = 20$ ($D/\lambda = 30$). Both zone plates share the parameters $N = 5$, $\epsilon_r = 2.53$, and $P = 4$.

than the zone plate with $F/\lambda = 15$. Contrary to expectations, however, the zone plate with $F/\lambda = 20$ has a smaller focusing gain (about 1 dB less) than the one with $F/\lambda = 15$, as can be seen by the respective proximity of the dots in Fig. 4.3 to the contour line for $FG = 26\,\text{dB}$.

This interesting result is caused by multiple reflections within the structure of the phase-correcting zone plate. Figure 4.7 shows the focusing gain FG as a function of the base thickness t/λ for the two zone plates marked by the dots in Fig. 4.3 and mentioned previously. For the figure, the wavelength in the dielectric is $\lambda_d = \lambda/\sqrt{\epsilon_r} = 0.629\lambda$, and $0 \leq t/\lambda \leq 0.629$ ($0 \leq t/\lambda_d \leq 1$). The zone plate with the focal length of $F/\lambda = 15$ has higher focusing gain when $t = 0.1\lambda = 0.159\lambda_d$ (indicated by dots in Fig. 4.7). Setting the base thickness to $t = 0.3\lambda = 0.477\lambda_d$, however, would reverse the result, and the zone plate with $F/\lambda = 20$ would outperform the zone plate with $F/\lambda = 15$ by more than 1 dB (indicated by crosses in Fig. 4.7). This shows that the presence and form of the ripples in Fig. 4.3 are dependant on the base thickness, t.

Matching layers are often placed on the surfaces of conventional lenses to reduce reflections and improve their performance, and we might expect the same to be true for the zone plate. To test this hypothesis, a dielectric, quarter-wave matching layer was placed on the front surface of the zone plate, as shown in Fig. 4.8(a). The thickness of the layer was $(\lambda/\sqrt{\epsilon_{rm}})/4$. For this case, the relative permittivity of the layer was $\epsilon_{rm} = \sqrt{\epsilon_r} \approx 1.59$.

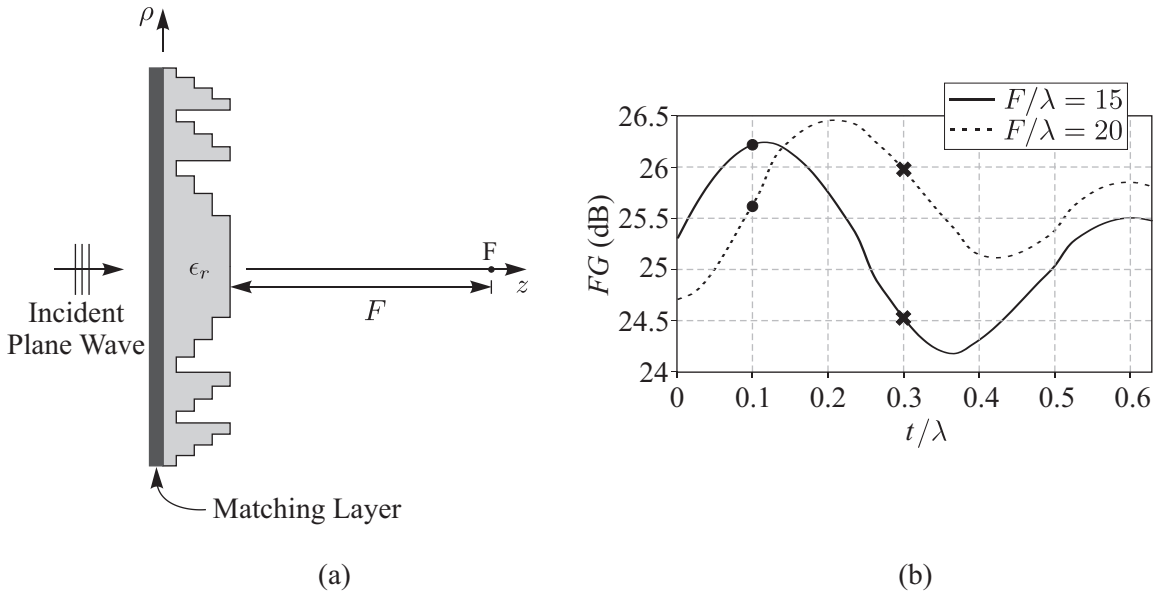

Figure 4.8: (a) Geometry of the grooved-dielectric, phase-correcting zone plate with a matching layer. (b) Focusing gain FG as the base thickness t/λ is varied for two similar zone plates with a matching layer. The solid line shows FG for a zone plate with $F/\lambda = 15$ ($D/\lambda = 26.5$), and the dashed line for a zone plate with $F/\lambda = 20$ ($D/\lambda = 30$). Both zone plates share the parameters $N = 5$, $\epsilon_r = 2.53$, and $P = 4$.

Figure 4.8(b) shows the effect of including the matching layer. It clearly alters the dependence of the focusing gain on the base thickness t/λ. For some values of t/λ, the layer increases FG as expected, while for other values of t/λ it decreases FG. This can be seen by comparing the points marked on the figures. When $t/\lambda = 0.1$ (dots), the matching layer increases FG for both designs ($F/\lambda = 15$ and 20) compared to Fig. 4.7. However, when $t/\lambda = 0.3$ (crosses), the addition of the matching layer results in a decrease in FG for both designs. From these results, it appears that the effectiveness of a simple quarter-wave matching layer for increasing the focusing gain of the zone plate must be evaluated for each design.

The choice of the base thickness controls the overall thickness of the zone plate and, as shown above, affects the focusing ability of the zone plate. Despite this, it has received a relatively small amount of attention in the literature [69]. In a practical design, a thickness $t > 0$ is necessary to support the zone plate. In an analysis of these devices that uses geometrical optics, the base thickness does not affect the focusing, because it imparts a

uniform phase shift for all of the incident field. In reality, however, t does determine how much of the incident energy is reflected from the dielectric-air interfaces and how the multiple reflections that occur within the zone plate produce constructive or destructive interference. Therefore, it is reasonable to assume that t can be optimized. An in-depth study, however, showed that there does not appear to be a simple, analytical method for optimizing t. The study also showed that for typical microwave or millimeter-wave zone plates, the change in the focusing gain due to varying t can be as much as 2 dB. The findings in this work agree with the conclusions drawn in recently-published work by Petosa, Gagnon, and Ittipiboon [70].

4.2.4 Effect of the Number of Phase Corrections Per Zone on Focusing Ability

In addition to the physical size of a zone plate, the number of phase corrections per full-wave zone P also has an effect on the focusing ability of a zone plate. The geometrical optics design methodology for a phase-correcting Fresnel zone plate, discussed in Chapter 1, predicts that increasing the number of phase corrections per full-wave zone will improve the focusing ability of the device. Extensive simulations with the BOR-FDTD method have shown this is not always true; a larger value for P does not guarantee improved focusing. Nevertheless, some general observations can be made about the effect of P on the focusing ability of a zone plate. For the zone plates presented in this chapter, there is generally a considerable improvement in focusing ability when the number of phase corrections per zone is increased from $P = 2$ to $P = 4$. Increasing P beyond four does not consistently improve the focusing, however. Figure 4.9 illustrates these points; it shows the focusing gain as the diameter is varied for zone plate antennas with $F/\lambda = 20$. Among the phase-correcting zone plates, the $P = 2$ case clearly has the lowest focusing gain FG for every value of the diameter D/λ. The $P = 4$ and $P = 8$ cases, however, have generally similar focusing gains, and the best choice between the two alternates as D/λ is changed. The difference between the focusing gains when $P = 4$ and $P = 8$ is generally within the variance observed by changing the base thickness, t. This suggests that the effect on the focusing gain due to internal reflection may be greater than the effect of increasing P from four to eight.

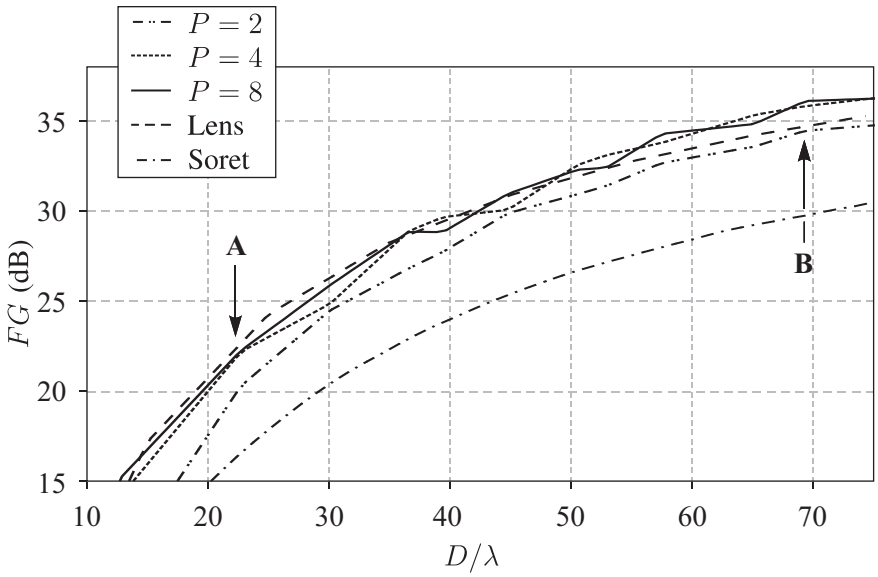

Figure 4.9: Focusing gain FG as the diameter D/λ is varied for zone plate antennas with $P = 2$, $P = 4$, and $P = 8$. $F/\lambda = 20$, $\epsilon_r = 2.53$, and $t/\lambda = 0.1$ for all of the zone plates. The focusing gain of a hyperbolic lens with $F/\lambda = 20$ and $\epsilon_r = 2.53$, and a Soret zone plate with $F/\lambda = 20$ are also shown for comparison.

Also shown on the graph are the focusing gains for hyperbolic lenses with $F/\lambda = 20$ and $\epsilon_r = 2.53$ and Soret zone plates with $F/\lambda = 20$. As expected, the focusing gains for the Soret zone plates, described in detail in Chapter 3, are not as large as the focusing gains for the grooved-dielectric, phase-correcting zone plates. Notice that the focusing gains for the lenses are slightly greater than those for the zone plates with $P = 4$ and $P = 8$ when $D/\lambda \lesssim 40$ ($F/D \gtrsim 0.5$). However, For $D/\lambda \gtrsim 40$ ($F/D \lesssim 0.5$), the zone plates actually outperform the hyperbolic lenses.

This counter-intuitive observation can be explained by examining the profile of these lenses. The thickness at the center of the hyperbolic lens, h, varies greatly over the range of lenses simulated to generate Fig. 4.9. To better visualize this, Fig. 4.10 shows the profile for examples of lenses and zone plates at two extremes of the range of diameters examined in this work. For the smaller values of D/λ, the ratio h/F is small. The lens can be considered thin and the customary, simple arguments for focusing apply. Figure 4.10(a) shows the profile of a hyperbolic lens with diameter $D/\lambda = 22.7$. This lens has a thickness $h/\lambda = 4.3$, so the ratio h/F is small: $h/F = 0.21$. The focusing gains for devices with this

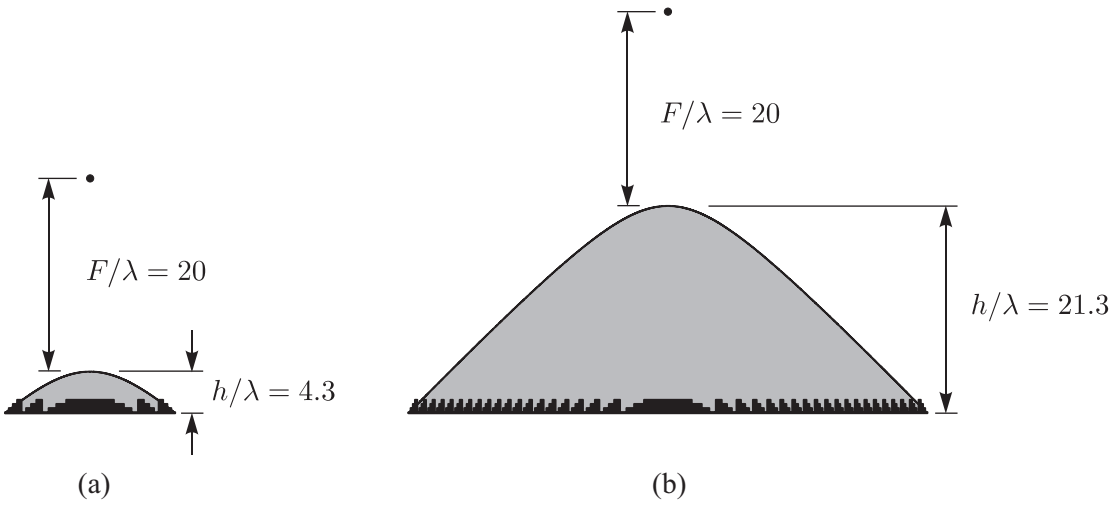

Figure 4.10: Profile for two hyperbolic lenses with $F/\lambda = 20$ and diameters (a) $D/\lambda = 22.7$ and (b) $D/\lambda = 69.3$. The profile for zone plates with the same focal length and diameter are also shown.

diameter are marked by point **A** in Fig. 4.9. For the larger values of D/λ, the ratio h/F is of the order one, so the lens can no longer be considered thin. Figure 4.10(b) shows the profile of a thick lens, with $D/\lambda = 69.3$ and $h/\lambda = 21.3$. The ratio of the thickness to the focal length is therefore $h/F = 1.07$. The focusing gains for devices with this diameter are marked by point **B** in Fig. 4.9. The profiles of the corresponding zone plates with $P = 4$ are also shown in black in Fig. 4.10. The zone plate have $N = 3$ and $N = 20$ zones, respectively. Referring back to Fig. 4.9, it can be seen that it is in the range where the hyperbolic lenses are thick (near point **B**) that the zone plate outperforms the lens.

4.2.5 Effect of Focal Shift on Focusing Ability

The BOR-FDTD simulations show that the actual focal point (i.e. the point of greatest focusing gain) of a microwave or millimeter-wave zone plate tends to be located closer to the zone plate than Eq. (1.2) predicts. This effect has been noted by other researchers for zone plates [36, 54, 71] as well as for traditional lenses [72].

An example of this effect is in Fig. 4.11, which shows the focusing gain FG along a portion of the z-axis for three different zone plates. The focal length is designed to be $F/\lambda = 10$ for all three zone plates and is marked by the solid black line in the figure. Each zone plate has a different number of zones: $N = 20$ ($F/D = 0.18$), $N = 15$ (0.22), and

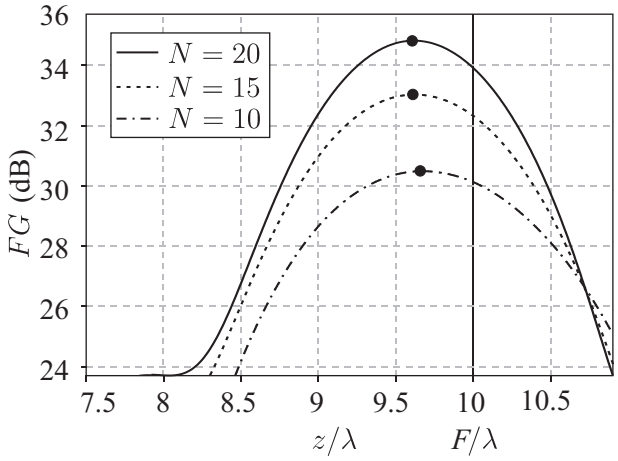

Figure 4.11: Focusing gain FG along the z-axis for zone plates with $N = 20$, $N = 15$, and $N = 10$. For all three zone plates, the focal length was designed to be $F/\lambda = 10$. The other parameters are $t/\lambda = 0.1$ and $\epsilon_r = 2.53$. The dots indicate the point of maximum focusing gain for each zone plate.

$N = 10$ (0.29). It is clear from Fig. 4.11 that the actual focal length of each zone plate antenna (the distance from the zone plate to the point of maximum focusing gain) is shorter than specified in the design. The decrease in FG at the designed focal point due to focal length shortening is 0.9 dB for the zone plate with $N = 20$, 0.7 dB for $N = 15$, and 0.4 dB for $N = 10$. As N is increased and the focal length F is held constant, the diameter D of the zone plate is increased according to (1.3), and the f-number is decreased. Figure 4.11, therefore, suggests that the reduction of focusing gain due to focal length shortening is more severe for zone plates with small f-numbers. Simulations for the other zone plates in the parametric study, Fig. 4.3, confirm this trend. The focal length shortening is, therefore, of greater concern for microwave and millimeter-wave zone plates, for which a small f-number is typical, than it is for optical zone plates.

To compensate for this displacement of the focal point, the value of F used in the standard design formulas can be made slightly longer than the desired distance to the focal point. One particular empirical correction that provides this compensation has been proposed by Hristov and Herben in [71]. They suggest an improvement to the zoning algorithm by adjusting the focal length in Eq. (1.3):

$$\rho_n = \sqrt{\left(\frac{n\lambda}{P}\right)^2 + \frac{2n\lambda\,(F + d/2)}{P}}, \tag{4.3}$$

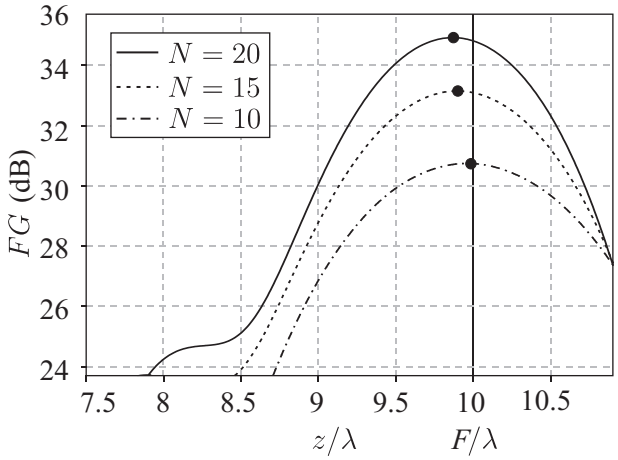

Figure 4.12: Focusing gain FG along the z-axis for zone plates designed using the alternative zoning rule defined in Eq. (4.3) with $N = 20$, $N = 15$, and $N = 10$. For all three zone plates, the focal length was designed to be $F/\lambda = 10$. The other parameters are $t/\lambda = 0.1$ and $\epsilon_r = 2.53$. The dots indicate the point of maximum focusing gain for each zone plate.

in which d is difference in thickness between consecutive subzones in a grooved-dielectric, phase-correcting zone plate and is calculated using Eq. (1.4). This correction is applied to zone plates with $P > 2$ by Wiltse in [73]. The values of ρ_n that are calculated from Eq. (4.3) are the same as the values that would be calculated from Eq. (1.3) for a zone plate with a focal length that is $d/2$ longer. Hence, the new formula is effectively the same as designing a zone plate with a slightly longer focal length.

BOR-FDTD simulations show that this technique does improve the focusing ability of a zone plate antenna. By designing zone plates with Eq. (4.3), or effectively forcing the focal length of the zone plate to be slightly longer than the original design, some of the natural shortening of the focal length can be offset and the point of greatest focusing gain can be moved closer to the desired focal point. The focusing gains for the three corresponding zone plates designed using Eq. (4.3) are plotted in Fig. 4.12. The point of maximum focusing gain is seen to be closer to the desired focal point ($F/\lambda = 10$) for all three of the designs than it is in Fig. 4.11.

Despite the obvious improvement seen from Fig. 4.11 to Fig. 4.12, the plots show that this technique is not necessarily optimal. In general, the focusing gain can be made even larger by further adjustments of the focal length in (1.3). For each of the zone plates in

Fig. 4.11, a different amount of adjustment to the focal length is necessary to optimize the focusing gain. In the proposed method, the focal lengths for the three zone plates are corrected by the same amount; however, because they all require correction in the same direction, the new zoning formula offers at least some improvement for each.

The discussion of improving the focusing gain by artificially increasing the designed focal length must be kept in perspective, however. It is important to note that the simulations for the zone plates used in the parametric study show that the decrease in the focusing gain, FG, due to the shift of the focal point is of the same order of magnitude as the aforementioned fluctuations in FG due to the choice of the number of phase corrections per zone P or the variation in the base thickness, t. Therefore, a true optimization for the focusing gain of the zone plate must involve a full electromagnetic analysis that attempts to remove any decrease in gain due to both of these factors.

4.2.6 Weight and Volume of Zone Plate Antennas

One of the advantages of Fresnel zone plate antennas over traditional hyperbolic lenses is the reduction in weight and volume. Figures 4.13-4.15 present design graphs that show the weight (and volume, which is proportional to weight) savings for zone plates with the same ranges of parameters that are presented in Figs. 4.3 and 4.5. The figures show lines of constant weight (volume) savings. This parameter is determined by calculating the volume of a hyperbolic lens with a given focal length F/λ and diameter D/λ and dividing by the volume of a zone plate with the same focal length and diameter. For example, for a zone plate with $P = 4$, $F/\lambda = 40$, and $D/\lambda = 60$ ($N = 10$), Fig. 4.13 shows that the weight savings ratio is slightly greater than eight. This means that the zone plate weighs more than eight times less than a lens with the same focal length and diameter. The zone plates and lenses are made from Rexolite and have a base thickness of $t/\lambda = 0.1$.

Figure 4.13 gives the ratio of the weight of the hyperbolic lens to the weight of the zone plate when $P = 4$. Figure 4.14 is for $P = 8$, and Fig. 4.15 is for the limit as $P \to \infty$. In the latter case, the zone plate profile is smooth, except for discontinuous jumps at the zone boundaries. As P is increased, the savings in weight decrease, although the amount of the

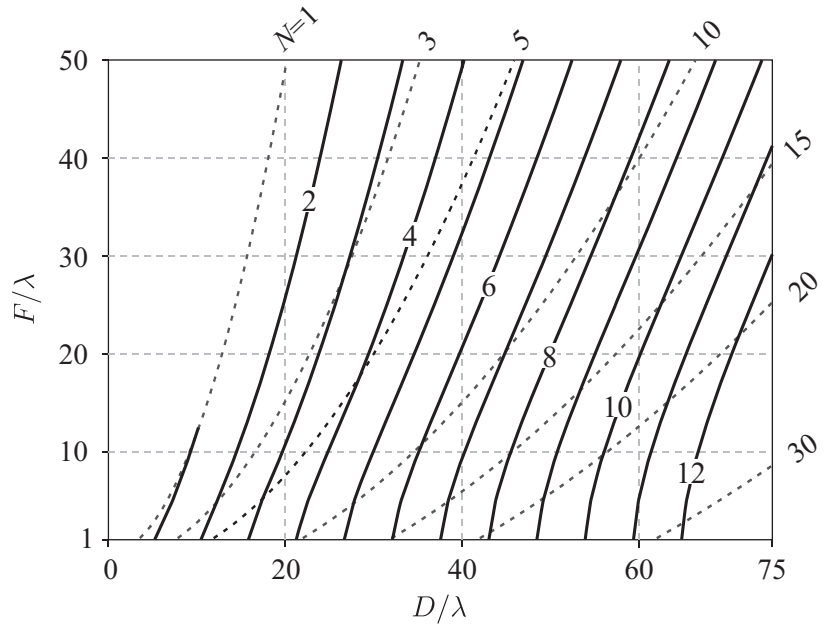

Figure 4.13: Design graph for the weight savings of zone plates with $P = 4$. The solid lines represent contours of constant weight savings (weight of the hyperbolic lens divided by the weight of the zone plate), while the dashed lines represent lines of constant number of full-wave zones N. $\epsilon_r = 2.53$, and $t/\lambda = 0.1$.

decrease is small. For the example presented above ($F/\lambda = 40$, $D/\lambda = 60$, and $N = 10$), the weight savings factors are 8.2, 7.1, and 6.3 for $P = 4$, $P = 8$, and $P \to \infty$, respectively.

4.3 Clarification of Zone Plate Performance Metrics

In the literature, zone plate antennas are often characterized by a few common metrics. However, the terminology used to refer to these metrics varies among researchers. This section is designed to clarify the relationship between these metrics and the results presented in this work.

The classical zone plate performance measure is that which is defined as efficiency in [45]. This same metric is alternately referred to as the phase efficiency [8], the diffraction efficiency [36, 74], or the aperture efficiency [69]. This term encapsulates the effect on the performance of a zone plate due to the phase approximation. It is useful for studying the effects of decreasing the step size for phase correction (increasing P), which has been shown in this chapter to be one of many factors that influence the focusing ability of a phase-correcting zone plate antenna.

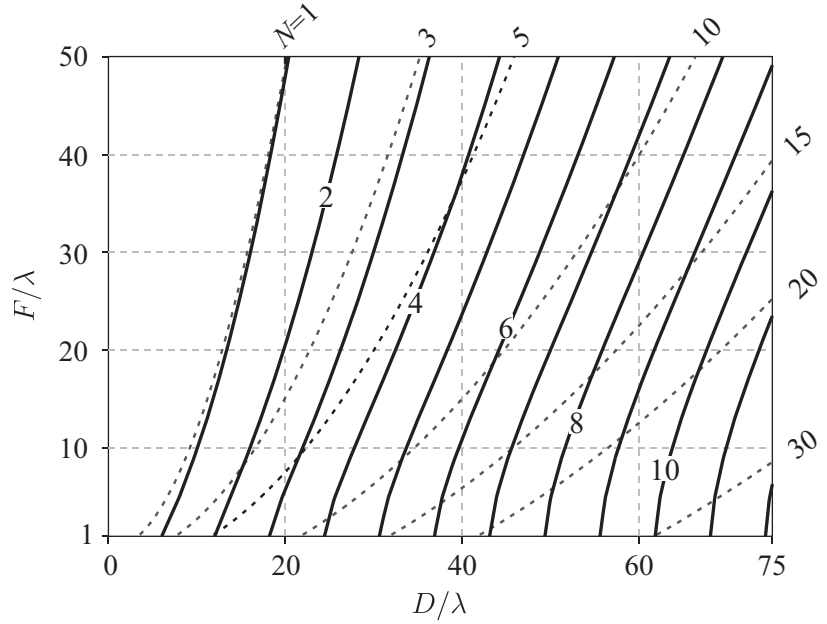

Figure 4.14: Design graph for the weight savings of zone plates with $P = 8$. The solid lines represent contours of constant weight savings (weight of the hyperbolic lens divided by the weight of the zone plate), while the dashed lines represent lines of constant number of full-wave zones N. $\epsilon_r = 2.53$, and $t/\lambda = 0.1$.

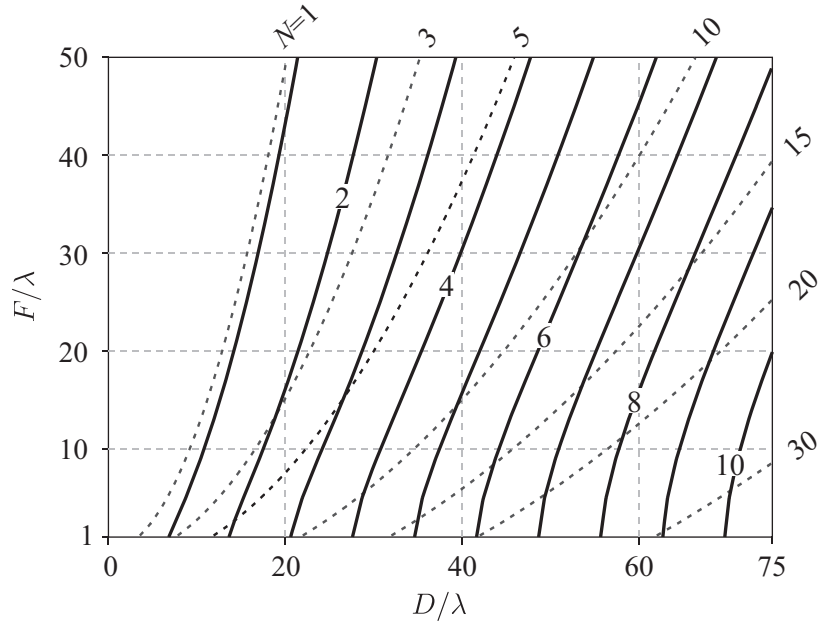

Figure 4.15: Design graph for the weight savings of zone plates with $P \to \infty$. The solid lines represent contours of constant weight savings (weight of the hyperbolic lens divided by the weight of the zone plate), while the dashed lines represent lines of constant number of full-wave zones N. $\epsilon_r = 2.53$, and $t/\lambda = 0.1$.

An efficiency can be calculated from the BOR-FDTD results. This is accomplished by comparing the focusing gain of a zone plate with a fixed value of P to the focusing gain for the same zone plate as P approaches infinity: $FG/FG_{P\to\infty}$. Of course, the continuous profile in the limit $P \to \infty$ cannot be modeled with the standard BOR-FDTD method, but the 'stair-case error' inherent in the method can be made acceptably small by increasing the level of discretization.

In Table 4.1, the efficiency calculated from the BOR-FDTD results is compared with the efficiency η computed using an approximate geometrical argument in [45]. Results are given for two antennas with fairly different parameters: $F/\lambda = 30$ and $N = 6$ ($F/D = 0.75$), and $F/\lambda = 12.5$ and $N = 20$ ($F/D = 0.21$). The two have the same material property, $\epsilon_r = 2.53$, and the physically unrealistic base thickness $t = 0$, which was chosen to isolate the effects of the phase approximation. For this comparison, the maximum value of the focusing gain was used. Recall from Sec. 4.2.5 that this occurs at a point slightly closer to the zone plate than F. The values computed with the BOR-FDTD method are seen to be comparable to the published efficiencies based on the approximate geometrical analysis.

4.4 Comparison with Measurements

To validate the BOR-FDTD analysis of grooved-dielectric, phase-correcting zone plate antennas, simulation results for problems with similar physical characteristics were compared to measurements available in the literature for both near- and far-field quantities. For the near-field tests, simulations of the field focused by a dielectric lens were compared to measurements. The far-field test was a comparison of the simulated and measured radiation patterns for a grooved-dielectric, phase-correcting zone plate antenna.

To test the accuracy of the BOR-FDTD simulations in the near-field, BOR-FDTD results were compared to Carswell's measurements for a doubly-hyperbolic lens [75]. He measured the electric field in the vicinity of the focal point of the lens using the experimental setup shown in Fig. 4.16. The source at the frequency 34.5 GHz ($\lambda = 0.869$ cm) was an open-ended waveguide (modeled in FDTD as a linearly polarized point source) located 27 cm from the polystyrene ($\epsilon_r = 2.54$ [66]) lens of diameter 27 cm. The lens was mounted

Table 4.1: Comparison of BOR-FDTD and published efficiency results for two zone plates: $\epsilon_r = 2.53$ and $t = 0$ for both.

$F/\lambda = 30,\ N = 6$		
P	$FG/FG_{P\to\infty}$	η [45]
$P = 2$	54.1%	40.5%
$P = 4$	80.4%	81.0%
$P = 8$	96.7%	95.0%
$P = 16$	99.5%	98.7%
$P \to \infty$	100%	100%

(a)

$F/\lambda = 12.5,\ N = 20$		
P	$FG/FG_{P\to\infty}$	η [45]
$P = 2$	57.5%	40.5%
$P = 4$	90.7%	81.0%
$P = 8$	95.8%	95.0%
$P = 16$	97.0%	98.7%
$P \to \infty$	100%	100%

(b)

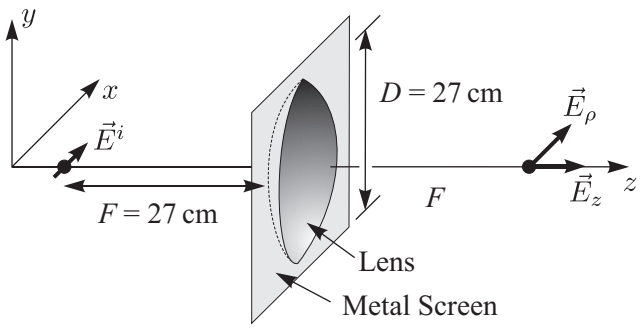

Figure 4.16: Experimental setup for measuring the components of the electric field near the focal point of the lens. $F = 27\,\text{cm}$, $D = 27\,\text{cm}$, and $\epsilon_r = 2.54$.

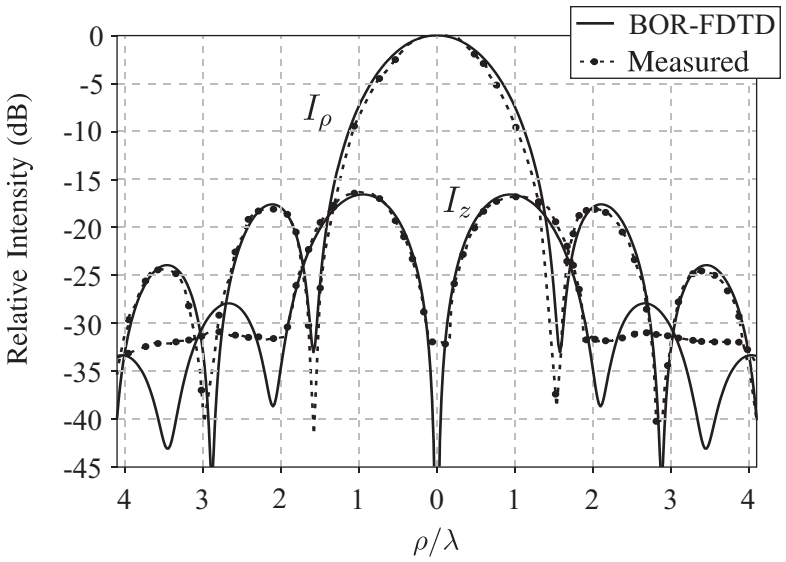

Figure 4.17: Relative intensity for the transverse (ρ) and longitudinal (z) components of the electric field focused by a hyperbolic lens. Measured data are from [75].

in a metal screen, and the electric field was measured near the focal point, which was 27 cm from the lens. With these measurements, Carswell showed, contrary to scalar theory, that in the focal plane there was a longitudinal component E_z to the electric field as well as the expected transverse component E_ρ. This observation is in agreement with the vector theory of Boivin and Wolf [76].

The intensities $I_\rho = |E_\rho|^2$ and $I_z = |E_z|^2$ computed with BOR-FDTD are compared with the measured results in Fig. 4.17. For the comparison, the peak amplitudes of both measured patterns were scaled to the computed values. This was necessary because of doubt as to the accuracy of the magnitude of the longitudinal field relative to the magnitude of the transverse field for the measurements. This doubt was also raised by Carswell when he compared the measured results to the theory of Boivin and Wolf [75]. The BOR-FDTD results are seen to be in relatively good agreement with the measured results for both field components.

Goldsmith gives the radiation pattern for a grooved-dielectric, phase-correcting zone plate fabricated from Rexolite, which was designed for use at 95 GHz and measured at 94 GHz [66]. The parameters for Goldsmith's zone plate were $F = 12.7$ cm, $P = 4$, $D = 9.53$ cm, $t = 0.19$ cm, and $N = 3$ (with the outermost subzone of the third full-wave zone

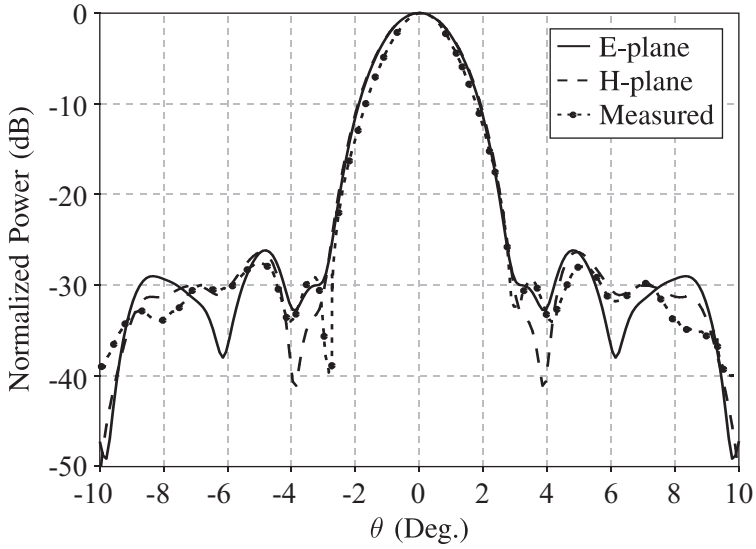

Figure 4.18: Normalized radiation pattern at 94 GHz for a phase-correcting zone plate with $F = 12.7\,\text{cm}$, $P = 4$, $D = 9.53\,\text{cm}$, $\epsilon_r = 2.53$, and $t = 0.19\,\text{cm}$. BOR-FDTD data are plotted in the E-plane and the H-plane. Measured data are from [66].

not included in the zone plate). The zone plate was illuminated with linearly-polarized radiation from a horn antenna. The field due to the horn was modeled as a Gaussian beam, in a manner similar to the horn for the focused-beam system, discussed in Sec. 2.3.2, Eq. (2.21). As specified in [66], the taper for the illumination was $-10\,\text{dB}$, that is, at the edge of the zone plate the illumination was $-10\,\text{dB}$ down from the value at the center of the zone plate. The Gaussian beam waist can be calculated to give an incident power pattern that satisfies this requirement. The plane (E or H) of the measured pattern is unspecified in [66]. Therefore, w_o was calculated separately to give a $-10\,\text{dB}$ taper for the two principal planes. The calculated values are $w_\text{o} = 0.31\,\text{cm}$ for the E-plane and $w_\text{o} = 0.32\,\text{cm}$ for the H-plane. The parameter z_o was specified by the measurement setup, $z_\text{o} = 27\,\text{cm}$.

The results from the BOR-FDTD simulation are plotted along with the measured results from [66] in Fig. 4.18. The agreement between the BOR-FDTD results and the measurements is reasonably good. The main beams in both the E- and H-planes of the BOR-FDTD results are similar to the measured main beam. The sidelobe level is also approximately the same in all three sets of data. The results in Figs. 4.17 and 4.18 provide confirmation that the BOR-FDTD method is correctly modeling dielectric focusing elements.

CHAPTER V

DESIGN OF A ZONE PLATE FOR A FOCUSED-BEAM MEASUREMENT SYSTEM

In the previous two chapters, design studies were presented for zone plate antennas that have applications in communications systems. These zone plates were designed to collimate radiation from a point source in the transmit mode, or to focus an incident plane wave in the receive mode. However, in many focusing systems, both the source and the focal point are located near the zone plate. For these focusing applications, a zone plate can be designed to replace the functionality of a doubly-hyperbolic lens, and this is the subject that will be addressed in this chapter.

A practical application for such a zone plate will also be examined in this chapter: A zone plate will be designed to be a focusing element in a free-space, focused-beam system to measure the electrical properties of materials. BOR-FDTD simulation results for both an existing lens and the zone plate designed to replicate its functionality will be presented. The lens will be used to establish performance requirements for zone plates used for this focusing application.

At the onset of this research, there were a few concerns about using zone plates for focusing applications. The most well-documented of these is their limited bandwidth [45]. As diffractive devices, zone plates are designed to work at one particular frequency, and performance degrades away from this frequency. In addition, there are a few specific requirements for focused-beam systems, as discussed in Chapter 1. The field at the sample must have a specified amplitude taper, must have phase uniformity, and must be linearly polarized. Unlike a hyperbolic lens, the profile of a zone plate is discontinuous, and there is concern about how this will affect these qualities. These concerns will also be addressed in this chapter.

In Sec. 1.5, the application of zone plates for focused-beam systems was introduced. The

primary motivating factors given for using zone plates in these systems were weight and cost savings, particularly at low frequencies. While low-frequency focused-beam measurement systems remain the target application for zone plates, the comparison of a doubly-hyperbolic lens and a zone plate was performed using scale models at frequencies in the range 8-12 GHz (X-band). This choice was made to keep project costs down and to simplify the procedures for experimentally validating the zone plate design.

5.1 Lens for the Focused-Beam System

In this study, a zone plate will be designed to replace a lens in an existing focused-beam measurement system at the Georgia Tech Research Institute (GTRI). Before discussing the design of the zone plate, a brief overview of the existing lens will be given. This lens is currently used in GTRI's standard focused-beam system for characterizing materials at frequencies in the range 4-18 GHz. The lens is constructed by placing two hyperbolic, plano-convex lenses back-to-back. For use in a focused beam system (see Fig. 1.8), the 'input' portion of the lens is oriented with the convex surface towards the horn, and the 'output' portion of the lens is oriented with the convex surface towards the sample under test. The geometry for this lens can be seen in Fig. 5.1, and its geometrical parameters are listed in Table 5.1. The hyperbolic profiles are described by the focal length (F_i and F_o) and the radii (r_i and r_o) for each respective half of the lens.

The lens requires a bracket to hold the two plano-convex halves together and to support the lens in the focused-beam system. The geometry for the mounting bracket is shown on one side of the lens in Fig. 5.1, shaded in gray. This bracket consists of two metal rings that completely surround the lens. The two lens halves are sandwiched between the rings, and six bolts are used to fasten the rings together. These bolts are not shown in the figure and are not included in the BOR-FDTD model of the lens because they are not rotationally symmetric.

5.2 Zone Plate for the Focused-Beam System

A zone plate was designed to replace the lens from Fig. 5.1 in a focused-beam system. The zone plate was designed with parameters similar to those of the lens to allow for a direct

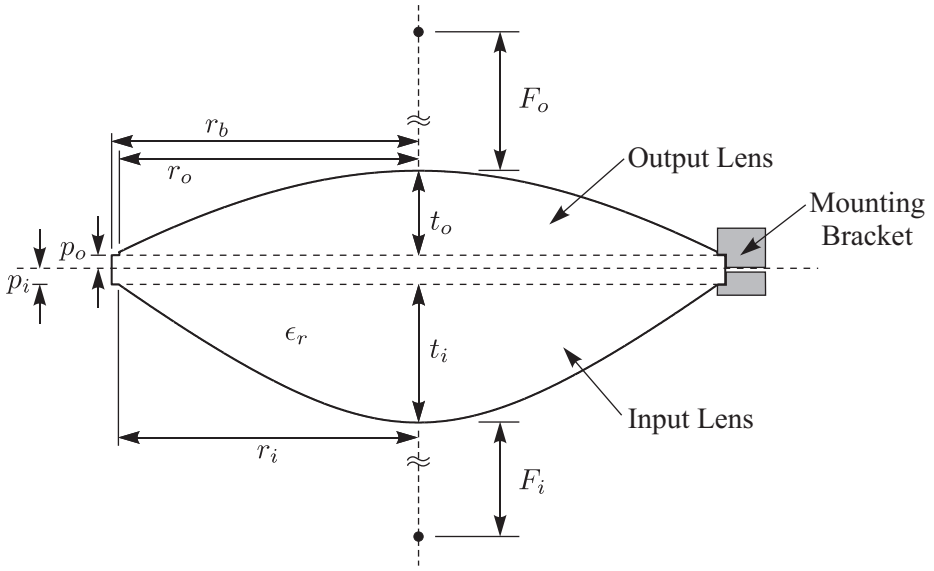

Figure 5.1: Geometry for the lens used in GTRI's standard focused-beam system.

Table 5.1: Parameters for the lens used in GTRI's standard focused-beam system.

Parameter	Symbol	Value
Relative Permittivity	ϵ_r	2.53 cm
Input Lens, Focal Length	F_i	35.98 cm
Input Lens, Thickness	t_i	13.50 cm
Input Lens, Radius	r_i	29.21 cm
Input Lens, Pedestal	p_i	1.27 cm
Output Lens, Focal Length	F_o	80.23 cm
Output Lens, Thickness	t_o	7.94 cm
Output Lens, Radius	r_o	29.21 cm
Output Lens, Pedestal	p_o	1.59 cm
Base Radius	r_b	30.48 cm

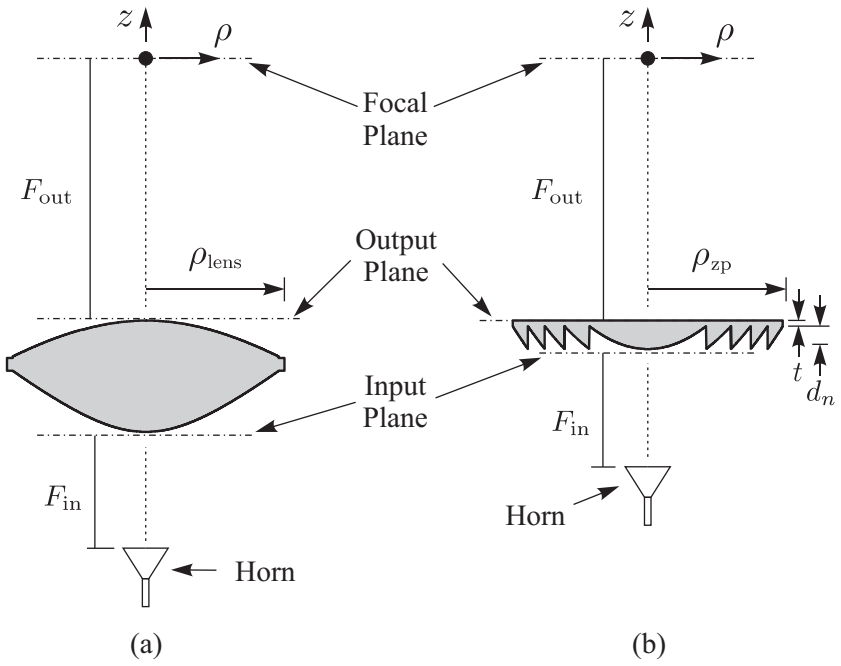

Figure 5.2: Geometry for (a) a doubly-hyperbolic lens and (b) a zone plate.

comparison. Both the zone plate and the lens were made from Rexolite, with the same base radius. The input and output focal lengths (F_{in} and F_{out}) of the zone plate were designed to be the same as the lens, and zone plate was divided into $N = 5$ full-wave zones. The design frequency for the zone plate was chosen to be the center of the frequency band of interest, $f = 10\,\text{GHz}$. Cross-sectional profiles for both the lens and the zone plate are shown in Fig. 5.2.

In Sec. 4.2.4, it was shown that the number of phase corrections per zone P does not significantly affect the power delivered to the focal point once $P \gtrsim 8$. For this zone plate, $P \to \infty$ was chosen, which gives a smooth profile with discontinuous jumps at the zone boundaries, as seen in Fig. 5.2(b). The goal of this work was to determine how the zoning concept affects focusing, so the zone plate profile that is most similar to the smooth lens profile was chosen. Historically, zone plates with a small number of phase corrections per zone were preferred to simplify manufacturing. With modern, computer-controlled manufacturing techniques, however, it is now possible to fabricate zone plates with $P \to \infty$. The manufacturing process for this zone plate is discussed in detail in Chapter 6. A zone plate with this profile is frequently referred to as a zoned Fresnel lens in reference to its

Table 5.2: Comparison of the physical properties of the existing lens and the zone plate designed to replace it.

	Lens	Zone Plate
Diameter	60.96 cm	59.59 cm
Base Thickness	-	1.27 cm
Maximum Thickness	24.30 cm	6.32 cm
Volume	34720 cm^3	10542 cm^3
Weight [1]	80.4 lb	24.4 lb
Weight Savings Factor [2]	-	3.3

similar appearance to the classical Fresnel lens (see Sec. 1.6).

The cross section of the zone plate in Fig. 5.2(b) shows that the side of the zone plate facing the focal plane is planar. This was an additional design requirement that was imposed to help simplify the manufacture of the zone plate. By designing one side to be planar, the attachment of the zone plate to the rotating platform of a lathe (called 'fixturing') is drastically simplified.

The profiles in Fig. 5.2 are drawn to scale and demonstrate the difference in thickness between the two devices. The maximum thickness of the zone plate is 25% of the thickness of the lens, and the weight of the zone plate is 30% of the weight of the lens, excluding the mounting brackets. A comparison of the physical parameters of the lens and the zone plate is given in Table 5.2.

5.2.1 Design Equations for the Zone Plate

The equations used to generate the profile for the non-planar side of the zone plate are discussed in this section. In Chapter 1, the design equations for Soret, folded, and grooved-dielectric, phase-correcting zone plates, designed to replace hyperbolic lenses, are given and discussed. A zone plate for a focused-beam system, however, must replace a doubly-hyperbolic lens, so a different set of design equations are required. The derivation of these

[1] Based on a density of 1.05 gcm^3 [77].
[2] Computed by dividing the volume of the lens by the volume of the zone plate.

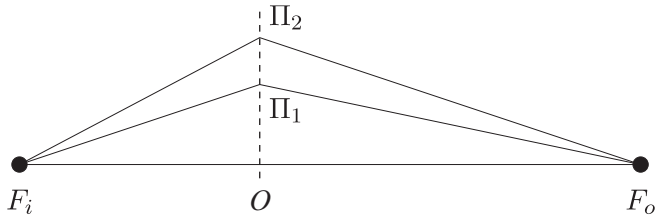

Figure 5.3: Geometry used to illustrate the definition of a full-wave Fresnel zone for a zone plate designed to replace a doubly-hyperbolic lens.

equations is similar to that for Eqs. (1.2)-(1.4) for the grooved-dielectric, phase-correcting zone plate. A full-wave Fresnel zone is now defined by the following requirement: The cumulative distance from the input focal point to the edge of a zone plus the distance from the edge of the zone to the output focal point must be a wavelength longer than same quantity for the previous zone. This is illustrated in Fig. 5.3: Π_1 and Π_2 are chosen such that $F_iO + OF_\mathrm{o} + \lambda = F_i\Pi_1 + \Pi_1 F_\mathrm{o}$ and $F_i\Pi_1 + \Pi_1 F_\mathrm{o} + \lambda = F_i\Pi_2 + \Pi_2 F_\mathrm{o}$. Applying this requirement gives rise to the new formula for the outer radius of the m^{th} full-wave zone:

$$\begin{aligned} \Pi_m &= \frac{1}{2}\left[(m\lambda + F_\mathrm{in} + F_\mathrm{out})^2 - 2\left(F_\mathrm{in}^2 + F_\mathrm{out}^2\right)\right. \\ &+ \left.\left(\frac{F_\mathrm{in}^2 - F_\mathrm{out}^2}{m\lambda + F_\mathrm{in} + F_\mathrm{out}}\right)^2\right]^{1/2}, \quad m = 1, 2, ..., N. \end{aligned} \tag{5.1}$$

When the subzones are numbered consecutively starting at the center of the zone plate, the outer radius ρ_n of the n^{th} subzone is

$$\begin{aligned} \rho_n &= \frac{1}{2}\left[\left(\frac{n\lambda}{P} + F_\mathrm{in} + F_\mathrm{out}\right)^2 - 2\left(F_\mathrm{in}^2 + F_\mathrm{out}^2\right)\right. \\ &+ \left.\left(\frac{F_\mathrm{in}^2 - F_\mathrm{out}^2}{n\lambda/P + F_\mathrm{in} + F_\mathrm{out}}\right)^2\right]^{1/2}, \quad n = 1, 2, ..., NP. \end{aligned} \tag{5.2}$$

The thickness d_n of the zone plate profile for each ρ_n is then calculated to satisfy Fermat's principle of least time:

$$\begin{aligned} d_n &= \frac{1}{\sqrt{\epsilon_r} - 1}\left[\sqrt{\Pi_1^2 + F_\mathrm{in}^2} + \sqrt{\Pi_1^2 + F_\mathrm{out}^2}\right. \\ &- \left.\sqrt{\rho_n^2 + F_\mathrm{in}^2} - \sqrt{\rho_n^2 + F_\mathrm{out}^2} + N_n\lambda\right], \quad n = 1, 2, ..., NP. \end{aligned} \tag{5.3}$$

in which Π_1 is the outer radius of the first zone. In Eq. (5.3), N_n takes on a value from 0 to $N-1$, depending on which zone the n^{th} subzone is in. For example, $N_n = 0$ when $1 \leq n \leq P$

(the first full-wave zone), and $N_n = 1$ when $P + 1 \leq n \leq 2P$ (the second full-wave zone). A base of thickness $t = 1.27\,\text{cm}$ ($t/\lambda = 0.46$) is added to each d_n for structural support.

In the particular case of $P \to \infty$, the design equations can be written in a simplified manner. Instead of calculating the thickness of the profile for specific values of ρ_n, the thickness of the smooth profile can be calculated for an arbitrary ρ. The thickness of the profile in full-wave zone between Π_m and Π_{m+1} (still defined by Eq. (5.1)) is

$$\begin{aligned} d(\rho) &= \frac{1}{\sqrt{\epsilon_r} - 1} \left[\sqrt{\Pi_1^2 + F_{\text{in}}^2} - \sqrt{\Pi_1^2 + F_{\text{out}}^2} \right. \\ &- \left. \sqrt{\rho^2 + F_{\text{in}}^2} - \sqrt{\rho^2 + F_{\text{out}}^2} + (m-1)\lambda \right]. \end{aligned} \tag{5.4}$$

When this version of the equation is used to generate a zone plate, care should be taken to sample ρ densely enough around outer edges of each zone ($\rho \approx \Pi_m$) to ensure that the discontinuous jump in the profile from one zone to the next is placed in the correct position

Zone plates designed with Eqs. (5.1)-(5.4) exhibit the same focal length shortening that was seen for the zone plates used in antennas (see Fig. 4.11). BOR-FDTD simulations were therefore used as part of the design process to adjust the zone plate to compensate for this focal length shift. The original value of F_{in} and F_{out} were 35.98 cm and 80.23 cm, respectively (from Table 5.1). Simulations were used to iteratively increase the values of F_{in} and F_{out} in Eqs. (5.1)-(5.4), adjusting the zone plate profile until the actual focal lengths of the zone plate coincided with the focal lengths of the doubly-hyperbolic lens. The adjusted values of F_{in} and F_{out} are 40.01 cm and 84.26 cm, respectively.

5.3 Comparison of the Zone Plate and the Lens

Sections 5.1 and 5.2 describe an existing lens and a zone plate designed to replace it. To evaluate the usefulness of this zone plate for focusing applications (particularly focused-beam systems), its focusing characteristics are compared with those of the lens. In particular, we are interested in the behavior of the two devices near the focal plane when they are illuminated by a pyramidal standard gain horn (Narda model 640), as shown in Fig. 5.2.

The BOR-FDTD method, described in detail in Chapter 2, was used to model the focusing by both the lens and the zone plate. The source, a pyramidal horn, was modeled as

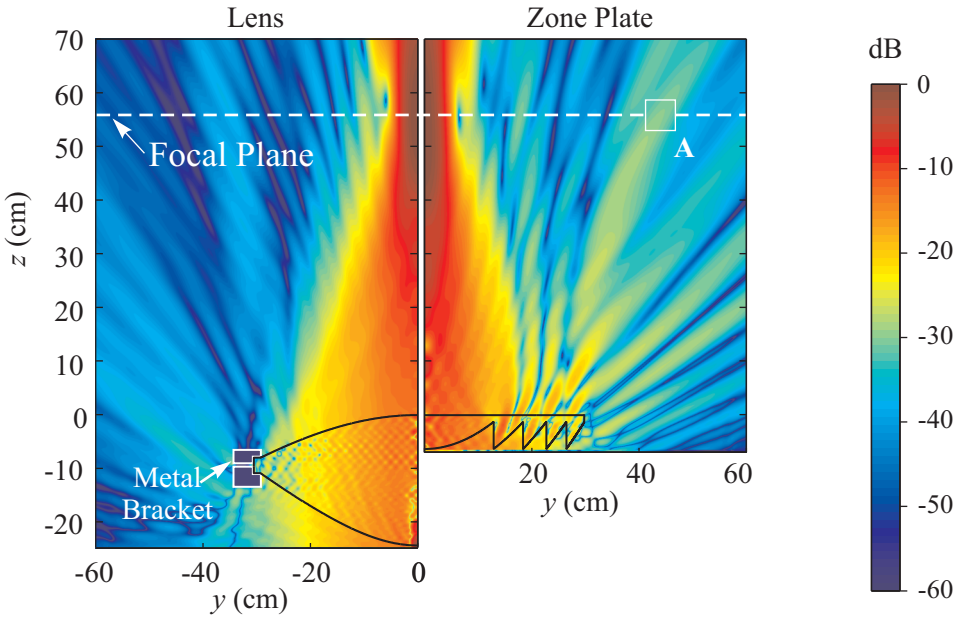

Figure 5.4: Magnitude of the z-component of the time average of the Poynting vector $\left|\hat{z} \cdot \langle \vec{S}(t) \rangle\right|$ in dB on a cross section in the yz-plane for the lens and the zone plate at $f = 10\,\text{GHz}$.

a Gaussian beam injector as explained in Sec. 2.3.2. The horn, fed by a WR90 waveguide, has a limited operating bandwidth (approximately 8-12 GHz). To simulate this limited bandwidth, the time-envelope of the source was chosen to be a modulated Gaussian pulse. Recall that the frequency content of a modulated Gaussian pulse can be controlled by choosing by choosing ω_o and τ_p in Eq. (2.12). To achieve the desired frequency range, these parameters were chosen to be $\omega_\text{o} = 6.28 \times 10^{10}\,\text{rad/sec}$ and $\tau_p = 1.61 \times 10^{-10}$.

Figure 5.4 shows the magnitude of the z-component of the time average of the Poynting vector $\left|\hat{z} \cdot \langle \vec{S}(t) \rangle\right|$ for both the lens and the zone plate, normalized to the maximum intensity for each device. This figure shows $\left|\hat{z} \cdot \langle \vec{S}(t) \rangle\right|$ plotted in dB, with red representing the greatest intensity and blue representing the least intensity. Outlines for the lens and zone plate are on the respective plots, and the dashed white line indicates the location of the focal plane. The solid white lines outline the metal mounting bracket that surrounds the lens. The scattering from the bracket is visible in the figure. For the zone plate, the bracket was made from Delrin ($\epsilon_r \approx 3.1$) to reduce the amount of scattering. The bracket for the zone plate, which will be discussed in more detail in Chapter 6, is not shown in Fig. 5.4.

This figure shows a definite similarity between the focusing of the two devices. Both the lens and the zone plate direct a majority of the incident power to a small spot on the focal plane. The figure shows that both devices focus power in a beam-like manner, tapering down to a spot on the focal plane and then expanding beyond the focal plane. The zone plate, however, clearly directs more power away from this spot than the lens; this is indicated by the diffraction bands that occur outside the spot. The bands are green in color and are roughly 30 dB below the point of highest power (at the center of the focal spot).

Looking at Fig. 5.4, the focusing by the lens and the zone plate appear to be qualitatively similar. The remainder of this section describes quantitative measures that further this comparison.

5.3.1 Time-Average Power Delivered to the Focal Spot

When comparing the zone plate and the lens, one metric of interest is the amount of power focused by each device. This can be quantified by looking at how much power is intercepted by a disc of radius ρ_d on the focal plane. To compute the time-average power received, the z-component of the time average of the Poynting vector $\langle \vec{S}(t) \rangle$ is integrated over the disc. The time-average Poynting vector $\langle \vec{S}(t) \rangle$ is the real part of the complex Poynting vector $\vec{S}_c$, so

$$P_{\text{rec}} = \int_0^{\rho_d} \int_0^{2\pi} \hat{z} \cdot \text{Re}(\vec{S}_c) \rho \, \text{d}\phi \, \text{d}\rho \, . \tag{5.5}$$

In Fig. 5.5, P_{rec} is plotted as a function of ρ_d for both the lens and the zone plate at $f = 10\,\text{GHz}$. For reference, the vertical black line indicates the point at which the radius of the disc of integration equals the radius of the lens or zone plate. For the figure, P_{rec} is normalized by P_{inj}, the injected power, which is the total time-average power supplied by the horn. If all of the power P_{inj} passed though the focal plane, then $P_{\text{rec}}/P_{\text{inj}} \to 1$ as $\rho_d \to \infty$.

The dashed line shows the power received for the lens. Most of the power is concentrated into a small region, $\rho_d \lesssim 5\,\text{cm}$. Beyond this region, the plot levels off at $P_{\text{rec}}/P_{\text{inj}} \approx 0.8$. Power lost to reflection and over-illumination of the lens accounts for the fact that not all of the power supplied by the horn is delivered to the focal spot ($P_{\text{rec}}/P_{\text{inj}}$ never reaches

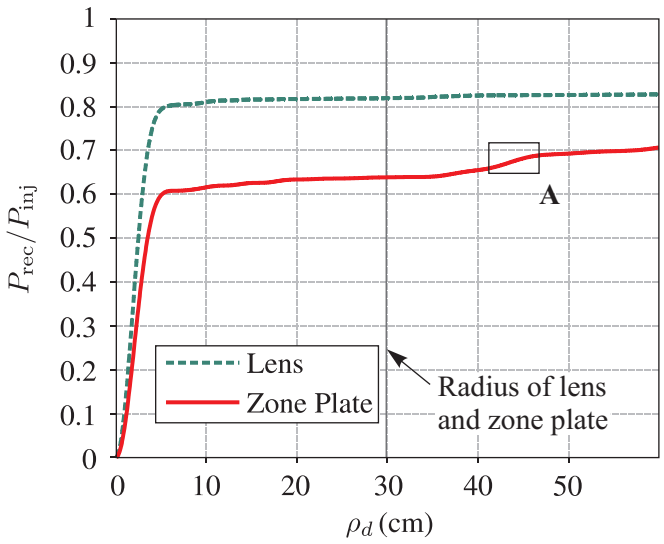

Figure 5.5: Fraction of the power supplied by the horn that passes through a disc of radius ρ_d in the focal plane for the lens and the zone plate at $f = 10\,\mathrm{GHz}$.

1). The solid line shows that the zone plate does not deliver as much power to the focal spot as the lens; it delivers slightly more than 60% of the injected power to the focal spot, $\rho_d \lesssim 5\,\mathrm{cm}$. Subsequent increase in ρ_d results in an increase in received power. This behavior can be understood by referring back to the z-component of the Poynting vector for the lens and the zone plate, which are plotted in Fig. 5.4. Tracing the dashed white line from the axis ($y = 0$) to the outer edge of the simulation space, it can be seen that a number of the diffraction bands are incident on the focal plane. These bands account for the step-like increases in $P_{\mathrm{rec}}/P_{\mathrm{inj}}$ for the zone plate in Fig. 5.5: As the radius is increased, more of this misdirected power is included in the integral, Eq. (5.5). A clear example of this occurs when ρ_d is slightly greater than 40 cm. This region is marked by a box labeled **A** in both Figs. 5.4 and 5.5. The increase in $P_{\mathrm{rec}}/P_{\mathrm{inj}}$ in Fig. 5.5 inside of this box corresponds to a region of relatively large $\left|\langle\vec{S}(t)\rangle\right|$ in Fig. 5.4. Because the intensity of the diffraction bands for the lens are lower than they are for the zone plate (by at least 10 dB), this effect is not as significant for the lens.

5.3.2 Size and Axial Position of the Focal Spot

In addition to comparing the amount of power delivered to the focal spot, it is also important to look at the size and axial position of this spot. For a plane parallel to the xy-plane at

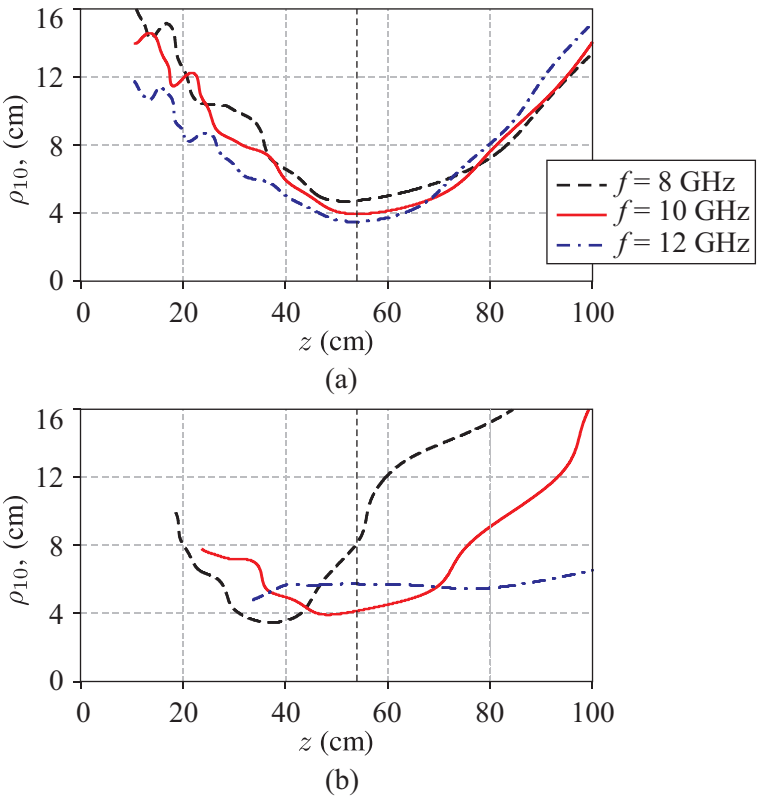

Figure 5.6: Radius of the -10 dB spot ρ_{10} for (a) the lens and (b) the zone plate for $f = 8$, 10, and 12 GHz. Here, z is the distance from the output plane of the lens or zone plate.

the distance z from the output plane of the lens or zone plate, the radius at which the power has decreased 10 dB from the on-axis value was determined and called ρ_{10}. For an ideal plane wave, ρ_{10} would be infinite for all z, because the field is invariant in the radial direction. For a Gaussian beam, the ρ_{10} would be the smallest at the waist of the beam, and its value at the waist would indicate how tightly the beam is focused. This metric can be used to compare the amplitude taper of the lens and the zone plate.

In Fig. 5.6, ρ_{10} is plotted for the lens (a) and zone plate (b) for three frequencies: $f = 8$ GHz (dashed black line), 10 GHz (solid red line), and 12 GHz (dash-dot blue line). This figure shows that both the lens and the zone plate are focusing in a beam-like manner. For the lens, the beam waist is located at approximately the same distance z from the output plane for all three frequencies. This distance is marked by the vertical dashed black line. As the frequency is lowered, the radius of the focal spot increases from 3.4 cm for $f = 12$ GHz (dash-dot blue line) to 4.6 cm for $f = 8$ GHz (dashed black line).

The results for the zone plate show a different trend. At the design frequency, $f = 10\,\text{GHz}$, the plot of ρ_{10} for the zone plate looks similar to that for the lens (solid red lines). The size and position of the waist is similar for the lens and the zone plate. However, as the frequency changes, the waist of the beam of the zone plate moves significantly. At $f = 8\,\text{GHz}$ (dashed black line), the waist gets closer to the zone plate, while it moves farther from the zone plate at $f = 12\,\text{GHz}$ (dash-dot blue line). At $f = 8\,\text{GHz}$, the region where ρ_{10} does not change much with changing z is smaller in the axial direction than it is at $f = 10\,\text{GHz}$. However, the general form of ρ_{10} remains similar to that of the lens: As z is increased, the spot becomes narrow, levels out at a well-defined waist, and then expands again. At $f = 12\,\text{GHz}$, the waist becomes less well-defined, indicating that the focusing mechanism is beginning to break down.

Figure 5.6 shows that the lens and the zone plate have different dependence on frequency. This can be better understood by examining the plot of $\left|\hat{z} \cdot \langle \vec{S}(t) \rangle\right|$ for both devices at all three frequencies in Figs. 5.7 and 5.8. In both sets of figures, the dashed white line represents the location of the beam waist for the lens when $f = 10\,\text{GHz}$. Comparing the two sets of figures, it is clear that the focusing from the lens is not highly dependent on frequency, whereas it is much more so for the zone plate. For the lens, the beam looks similar at all three frequencies, with only a minor shift in the location of the waist. Contrast this with the plots for the zone plate. When $f = 8\,\text{GHz}$ (Fig. 5.8(a)), the waist of the beam is closer to the zone plate. For the zone plate when $f = 12\,\text{GHz}$ (Fig. 5.8(c)), there is no clearly defined beam waist and the field looks more like that of a collimated beam.

5.3.3 Phase Uniformity over the Focal Spot

Another metric that is important for focused-beam systems and in many focusing applications is the uniformity of the phase over the focal spot. This is quantified by computing the root mean square (RMS) deviation in phase from a uniform value over the disc of radius ρ_{10} at each axial position z. The values used for ρ_{10} in this calculation are those plotted in Fig. 5.6. For an ideal plane wave, the phase deviation would be zero for all z, and for a Gaussian beam, the phase deviation would be only exactly zero at the beam waist [39].

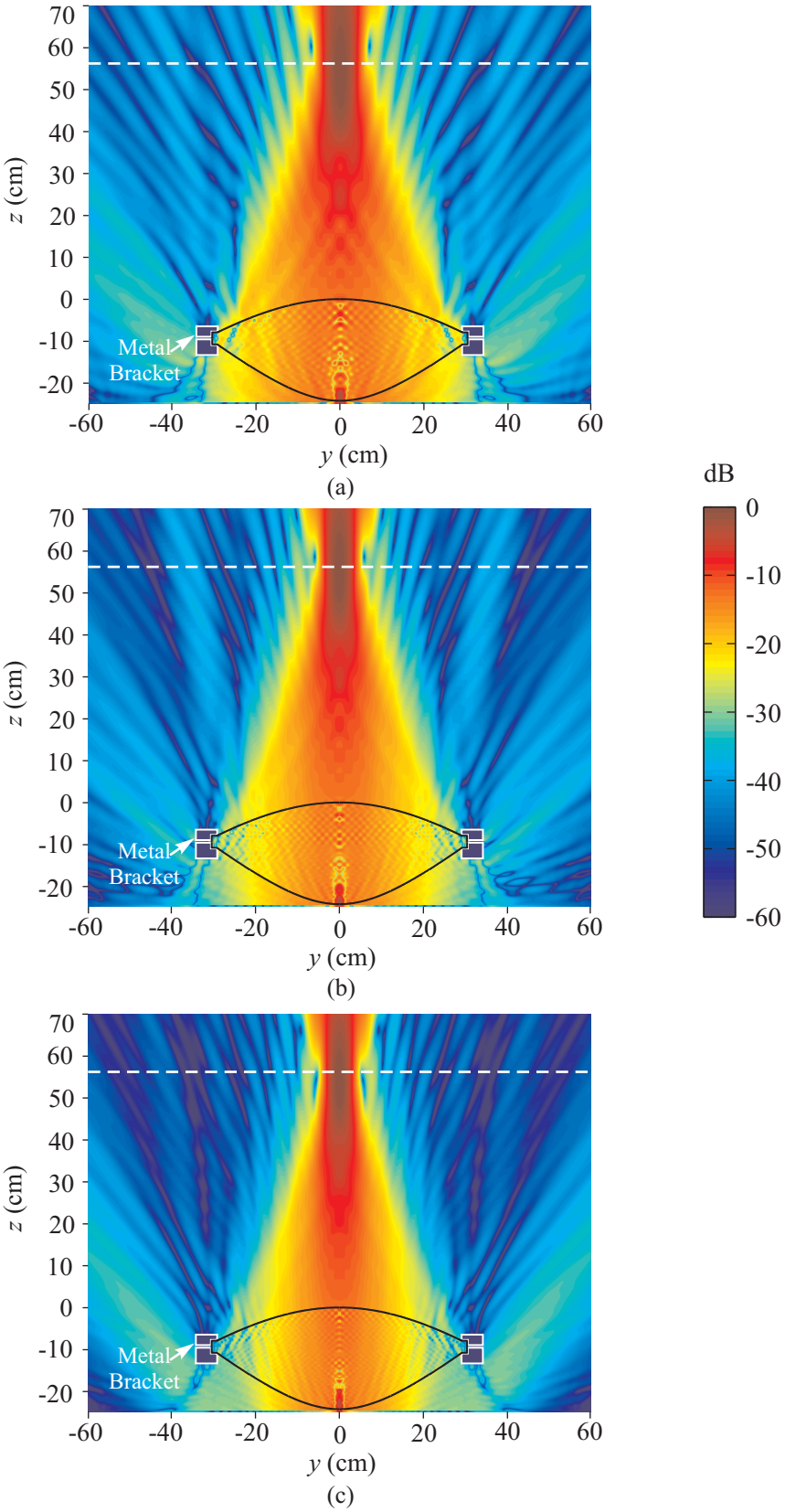

Figure 5.7: $\left|\hat{z} \cdot \langle \vec{S}(t) \rangle\right|$ in dB on a cross section in the yz-plane for the lens at the frequency (a) $f = 8\,\text{GHz}$, (b) $f = 10\,\text{GHz}$, and (c) $f = 12\,\text{GHz}$.

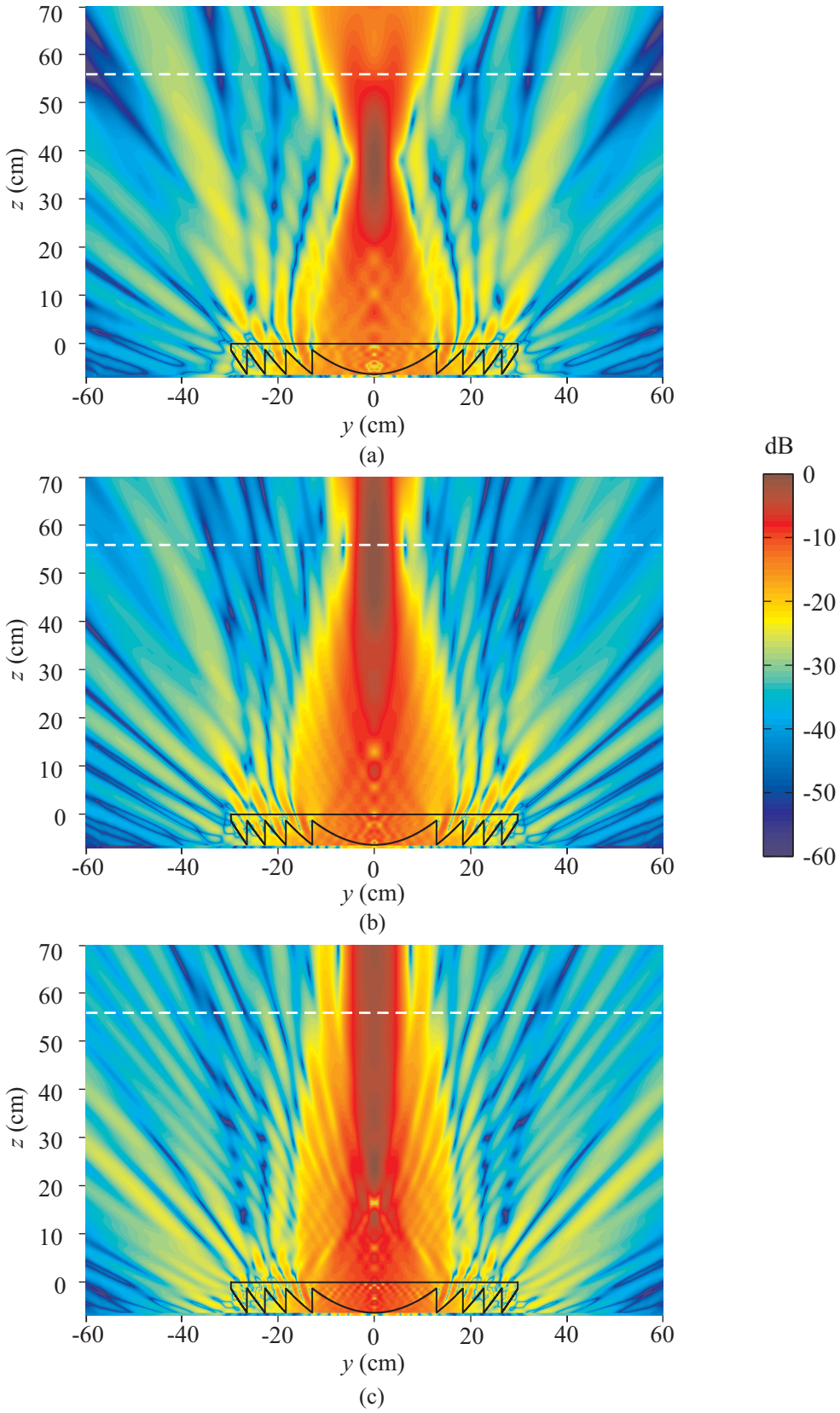

Figure 5.8: $\left|\hat{z} \cdot \langle \vec{S}(t) \rangle\right|$ in dB on a cross section in the yz-plane for the zone plate at the frequency (a) $f = 8\,\text{GHz}$, (b) $f = 10\,\text{GHz}$, and (c) $f = 12\,\text{GHz}$.

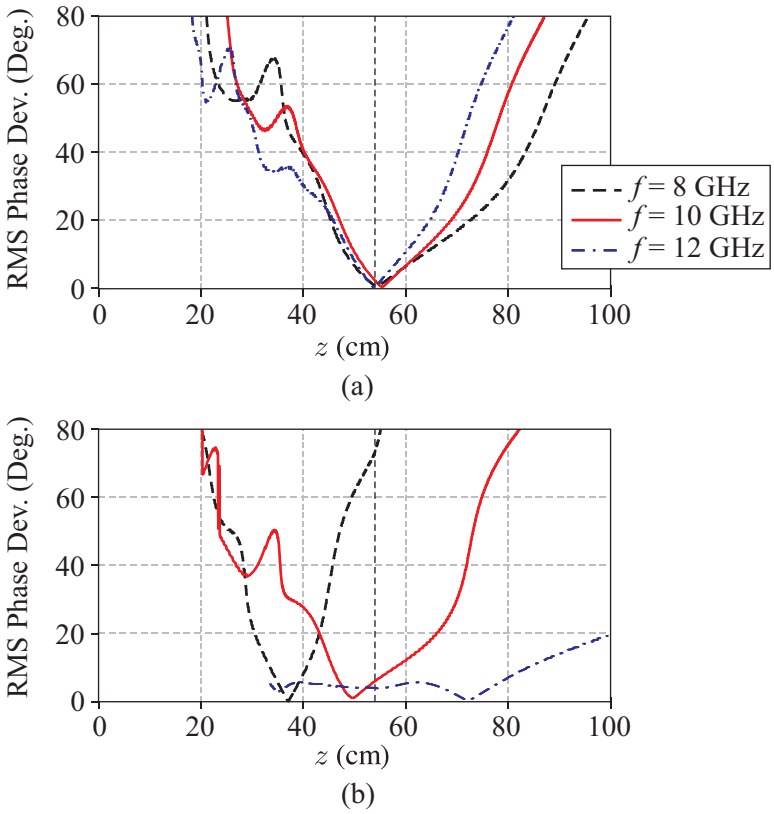

Figure 5.9: Deviation in phase over the -10 dB spot for (a) the lens and (b) the zone plate at the frequency $f = 8$, 10, and 12 GHz.

Figure 5.9 shows the phase deviation as a function of axial distance from both the lens (a) and the zone plate (b) at $f = 8$, 10, and 12 GHz. As in Fig. 5.6, the vertical dashed black line indicates the location of the waist for the lens when $f = 10$ GHz. For both devices, the phase deviation is very close to zero at one point for each of the frequencies. At this point, the deviation for the lens ranges from 0.2° to 0.6° over the frequency range. The deviation for the zone plate ranges from 0.2° to 0.9°. The locations of these points correspond to the locations of minimum ρ_{10} in Fig. 5.6 and, therefore, follow the same trends: The waist of the beam for the lens stays at a fixed distance as the frequency is varied, while it moves for the zone plate.

Based on the results in Sections 5.3.2 and 5.3.3, the zone plate behaves like the doubly-hyperbolic lens at the design frequency: The focal spot is of similar size and location, and the uniformity of the phase at the beam waist is comparable. The zone plate appears

to be a suitable replacement for the lens at the design frequency. Away from the design frequency, the location of the beam waist for the zone plate is significantly more frequency-dependent than it is for the lens. In addition, the focusing mechanism of the zone plate begins to break down as the frequency moves farther away from the design frequency. The importance of these bandwidth limitations, of course, depends on the application. The particular application of zone plates to a focused-beam system will be considered in the next section.

5.4 Application of Zone Plates to a Focused-Beam System

The results from the comparison in the previous section can be applied to study the feasibility of replacing lenses with zone plates in a focused-beam measurement system. In this section, the focusing characteristics of the zone plate will be examined in light of this particular application.

The limitation on the power delivered to the focal spot of the zone plate, discussed in Sec. 5.3.1 is, by itself, not significant. Calibration procedures for the focused-beam system allow the measurements to be independent of the amount of power delivered to the sample. However, the fact that a significant amount of power can be sent in directions away from the focal spot can become important. One of the assumptions of the focused-beam technique is that the edges of the sample are outside the region that is strongly illuminated. If zone plates are used and an edge of the sample is located at a point that receives significant power, such as in a diffraction band, some of this power may be scattered back to one or both of the horns. For example, if a sample edge is located inside of box **A** in Fig. 5.4, where there is a relatively large amount of power, there is the potential for errors in the material measurements made using the focused-beam system. A combination of techniques can be used to solve this problem. Absorber can be placed around the edges of the sample to reduce unwanted scattering. The signals received by the horns can also be time gated to remove unwanted reflections from either an edge of the sample or from elsewhere in the system. The time-gating procedure is not a unique requirement of the zone plate system; it is also necessary for the lens system.

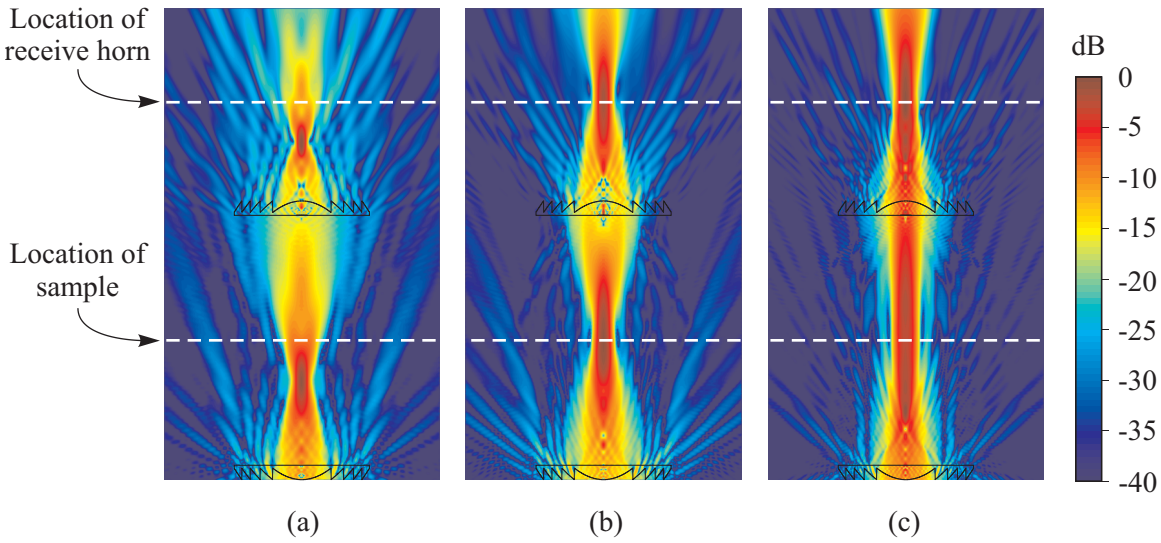

Figure 5.10: $\left|\hat{z}\cdot\langle\vec{S}(t)\rangle\right|$ in dB on a cross section in the yz-plane for a system of two zone plates at the frequency (a) $f = 8\,\text{GHz}$, (b) $f = 10\,\text{GHz}$, and (c) $f = 12\,\text{GHz}$.

The frequency-dependant shift in the beam waist is a concern that must be accounted for in a focused-beam system that uses zone plates. To see how this shift can adversely affect a focused-beam system, examine Fig. 5.10. In this figure, the magnitude of the z-component of the time-average Poynting vector $\left|\hat{z}\cdot\langle\vec{S}(t)\rangle\right|$ is plotted for a system of two zone plates for $f = 8$, $f = 10$, and $f = 12\,\text{GHz}$, respectively. The source in these figures is located below the bottom zone plate. The distance between the two zone plates in all three cases is twice the output focal length of the zone plate when $f = 10\,\text{GHz}$. To use this system of zone plates for focused-beam measurements, a sample of material would be placed halfway between each set of zone plates. The sample location is indicated by the dashed while line in between the zone plates in Fig. 5.10. A second dashed white line in each of the figures indicates the position of the receive horn. The sample location is clearly at the beam waist when $f = 10\,\text{GHz}$. When $f = 8\,\text{GHz}$, the sample is not at the waist and the receive horn is not located at the correct position. When $f = 12\,\text{GHz}$, there is no clearly defined waist between the zone plates, although the receive horn is located in an acceptable position.

Figure 5.11 shows the 10 dB radius ρ_{10} for this same system of two zone plates. Notice that there are now two beam waists. The observations that were made about Fig. 5.8 are reinforced by this figure: At the design frequency, $f = 10\,\text{GHz}$ (solid red line), one waist is

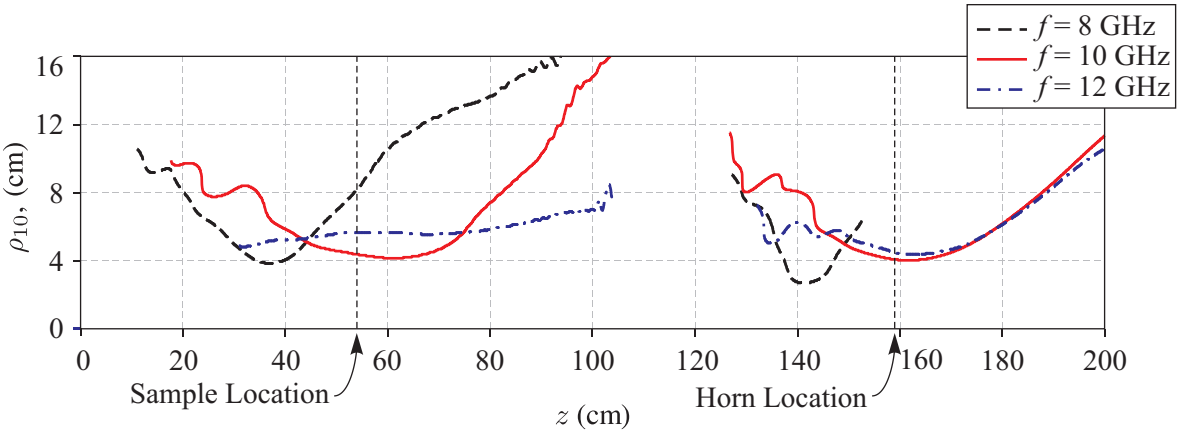

Figure 5.11: Radius of the -10 dB spot for the zone plate for $f = 8$, 10, and 12 GHz. Here, z is the distance from the output plane of the input zone plate.

between the lenses at the sample location (indicated a dashed black line) and the other is at the location of the receive horn (also indicated by a dashed black line). When $f = 8$ GHz (dashed black line), the shifted waists can be seen, as can the ambiguous nature of the waist at the sample when $f = 12$ GHz (dash-dot blue line).

One approach to overcome this problem is to compensate for the shift in the beam waist by moving the zone plates with respect to the sample at each frequency. To implement this idea, BOR-FDTD simulations or measurements would be used to determine the behavior of the focal length as a function of frequency. Using this knowledge, the zone plates and sample could be rearranged so that the space between the zone plate would be twice the focal length at a particular frequency. The sample would then be placed halfway between the zone plates, and its material properties could be measured at that frequency. This process could then be repeated for every desired frequency. The drawback of this approach is that some of the simplicity of the focused-beam system is lost, and the system becomes less convenient to use.

A good compromise between optimizing the position of the sample at each frequency and ease-of-use is to choose a few different spacings and then measure a band of frequencies for each of these spacings. This idea takes advantage of the fact that there is a region around the waist at each frequency for which the amplitude taper and phase uniformity appear to be near the optimal values achieved exactly at the waist. If the focused-beam

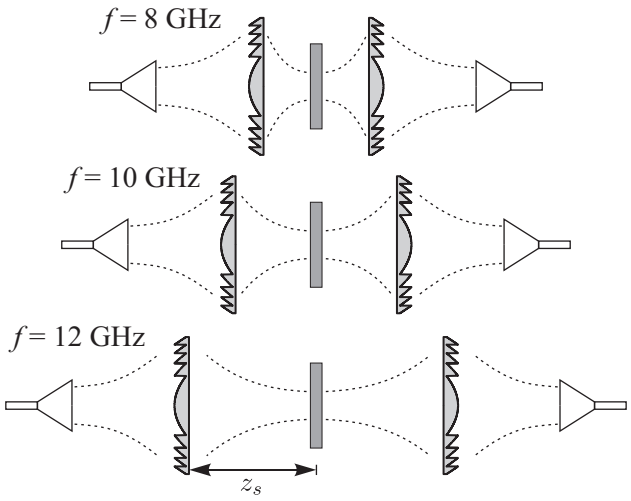

Figure 5.12: Schematic diagram of a focused-beam measurement system with zone plate focusing elements. The spacing between the zone plates and the sample z_s is adjusted for three frequencies.

system was configured so that the sample was placed *near* the beam waist, it is reasonable to expect that the focused-beam measurement system would still give acceptable results.

The proposed idea is illustrated for three frequencies in Fig. 5.12: The zone plates are closest together for measurements around 8 GHz and farthest apart for measurements around 12 GHz. The spacings z_s are determined by the locations of minimum phase deviation; for the zone plate considered in Fig. 5.9 these spacings are: $z_s = 38\,\text{cm}$ for $f = 8\,\text{GHz}$, $z_s = 55\,\text{cm}$ for $f = 10\,\text{GHz}$, and $z_s = 72.4\,\text{cm}$ for $f = 12\,\text{GHz}$. BOR-FDTD simulations were used to examine this idea. Three simulations were run for the three configurations shown in Fig. 5.12. The magnitude of the z-component of the time-average Poynting vector $\left|\hat{z} \cdot \langle \vec{S}(t) \rangle\right|$ near the pair of zone plates is plotted in dB in Fig. 5.13. The results shown are for the respective frequencies (e.g., in Fig. 5.13(a), the spacing z_s is set for $f = 8\,\text{GHz}$ and $\left|\hat{z} \cdot \langle \vec{S}(t) \rangle\right|$ is plotted for $f = 8\,\text{GHz}$). In this figure, the sample location (indicated by the dashed line) now coincides with the beam waist at each frequency. The distance from the output zone plate to the receive horn is held constant for all three frequencies. This is done to simplify the process of reconfiguring the system between measurements; the horn and the zone plate can be moved towards or away from the sample as a single unit.

The -10 dB radii ρ_{10} for the rearranged systems are plotted in Fig. 5.14(a). For this

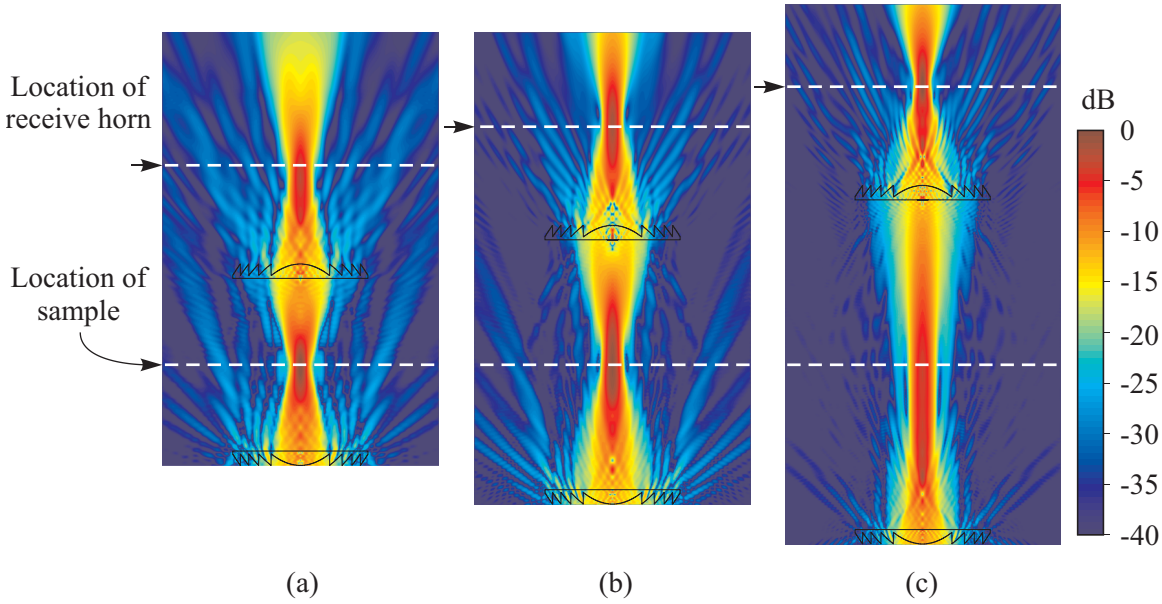

Figure 5.13: $\left|\hat{z}\cdot\langle\vec{S}(t)\rangle\right|$ in dB on a cross section in the yz-plane for a system of two zone plates at the frequency (a) $f = 8\,\text{GHz}$, (b) $f = 10\,\text{GHz}$, and (c) $f = 12\,\text{GHz}$. The spacing between the zone plates is chosen separately for each frequency.

figure, the axis has been modified so that ρ_{10} is plotted relative to the locations of the two waists of each system. The waist associated with the sample location is plotted using a coordinate system centered at z_s, and the waist associated with the receive horn is plotted using a coordinate system centered at the location of the horn z_{horn}. For reference, the locations of the centers of both of these coordinate systems are shown in Fig. 5.14(b). Figure 5.14(a) shows that the beam waists for both the sample and the horn are now in approximately the correct place when $f = 8$ and $f = 10\,\text{GHz}$. When $f = 12\,\text{GHz}$, the waist for the horn is in approximately the correct place.

The results presented in this chapter give us confidence that zone plates can be used for focused-beam systems. At the beginning of this research, there were four primary concerns regarding zone plates for focusing applications: the amplitude taper, and phase uniformity, the polarization of the field, and the bandwidth of the device. In Sec. 5.3, the amplitude taper and phase uniformity were shown to be similar to the lens at the design frequency. The polarization of the field at the beam waist will be examined using measurements of the field in Chapter 6. The frequency-dependent behavior of the zone plate was studied, and the

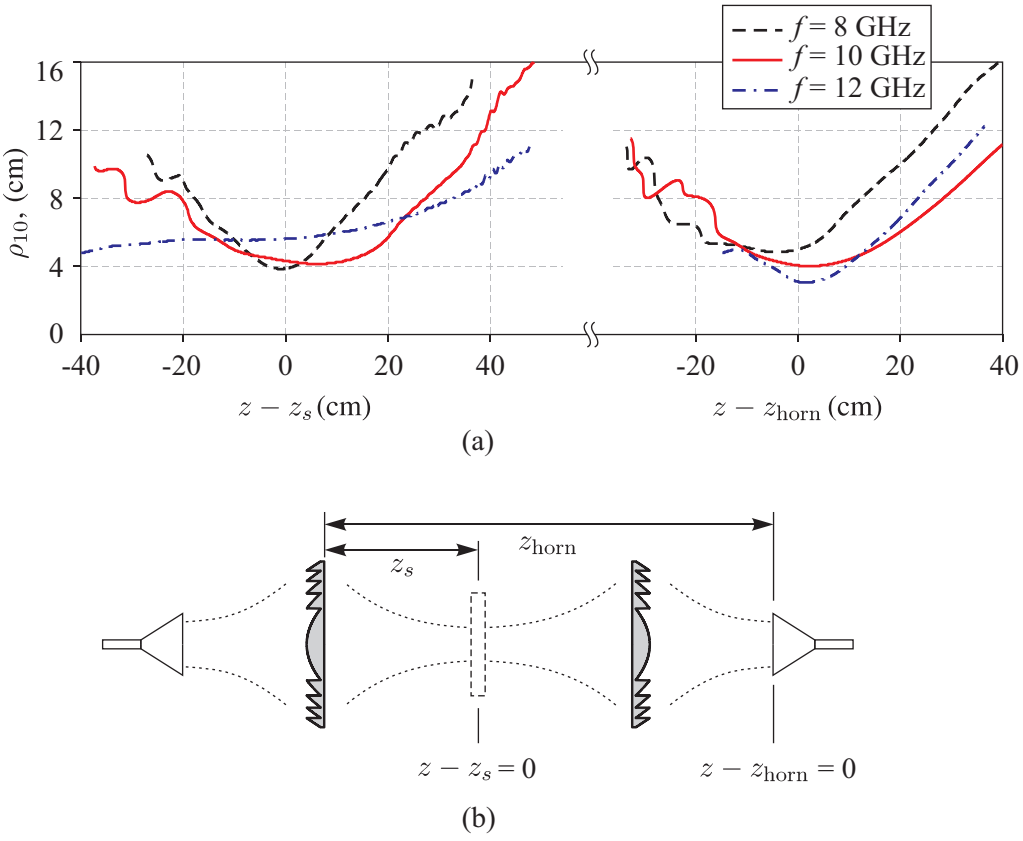

Figure 5.14: (a) Radius of the -10 dB spot for the zone plate for $f = 8$, 10, and 12 GHz. Here, z is the distance from the output plane of the input zone plate. The spacing between the zone plates is chosen separately for each frequency. (b) Schematic showing the coordinate system used.

beam waist was shown to move as the frequency was changed. In this section, a technique was proposed to compensate for the frequency dependence by adjusting the configuration of a focused-beam system for a few distinct frequencies. BOR-FDTD simulations of a focused-beam system with two zone plates arranged in multiple configurations indicate that this may be an effective solution. This technique is experimentally explored in the next section.

CHAPTER VI

EXPERIMENTAL STUDY OF A ZONE PLATE FOR A FOCUSED-BEAM MEASUREMENT SYSTEM

In this chapter, experimental results for the study of the application of zone plates to free-space, focused-beam measurement systems are presented. The fabrication of the zone plate is discussed, and measurements of the electric field in a volume surrounding the focal point of both the zone plate and the doubly-hyperbolic lens that the zone plate was designed to replace are presented. These data are used to validate the BOR-FDTD simulations and to further the comparison of the zone plate with the lens. A set of two zone plates is used to perform measurements of the electrical properties of different dielectric sheets, and the results are compared to the results from a standard system which uses two doubly-hyperbolic lenses and to values from the literature, when possible.

6.1 Fabrication of the Zone Plate

The zone plate presented in Chapter 5 was fabricated by selectively removing material from a slab of Rexolite using computer numerical controlled (CNC) manufacturing techniques. CNC manufacturing is based on the premise that software can be written to control the movements of different cutting tools. The software is generated from drawings of the part to be manufactured. This process allows complicated parts to be machined with great accuracy.

An engineering drawing of the zone plate was created using SolidWorks[1], a three-dimensional computer-aided design (CAD) software package. This drawing included all of the geometrical properties of the zone plate, including a mathematical representation of the curve that is rotated about the axis of symmetry to generate the profile. SolidWorks can generate both three-dimensional models and two-dimensional drawings. In Fig. 6.1, a

[1]Copyright Dassault Systems

two-dimensional drawing of the zone plate is shown. The dimensions in this drawing are given in inches. The SolidWorks drawing of the zone plate was converted into software that was used to control the movements of cutting tools by Kurt Wiesmayer of Wiesmann Tool, Inc., Alpharetta, Georgia.

The zone plate was made of Rexolite 1422 purchased from C-Lec Plastics[2]. The dimensions of the piece of Rexolite received from C-Lec Plastics were 6.35 cm by 60.96 cm by 60.96 cm (2.5 in by 24 in by 24 in), with positive tolerances only (meaning that the piece was guaranteed to be at least this size). This was important because the thickness of the zone plate (see Table 5.2) is 6.32 cm.

The actual process of machining of the zone plate was done in two steps. The first step was to use a milling machine to 'rough out' the general shape of the zone plate. The zone plate was mounted on a platform in the milling machine, and a rotating cutting bit then cut a coarse approximation to the zone plate. Figure 6.2(a) shows a photograph of the milling machine and two zone plates after this phase of the fabrication was completed. Figure 6.2(b) is a closeup photograph of a zone plate. Notice the step-like approximation to the profile of the zone plate.

A lathe was then used to remove the remainder of the material. The zone plate was mounted to a rotating platform and the location of a cutting tool was controlled by a computer to shave away a small amount of material at a time until the exact profile specified for the zone plate was obtained. Figure 6.3(a) shows a photograph of the lathe in the process of shaping the zone plate. Figure 6.3(b) shows a closeup photograph of the cutting tool and the zone plate. Notice that the profile is smooth for the outer zone, which has already been cut. Also notice the white shavings of Rexolite, which give an indication of how little material is removed at a time. The inner zones have not yet been cut and are as they were after the milling step. The combination of using a milling machine to remove the bulk of the material and a lathe to finish the profile allowed tight tolerances to be achieved. A typical dimension of the finished zone plate differs by less than .005 inch from the specified value.

[2]Rexolite is a registered trademark of C-Lec Plastics, www.rexolite.com.

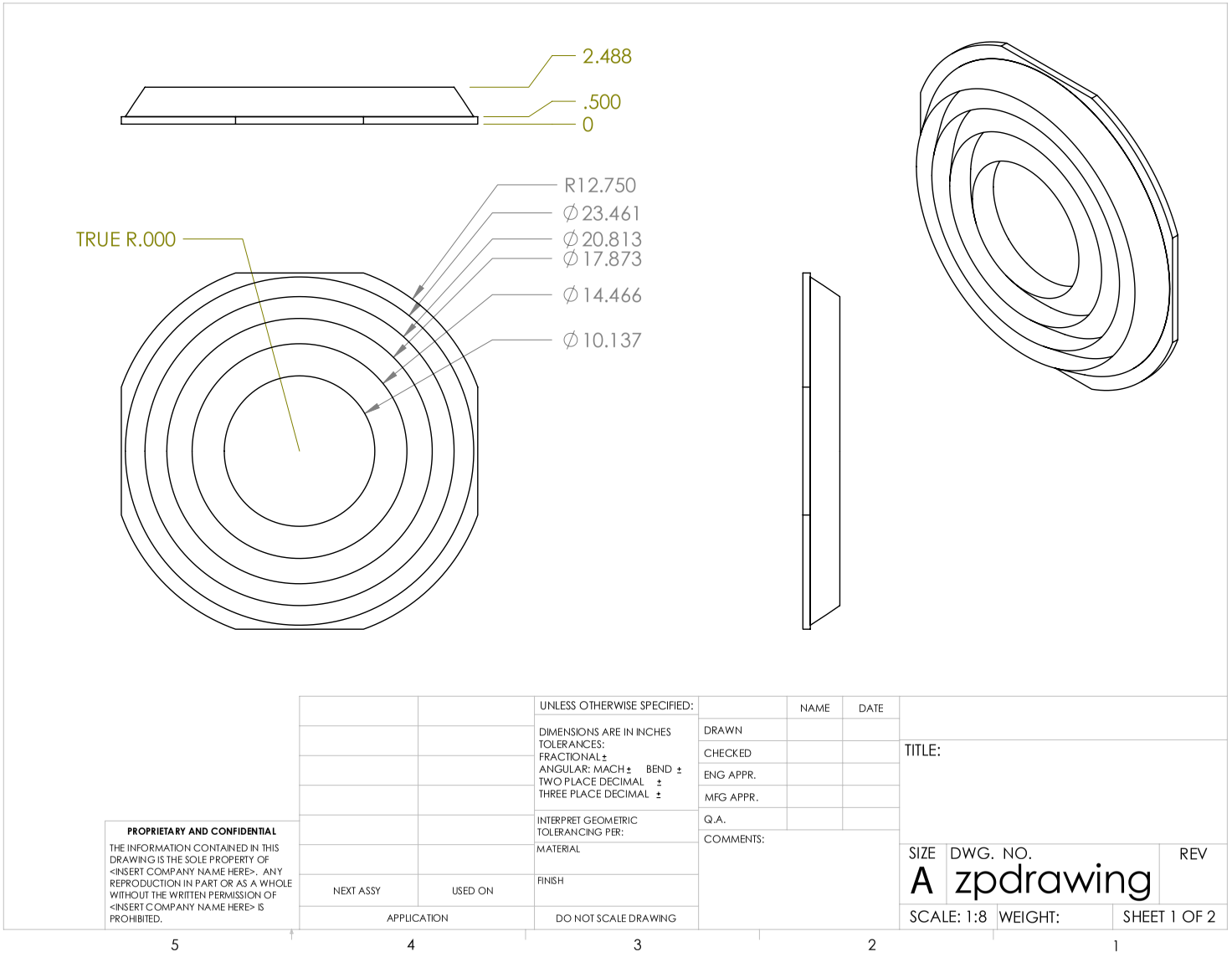

Figure 6.1: Engineering drawing of the zone plate to be manufactured.

(a)

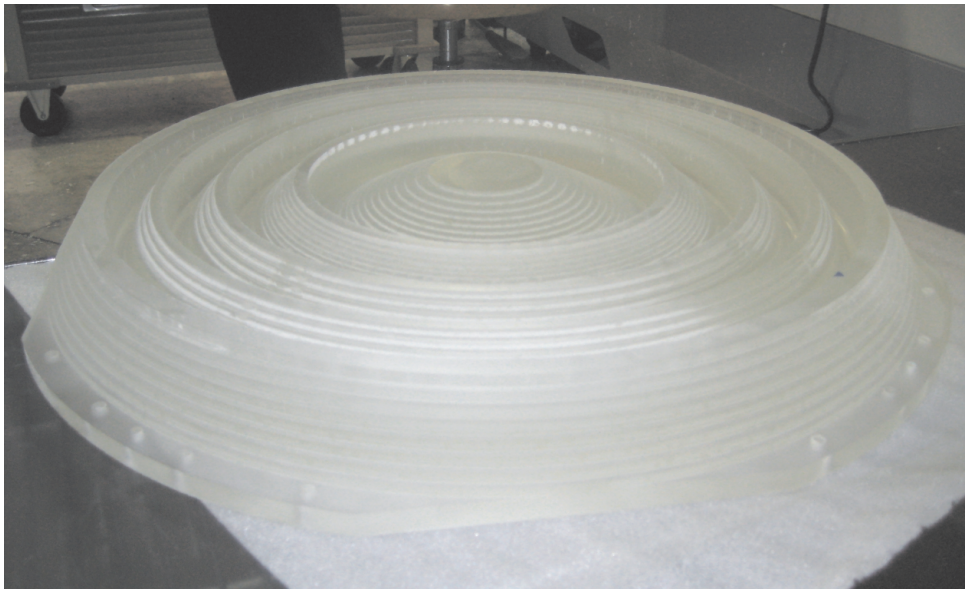

(b)

Figure 6.2: Photographs of (a) the milling machine at Wiesmann Tool, Inc. and (b) the zone plate after the milling process.

(a)

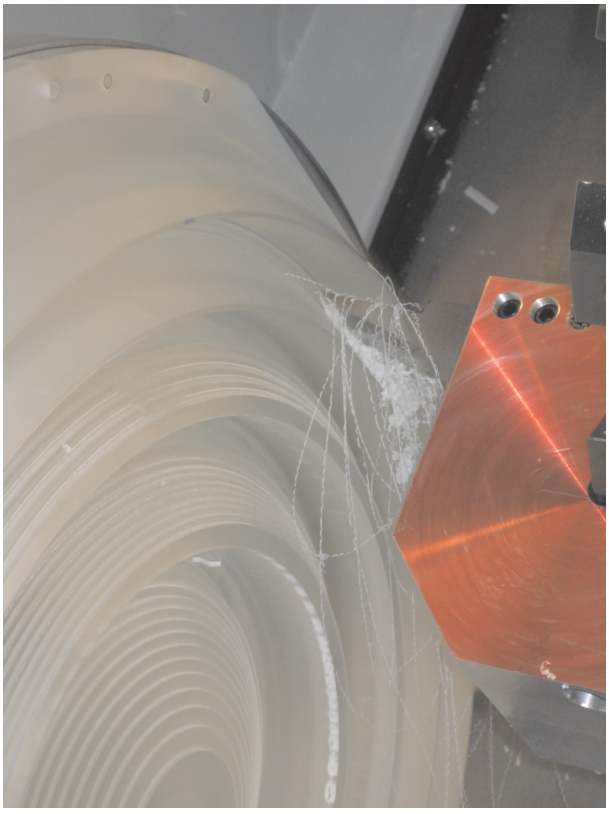

(b)

Figure 6.3: Photographs of (a) the lathe in the process of shaping the zone plate at Wiesmann Tool, Inc. and (b) the cutting tool and the zone plate in the lathe.

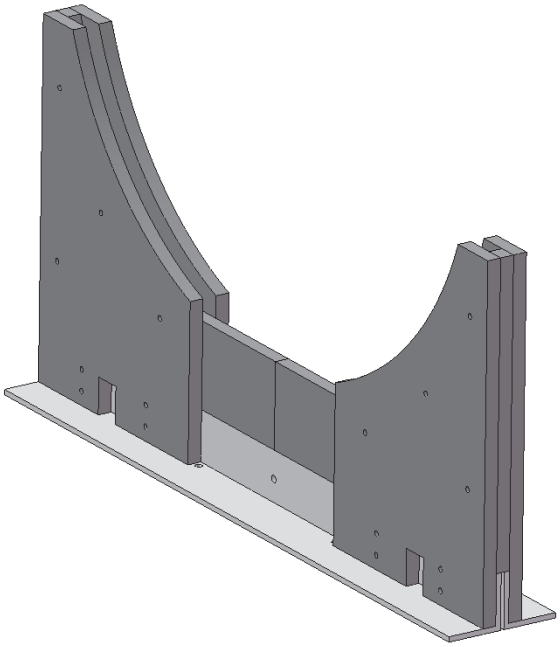

Figure 6.4: SolidWorks drawing of the bracket for the zone plate.

A bracket was designed to support this zone plate in a vertical position. The bracket was made from 1.27 cm thick pieces of Delrin[3], which was chosen because it is mechanically rigid and machinable. It will not sag or bend significantly when supporting the weight of the zone plate, which is important in order to maintain alignment. These pieces were bolted together to create a u-shaped channel. Notice that in the drawing for the zone plate, Fig. 6.1, a lip was left around the outside of the device. This lip is an extension of the zone plate base, and therefore has a thickness $t = 1.27$ cm. At its widest, the lip extends 2.6 cm beyond the outer radius of the zone plate, with a radius of 32.38 cm. At its narrowest point (the center of each of the flat edges) the distance from the center of the zone plate to the edge is limited by the size of the piece of Rexolite and is 30.48 cm. This lip slides into the groove made by the bracket, and the flat edge rests on the bracket, supporting the weight of the zone plate. The groove provides front-to-back stability and keeps the zone plate oriented at a 90° angle with respect to the base. Figure 6.4 shows a three-dimensional SolidWorks model of the bracket. The dark-colored parts (six pieces) are made from Delrin. The Delrin bracket ($\epsilon_r \approx 3.1$ [78]) scatters less of the incident field than a metal bracket would. The

[3]Delrin is a registered trademark of E. I. du Pont de Nemours and Company (DuPont), www.dupont.com.

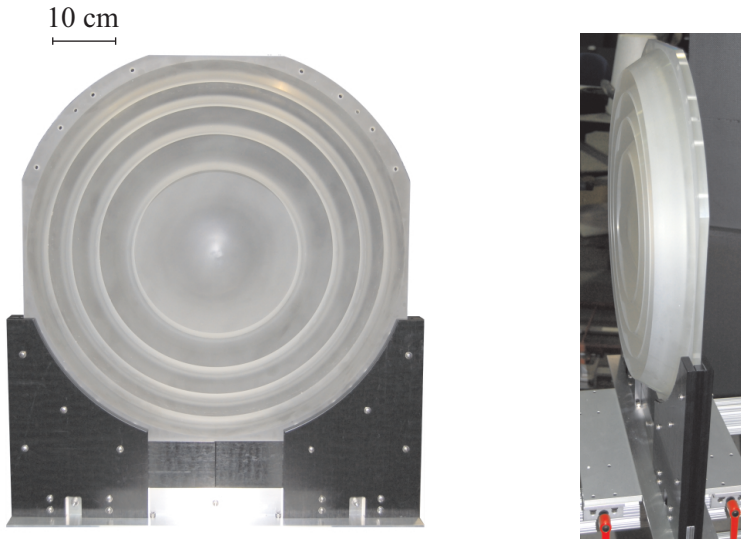

(a) (b)

Figure 6.5: Photographs of the zone plate and bracket from (a) the front and (b) the side.

light-colored base seen in Fig. 6.4 is made from two Aluminum 'angles' (L-shaped pieces with a 90° angle). A thin piece of Aluminum is used as a spacer between the two angles. This bracket was also machined by Wiesmann Tool.

Photographs of the completed zone plate supported by the assembled bracket are shown in Fig. 6.5.

6.2 Experimental Procedure to Study Focusing

The focusing characteristics of this zone plate and the lens used for GTRI's existing focused-beam system were studied experimentally. Measurements of the electric field were made throughout the volume surrounding the focal point for both the zone plate and the doubly-hyperbolic lens. These measurements were used to validate the conclusions drawn from the BOR-FDTD study of Chapter 5 and to further the comparison of the two devices.

Measurements of the field were taken using an existing experimental facility at GTRI, called the 'beamscan system'. This system consists of a horn, the zone plate or lens, an electric field probe, and a system of rails and linear positioners. Diagrams of the experimental setup are shown in Fig. 6.6. Figure 6.6(a) shows the coordinate system that will be used for the remainder of the work. The horn shown in the diagram is a pyramidal standard

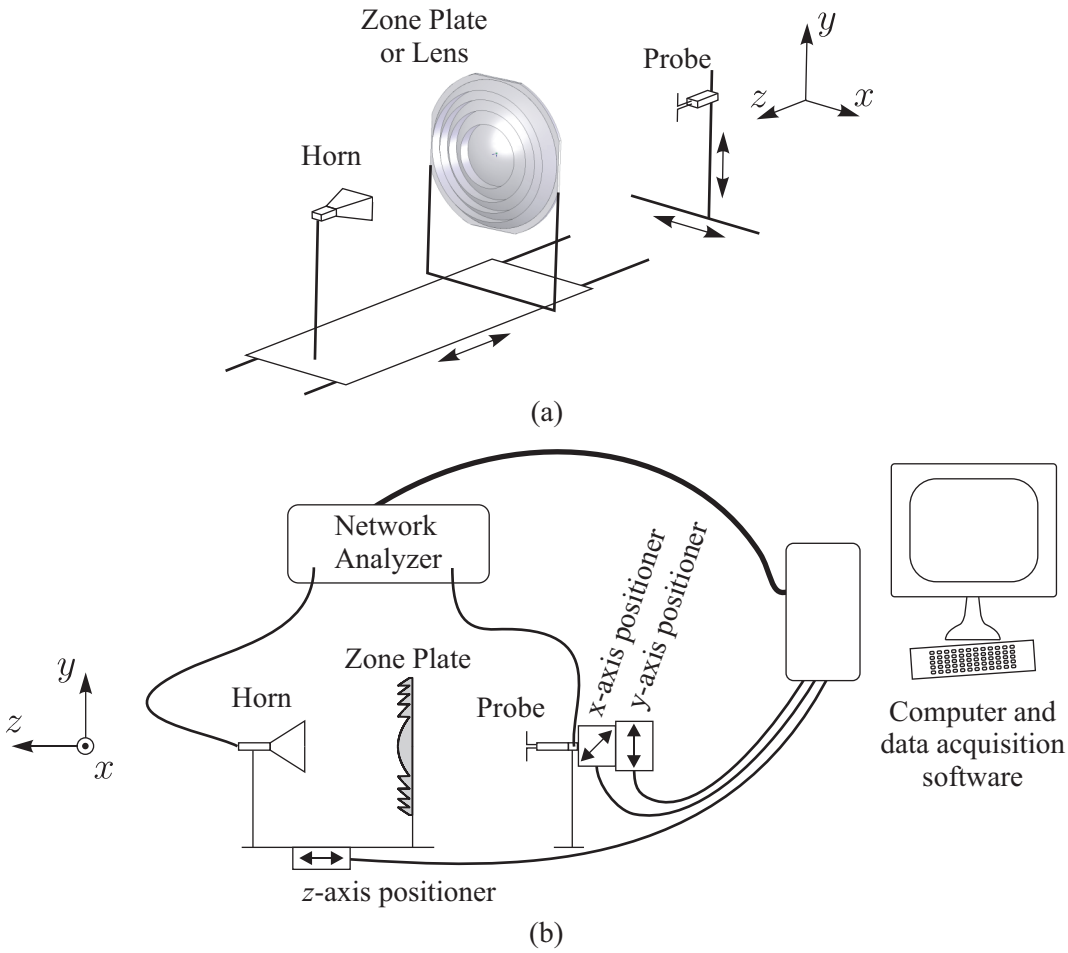

Figure 6.6: Schematic diagrams of the beamscan system showing (a) the coordinate system used and (b) the relationship between the components of the system.

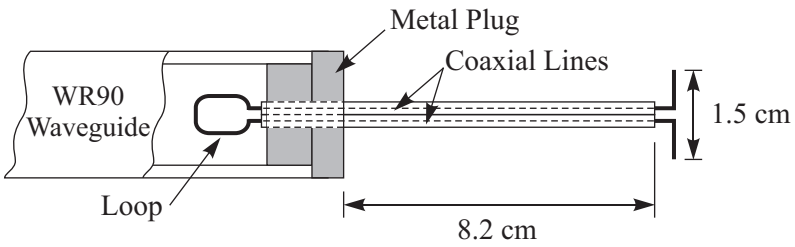

Figure 6.7: Schematic diagram of the dipole probe.

gain horn (Narda model 640). This particular horn was chosen for its linear polarization and its relatively symmetric radiated field. The horn is oriented so that the electric field is polarized in the y-direction. The distance between the horn and the front of the zone plate (or lens) is fixed at 43.2 cm for all of the measurements and simulations presented in this work.

A system of three linear positioners allows the probe to be moved in the x-, y-, and z-directions with respect to the zone plate or lens. A network analyzer connected to the horn and the probe, as shown in Fig. 6.6(b), is used to measure the magnitude and phase of the desired field component. Data acquisition software is interfaced with the network analyzer and the linear positioners to automate this process[4], as shown in Fig. 6.6(b). A graphical user interface allows the user to enter the parameters of the particular measurement to be performed, such as the range of frequencies and positions to be scanned.

For this work, a new probe was designed to measure the electric field focused by the zone plate and the lens. Using this probe, each individual measurement samples the field over a small area, rather than averaging the field over a larger area like a horn or open-ended waveguide probe would. This facilitates the comparison of the measured field values with those from the simulations. A diagram of the probe is in Fig. 6.7. The dipole probe is made from a pair of semi-rigid coaxial lines. The exposed center conductor of each line forms one arm of the dipole, and the two lines are run through a plug in the end of a WR90 waveguide. Inside the waveguide, the exposed center conductors of the lines are connected to form a loop which couples to the magnetic field in the waveguide. Notice that the probe

[4]The automated data acquisition software was written by members of the Signature Technology Laboratory (STL) at GTRI.

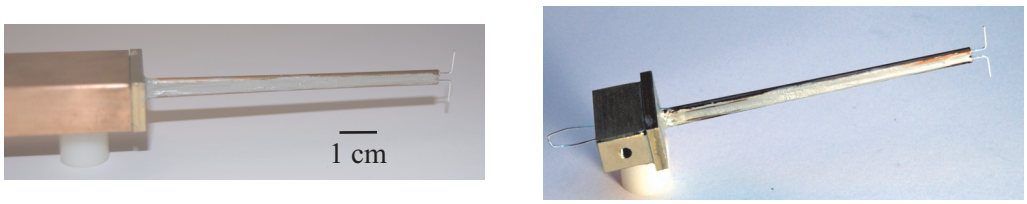

(a) (b)

Figure 6.8: Photograph of the dipole probe (a) attached to the WR90 waveguide and (b) free-standing with the loop visible.

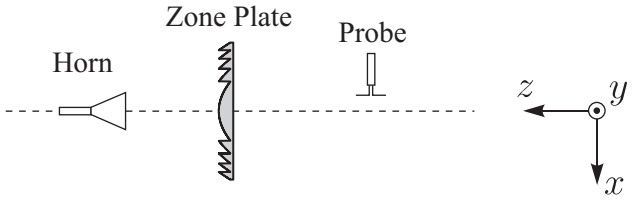

Figure 6.9: Schematic diagram of the beamscan system configured to measure the z-component of the electric field.

is a balanced structure. Photographs of the probe are in Fig. 6.8. Figure 6.8(a) shows the probe with the metal plug inserted into the waveguide, and Fig. 6.8(b) shows the probe with the loop visible.

The probe can be oriented to measure the x- or y-component of the electric field. The y-component is measured when the probe is oriented as it is drawn in Fig. 6.6(a), and the x-component is measured when the probe is rotated by 90°. The z-component can also be measured, although the accuracy and the physical range for the measurements were restricted in this configuration by the presence of the coaxial lines. To measure the z-component of the field, the probe is oriented as shown in Fig. 6.9. This figure shows a top-down view of the measurement system. When the probe is positioned at a location $x < 0$, as it is in the figure, the scattering from the waveguide and the coaxial lines does not have a large effect on the measurement of the field. When the probe is positioned at a location $x > 0$, however, the waveguide and coaxial lines are located in the region where the field is most intense, and scattering from these components of the probe introduces an error in the measurements of the field.

The region around the beamscan system was surrounded by foam absorber to reduce reflections from other objects in the room. A photograph of the beamscan system configured to measure the field focused by the zone plate is shown in Fig. 6.10. The probe is located at the end of a pyramid of absorber on the left side of the photograph, and the x- and y-axis rails are covered by absorber.

6.3 Experimental Study of Lens and Zone Plate Focusing

The system shown in Fig. 6.10 was used to measure the field in a volume surrounding the focal region of both the existing lens and the newly-fabricated zone plate. In this section, the measured data are presented and compared to data obtained from BOR-FDTD simulations. These data are used to give a more detailed comparison of the lens and the zone plate. Specifically, data related to the characteristics required of a focusing element in a focused-beam system will be presented, evaluated, and compared for both the zone plate and the lens. These characteristics include the amplitude taper, phase uniformity, and linearity of the polarization at the waist of the beam as well as the bandwidth over which the device can be used.

The full set of measured data are presented in Appendix A. These data have value beyond just the comparative function they serve in this chapter. The measurements performed for this work represent a more detailed look at the field in the focal region of the lens for GTRI's standard focused-beam system than previously existed. The data for the zone plate can serve as a useful tool for designing zone plates for any application. Appendix A provides a record of these measurements.

To determine if a zone plate can replace a doubly-hyperbolic lens, the first step is to validate that the zone plate is indeed working as a focusing element. To do this, the behavior of the field along the z-axis is of interest. $|E_y|$ is plotted as a function of the distance from the zone plate and the lens at the design frequency of the zone plate ($f = 10\,\text{GHz}$) in Fig. 6.11. The red (solid) lines are for the BOR-FDTD simulations, and the blue (dashed) lines are for the measurements. There is good agreement between the simulations and measurements for both devices. The location of the maximum $|E_y|$ is approximately the

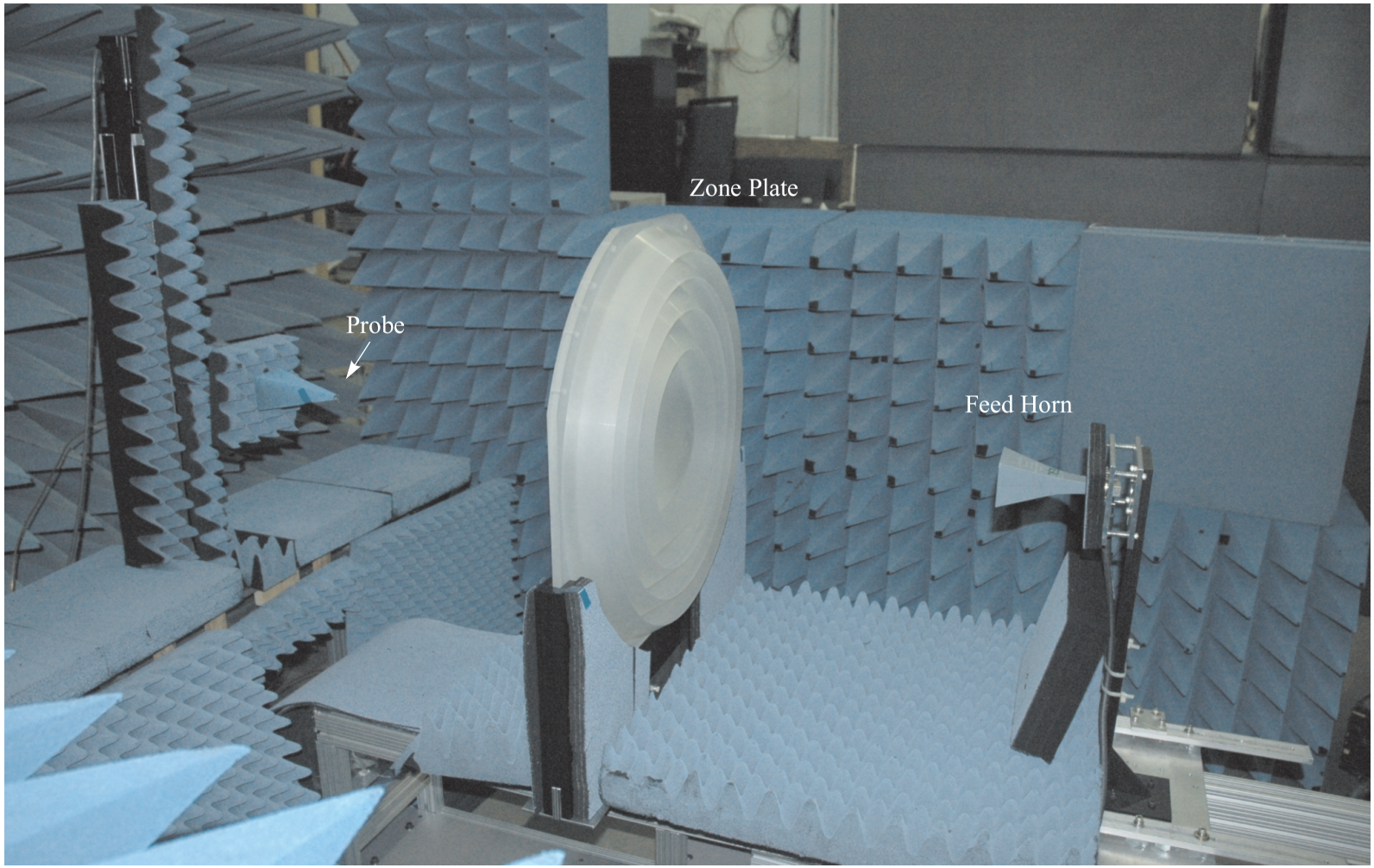

Figure 6.10: Photograph of the experimental setup for measuring the electric field in the focal region of the zone plate.

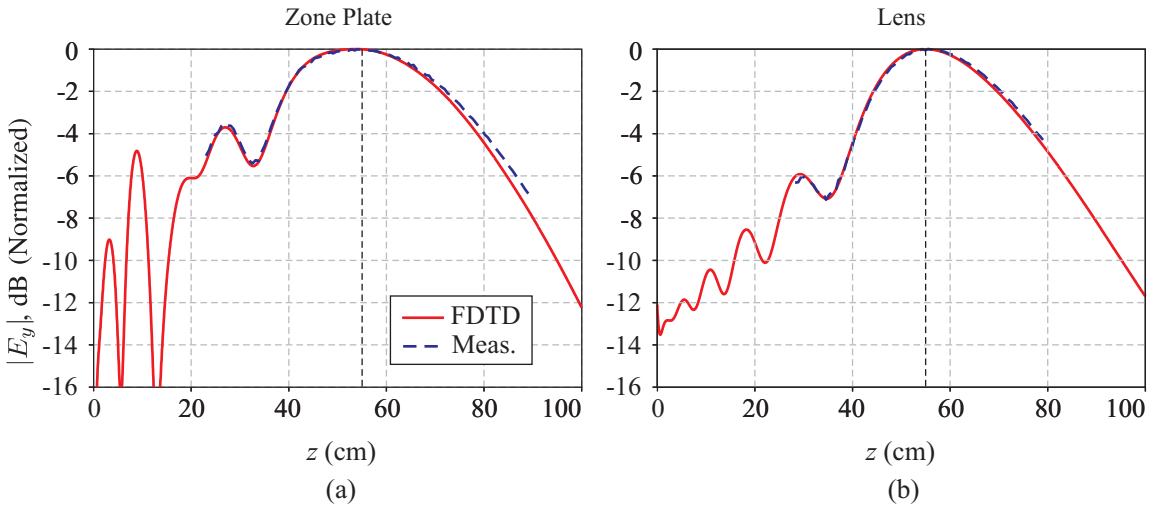

Figure 6.11: Measured and simulated (FDTD) results for the electric field E_y along the z-axis when $f = 10\,\text{GHz}$. The magnitude E_y at $f = 10\,\text{GHz}$ for the (a) the zone plate (b) the lens are plotted as a function of the distance from the respective focusing element.

same distance from the zone plate as it is from the lens. In both figures, the dashed black line is located at $z = 55\,\text{cm}$, the location of the maximum field value for the lens. The lens focuses the field to a narrower region along the axis than the zone plate does, however.

6.3.1 Amplitude Taper

One of the most important requirements for a zone plate in a focused-beam measurement system, which has been discussed repeatedly throughout this document, is the need for the amplitude of the field focused by the zone plate to have a similar taper to that focused by the lens. The amplitude taper for the two devices can be examined in Fig. 6.12, which shows the field for the design frequency of the zone plate, $f = 10\,\text{GHz}$. The magnitude of the y-component of the electric field $|E_y|$ for the zone plate is plotted in dB in Fig. 6.12(a) for two cuts. The red lines are for horizontal cuts ($y = 0$) and the blue lines are for vertical cuts ($x = 0$), all on the focal plane ($z = 55\,\text{cm}$ from the output plane of the zone plate or the lens). The solid lines are for the BOR-FDTD simulations, and the dashed lines are for the measurements (the field is sampled every 6.35 mm). The same quantities are plotted for the lens in Fig. 6.12(b). The figures show good agreement between the simulations and the measurements, both in the main beam and in the sidelobes.

A comparison of the zone plate and lens shows that the amplitude taper is similar for

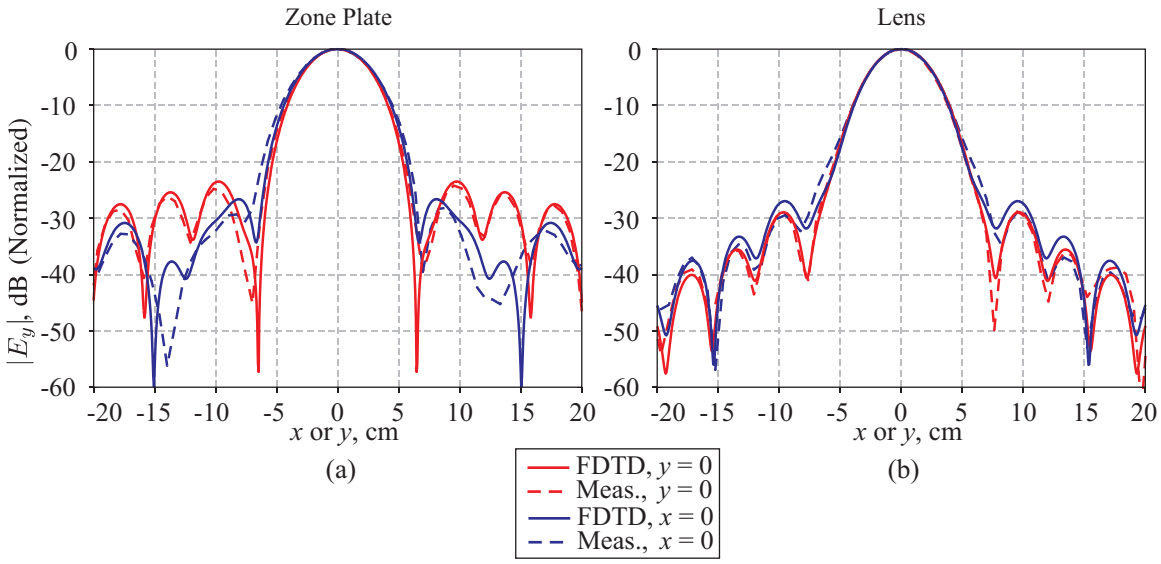

Figure 6.12: Measured and simulated (FDTD) results for the magnitude of the electric field E_y on the focal plane for (a) the zone plate and (b) the lens.

both devices. Both have a main beam of similar size (with a radius of 6.5 cm for the zone plate and 7.7 cm for the lens). At the edge of the main beam, the field is down at least 30 dB for both devices. Note, however, that the sidelobes for the lens are generally lower than for the zone plate.

Figure 6.13 shows the magnitude of E_y in dB for the zone plate and the lens for two planar cuts through the focal point: a horizonal cut (xz-plane) in (a) and (c), and a vertical cut (xy-plane) in (b) and (d). Measured results are plotted on the left of each figure, and FDTD results are plotted on the right, with red representing the highest intensity and blue representing the lowest intensity. The field was measured at points spaced $\Delta x = 6.35$ mm ($\Delta x/\lambda \approx 0.21$) apart; this causes the pixelation in the figures for the measured field. Each of these plots show good agreement between the simulations and measurements.

Figures 6.12 and 6.13 support the conclusion of the BOR-FDTD comparison in Chapter 5: based on the amplitude taper of the field focused by the zone plate, the zone plate appears to be an acceptable replacement for the lens at the design frequency.

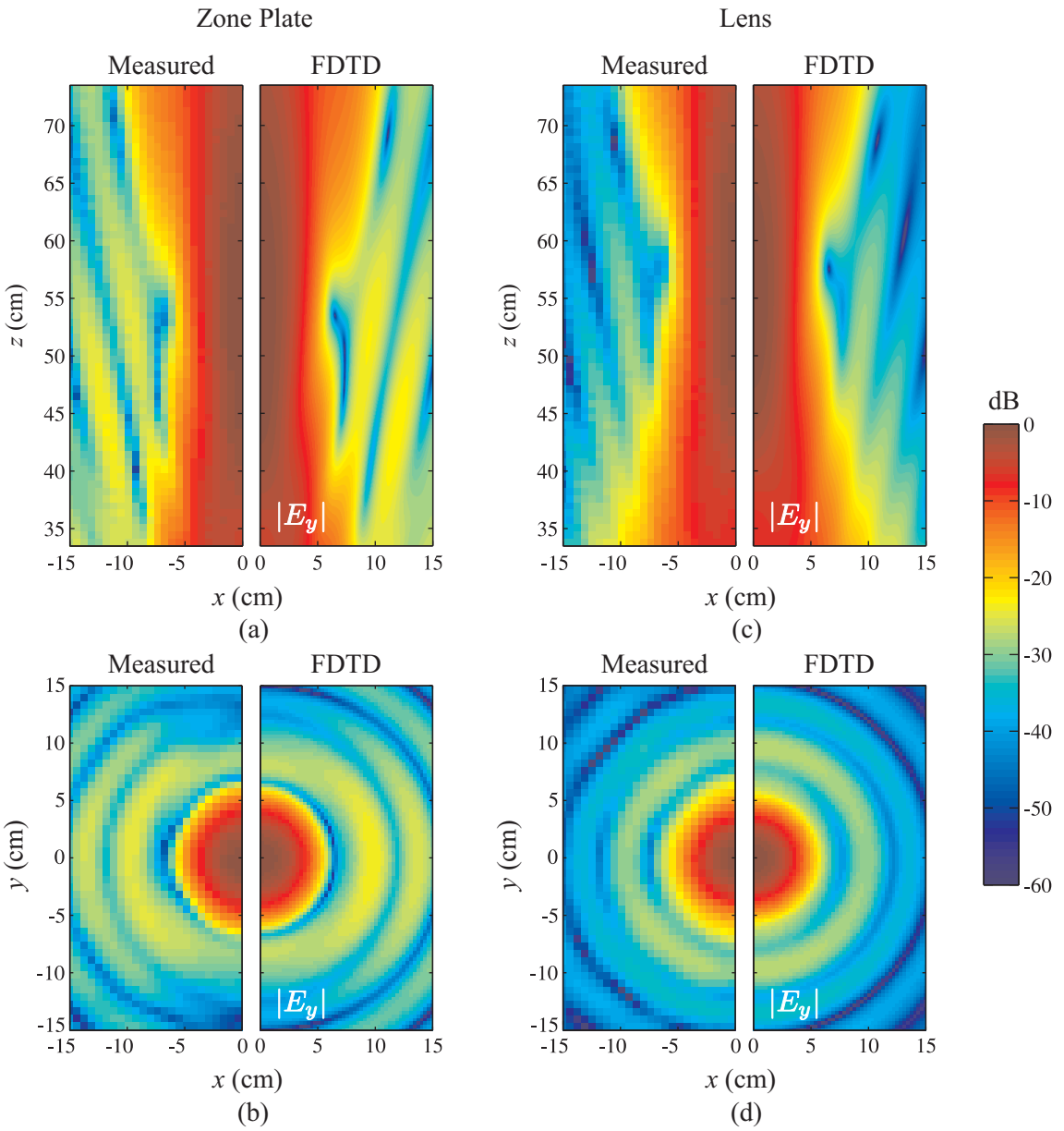

Figure 6.13: Magnitude of E_y at $f = 10\,\text{GHz}$ for (a) a horizontal cut (xz-plane), and (b) a vertical cut (xy-plane) through the focus of the zone plate. The same two cuts are plotted for the lens in (c) and (d).

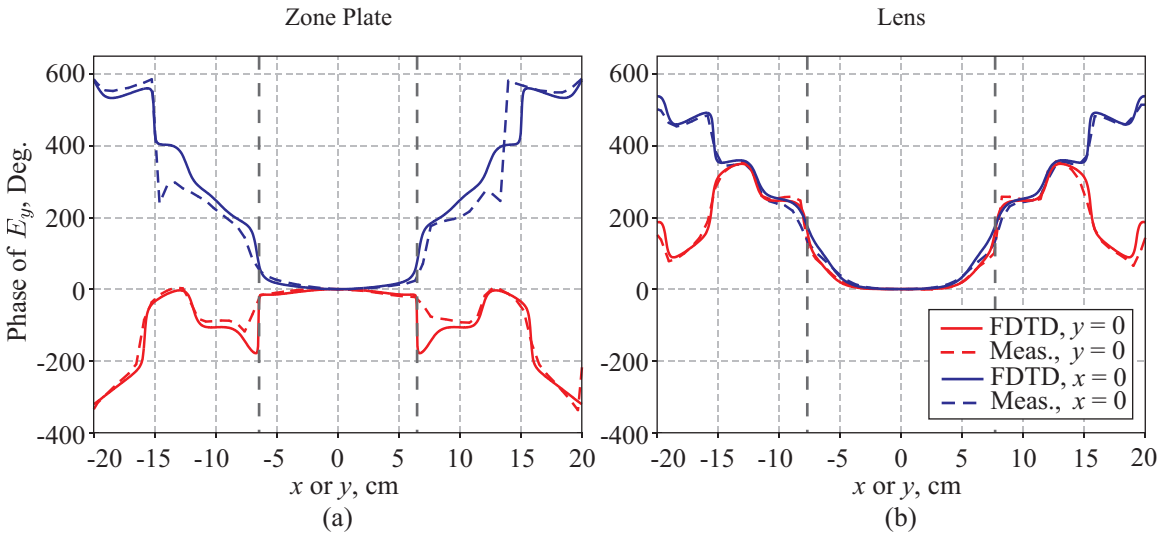

Figure 6.14: Measured and simulated (FDTD) results for the phase of the electric field E_y on the focal plane for (a) the zone plate and (b) the lens. The dashed black lines indicate the extent of the main beam from Fig. 6.12.

6.3.2 Phase Uniformity

The behavior of the phase in the focal region is also important. The phase of E_y for two cuts through the focal plane is plotted in degrees in Fig. 6.14. The line conventions are the same as in Fig. 6.12: The red lines are for horizontal cuts ($y = 0$) and the blue lines are for vertical cuts ($x = 0$). The solid lines are for the BOR-FDTD simulations, and the dashed lines are for the measurements. In this figure, the vertical dashed black lines indicate the extent of the main beam (the region between the first nulls in Fig. 6.12). Again, there is good agreement between the simulated and measured results, particularly in the main beam, for both the zone plate and the lens. The phase of the field focused by the zone plate (Fig. 6.14(a)) is comparably uniform in the main beam to the phase of the field focused by the lens (Fig. 6.14(b)). At the edge of the main beam focused by the zone plate (x or $y = 6.5\,\text{cm}$), the phase for the vertical cut ($x = 0$) has shifted by about 75°. At the same distance from the axis, the phase for the same cut of the field focused by the lens has shifted by about 100°.

The phase on the xz-plane is plotted for both the zone plate (Fig. 6.15(a)) and the lens (Fig. 6.15(b)) when $f = 10\,\text{GHz}$, with measured data on the left and simulated data on the

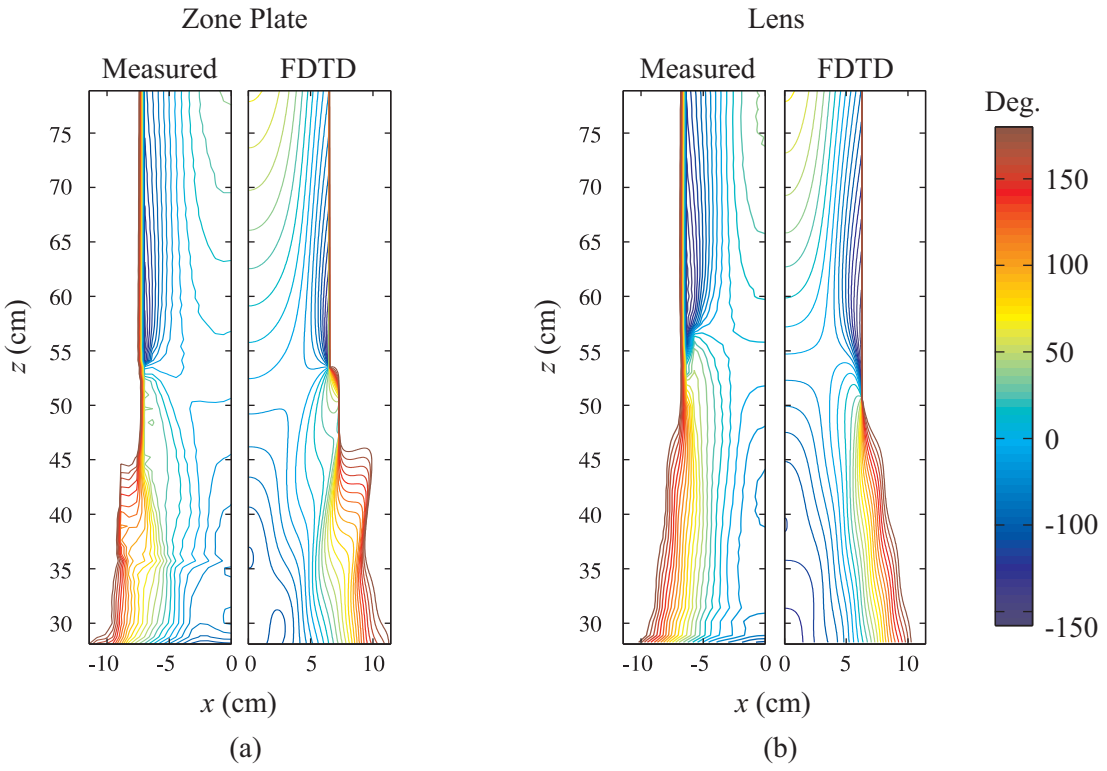

Figure 6.15: Phase of E_y at $f = 10\,\text{GHz}$ for a horizontal cut (xz-plane) through the focus of (a) the zone plate and (b) the lens.

right. Contours of constant phase are spaced 10° apart and are color coded. The value of the phase is set to zero at $z = 55\,\text{cm}$, and the color scale is referenced to this value, with red representing a positive phase shift and blue representing a negative phase shift. The dominant feature of the phase in the region shown is the linear component of the phase due to the distance from the zone plate. This component has been subtracted to enhance the detail of the phase in the focal region. What remains is a much smaller linear component along the axis (notice the phase progression as z increases). This linear trend is similar to the predicted linear phase component of an ideal Gaussian beam [39]. For any particular value of z, as x is increased, the phase falls off with increasing distance from the axis. There is value of z for which this falloff is slowest (i.e. the phase is flattest). Comparing the location of the flattest phase with the location of the waist from the amplitude plots shows that these points are nearly at the same distance from the zone plate, as expected. The agreement between the measurements and simulations is reasonably good: The same general

characteristics are seen in both, and the location of the flattest phase in the measured data is close to that of the simulated data. Additionally, the linear phase shift with increasing z along the axis is similar in both the measurements and simulations. Figure 6.15 also shows a distinct similarity between the phase of the field focused by the zone plate and the phase of the field focused by the lens. Particularly near the axis, the phase appears to behave in the same way for both devices. This observation agrees with the conclusions from Chapter 5: at the design frequency, the phase of the field focused by the zone plate appears to be acceptably uniform.

Collectively, Figs. 6.12-6.15 confirm that the zone plate is focusing energy in the manner of a Gaussian beam and that this focusing is similar to the focusing by the lens. In Figs. 6.13(a) and (c), the beam-like nature of the focused field can be seen: The field focused by the zone plate tapers to a waist near $z = 55\,\text{cm}$ and then expands with increasing distance from the zone plate. The field focused by the lens has the same general characteristics, although the waist is closer to $z = 56\,\text{cm}$. The cuts in the xy-plane through the waist in Figs. 6.13(b) and (d) clearly show the focal spot produced by both the zone plate and the lens. In these plots, one of the most noticeable differences is that the sidelobes for the zone plate are larger than for the lens. This was also seen in Figs. 6.12. Finally, Fig. 6.15 shows that the phase flattens out near the waist for both devices.

6.3.3 Linear Polarization

In a focused-beam measurement system, the field near the waist of the beam (near the sample) is treated as a linearly polarized plane wave. The measurement system is configured so that the field from the horn in polarized in the y-direction. In this section, the other two components of the electric field, E_x and E_z, will be studied to determine if the field focused by a zone plate can be considered to be linearly polarized. In addition, measurements of the other components of the electric field are also useful to confirm the accuracy of the BOR-FDTD simulations.

The magnitude of E_x in the xy-plane through the focus is plotted for the zone plate and the lens when $f = 10\,\text{GHz}$ in Fig. 6.16. The agreement between the measured and

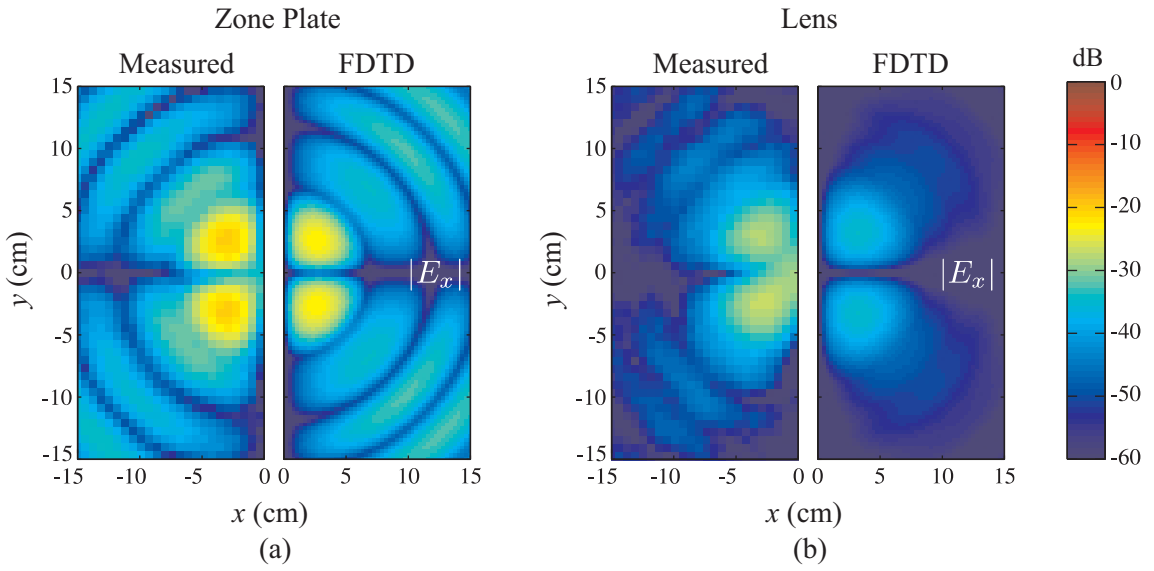

Figure 6.16: The magnitude of E_x in the xy-plane at $f = 10\,\text{GHz}$ through the focus for (a) the zone plate and (b) the lens.

simulated values of E_x is reasonably good. The measured values of $|E_x|$, for both devices, are generally larger than the simulated values. This is likely due to imperfect alignment of the components of the beamscan system, particularly the horn and the dipole, and imperfect construction of the dipole probe. The color scale is the same for these figures as for Fig. 6.13, so it can be seen that the maximum value of $|E_x|$ for the zone plate is about 20 dB less than the maximum of $|E_y|$. The E_x component is even smaller for the lens; the maximum value of $|E_x|$ for the lens is about 30 dB less than the maximum of $|E_y|$. Notice that outside of the spots of largest intensity, $|E_x|$ falls off more quickly for the lens than it does for the zone plate, which has a distinct pattern of sidelobes.

Figure 6.17 shows the presence of a z-component of the electric field in both the simulations and the measurements. The magnitude of E_z in a plane parallel to the yz-plane is plotted for the zone plate and the lens when $f = 10\,\text{GHz}$ in Figs. 6.16(a) and (c), and $|E_z|$ is plotted in a xy-plane for the zone plate and the lens when $f = 10\,\text{GHz}$ in Figs. 6.16(b) and (d). The yz-plane for these measurements and simulations is *not* through the focal point, but is instead offset by $x = -0.64\,\text{cm}$ for the reasons explained in the discussion of Fig. 6.9. For the same reasons, the plots for the xy-plane also do not go all the way to $x = 0$.

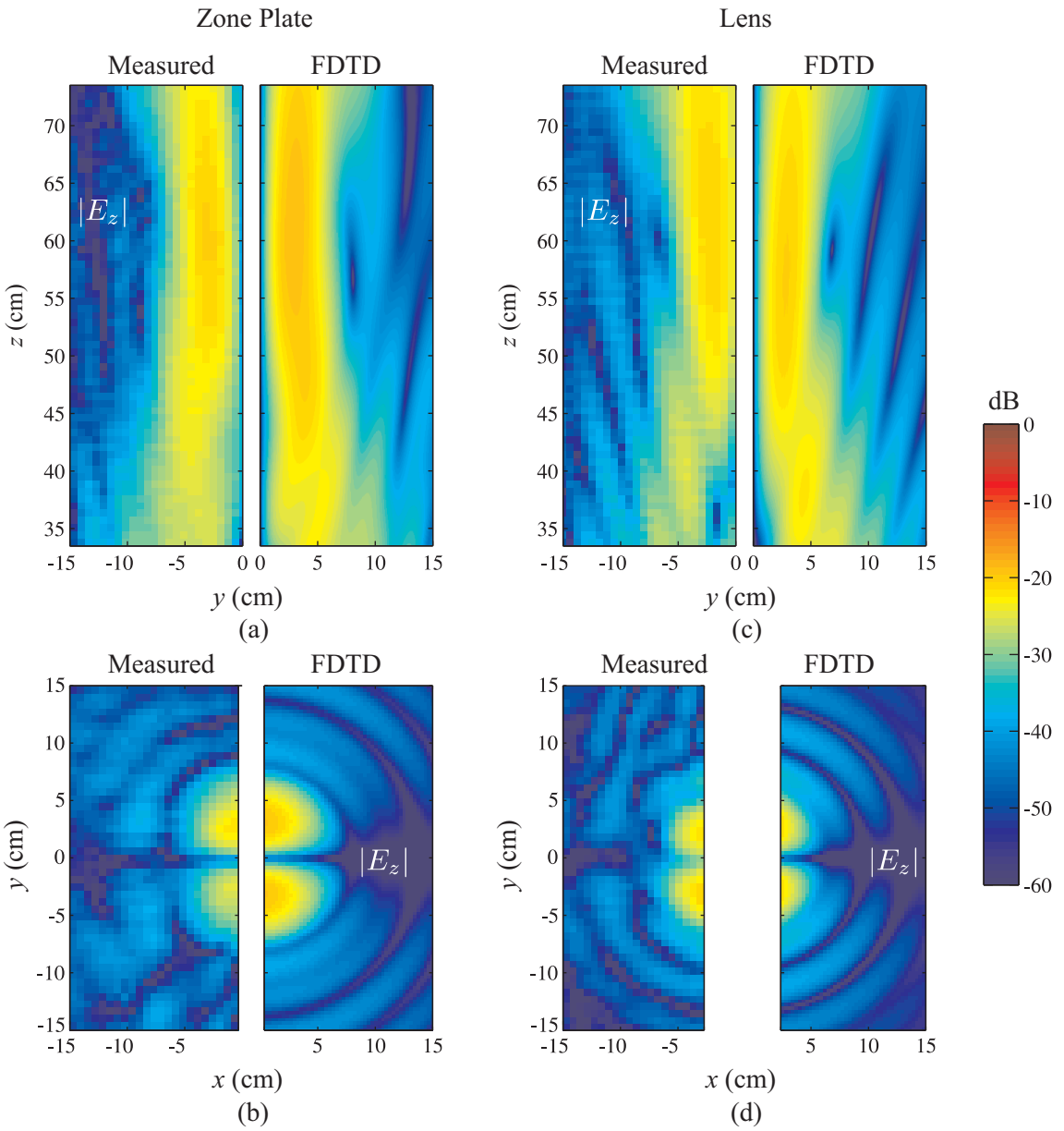

Figure 6.17: Magnitude of E_z at $f = 10\,\text{GHz}$ for (a) a vertical cut (yz-plane) through the plane $x = -0.64\,\text{cm}$, and (b) a vertical cut (xy-plane) through the focus of the zone plate. The same two cuts are plotted for the lens in (c) and (d).

Although $E_z = 0$ for an ideal plane wave, the field for an ideal Gaussian beam has a small (non-zero) z-component [39]. E_z is therefore a particularly interesting metric for evaluating the accuracy of the BOR-FDTD simulations and the sensitivity of the measurement system. Because of the probe design, the measurements for E_z are not as accurate as they are for E_x and E_y. However, the results in Fig. 6.17 agree well enough to indicate that the FDTD model is correctly accounting for E_z. The value of $|E_z|$ in the focal region looks similar for both the zone plate and the lens. In Figs. 6.17(a) and (c) the intensity near the focal plane is small on the axis for both devices. Moving away from the axis by increasing or decreasing x, the intensity increases and then tapers back off to near zero. This is the form of $|E_z|$ predicted for an ideal Gaussian beam [39]. The scale of these plots is the same as the scale for Figs. 6.13 and 6.16, so it can be seen that $|E_z|$ is at least 20 dB smaller than $|E_y|$.

The results in Figs. 6.13, 6.16, and 6.17 show that the field at the beam waist is nearly linearly polarized: the x- and z-components of the field are at least 20 dB below the y-component of the field. This is important for the application of the zone plate to a focused-beam system; these results show that it is reasonable to treat the field focused by the zone plate as a plane wave near the beam waist.

The measured data presented in this section illustrate a few important concepts. A direct comparison of the zone plate and the lens at the design frequency indicates that the zone plate is an acceptable replacement for the lens in a free-space, focused-beam measurement system. Additionally, the BOR-FDTD simulations were shown do a good job of predicting the actual focusing by both the zone plate and the lens.

6.3.4 Bandwidth

In Chapter 5, simulations showed that the beam waist of the zone plate shifts from its intended location away from the design frequency. This has an effect on the usable bandwidth of the zone plate in a focused-beam measurement system. The conclusions about the frequency dependence of the zone plate from Chapter 5 are supported by measurements taken for $f = 8$ GHz and $f = 12$ GHz. In this section, a sample of these measurements will be presented and discussed.

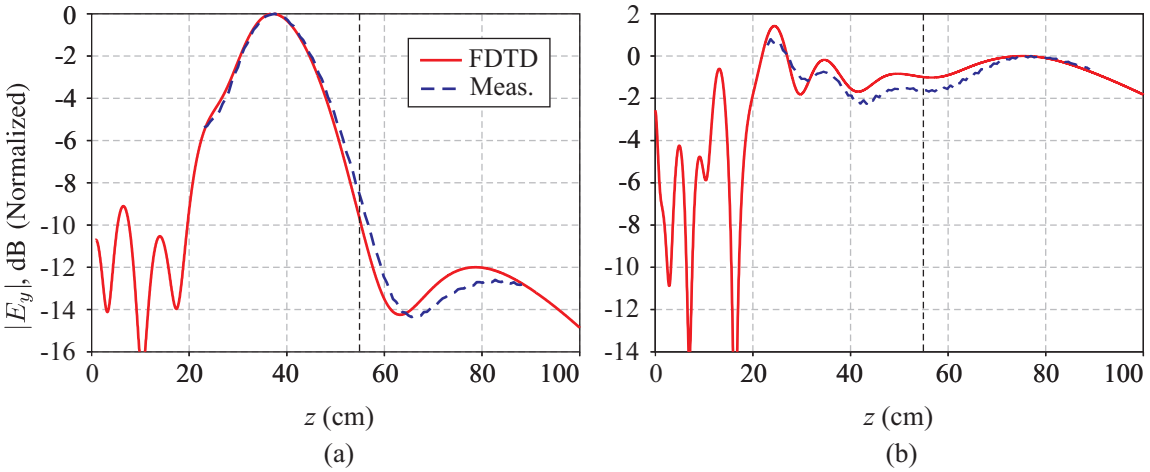

Figure 6.18: Measured and simulated (FDTD) results for the electric field E_y along the z-axis for the zone plate. The magnitude E_y at (a) $f = 8\,\text{GHz}$ and (b) $f = 12\,\text{GHz}$ is plotted as a function of the distance from the respective focusing element.

Figure 6.18 shows $|E_y|$ plotted as a function of the distance from the zone plate when $f = 8\,\text{GHz}$ and $f = 12\,\text{GHz}$. The vertical dashed black line in both figures is the location of the beam waist for the lens when $f = 10\,\text{GHz}$ ($z = 55\,\text{cm}$). The agreement between the simulations and the measurements is not quite as good when $f = 12\,\text{GHz}$. Nevertheless, the shift of the beam waist as the frequency differs from the design frequency is quite evident from the figure.

In Fig. 6.19, the magnitude of E_y on the xz-plane through the focus is plotted in dB for the zone plate and the lens for the same two frequencies. Figs. 6.19(a) and (c) are for $f = 8\,\text{GHz}$ and (b) and (d) are for $f = 12\,\text{GHz}$. These figures clearly show that the field focused by the zone plate at these frequencies looks different from the field focused at the design frequency, $f = 10\,\text{GHz}$. The field focused by the lens looks similar, however, for all three frequencies: $f = 8\,\text{GHz}$ (Fig. 6.19(c)), $f = 10\,\text{GHz}$ (Fig. 6.13(c)), and $f = 12\,\text{GHz}$ (Fig. 6.19(d)).

The complete set of measured and simulated data for the zone plate and lens at the frequencies $f = 8$, 10, and $12\,\text{GHz}$ is compiled in Appendix A. In general the agreement between the measured and simulated results is quite good. This is especially true for measured and simulated data when $f = 8$ and $f = 10\,\text{GHz}$. The measurements for $f = 8$ and $f = 12\,\text{GHz}$ support the conclusions from Chapter 5 about the frequency-dependent

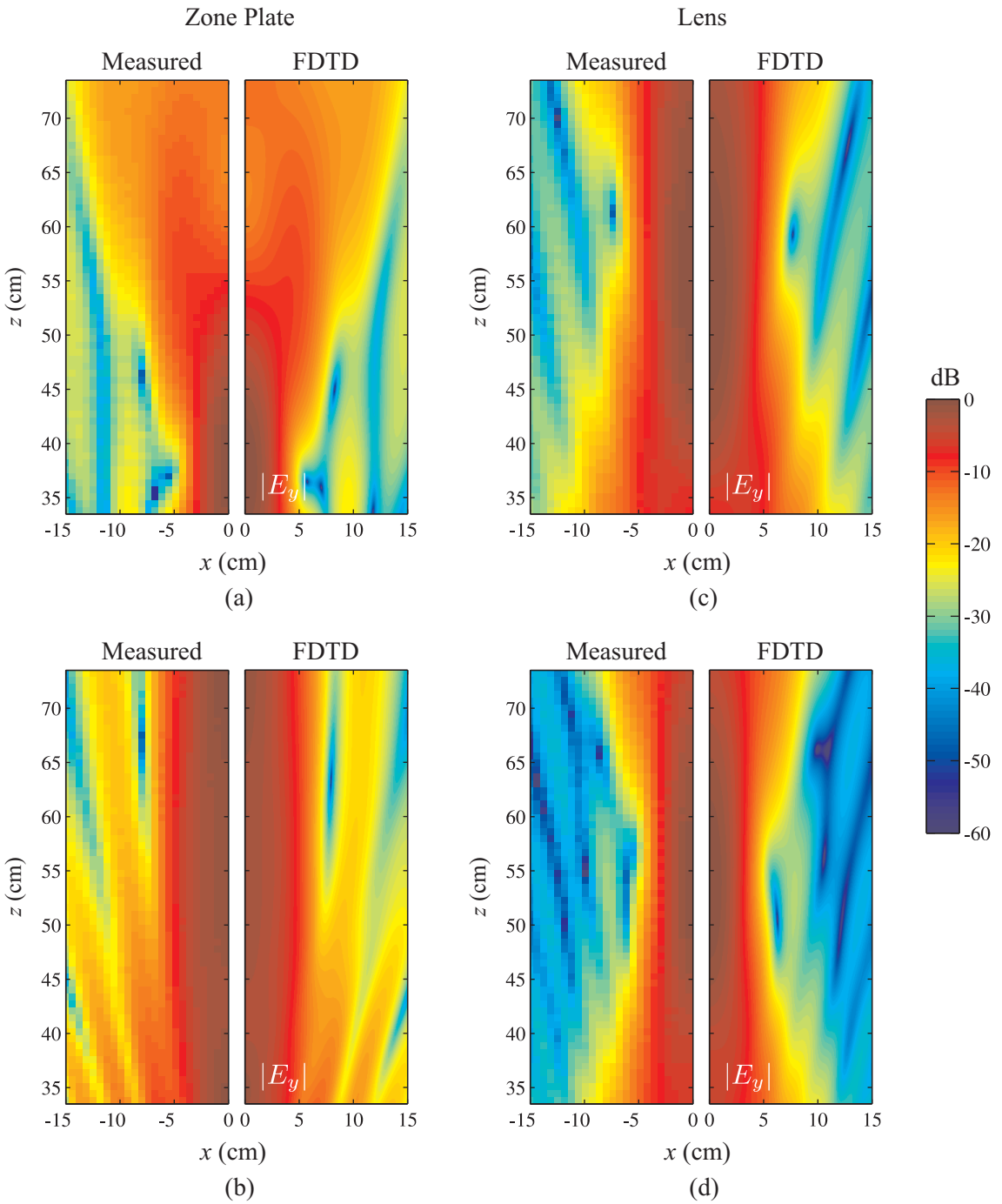

Figure 6.19: Magnitude of E_y for a horizontal cut (xz-plane) through the focus of the zone plate when (a) $f = 8\,\text{GHz}$ and (b) $f = 12\,\text{GHz}$. The same two cuts are plotted for the lens in (c) and (d).

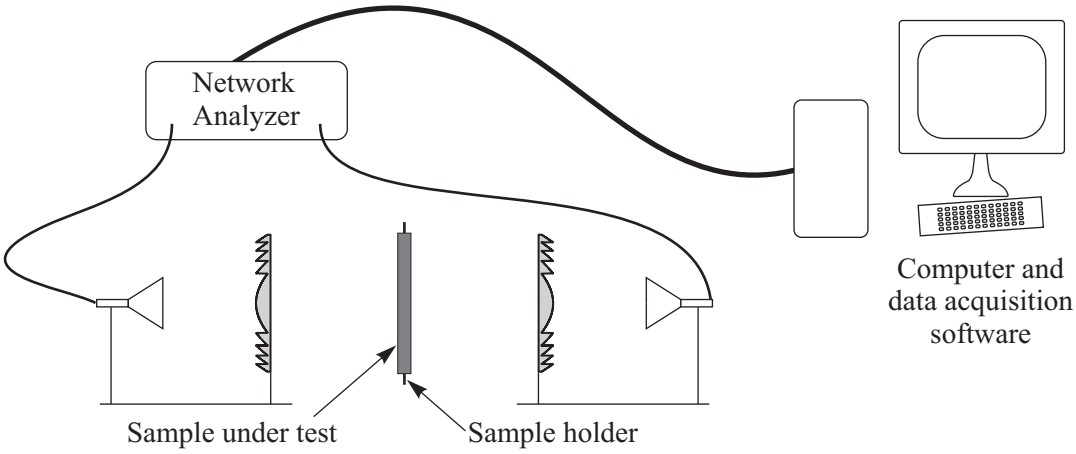

Figure 6.20: Schematic diagram of the free-space focused-beam system.

nature of the zone plate.

6.4 Experimental Procedure to Test Focused-Beam System that uses Zone Plates

In Chapter 5, BOR-FDTD simulations were used to begin to evaluate zone plates for use as focusing elements in focused-beam systems. The focusing from the zone plate was found to be frequency dependent, and a method for compensating for this frequency dependence was proposed. Based on BOR-FDTD simulations, this method appeared to be a promising solution to extend the usable bandwidth of the zone plate. To fully test the zone plate for this application, a complete focused-beam system using two zone plates was constructed and used to measure the complex permittivity of different materials. To evaluate the accuracy of the system, these measurements were compared to measurements for the same materials made with a focused-beam system with two lenses. When possible, measured permittivities were also compared to published values.

The focused-beam system that was used for these tests was based on the setup for GTRI's standard focused-beam system. A diagram of the system is in Fig. 6.20, and photographs of the focused-beam system are shown in Figs. 6.21 and 6.22. Figure 6.21 is a photograph of the focused-beam system that uses zone plates as focusing elements. Notice that the sample holder is surrounded by absorbing foam, as suggested in Sec. 5.4. Figure 6.22 is a photograph of the system that uses lenses as focusing elements. In this

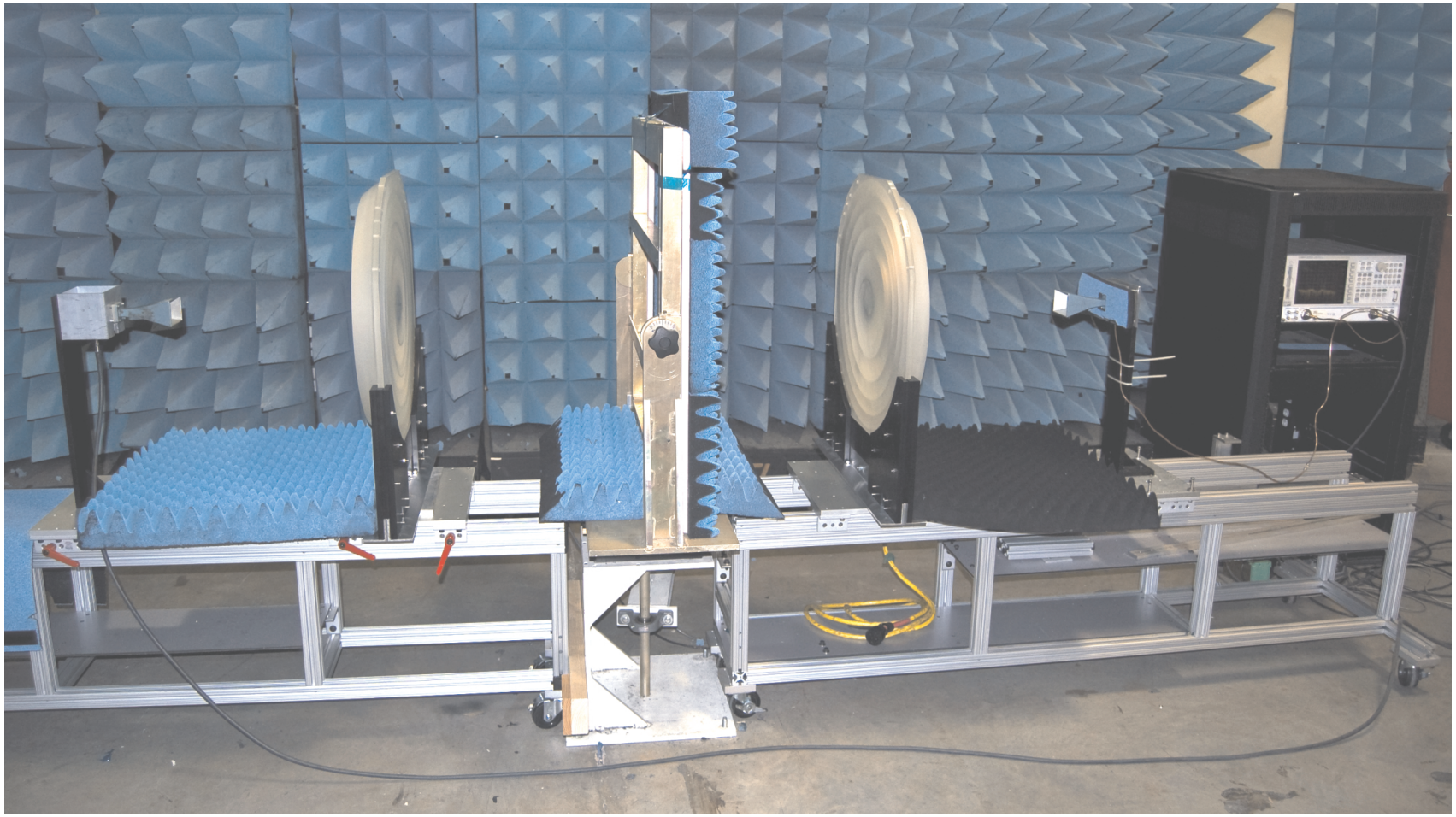

Figure 6.21: Photograph of the focused-beam system with zone plates used as the focusing elements.

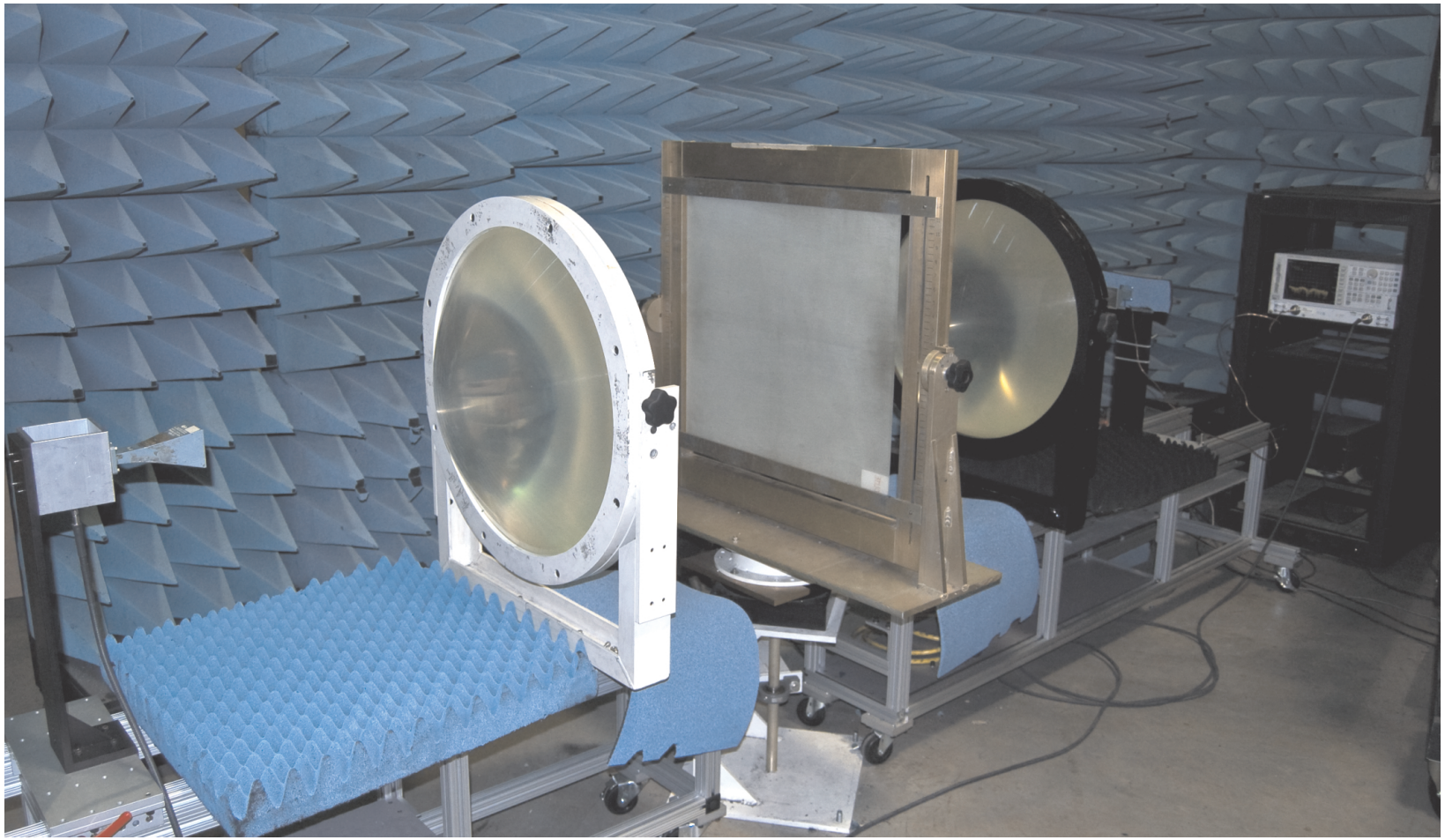

Figure 6.22: Photograph of the focused-beam system with lenses used as the focusing elements and a dielectric sheet in the sample holder.

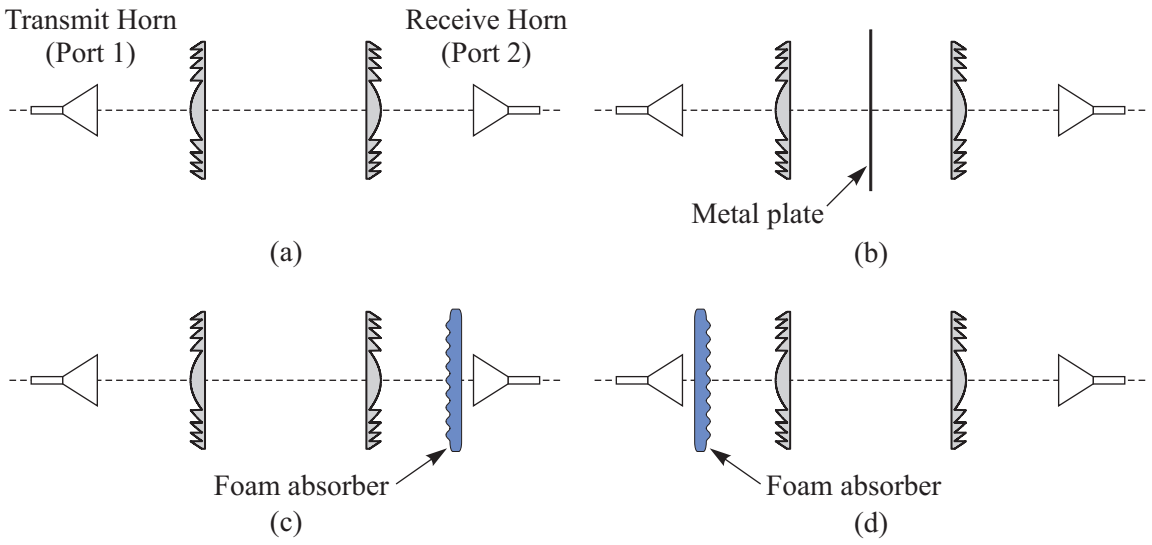

Figure 6.23: Schematic diagram of the four configurations necessary for a response and isolation calibration for the focused-beam system.

photograph, a sheet of Rexolite is visible in the sample holder.

The distance from the both horns to the closest surface of the zone plate or lens is 43.2 cm. The distance between the zone plates is $2z_s$ ($2z_s = 110\,\text{cm}$ when the system is configured for $f = 10\,\text{GHz}$), and the sample is placed halfway between the zone plates. The transmit horn and the receive horn are connected to ports one and two of the network analyzer, respectively. Data acquisition software on a personal computer controls the network analyzer and records scattering parameter (S-parameter) data. Before the permittivities can be calculated, the recorded data must be post-processed in two steps: a calibration step and a time-gating step.

6.4.1 Calibration and Time Gating

The calibration is applied to the data using the same procedures that are used for GTRI's standard focused-beam system. The calibration explained in [79] is used: A response and isolation calibration is made for each of the S-parameters. This requires eight distinct measurements in four different configurations. Figure 6.23 is a schematic diagram of these four configurations. Using the configuration in Fig. 6.23(a), the transmission response coefficients S_{21}^{res} and S_{12}^{res} are measured. A metal plate of known thickness is placed in the

sample holder, as shown in Fig. 6.23(b), and the reflection response coefficients S_{11}^{res} and S_{22}^{res} and the transmission isolation coefficients S_{21}^{iso} and S_{12}^{iso} are measured. For all four of these measurements, the metal plate is left in place and its thickness is mathematically accounted for. Finally, the two configurations in Figs. 6.23(c) and (d) are used to measure the reflection isolation coefficients S_{11}^{iso} and S_{22}^{iso}, respectively. In these configurations, a piece of broad-band foam absorber placed in front of one of the horns is treated as a matched load. These coefficients can then be used to calibrate the S-parameters measured with the sample in place:

$$S_{ij}^{\text{cal}} = \frac{S_{ij}^{\text{meas}} - S_{ij}^{\text{res}}}{S_{ij}^{\text{res}} - S_{ij}^{\text{iso}}} \ , \tag{6.1}$$

in which ij = 11, 12, 21, or 22. Additionally, the thickness of the metal plate t_m is accounted for by multiplying S_{11}^{cal} and S_{22}^{cal} by $e^{-jk_o t_m}$ to adjust the reference plane for the measurements. All four S-parameters are multiplied by $e^{jk_o t_s}$ to account for the space taken up by the sample to be measured, which has a thickness of t_s.

The time-gating procedure is also done in post-processing. The calibrated, frequency-domain measurement data (S_{ij}^{cal}) are convolved with a Kaiser window. This procedure is mathematically equivalent to multiplying the time-domain data by a finite window. This windowing removes unwanted reflections, including multiple reflections between the zone plate or lens and the sample.

6.4.2 Calculation of Permittivity

The calibrated and time-gated data can be used to calculate the permittivity of the dielectric sheet. The process of computing dielectric properties from these measurements is called the 'inversion' of the measurements. There are a number of different ways to perform this inversion. Two of the most common techniques are applied in this work. Both methods treat the field near the beam waist as a plane wave. Using this assumption, the formulas for a plane wave incident on a dielectric sheet can be used to find the theoretical values of the S-parameters for sheets of different permittivity and permeability. By finding the theoretical S-parameters that most closely match the measured S-parameters, the material properties of the sample can be determined.

One technique involves computing the permittivity of the sample using a single calibrated measurement, in this case S_{21}^{cal} [43]. Newton's method is used to iteratively solve for the permittivity. The theoretical value of S_{21}^{pw} for a plane wave incident on a dielectric sheet of thickness l can be written as a function of the permittivity of the sample [43] for a given frequency:

$$S_{21}^{\text{pw}}(\epsilon_r) = \frac{\tau\left(1-\Gamma^2\right)}{1-\tau^2\Gamma^2}\,. \tag{6.2}$$

In this equation,

$$\Gamma(\epsilon_r) = \frac{1-\sqrt{\epsilon_r}}{1+\sqrt{\epsilon_r}}\,, \tag{6.3}$$

and

$$\tau(\epsilon_r) = e^{-jk_o l\sqrt{\epsilon_r}}, \tag{6.4}$$

in which $k_{\text{o}} = 2\pi/\lambda$ is the propagation constant in free space. The actual permittivity can be found at each frequency by solving for the root of the equation created by subtracting the theoretical and measured values of S_{21},

$$S_{21}^{\text{cal}} - S_{21}^{\text{pw}}(\epsilon_r) = 0\,. \tag{6.5}$$

The value of ϵ_r for which Eq. (6.5) is minimized is assumed to be the permittivity of the material.

The second technique used is based on the inversion algorithm for the transmission/reflection method for waveguide or coaxial line measurements in [80]. All four of the S-parameter measurements are used in this iterative inversion algorithm. Using all four measurements results in a system of equations for which there are more independent equations than unknowns, and the extra equations can be used to eliminate errors due to a slight displacement of the sample from the calibration plane. For this reason, this technique is better suited for warped samples [79]. The procedure is similar to the single measurement method: all four S-parameters are written as a system of equations in terms of the complex permittivity and permeability of a material. An iterative solver is used to find the closest match of the measured S-parameters to the theoretical S-parameters.

The software to perform the inversion of the measurements was written by Dr. John Schultz of STL/GTRI.

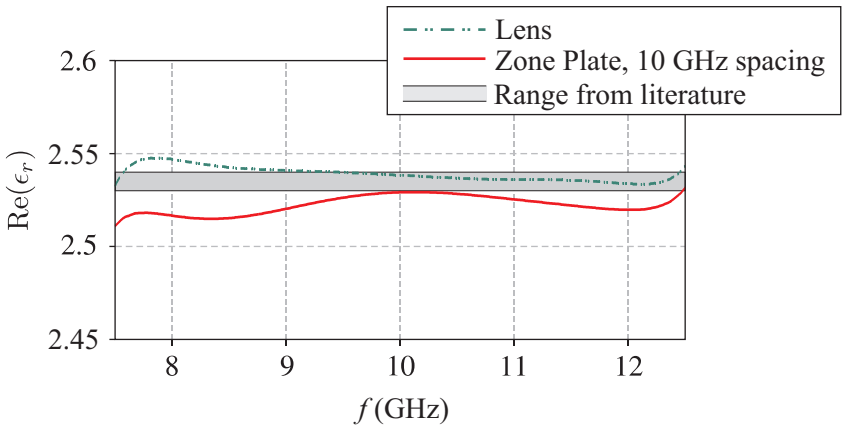

Figure 6.24: The real part of the relative permittivity for a sheet of Rexolite determined by focused-beam measurements. Measurements were made using two lenses and using two zone plates with the spacing for the zone plates set for $f = 10\,\text{GHz}$.

6.5 Experimental Study of Focused-Beam System

The measurement system described in Sec. 6.4 was used to measure the permittivity of a few different dielectric materials. The measured permittivity values were compared to results from a focused-beam system that uses two doubly-hyperbolic lenses and, when available, to published values.

6.5.1 Rexolite

The first sample measured with the system was a sheet of Rexolite (cross-linked polystyrene). The sheet has a thickness of 0.32 cm and is 60.96 cm by 60.96 cm in the other two dimension (this sheet can be seen in the sample holder in Fig. 6.22). The values of the real part of the relative permittivity for Rexolite found in the literature are in the range $2.53 < \text{Re}(\epsilon_r) < 2.54$ [77, 81–83]. In Fig. 6.24, the green line (dash-dot-dot) is the measured result using two doubly-hyperbolic lenses, and the red (solid) line is the measured result using two zone plates with the spacing set for $f = 10\,\text{GHz}$. The gray box shows the range of values found in the literature. The permittivities were inverted from the measurements using the single measurement technique. The four-measurement technique gave similar results.

The RMS deviation from the average of the values from the literature, $\text{Re}(\epsilon_r) = 2.536$,

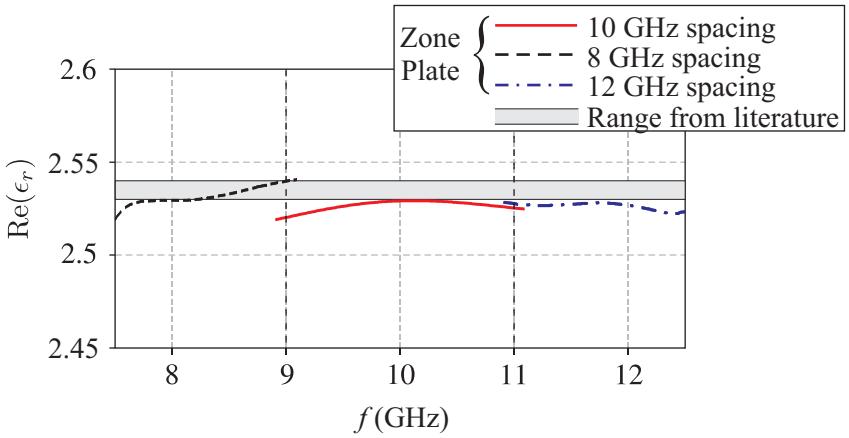

Figure 6.25: The imaginary part of the relative permittivity for a sheet of Rexolite determined by focused-beam measurements. Measurements were made using two zone plates with the spacing set for $f = 8$, 10, and 12 GHz.

was computed for both the lens and the zone plate over the frequency range 8-12 GHz. The deviation for the lens was 0.18%, while for the zone plate it was 0.53%. From Fig. 6.24, it is clear that the most accurate measurements made with the zone plate system are around the design frequency, $f = 10$ GHz.

If the technique proposed in Chapter 5 is implemented, and the zone plate system is reconfigured with the correct spacing for $f = 8$, 10, and 12 GHz as in Fig. 5.12, then the agreement between the measurements and the published value improves in the region around these respective frequencies. This suggests that the three measurements made with the zone plates in different configurations could be stitched together to get a more accurate measurement across the entire frequency band. This technique is illustrated in Fig. 6.25. The black (dashed), red (solid), and blue (dash-dot) lines are for the permittivity measured using two zone plates with the spacing set for $f = 8$, 10, and 12 GHz, respectively. Comparing this measurement with the measurement for the $f = 10$ GHz spacing alone (red line) in Fig. 6.24, a clear improvement can be seen. The RMS deviation from the published value improves from 0.53% for the measurement in Fig. 6.24 to 0.31% for the measurement in Fig. 6.25.

The values of the imaginary part of the relative permittivity for Rexolite found in the literature are in the range $1.09 \times 10^{-3} < \mathrm{Im}(\epsilon_r) < 1.67 \times 10^{-3}$ [77, 81–83]. Figure 6.26

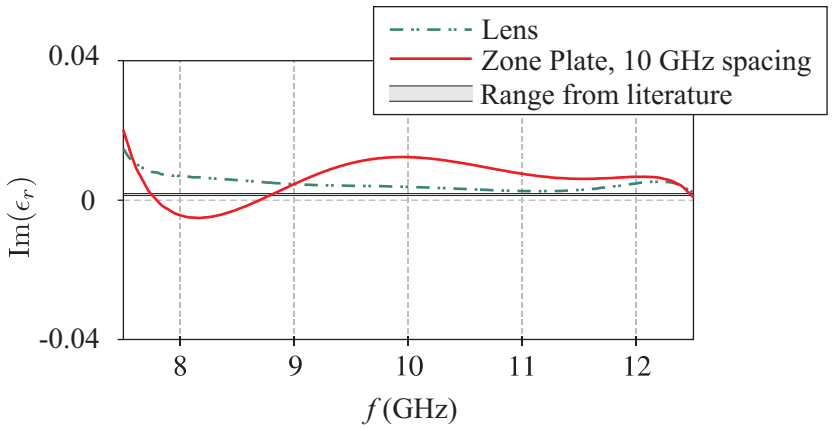

Figure 6.26: The imaginary part of the relative permittivity for a sheet of Rexolite determined by focused-beam measurements. Measurements were made using two lenses and using two zone plates with the spacing for the zone plates set for $f = 10\,\text{GHz}$.

gives the measured values of the imaginary part of the permittivity. The green line (dash-dot-dot) is the measured result using two doubly-hyperbolic lenses, and the red (solid) line is the measured result using two zone plates with the spacing set for $f = 10\,\text{GHz}$. The gray box shows the range of values found in the literature. This plot shows that the lens performs better than the zone plate for this measurement. However, when $\text{Im}(\epsilon_r)$ is small relative to $\text{Re}(\epsilon_r)$, as it is for Rexolite, it generally cannot be determined accurately with a free-space system. A measurement system with a higher quality factor (Q) is necessary to get accurate measurements of $\text{Im}(\epsilon_r)$ for a low-loss material like Rexolite [84].

6.5.2 Teflon

The two focused-beam systems were also used to measure the permittivity of a 0.32 cm thick sheet of Teflon[5] (polytetrafluoroethylene). This sheet is slightly smaller than the sheet of Rexolite (approximately 30.48 cm by 45.72 cm in the other two dimensions). The measurements of Teflon posed an additional difficulty because of the flexible nature of the material. The sheet had been stored in way that left it slightly warped, which can adversely affect the accuracy of focused-beam measurements [79]. An attempt to flatten the sheet was made, and care was used when placing the sheet in the sample holder. Nevertheless, the sheet of Teflon was still slightly warped when the measurement was taken.

[5]Teflon is a registered trademark of E. I. du Pont de Nemours and Company (DuPont).

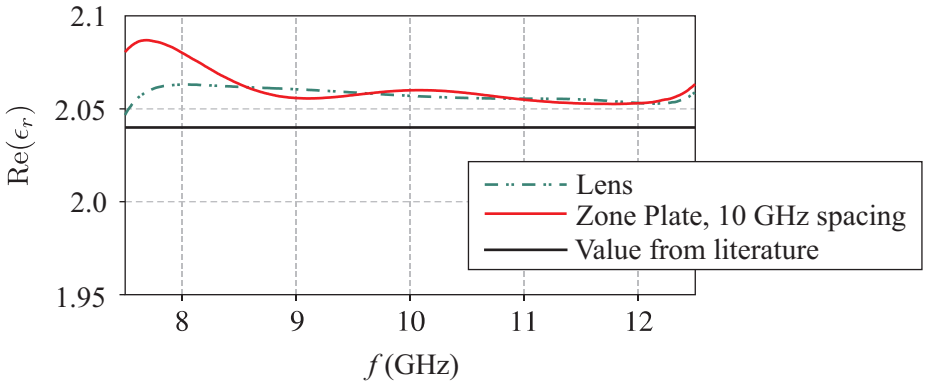

Figure 6.27: The real part of the relative permittivity for a sheet of Teflon determined by focused-beam measurements. Measurements were made using two lenses and using two zone plates with the spacing for the zone plates set for $f = 10\,\text{GHz}$.

The relative permittivity of Teflon, based on accurate measurements in the literature, is $\epsilon_r = 2.04$ [82]. The measured values of the relative permittivity are given in Fig. 6.27. The green line (dash-dot-dot) is the measured result using two doubly-hyperbolic lenses, and the red (solid) line is the measured result using two zone plates with the spacing set for $f = 10\,\text{GHz}$. The black line shows the value from the literature. Because the sample is warped, the four-measurement inversion technique is used to solve for the permittivity of the Teflon sheet. Despite the use of this technique, the value of ϵ_r measured using both systems is slightly higher than the value from the literature.

If the system is reconfigured in the same was as it was for the Rexolite sample and the measurements are stitched together, an improvement in accuracy is seen. The black (dashed), red (solid), and blue (dash-dot) lines are for the permittivity measured using two zone plates with the spacing set for $f = 8$, 10, and 12 GHz, respectively. The RMS deviation from the published value improves from 1.12% for the measurement in Fig. 6.24 to 0.93% for the measurement in Fig. 6.25. The RMS deviation from the published value for the lens measurement is slightly better, 0.88%.

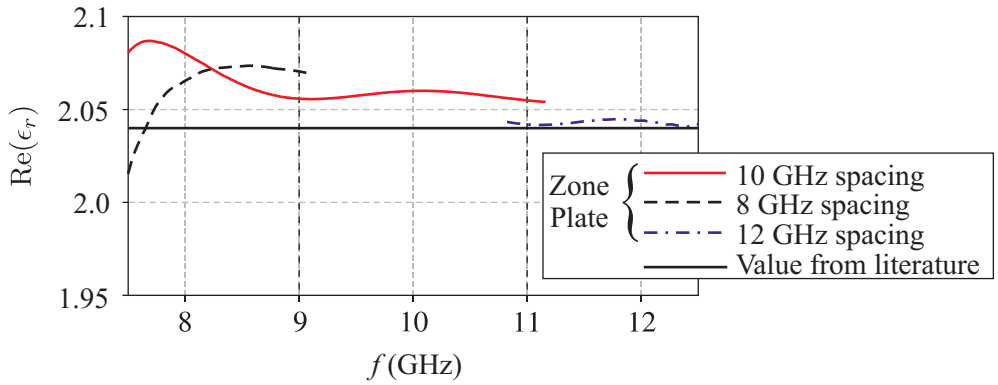

Figure 6.28: The real part of the relative permittivity for a sheet of Teflon determined by focused-beam measurements. Measurements were made using two zone plates with the spacing set for $f = 8$, 10, and 12 GHz.

6.5.3 Stycast

A sample of Stycast[6] was also measured in the same way as the Rexolite and Teflon samples. The sheet of Stycast is 0.66 cm thick and is 30.48 cm by 30.48 cm in the other dimensions. The relative permittivity of the sheet is expected to be $\epsilon_r \approx 8$, although the exact value is not specified. The permittivity determined from measurements with the system that uses zone plates will therefore be directly compared to that of the system that uses lenses. Because this sample is electrically thicker than the other samples ($t/\lambda_d > 1/2$), the four-measurement inversion method failed to converge to a solution. The single-measurement inversion method was used instead. Figure 6.29 shows the measured values of the permittivity when the spacing for the zone plates is set for $f = 10$ GHz. In this figure, the agreement between the permittivities determined by the two systems is fairly good. The results from the reconfigured system are shown in Fig. 6.29. This system is configured in the same way as for the Rexolite and Teflon sheets. In this case, the agreement for the compiled measurement in Fig. 6.30 is similar to the agreement for the single-configuration measurement in Fig. 6.29.

The experiments presented in this section were designed to determine if zone plates are suitable replacements for doubly-hyperbolic lenses in free-space, focused-beam measurement

[6]Stycast is currently marketed under the name ECCOSTOCK by Emerson & Cuming Microwave Products

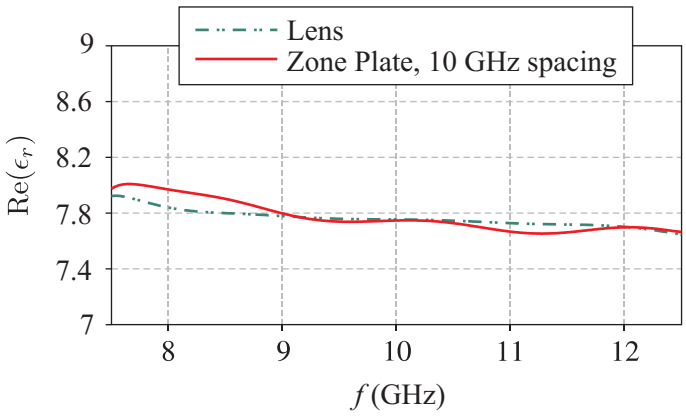

Figure 6.29: The real part of the relative permittivity for a sheet of Stycast determined by focused-beam measurements. Measurements were made using two lenses and using two zone plates with the spacing for the zone plates set for $f = 10\,\text{GHz}$.

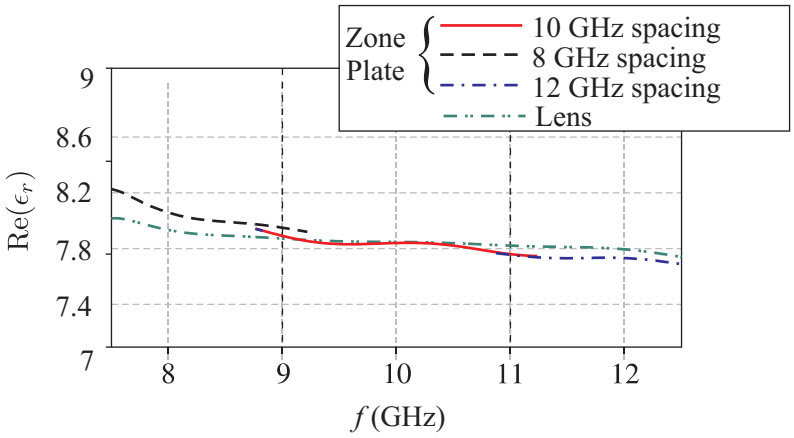

Figure 6.30: The real part of the relative permittivity for a sheet of Stycast determined by focused-beam measurements. Measurements were made using two zone plates with the spacing set for $f = 8$, 10, and 12 GHz.

systems. When the system is configured so that the spacing between the zone plates is correct for $f = 10\,\text{GHz}$, the values of the permittivity measured by the system agree reasonably well with the values measured by the system that uses lenses and with the published values. This is particularly true for frequencies near the design frequency, $f = 10\,\text{GHz}$. The technique proposed in Chapter 5 to account for the frequency-dependent shift of the beam waist was experimentally tested. Three different configurations of the focused-beam system were used to make measurements over the frequency range $f = 8\text{-}12\,\text{GHz}$. Measurements of three different dielectric samples (Rexolite, Teflon, and Stycast) showed that when this technique is used, the focused-beam system that uses zone plates as focusing elements can measure permittivity values with accuracy that is similar to a system that uses lenses as focusing elements. The calculations and measurements from this work give us confidence that zone plates can be used in a free-space, focused-beam measurement system designed to work at low frequencies, as discussed in Chapter 1.

CHAPTER VII

NON-TRADITIONAL ZONE PLATE DESIGNS: A TOPIC FOR FUTURE RESEARCH

The Fresnel zone plates studied in this work are designed using the optical, ray-tracing principles discussed in Chapter 1, in Eqs. (1.2)-(1.4), and Chapter 5, in Eqs. (5.1)-(5.3). Zone plates designed in this manner have been successfully applied in antennas for communications and in free-space, focused-beam measurement systems. With the power of the BOR-FDTD method available, a question naturally arises: Given roughly the same volume of material, could the BOR-FDTD method be used to develop a better focusing element than the traditional zone plate? This question is particularly interesting for zone plates with low values of F/D, like those used in microwave or millimeter-wave applications, for which a full-electromagnetic analysis like the BOR-FDTD method has been shown to offer an advantage over other analysis methods.

This is a broad, open-ended question, and there are many ways to approach this problem. However, some insight into this question can be acquired by choosing a technique, applying it, and examining the results. In this chapter the particular option that will be examined is optimization of a zone plate using a genetic algorithm (GA). Any optimization routine is most beneficial when it is used to design a zone plate for a specific application, with well defined physical parameters (such as diameter, focal length, and thickness) and performance goals. This makes it difficult to draw general conclusions about the benefit offered by these techniques. To begin to address this question, two specific zone plates are designed using a GA.

The two examples considered in this chapter are based on the two specific applications of zone plates studied in this work. A GA is used to optimize the amount of power focused by two types of grooved-dielectric, phase-correcting zone plates: one for antenna applications and the other for use in a free-space, focused-beam measurement system. The performance

of the optimized zone plates is compared to the performance of traditionally-designed zone plates and to hyperbolic (or doubly-hyperbolic) lenses with the same focal lengths and diameters. Of course, there are many other applications and performance metrics for which the optimization of a zone plate could be useful. Some examples include an antenna with two or more distinct frequencies of operation or a zone plate with the minimal weight needed to meet a certain performance metric.

Zone plates are good candidates for optimization because of their complicated nature; changes in the geometry bring about changes in the focusing ability of the devices in ways that are typically not obvious to the designer. However, the complexity of the zone plate, particularly when analyzed with a full-electromagnetic simulator like BOR-FDTD, makes the optimization difficult by traditional methods. A genetic algorithm was chosen to perform the optimization because it is especially useful for optimizing problems with highly complex cost functions [85].

In this chapter, a brief overview of the genetic algorithm is presented, and the specific formulation of the optimization procedure for zone plates is discussed. Optimization studies for the two different zone plates are then presented. Knowing that it is unrealistic to expect to find the best possible solution for a problem as complicated as the optimization of a zone plate, the work presented in this chapter is intended to begin to answer the question posed earlier and to lend insight into non-traditional zone plate designs. This is a topic that would be interesting to expand upon in the future.

7.1 Overview of the Genetic Algorithm

There are many excellent references on genetic algorithms in the literature [85, 86], so only a brief overview will be presented here. A genetic algorithm operates on a series of designs, in this case zone plates, collectively called the *population*. Initially, the population can be either random, seeded with specific designs, or some combination of both. Each zone plate is called an *individual*, and the information defining the profile of each individual is encoded in a *chromosome*. Each individual is given a *fitness* score based on its focusing performance. The genetic algorithm then uses a natural selection technique to generate a new population:

To create each member of the new *generation*, two members (called *parents*) are chosen from the previous generation and a *crossover* operation is performed, combining the information in the chromosome of each parent to form a new individual. The two parents that are used to generate each new individual are chosen statistically so that the designs with the highest fitness are more likely to contribute to the new generation. Random *mutations*, or changes in small portions of the chromosome, are applied to the new population, and the fitness of each individual in the new population is calculated. By repeatedly applying this concept, the strongest traits are passed on from one generation to the next, and the fitness of each progressive generation should improve. After a specific number of iterations or after a certain performance goal has been satisfied, the process is terminated. This technique has been successfully applied to many problems in the field of electromagnetics [86].

7.2 Formulation of the Optimization Problem

The genetic algorithm is a powerful tool, but in order to generate meaningful results, the problem must be properly formulated. In this section, the details of optimizing a zone plate with a genetic algorithm will be presented.

To ensure that the outcome of the GA optimization remains relevant to the work presented in this document, a few restrictions will be applied to the optimization process. The 'zoning concept' will be maintained, meaning that any design developed by the optimization routine will be comprised of rotationally symmetric regions over which the profile is continuous. Discontinuous jumps will be allowed at the boundaries of these regions (like at the boundaries of each zone in a traditional zone plate). The restriction to rotationally symmetric devices allows the BOR-FDTD method to be used.

Based on the desired application and size of the zone plate, the focal length F, the maximum overall thickness T, the base thickness t, and the diameter D of the zone plate are specified. There are then two ways that the optimization can be performed. The genetic algorithm can modify these parameters directly, and the traditional design equations can then be used to generate the profile. Alternatively, these parameters can be fixed and the profile of the zone plate can be adjusted to optimize the performance. The latter method

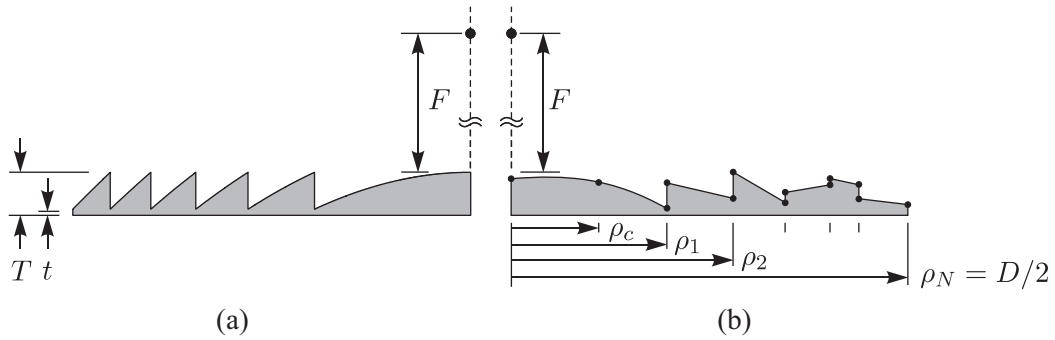

Figure 7.1: Schematic diagram of the geometry of (a) a traditionally-designed zone plate and (b) an example of a zone plate evaluated by the genetic algorithm.

results in a zone plate that does not conform to the traditional design equations. This is the approach taken in this work.

To use this approach, the profile of the zone plate must be described in a slightly different manner than the profiles of the zone plates in Chapters 4 and 5. Instead of dividing each zone into a number of subzones, each zone is represented by a mathematically defined curve. For the first zone (the central zone), this curve is a cubic spline with one control point and two end points. The remainder of the zones are represented by straight line segments. This method keeps the zoning concept intact, but drastically simplifies the number of parameters that are needed to represent the profile (and therefore the number of parameters to be optimized). Because of the way that the spline for the first zone is described, the control point can be chosen such that the thickness exceeds that maximum specified thickness T or is less than the base thickness t. In these cases, any part of the profile thicker than T or thinner than t is truncated to these respective limits. The number of zones N is also specified. In the optimization studies in this work, N is set to be slightly greater than it would be for a traditionally-designed zone plate with the same focal length F and diameter D. This was done to give the GA more free parameters to work with. The GA is free to remove these extra zones by setting their widths to be zero.

This method of describing a zone plate can be understood by looking at an example. A schematic diagram of a traditionally-designed zone plate is in Fig. 7.1(a), and a profile of a zone plate represented using the new method is in Fig. 7.1(b). Each of the solid

dots in Fig. 7.1(b) represents the thickness of the profile at a certain point, and each of the lines below the zone plate represents the distance from the center of the zone plate at which these thicknesses occur. Notice that every radius from ρ_1 to ρ_N is associated with two thicknesses, which are connected with a vertical line. Together, these thicknesses and distances completely describe the curves that make up the zone plate profile (notice that there is a control point in the first zone to describe the spline). Each of these parameters is represented by a binary number, and these binary numbers are concatenated to form the chromosome (a binary string) that represents the profile of the zone plate.

The optimization was performed using a combination of the *Genetic Algorithm and Direct Search Toolbox* in MATLAB[1] and custom BOR-FDTD modeling software (discussed in Chapter 2). MATLAB was used to generate the initial population and to perform the crossover and mutation functions. To determine the fitness of each member of the population, MATLAB called the BOR-FDTD routine on a parallel cluster of computers and processed its output. The actual fitness function depends on the specific application of the zone plate and therefore will be discussed separately in the following sections. The drawback of using a FDTD simulator is that it takes a relatively long time to determine the fitness of each generation. Even on a parallel cluster of computers, some of the studies presented in this work required up to 15 minutes to evaluate the fitness of a single generation. This limited the size of the population to 40 individuals and the number of generations per optimization to 500.

At the completion of an optimization, a hill-climbing algorithm can optionally be used to make minor adjustments to the best individual. The hill-climbing algorithm sequentially changes each bit of the chromosome and re-evaluates the fitness; if the fitness improves, the chromosome is permanently changed. The next bit is then flipped and the process is continued until each bit has been tested. If a change is made to any bit, the entire process is repeated until each individual bit of the chromosome can be flipped without improving the design. For convenience, the entire process from the generation of the initial population to the optional hill-climbing of the best individual will be referred to as an *optimization run*

[1]Copyright The MathWorks, Inc.

for the remainder of this document.

7.3 Optimization of a Zone Plate for Antenna Applications

A genetic algorithm optimization was performed for a grooved-dielectric, phase-correcting zone plate designed for use in antenna applications. A detailed description of zone plates for this application is given in Chapter 4. A traditionally-designed zone plate similar to that shown in Fig. 4.1(b) was used as the starting point for the optimization study. The zone plate has a focal length of $F/\lambda = 30$, a diameter of $D/\lambda = 39.8$, a base thickness of $t/\lambda = 0.1$, a total thickness of $T/\lambda = 1.8$, and is made from Rexolite ($\epsilon_r = 2.53$). The zone plate in Fig. 4.1(b) has $N = 6$ zones, but the profile for the optimized zone plate was allowed to have up to $N = 8$ zones.

The fitness function used for this optimization is the focusing gain FG. Recall from Eq. (3.1) that FG is the ratio of the magnitude of the axial component of the time-average Poynting vector at the focal point to the magnitude of the axial component of the time-average Poynting vector for the incident plane wave:

$$FG = \frac{\left|\mathrm{Re}[\hat{z} \cdot \vec{S}_c^{\mathrm{scat}}]\right|}{\left|\mathrm{Re}[\hat{z} \cdot \vec{S}_c^{i}]\right|}. \tag{7.1}$$

Five different optimization runs were completed (40 individual per generation for 500 generations). Each run started with a different initial population. Three of these initial populations were randomly generated, while two were seeded with a particular zone plate design and some randomly mutated variations of this design. The design used to seed the initial populations was the optimized design for focused-beam applications, which will be discussed in detail in Sec. 7.4. The fitness value of the best member of the population for each generation is plotted in Fig. 7.2 for all five runs. The solid dots at the end of the lines for runs 4 (black line) and 5 (magenta line) are the fitness values after completing the hill-climbing procedure on these two designs. Notice that the hill-climb results in only a small improvement in the focusing gain. The dashed black lines in the figure show the focusing gain of a reference design (a traditional design identical to that in Fig. 4.1(b), but with $P \to \infty$ instead of $P = 4$) and of the hyperbolic lens shown in Fig. 4.1(a). The

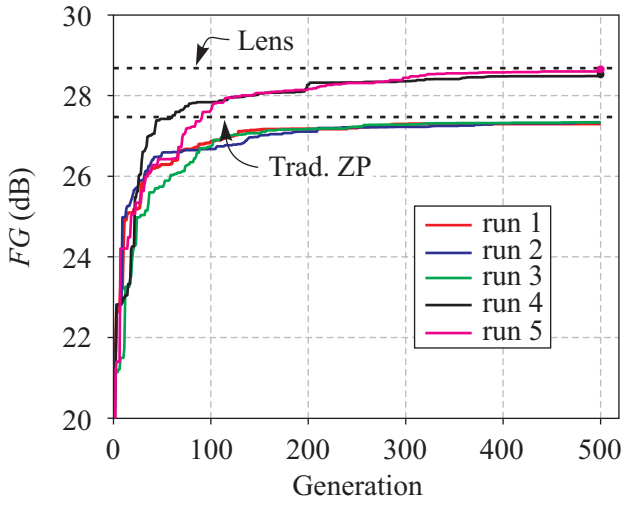

Figure 7.2: The fitness value FG (in dB) for the best member of the population in each generation. The optimization is for a zone plate for antenna applications.

figure shows that the randomly seeded optimizations, runs 1-3 (red, blue, and green lines), resulted in designs that do not perform as well as the traditionally-designed zone plate. The optimizations with initial populations that were seeded, runs 4 (black line) and 5 (magenta line), however, resulted in designs that outperformed this zone plate. This figure shows the value of seeding the population: A good solution can be found more quickly, which is important because the size of the initial population and the number of generations is restricted by the computational requirements of the fitness function.

The best individual (the design from run 4 after the hill-climbing operation) will be examined in more detail in the remainder of this section and will be referred to as the *GA winner*. The GA winner is compared with the traditionally-designed zone plate and the hyperbolic lens in Fig. 7.3. In this figure, the magnitude of the z-component of the time-average Poynting vector $\left|\hat{z} \cdot \langle \vec{S}(t) \rangle\right|$ is plotted in dB for the lens, the traditionally-designed zone plate, and the GA winner for the design frequency of the zone plate, $f = 10\,\text{GHz}$. The profiles of these devices are outlined in black in the figure, and the long dashed white lines indicate the desired location for the focal point, F. A few interesting observations can be made from this figure. It is clear that both zone plates (Figs. 7.3(b) and (c)) focus power to the focal point. It appears, however, that both suffer from slight focal length shortening, meaning that the point of maximum focusing gain is closer to the zone plate

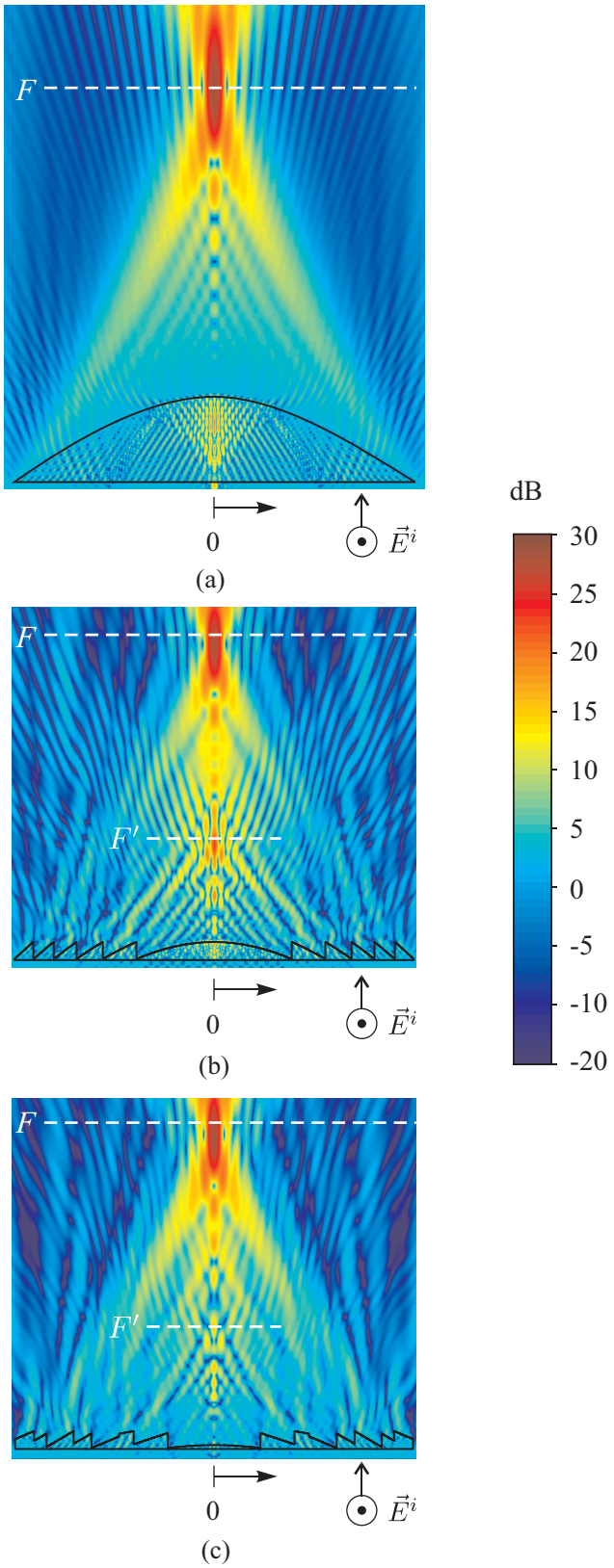

Figure 7.3: $\left|\hat{z} \cdot \langle \vec{S}(t) \rangle\right|$ in dB for $f = 10\,\text{GHz}$ on a cross section in the yz-plane for (a) the lens, (b) the traditionally-designed zone plate, and (c) the GA winner designed for antenna applications.

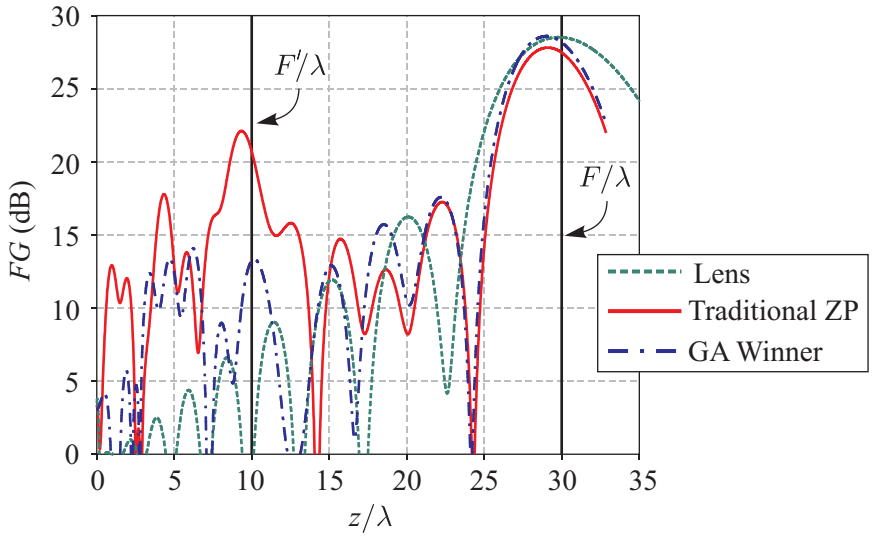

Figure 7.4: Focusing gain FG along the z-axis for the lens, the traditionally-designed zone plate, and the GA winner.

than it is designed to be. This point will be further examined later in this section. Notice also that the profile for the GA winner looks somewhat similar to a traditionally-designed zone plate. One of the most obvious differences is in the first (center) zone, which has been made smaller in the radial direction and consequently thinner. This effectively changes the amount of phase shift imparted at the center of the zone plate. This is sometimes called the 'reference phase' of the zone plate, and it is a design parameter that has received some attention for Soret zone plates in the literature [87]. Another interesting observation can be made about the behavior of the zone plates at the distance $F' = F/3$. This distance is marked by the short dashed white line in Figs. 7.3(b) and (c). For the traditionally-designed zone plate, there is an area in which the Poynting vector has a high intensity located at this point (colored red in the figure). This is the secondary focal point of the zone plate that is well-documented in the literature [67]. Interestingly, this feature is much smaller for the optimized design.

Additional insight into these designs can be gained by looking at the distribution of power along the z-axis. In Fig. 7.4, the focusing gain FG is plotted for each point along this axis when $f = 10\,\text{GHz}$. In this figure, $z = 0$ is located at the output plane of the zone plate or the lens. The focal length shortening for the traditionally-designed zone plate is

apparent in this figure. It is interesting to note that a similar focal length shortening exists for the GA winner. This indicates that, as expected, this design is probably not the best design possible. While the maximum value of the z-component of the Poynting vector is greater for the GA winner than it is for the lens, the focal length shortening means that the lens still has a greater focusing gain FG at $F/\lambda = 30$. The great reduction in the amplitude at the secondary focal point at F' is clearly visible in Fig. 7.4. It is possible that this is one of that factors that allows the GA winner to have a focusing gain that is greater than the traditionally-designed zone plate.

Figures 7.2-7.4 show that the genetic algorithm successfully improved the design of the zone plate, although the improvement in focusing gain was small ($FG = 28.6\,\mathrm{dB}$ for the GA winner versus $FG = 27.8\,\mathrm{dB}$ for the traditional zone plate). The significance of this improvement depends on the particular system for which the antenna is designed.

7.4 Optimization of a Zone Plate for Application to a Focused-Beam System

A genetic algorithm optimization was also performed for a zone plate designed to replace a doubly-hyperbolic lens in a focused-beam system. A detailed description of zone plates for this application is given in Chapter 5. The starting point for the optimization is the zone plate that was manufactured for the experimental study in Chapter 6. Based on this zone plate, in the optimization study the maximum total thickness is restricted to $T = 6.35\,\mathrm{cm}$ and the base thickness is set to $t = 1.27\,\mathrm{cm}$. The diameter is $D = 59.7\,\mathrm{cm}$ and the design frequency is $f = 10\,\mathrm{GHz}$. The traditionally-designed zone plate has $N = 5$ zones, while the profile for the optimization was allowed to have up to $N = 8$ zones.

The fitness function for this zone plate is based on the amount of power intercepted by a disc of radius ρ_d on the focal plane. Using the definition of P_{rec} from Eq. (5.5), the fitness function is

$$F_{\mathrm{fit}} = \frac{P_{\mathrm{rec}}}{P_{\mathrm{inj}}} = \frac{1}{P_{\mathrm{inj}}} \int_0^{\rho_{\mathrm{fit}}} \int_0^{2\pi} \hat{z} \cdot \mathrm{Re}(\vec{S}_c) \rho \, \mathrm{d}\phi \, \mathrm{d}\rho \,, \tag{7.2}$$

in which P_{inj} is the injected power (the total time-average power supplied by the horn). Examining Fig. 5.5, most of the power focused by the lens is concentrated into a disc

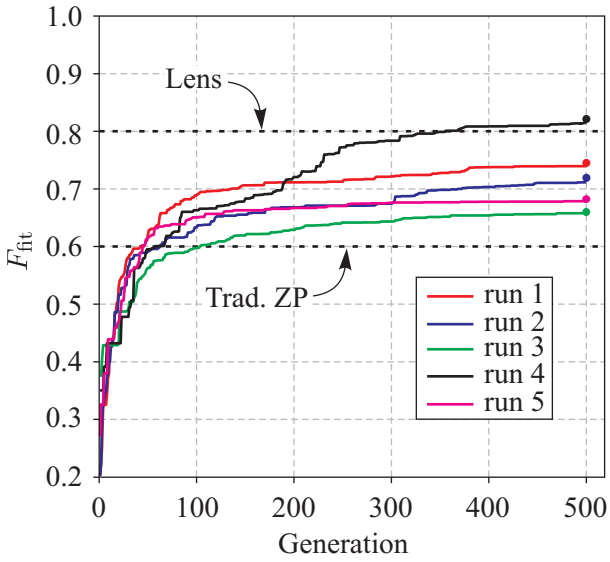

Figure 7.5: The fitness value F_{fit} for the best member of the population in each generation. The optimization is for a zone plate for focused-beam applications.

with radius $\rho_d = 6.35\,\text{cm}$, and therefore the radius chosen for the calculation of the fitness function is $\rho_{\text{fit}} = 6.35\,\text{cm}$.

As was the case in Sec. 7.3, five optimization runs were performed, each with a different initial population. In this case, however, the initial population was random for all five runs. The fitness value of the best member of the population for each generation is plotted in Fig. 7.5 for all five runs. The solid dot at the end of each of the lines is the fitness value after completing the hill-climbing procedure. As in Fig. 7.2, this procedure did not make a significant improvement to any of the designs. The black dashed lines represent the fitness of the traditionally-designed zone plate and the lens. The figure shows that all five of the optimization runs resulted in designs that outperform the traditionally-designed zone plate. One of the simulation runs (run 4, black line) produced a zone plate that outperforms the lens. The best individual from each generation (marked by the dots in Fig. 7.5) and randomly mutated copies of these individuals were used to generate a new population. An optimization run using this initial population failed to produce a result that was better then the result of run 4. The design from run 4 will be examined in more detail and will be again be referred to as the GA winner.

To study the focusing of this design, $\left|\hat{z}\cdot\langle\vec{S}(t)\rangle\right|$ is plotted in Fig. 7.6 for the lens, the

traditionally-designed zone plate, and the GA winner for the design frequency of the zone plate, $f = 10\,\text{GHz}$. In this figure, the dashed white line indicates the location of the focal plane of the lens, and it is the same distance from the output plane of all three devices ($z = 55\,\text{cm}$). The profiles of the respective devices are outlined in black. The focusing by the GA winner clearly behaves like the lens and the zone plate. The amplitude at the focal point is slightly higher and the sidelobes on the focal plane are slightly lower than the traditionally-designed zone plate. Notice that the profile for the GA winner looks distinctly different than the profile for the traditionally-designed zone plate, a fact that will be examined in more detail later in this section. First, however, the performance of this design will be evaluated in a more quantitative way.

In Fig. 7.7, $P_{\text{rec}}/P_{\text{inj}}$ is plotted as a function of ρ_d for the lens and both zone plates at $f = 10\,\text{GHz}$. The vertical black line indicates the radius ρ_{fit} used in the calculation of the fitness function. At this point, both the lens (dashed green line) and GA winner (dash-dot blue line) deliver more than 80% of the incident power to a disc of radius ρ_{fit} compared to only approximately 60% of the incident power for the traditionally-designed zone plate. The genetic algorithm has designed a zone plate that performs as well as the doubly-hyperbolic lens for this particular metric at the frequency $f = 10\,\text{GHz}$. It is important to note, however, that the GA winner suffers from one of the same problems as the traditionally-designed zone plate: As ρ_d is increased beyond $\rho_d \approx 30\,\text{cm}$, there is an increase in the received power. As was explained in the discussion of Fig. 5.5, this increase is due to power directed into diffraction bands. Recall from Sec. 5.4 that these diffraction bands can introduce errors in the measurements of electromagnetic properties by the focused-beam system if the edge of a sample lies within with a diffraction band.

Based on the power delivered to the focal plane, the zone plate designed by the GA appears to be a promising candidate to replace the lenses in a focused-beam system. An important question remains, however: Does the improvement in $P_{\text{rec}}/P_{\text{inj}}$ come at the expense of the other focusing characteristics of the zone plate? In particular, the amplitude taper, phase uniformity, and bandwidth must be similar to the traditionally-designed zone plate to ensure that the new zone plate can achieve results similar to those presented in

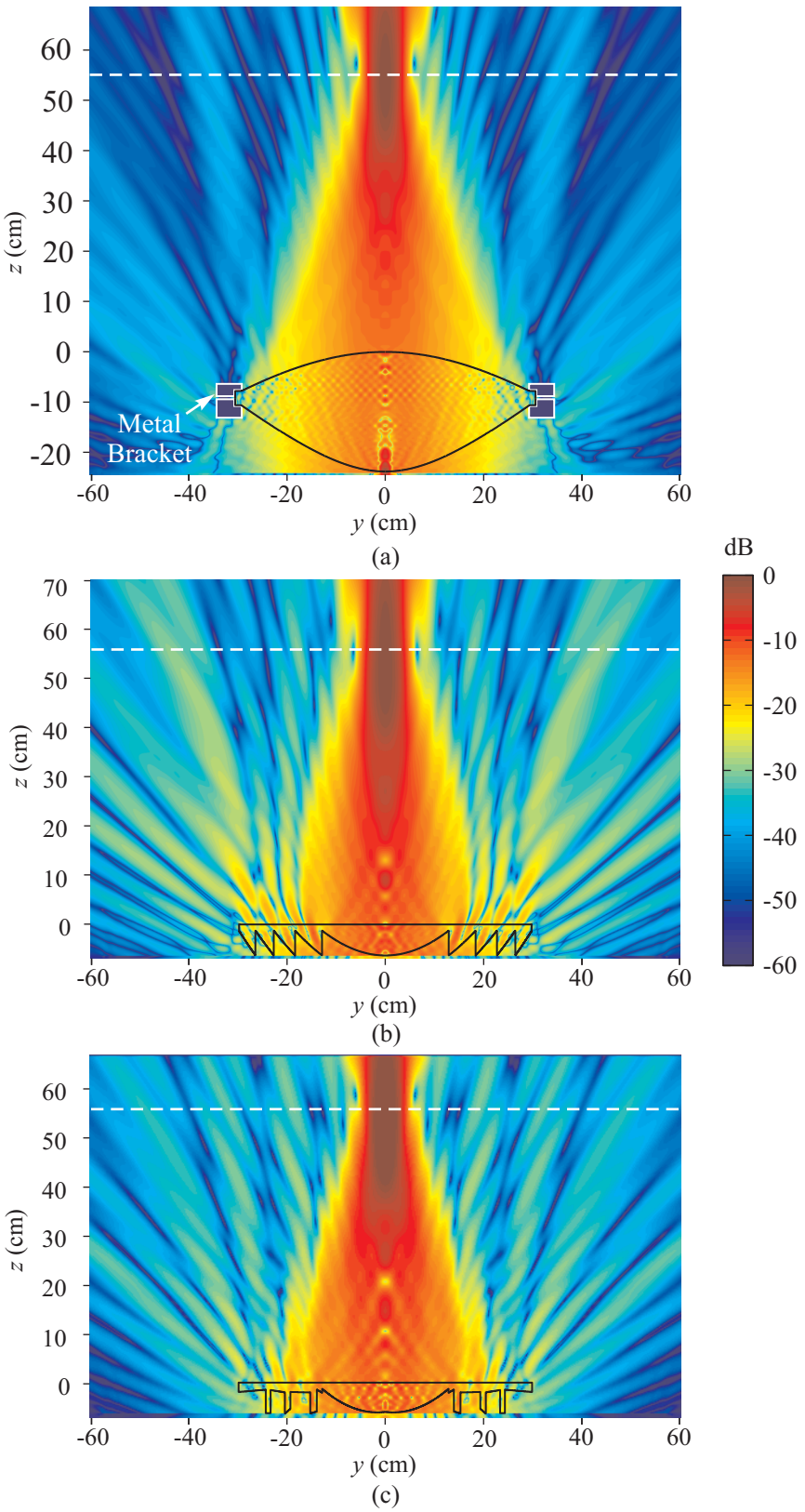

Figure 7.6: $\left|\hat{z} \cdot \langle \vec{S}(t) \rangle\right|$ in dB for $f = 10\,\text{GHz}$ on a cross section in the yz-plane for (a) the lens, (b) the traditionally-designed zone plate, and (c) the GA winner designed for focused-beam applications.

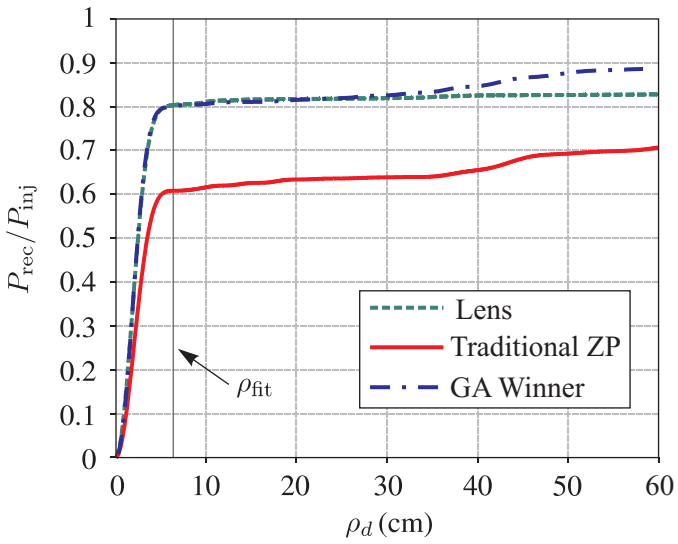

Figure 7.7: Fraction of the power supplied by the horn that passes through a disc of radius ρ_d in the focal plane for the lens, the traditionally-designed zone plate, and the GA winner (all at $f = 10\,\mathrm{GHz}$).

Chapter 6 when it is used in a focused-beam system. These characteristics can be compared with the traditionally-designed zone plate by examining the -10 dB spot size and the phase deviation over this spot. The radius of the -10 dB spot in Fig. 7.8(a) is indicative of the amplitude taper of the field focused by the zone plate. The radius looks similar for both zone plates at all three frequencies. The phase deviation, plotted in Fig. 7.8(b) looks somewhat similar as well, but the locations of the points of minimum phase deviation are different for all three frequencies. When $f = 10\,\mathrm{GHz}$, the location of minimum phase deviation for the GA winner is located closer to the dashed black line, which marks the focal length of the double-hyperbolic lens, than it is for the traditionally-designed zone plate. This illustrates the ability of the genetic algorithm to optimize the focal length of a zone plate to improve its performance.

Unlike the zone plate that was designed for antenna applications in Sec. 7.3, the design produced by the GA for this application and shown in Fig. 7.6(c) does not look like a traditional zone plate. The first (center) zone is similar to the traditionally-designed zone plate. Beyond this first zone, however, the GA winner has a series of three narrow ridges of dielectric, extending approximately from the base to the maximum thickness. Typically, zone plates are designed based on refractive principles (ray-tracing), but the ridges in this

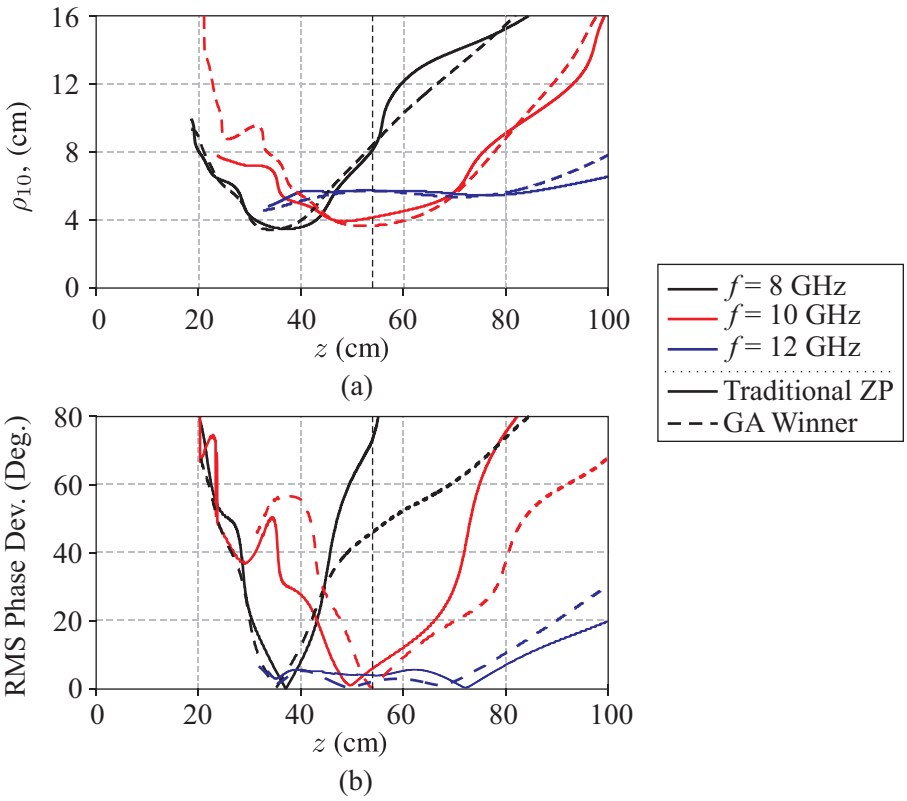

Figure 7.8: (a) Radius of the -10 dB spot ρ_{10} and (b) deviation in phase over the -10 dB spot for the traditionally-designed zone plate and the GA winner when f = 8, 10, and 12 GHz.

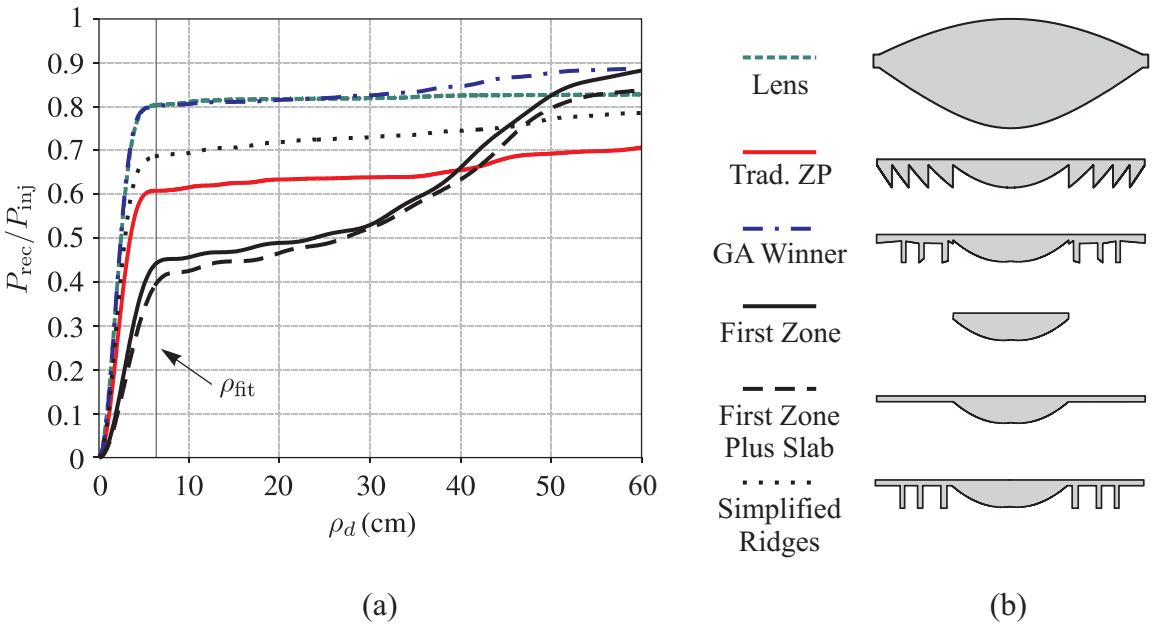

Figure 7.9: (a) $P_{\text{rec}}/P_{\text{inj}}$ for the lens, the traditionally-designed zone plate, the GA winner, and variants of the GA winner, all at $f = 10\,\text{GHz}$. (b) The profile of each of the devices for which $P_{\text{rec}}/P_{\text{inj}}$ is shown.

design produced by the GA appear to be strictly diffractive elements. It is worth noting that the GA winner achieves an even greater weight savings compared to the lens than the traditionally-designed zone plate, despite the minimization of the weight not having been factored into the optimization. The weight of the GA winner is only 22% of the weight of the lens which is 72% of the weight of the traditionally-designed zone plate.

Because the GA winner looks significantly different than the traditionally-designed zone plate, a series of simulations was run to examine the major characteristics of this design. The results of this study are presented in Fig. 7.9(a), which shows $P_{\text{rec}}/P_{\text{inj}}$ as a function of ρ_d for the lens, the traditionally-designed zone plate, and several variations of the GA winner. The profile of the device corresponding to each line in Fig. 7.9(a) is shown in Fig. 7.9(b). $P_{\text{rec}}/P_{\text{inj}}$ for the lens (dashed green line), the traditionally-designed zone plate (solid red line), and the GA winner (dash-dot blue line) were previously shown in Fig. 7.7, and are repeated here for the purpose of comparison. The value of $P_{\text{rec}}/P_{\text{inj}}$ for a zone plate consisting only of the first zone of the GA winner (solid black line) shows that while the first zone makes an important contribution to the focusing ability of the zone plate, there

is a significant amount of power focused by the outer zones as well. Adding a flat base of the correct radius to the first zone actually causes a small decrease in the amount of power focused (dashed black line). A profile which is an approximation to the GA winner was also modeled to evaluate the impact of the dielectric ridges. The ridges were modeled as annuli of dielectric, placed at the locations of the ridges for the GA winner, with a height stretching from the base to the maximum allowable thickness. Comparing the plot of $P_{\mathrm{rec}}/P_{\mathrm{inj}}$ for this device (dotted black line) to the plot for the first zone only (solid black line) shows that these ridges are responsible for much of power focused by the new zone plate. In fact, this simplified design outperforms the traditionally-designed zone plate (solid red line). The GA winner (dash-dot blue line) improves on this design further by adjusting the angles at the tops of the ridges and in the regions between the ridges, to reach a performance level that is as good as the lens (dashed green line).

Figures 7.6-7.8 show that the zone plate designed using the genetic algorithm can deliver power to the focal plane in a way that is similar to the lens and that it has better phase deviation characteristics than the traditionally-designed zone plate. These improvements are potentially beneficial for zone plates used in a focused-beam measurement system. However, the same major limitations of the traditionally-designed zone plate are still present for the GA winner. The frequency dependence is similar, and power is still delivered to diffraction bands which can lead to scattering from the edges of a sample, though these bands are smaller in amplitude than for the traditional design (see Fig. 7.6).

7.5 Value of the GA Optimization

Both the zone plate optimized for antenna applications and the zone plate optimized for use in a focused-beam system perform better then their traditionally-designed counterparts. The genetic algorithm is clearly capable of improving the design of a zone plate. This raises an important question: Do the improvements seen warrant the use of this non-traditional design method?

There is no straightforward answer to this question. The value of the improvement is entirely dependent on the application. For the two applications shown in this chapter, the

performance improvements were somewhat incremental in nature. In situations for which a traditionally-designed zone plate cannot meet the design specifications or if some sort of special behavior is desired (e.g. multiple focal points or multiple frequencies of operation), a non-traditional design method might be worthwhile.

One consideration is the amount of time and computational power required to generate the designs. The design of each of the zone plates described in this chapter using the GA required approximately one week on a parallel cluster of computers, whereas traditional zone plates take only seconds to design on a single computer. If a zone plate is being designed for a particular application and the resources to perform this type of non-traditional design are available, then improved performance can likely be realized.

CHAPTER VIII

CONCLUSIONS

In this research, Fresnel zone plates were studied using an accurate, full-electromagnetic simulator based on the body-of-revolution finite-difference time-domain (BOR-FDTD) method. Simpler methods for analyzing a zone plate were discussed and compared to the BOR-FDTD method. It was shown that the BOR-FDTD method allows a more complete analysis of the focusing by a zone plate, and that this is particularly important for zone plates with a low focal length to diameter (F/D) ratio. This computational tool was then used to investigate zone plates for two different applications: zone plates for use as antennas in communication systems and zone plates used as focusing elements in a free-space, focused-beam system to measure the electrical properties of materials. Through these applications, many aspects of zone plate focusing were studied in a more in-depth manner than they have been in the past. The conclusions from these studies are applicable for the design of any zone plate.

First, a design study was performed for Soret and folded zone plates for antenna applications. New design graphs were generated that relate the three primary design parameters of these zone plates (the focal length F/λ, the diameter D/λ, and the number of half-wave zones, N_{Soret}) to their focusing gain FG, a metric that is independent of any feed. Additional design graphs were generated for a more physically realistic metric, the gain G for antennas with a particularly sized aperture feed. These design graphs were used to make general statements about the effect of the design parameters on the focusing ability of a zone plate. Both gains (FG and G) increase as F/λ or N_{Soret} is increased while the other parameter is held fixed. As this happens, however, the incremental increase eventually tapers off. If the diameter, D/λ, is held constant and focal length, F/λ, is increased, both metrics initially increase, reach a maximum, and then decrease. The maximum achievable values of FG and G for Soret and folded zone plates are plotted as a function of the diameter of the zone plate.

Results from the BOR-FDTD analysis of the Soret zone plate were also compared with those from frequently used approximate analysis methods. The results from the approximate methods were shown to diverge from those of the BOR-FDTD method as F/D becomes small, which validates the motivation for the use of the full-electromagnetic method in this work.

The design study was repeated for grooved-dielectric, phase-correcting zone plates, also intended for use in antenna applications. These design graphs showed a similar relationship between the parameters and the focusing ability. However, this study also showed that the focal length, the base thickness, the number of phase corrections per zone, and the presence of a matching layer affect the focusing ability in ways that are unexpected, based on the simpler techniques often used to analyze zone plates. The effect of each of these parameters was evaluated individually. For the zone plates studied in the work, the choice of base thickness was found to change the focusing gain by as much as 2 dB because of reflections within the zone plate. A matching layer was added and was not found to be beneficial for reducing the effect of these reflections. An in-depth study showed that there does not appear to be a simple, analytical method for optimizing the base thickness. Additionally, it was shown that increasing the number of phase corrections per zone beyond $P \gtrsim 8$ does not necessarily increase the focusing gain of the zone plate. Finally, the actual focal length of the zone plate was found to consistently be slightly shorter than the desired focal point. This focal length shortening becomes more severe as the ratio F/D is decreased, making it more of a concern for microwave and millimeter-wave zone plates than it is for optical zone plates. To compensate for this effect, the focal length can be intentionally designed to be slightly longer than desired.

Next, zone plates were evaluated for use in free-space, focused-beam systems to measure the electrical properties of materials. One of the major advantages of zone plates for focused-beam systems is the reduction in volume and weight compared to a doubly-hyperbolic lens. These advantages may allow the zone plate to be used in low-frequency systems, for which the lenses are prohibitively large. New design equations were used in conjunction with BOR-FDTD simulations to develop a zone plate to replace the doubly-hyperbolic lenses

that are used in GTRI's standard focused-beam system. In order for the zone plate to be used in the focused-beam system, there are ceratin requirements for the field focused by the zone plate. To determine if the zone plate could satisfy these requirements, both BOR-FDTD simulations and measurements were used to compare the zone plate with the existing lens. The zone plate was fabricated, and measurements of the electric field over a volume surrounding the focal point were compared to measurements taken for the lens. Based on these comparisons, the requirements were addressed individually. The zone plate delivers less power to its focal spot than the lens, but the amplitude taper, phase uniformity, and linearity of the polarization of the field focused by the zone plate were found to be similar to that of the field focused by the lens for the design frequency of the zone plate, $f = 10\,\mathrm{GHz}$. The location of the beam waist for the zone plate, however, was shown to move as a function of frequency.

To complete the evaluation of zone plates in a focused-beam system, a complete system using two zone plates as focusing elements was assembled. Measurements of a dielectric sample over a range of frequencies showed that a zone plate system can produce results that are comparable to a lens system, but that care must exercised in interpreting the results, particularly away from the design frequency. A technique that accounted for the frequency-dependent shift of the focal point was presented and shown to offer the potential to improve results. The calculations and measurements from this research give us confidence that zone plates can be used in a focused-beam measurement system designed to work at low frequencies.

Finally, a topic for future research was presented. The open-ended question was posed: Can the power of the BOR-FDTD method be used to design a better focusing element than the traditional zone plate using roughly the same amount of material? An analysis of one particular design technique was presented. A genetic algorithm was used to optimize grooved-dielectric, phase-correcting zone plates for an antenna application and for application in a focused-beam system. The study showed that the performance of the optimized zone plates for both applications was better than the traditionally-designed zone plates. The optimized zone plate for the antenna application had a profile that looked similar to

a traditionally-designed zone plate. Simulations showed that the focusing gain was higher and the undesirable secondary focal point had been removed. The optimized design for the focused-beam application did not look like a traditional zone plate, but nevertheless was able to match the performance of the doubly-hyperbolic lens in terms of the amount of power delivered to the focal spot when $f = 10\,\mathrm{GHz}$. It is clear that the genetic algorithm can improve the performance of a zone plate, but the value of the improvement can only be judged in light of the particular application of the zone plate.

APPENDIX A

MEASURED AND SIMULATED DATA FOR THE ZONE PLATE AND LENS

This appendix contains the results of the study of the zone plate for the focused-beam system and the lens it was designed to replace. The measurement procedure is described in Chapter 6, and the body-of-revolution finite-difference time-domain method used to simulate the zone plate and lens is described in Chapter 2. Measured and simulated field values are presented for both the zone plate and the lens. The results are presented for three frequencies: $f = 8$, $f = 10$, and $f = 12\,\mathrm{GHz}$.

The following figures are included in this appendix for both the zone plate and the lens at all three frequencies:

- $|E_y|$ along the z-axis.
- $|E_y|$ on the designed focal plane.
- Phase of E_y on the designed focal plane.
- $|E_y|$ on the xz-plane.
- $|E_y|$ on the yz-plane.
- Phase of E_y on the xz-plane.
- Phase of E_y on the yz-plane.
- $|E_y|$ on the xy-plane.
- $|E_x|$ on the xy-plane.
- $|E_z|$ on the xy-plane.
- $|E_z|$ on the yz-plane.

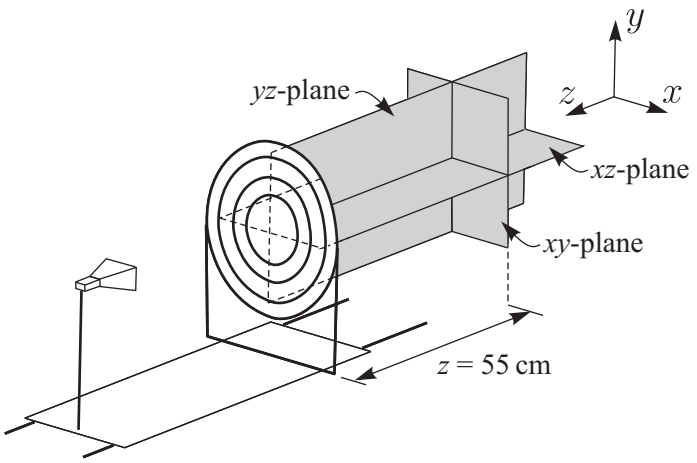

Figure A.1: Schematic diagram of the coordinate system for the measured and simulated field values.

The coordinate system used for the data presented in this Appendix is shown in Fig. A.1. In this figure, the distance from the output plane of the zone plate (or lens) to the xy-plane is $z = 55\,\text{cm}$. This is the focal length of the lens and zone plate when $f = 10\,\text{GHz}$. In the figure captions, this is referred to as the 'designed focal length'. In all of the data presented in this Appendix, the parameter z is the distance from the output plane of the zone plate or lens. Unless specifically noted in a figure caption, the xy-, xz-, and yz-planes shown in Fig. A.1 are those on which the field was measured and simulated.

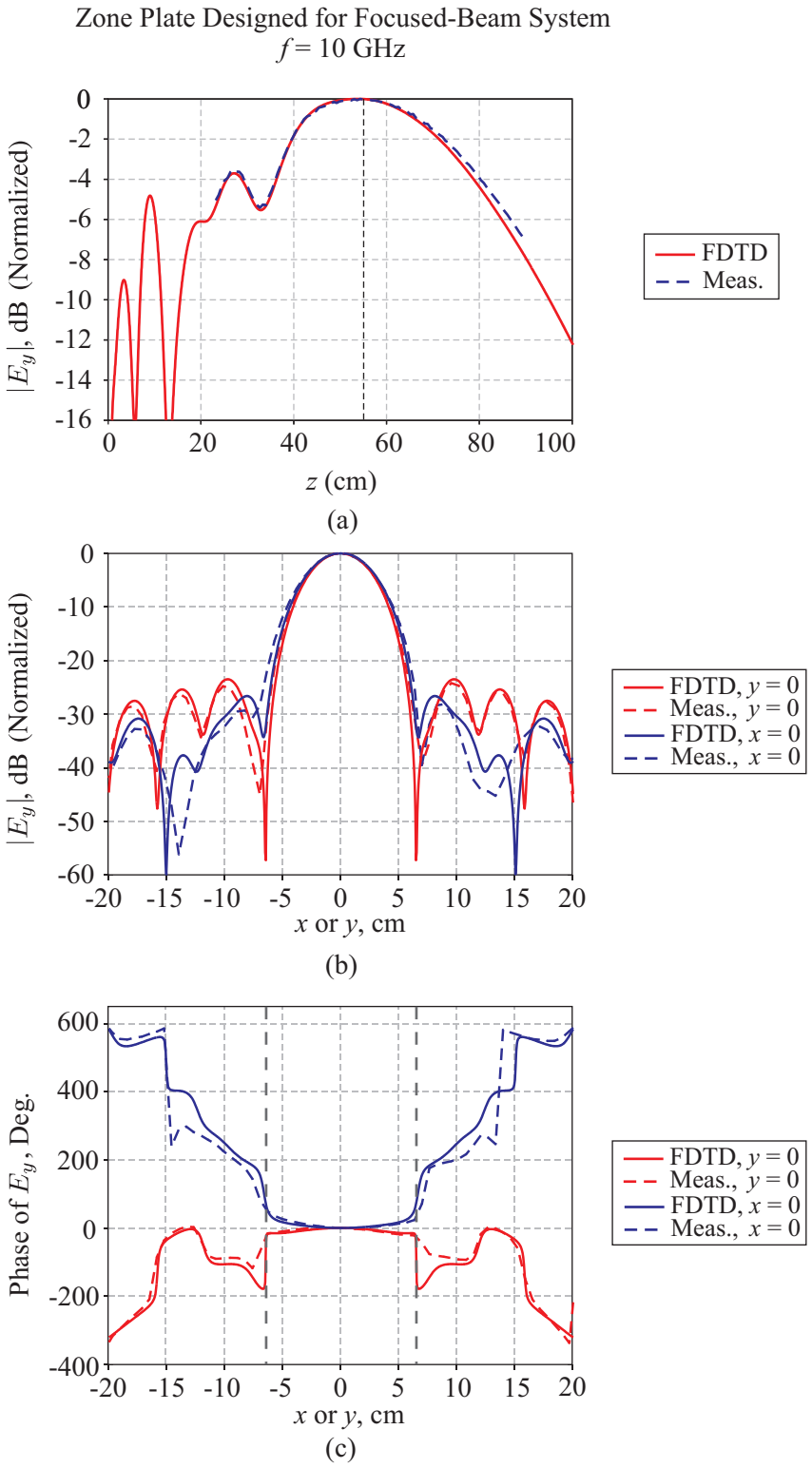

Figure A.2: Measured and simulated (FDTD) results for the electric field E_y of the zone plate when $f = 10\,\text{GHz}$. (a) $|E_y|$ along the z-axis, with $z = 0$ located at the output plane of the zone plate. The dashed back line indicates the designed focal length. (b) Magnitude and (c) phase of E_y on the designed focal plane ($z = 55\,\text{cm}$). The dashed black lines in (c) indicate the extent of the main beam.

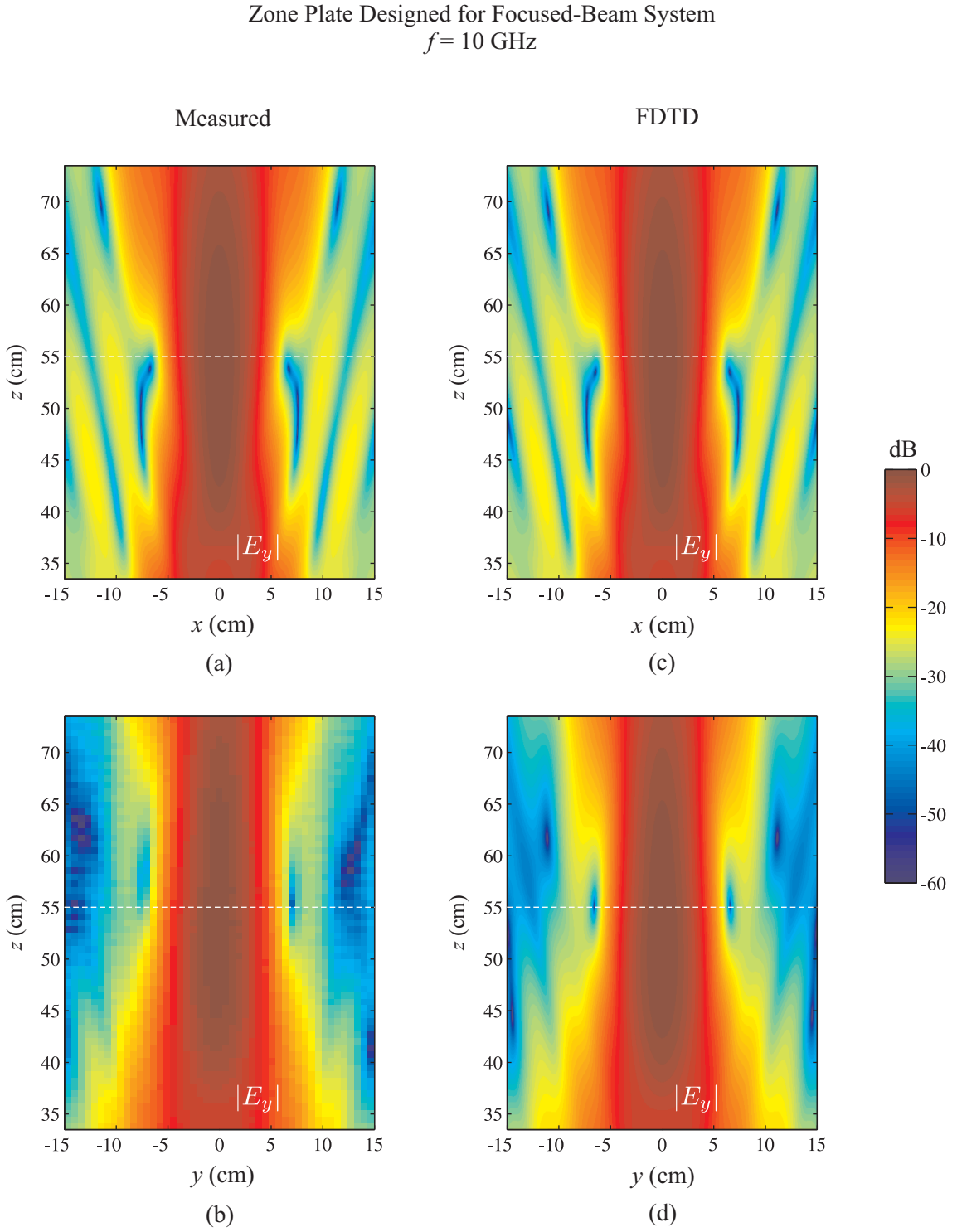

Figure A.3: Magnitude of E_y at $f = 10\,\text{GHz}$ for the zone plate for (a) and (c) a horizontal cut on the xz-plane and (b) and (d) a vertical cut on the yz-plane. Figures (a) and (b) are for measurements and figures (c) and (d) are for FDTD simulations. The dashed white line is the location of the designed focal point.

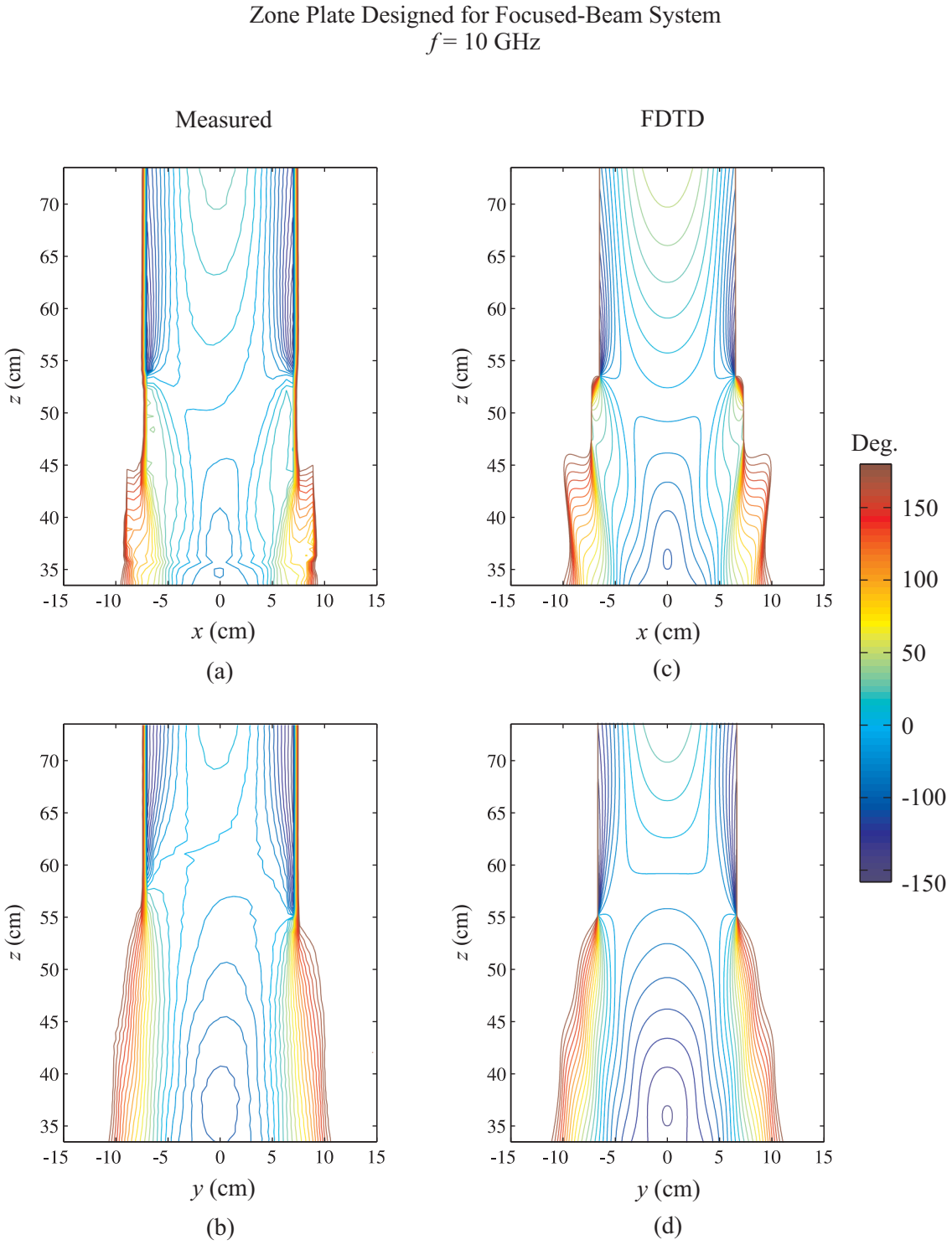

Figure A.4: Phase of E_y at $f = 10\,\text{GHz}$ for the zone plate for (a) and (c) a horizontal cut on the xz-plane and (b) and (d) a vertical cut on the yz-plane. Figures (a) and (b) are for measurements and figures (c) and (d) are for FDTD simulations.

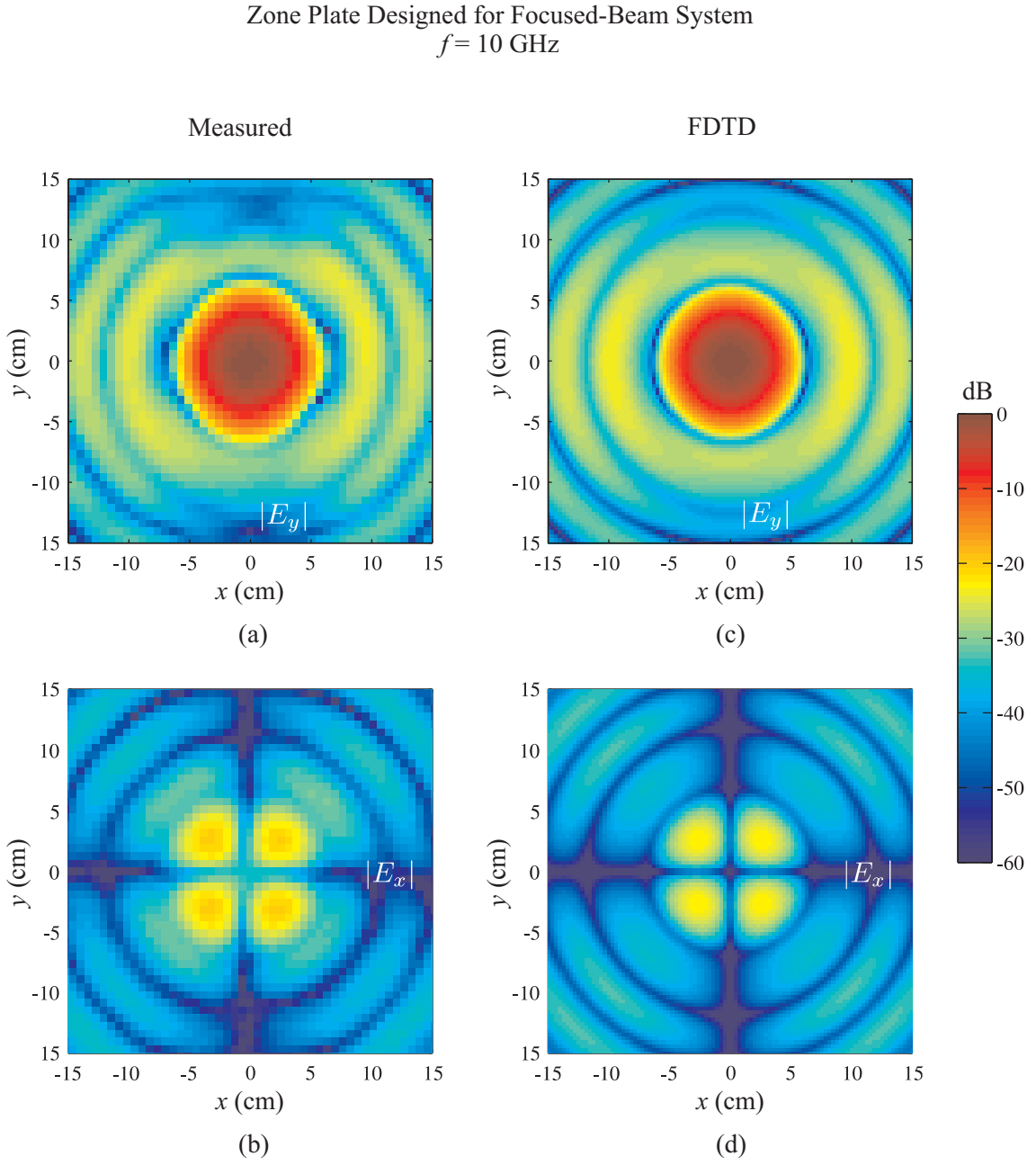

Figure A.5: Magnitude of (a) and (c) E_y and (b) and (d) E_x for a vertical cut (xy-plane) through the designed focal plane of the zone plate when $f = 10\,\text{GHz}$. Figures (a) and (b) are for measurements and figures (c) and (d) are for FDTD simulations.

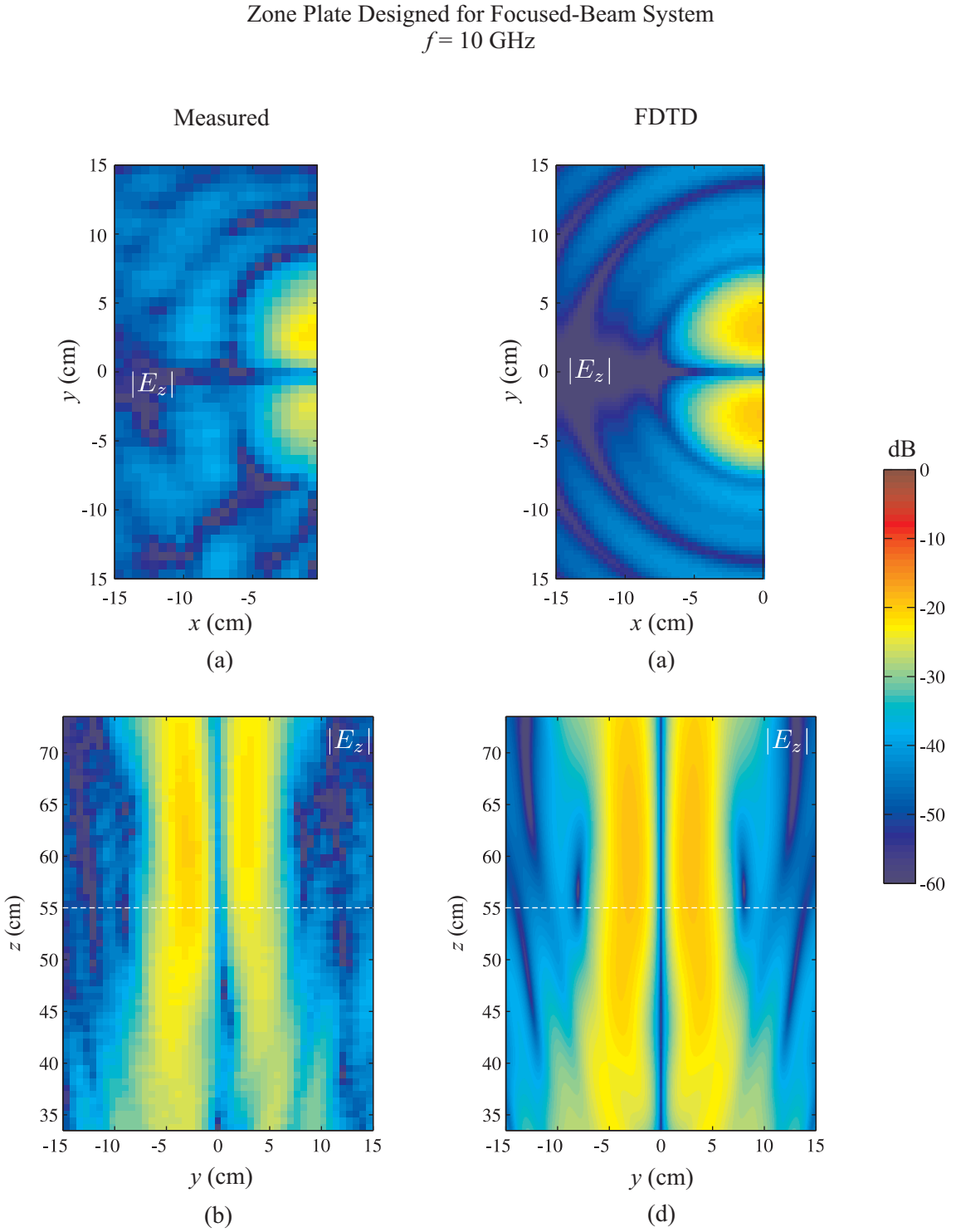

Figure A.6: Magnitude of E_z for (a) and (c) a vertical cut (xy-plane) through the designed focal plane of the zone plate and (b) and (d) a vertical cut (yz-plane) through the plane $x = -0.64\,\text{cm}$ when $f = 10\,\text{GHz}$. Figures (a) and (b) are for measurements and figures (c) and (d) are for FDTD simulations.

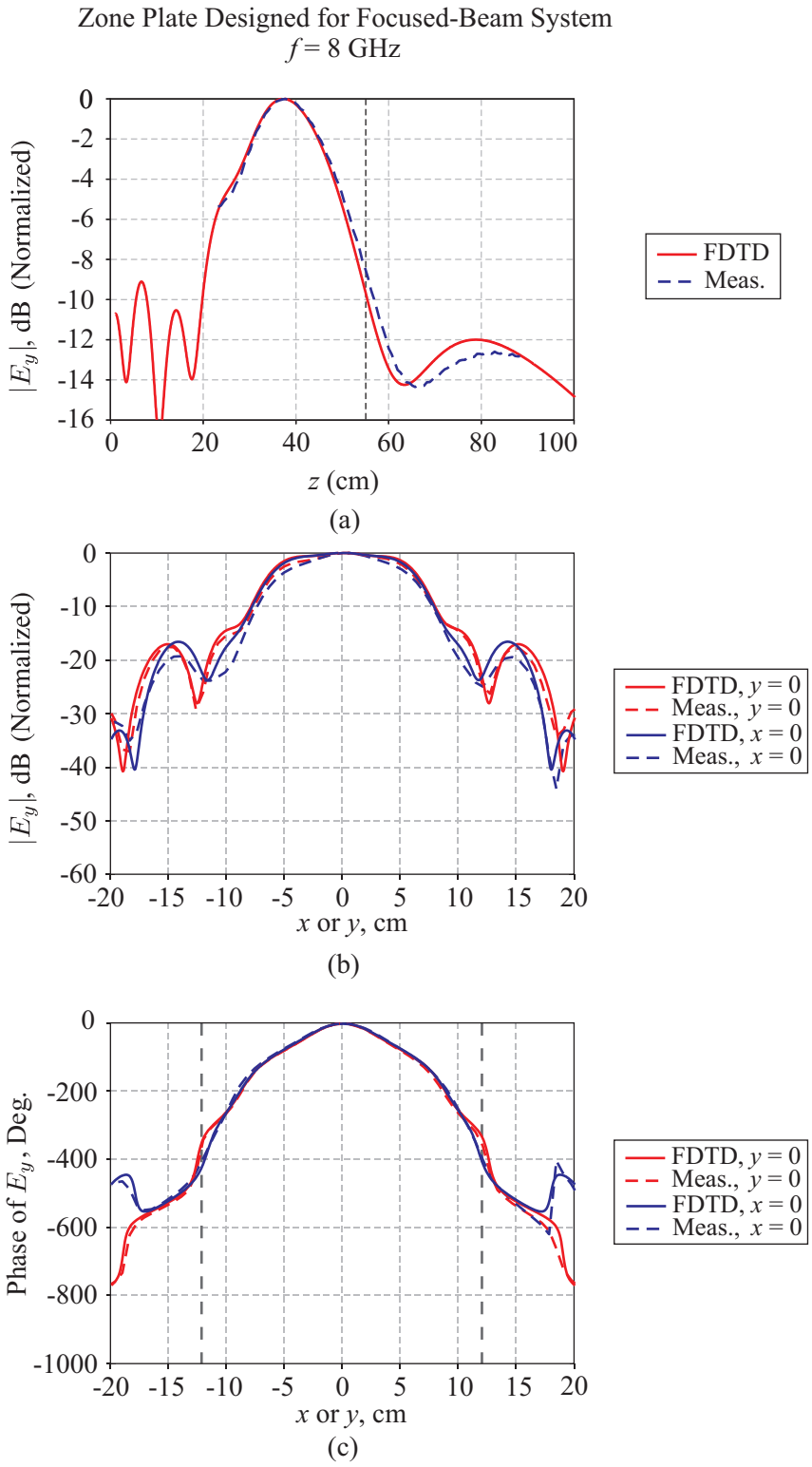

Figure A.7: Measured and simulated (FDTD) results for the electric field E_y of the zone plate when $f = 8\,\text{GHz}$. (a) $|E_y|$ along the z-axis, with $z = 0$ located at the output plane of the zone plate. The dashed back line indicates the designed focal length. (b) Magnitude and (c) phase of E_y on the designed focal plane ($z = 55\,\text{cm}$). The dashed black lines in (c) indicate the extent of the main beam.

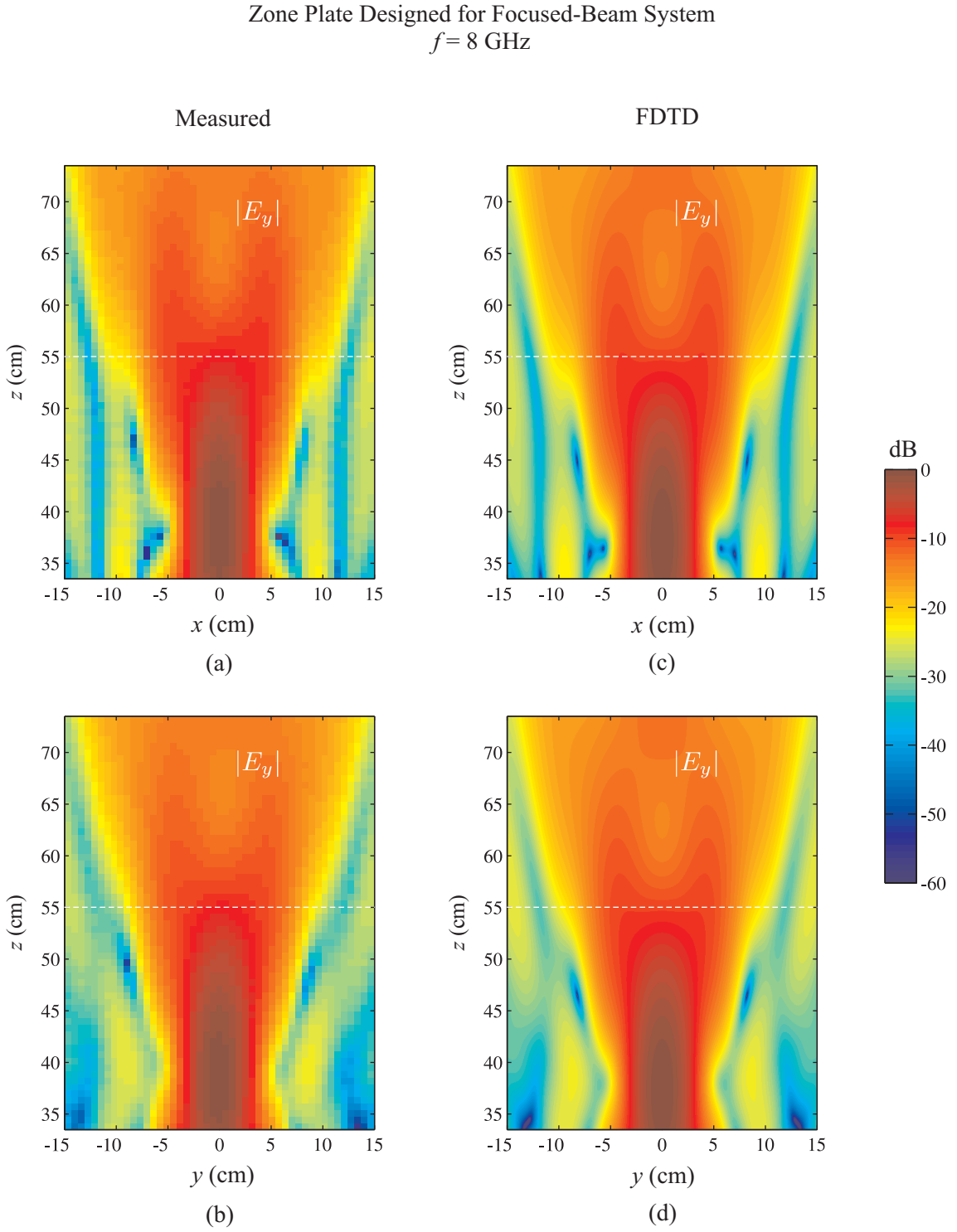

Figure A.8: Magnitude of E_y at $f = 8\,\text{GHz}$ for the zone plate for (a) and (c) a horizontal cut on the xz-plane and (b) and (d) a vertical cut on the yz-plane. Figures (a) and (b) are for measurements and figures (c) and (d) are for FDTD simulations. The dashed white line is the location of the designed focal point.

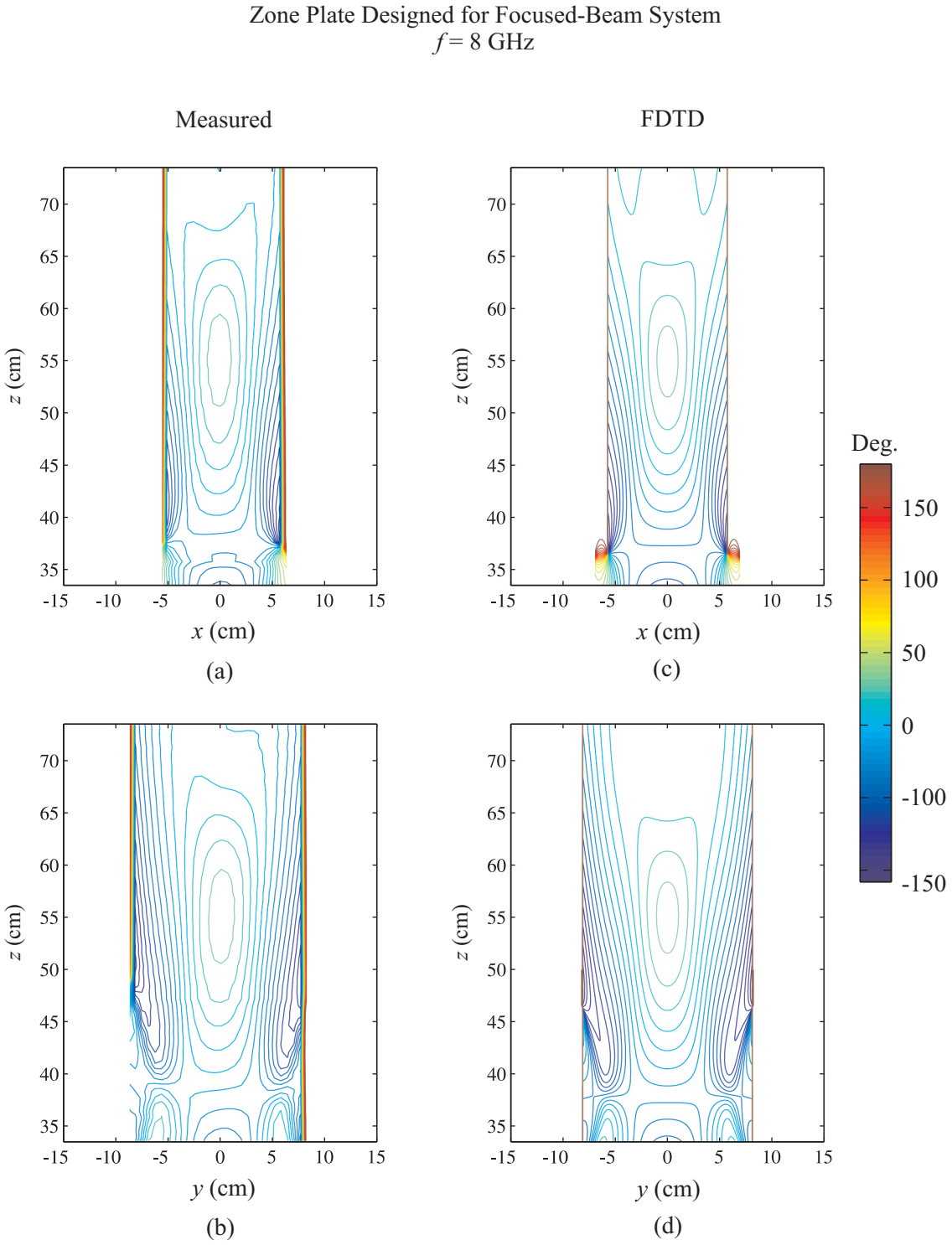

Figure A.9: Phase of E_y at $f = 8\,\text{GHz}$ for the zone plate for (a) and (c) a horizontal cut on the xz-plane and (b) and (d) a vertical cut on the yz-plane. Figures (a) and (b) are for measurements and figures (c) and (d) are for FDTD simulations.

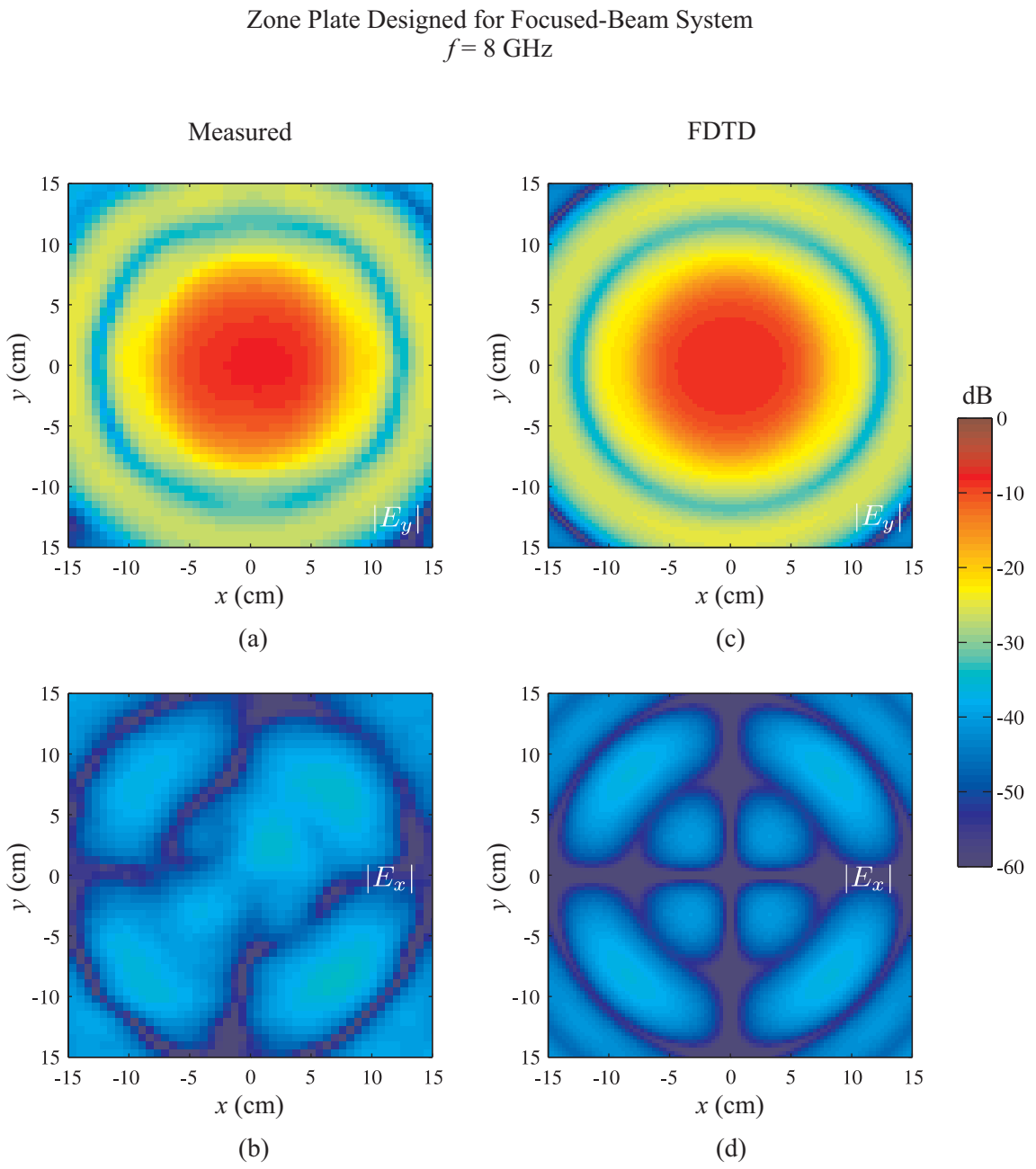

Figure A.10: Magnitude of (a) and (c) E_y and (b) and (d) E_x for a vertical cut (xy-plane) through the designed focal plane of the zone plate when $f = 8\,\text{GHz}$. Figures (a) and (b) are for measurements and figures (c) and (d) are for FDTD simulations.

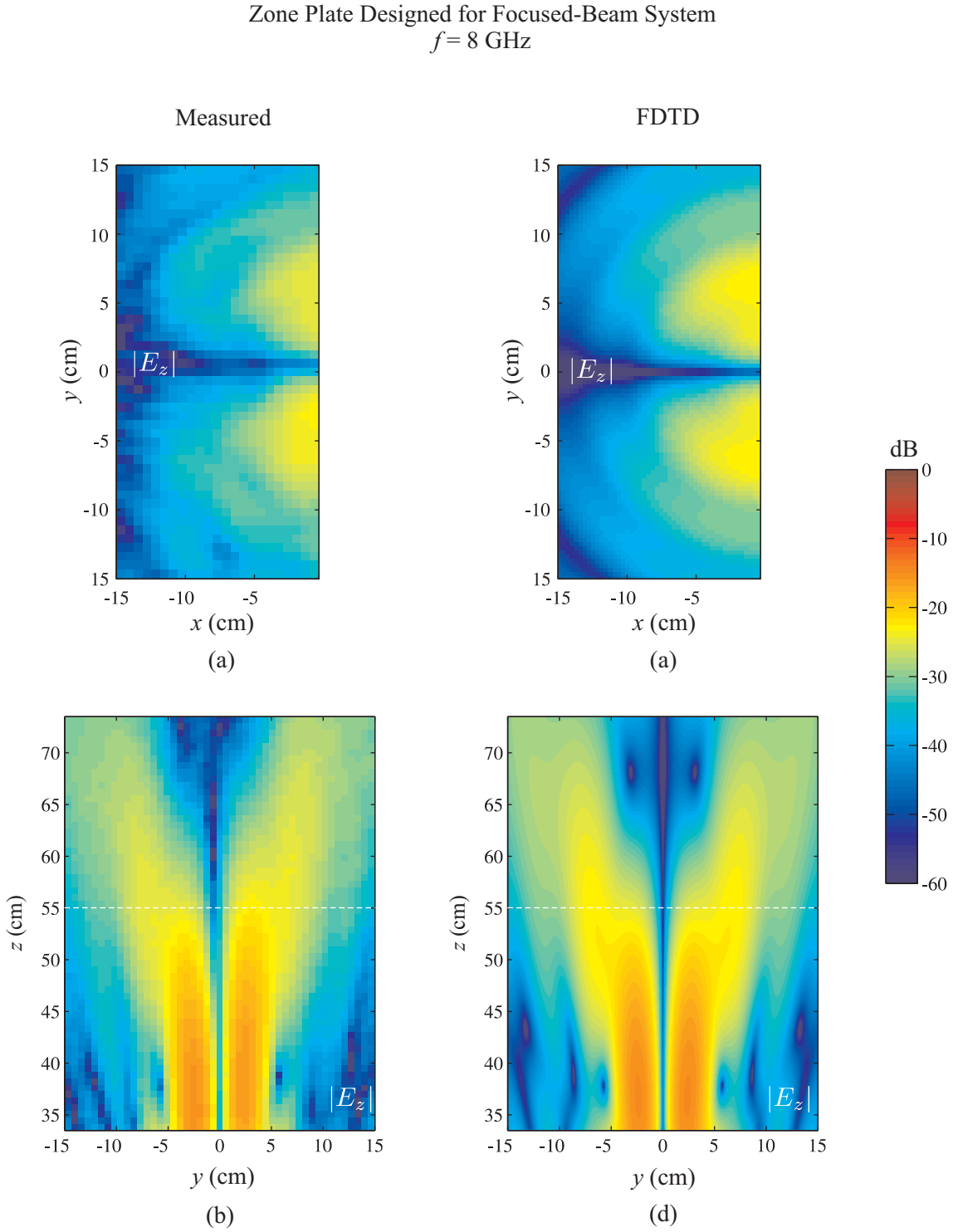

Figure A.11: Magnitude of E_z for (a) and (c) a vertical cut (xy-plane) through the designed focal plane of the zone plate and (b) and (d) a vertical cut (yz-plane) through the plane $x = -0.64\,\text{cm}$ when $f = 8\,\text{GHz}$. Figures (a) and (b) are for measurements and figures (c) and (d) are for FDTD simulations.

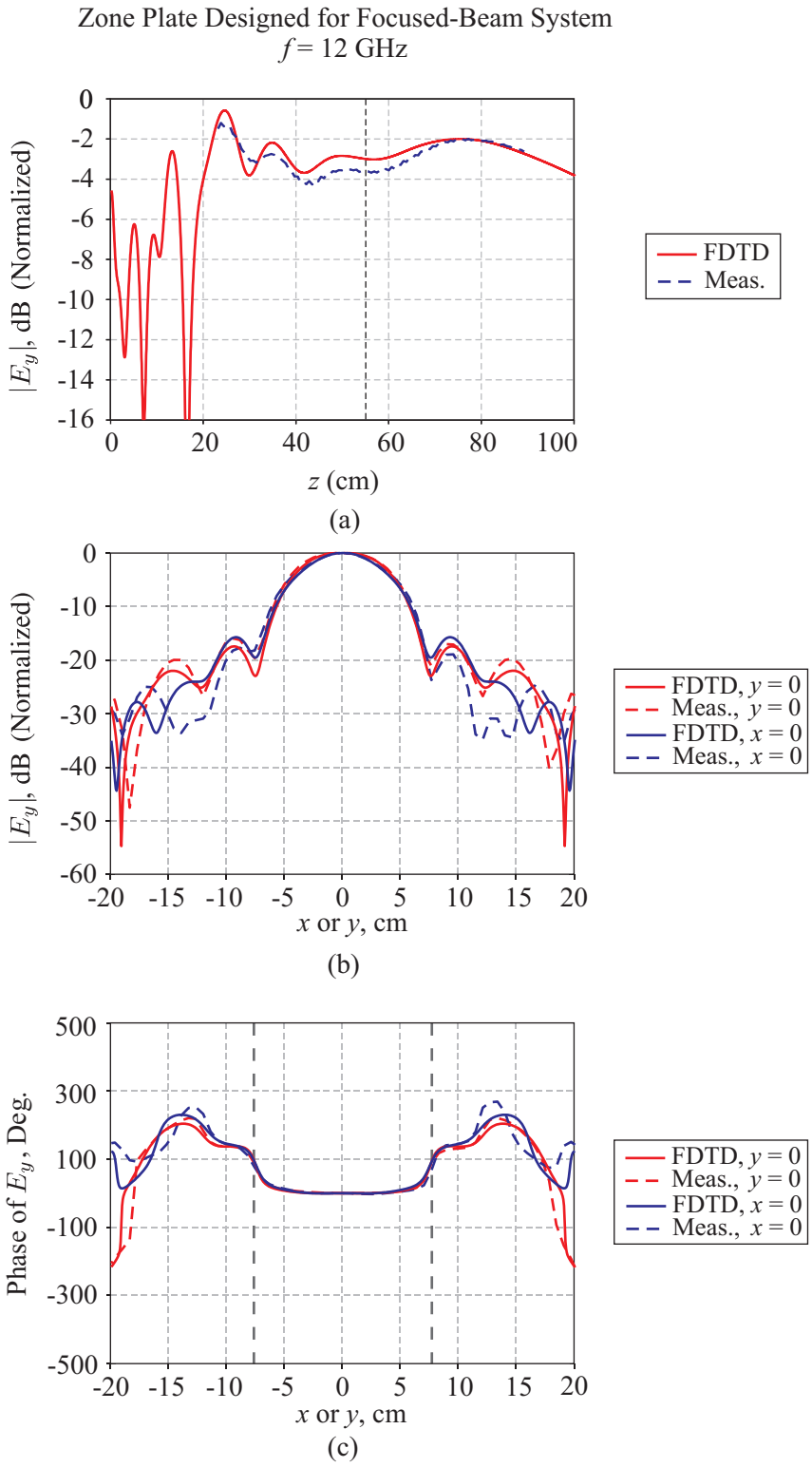

Figure A.12: Measured and simulated (FDTD) results for the electric field E_y of the zone plate when $f = 12\,\text{GHz}$. (a) $|E_y|$ along the z-axis, with $z = 0$ located at the output plane of the zone plate. The dashed back line indicates the designed focal length. (b) Magnitude and (c) phase of E_y on the designed focal plane ($z = 55\,\text{cm}$). The dashed black lines in (c) indicate the extent of the main beam.

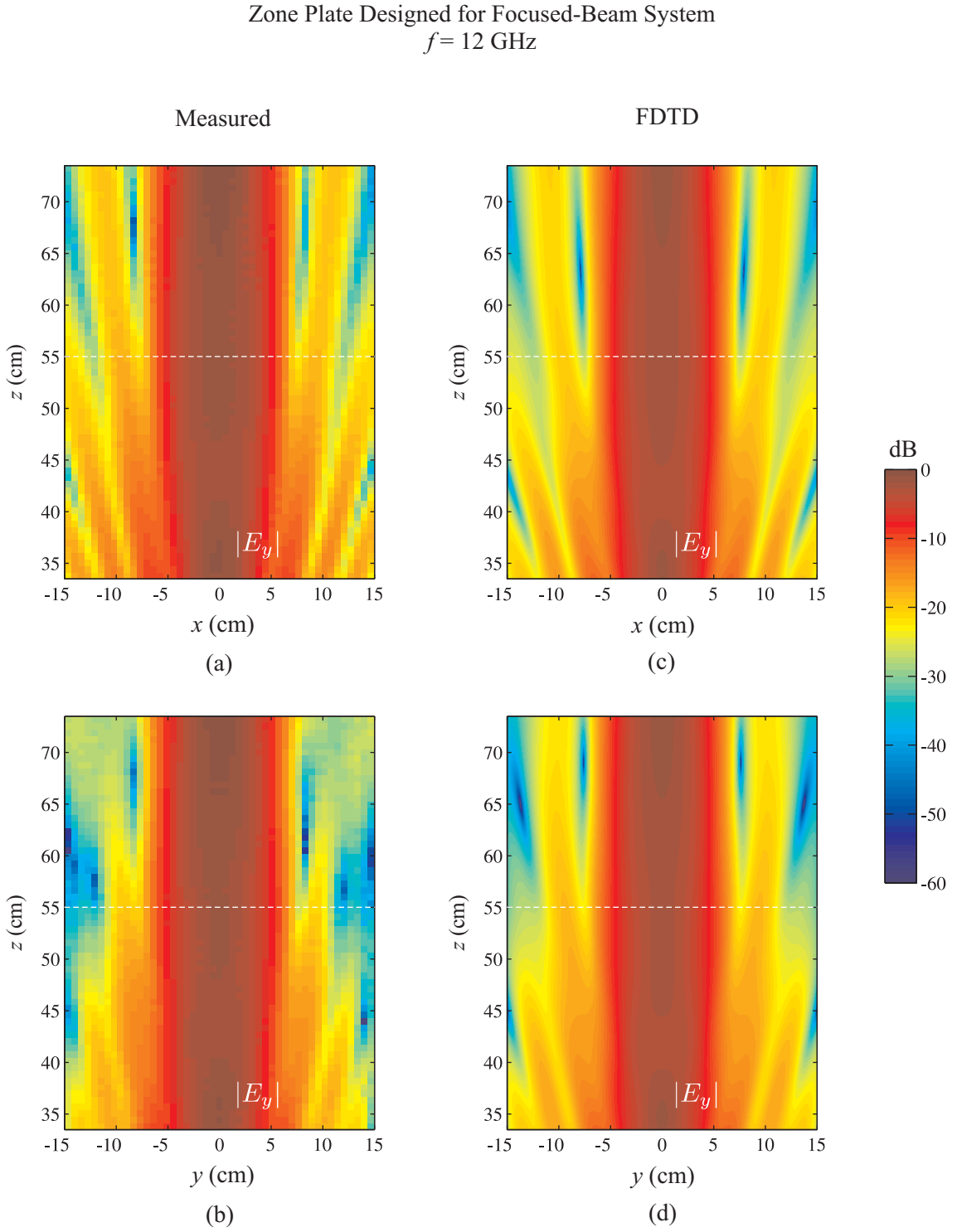

Figure A.13: Magnitude of E_y at $f = 12\,\text{GHz}$ for the zone plate for (a) and (c) a horizontal cut on the xz-plane and (b) and (d) a vertical cut on the yz-plane. Figures (a) and (b) are for measurements and figures (c) and (d) are for FDTD simulations. The dashed white line is the location of the designed focal point.

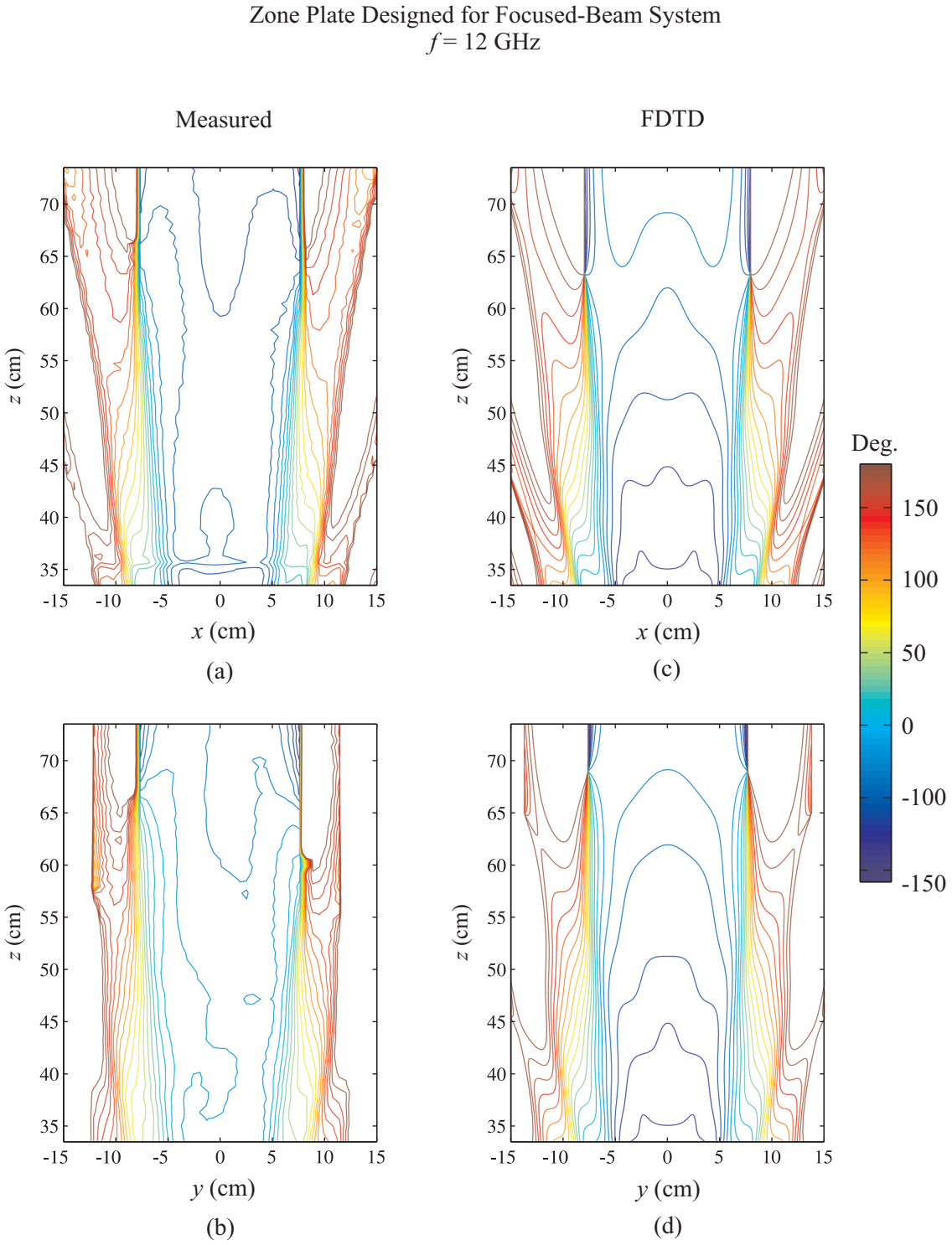

Figure A.14: Phase of E_y at $f = 12\,\text{GHz}$ for the zone plate for (a) and (c) a horizontal cut on the xz-plane and (b) and (d) a vertical cut on the yz-plane. Figures (a) and (b) are for measurements and figures (c) and (d) are for FDTD simulations.

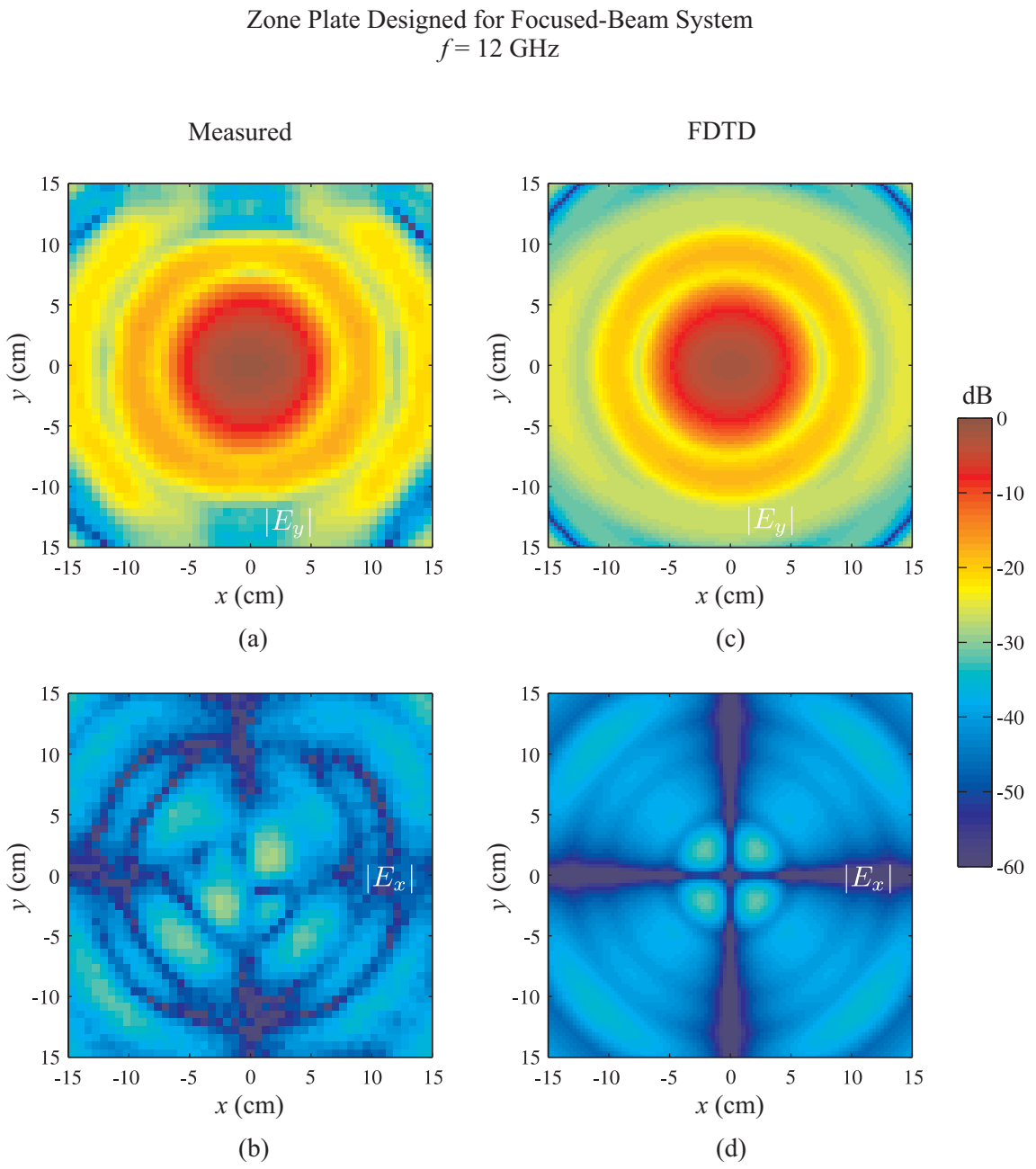

Figure A.15: Magnitude of (a) and (c) E_y and (b) and (d) E_x for a vertical cut (xy-plane) through the designed focal plane of the zone plate when $f = 12\,\text{GHz}$. Figures (a) and (b) are for measurements and figures (c) and (d) are for FDTD simulations.

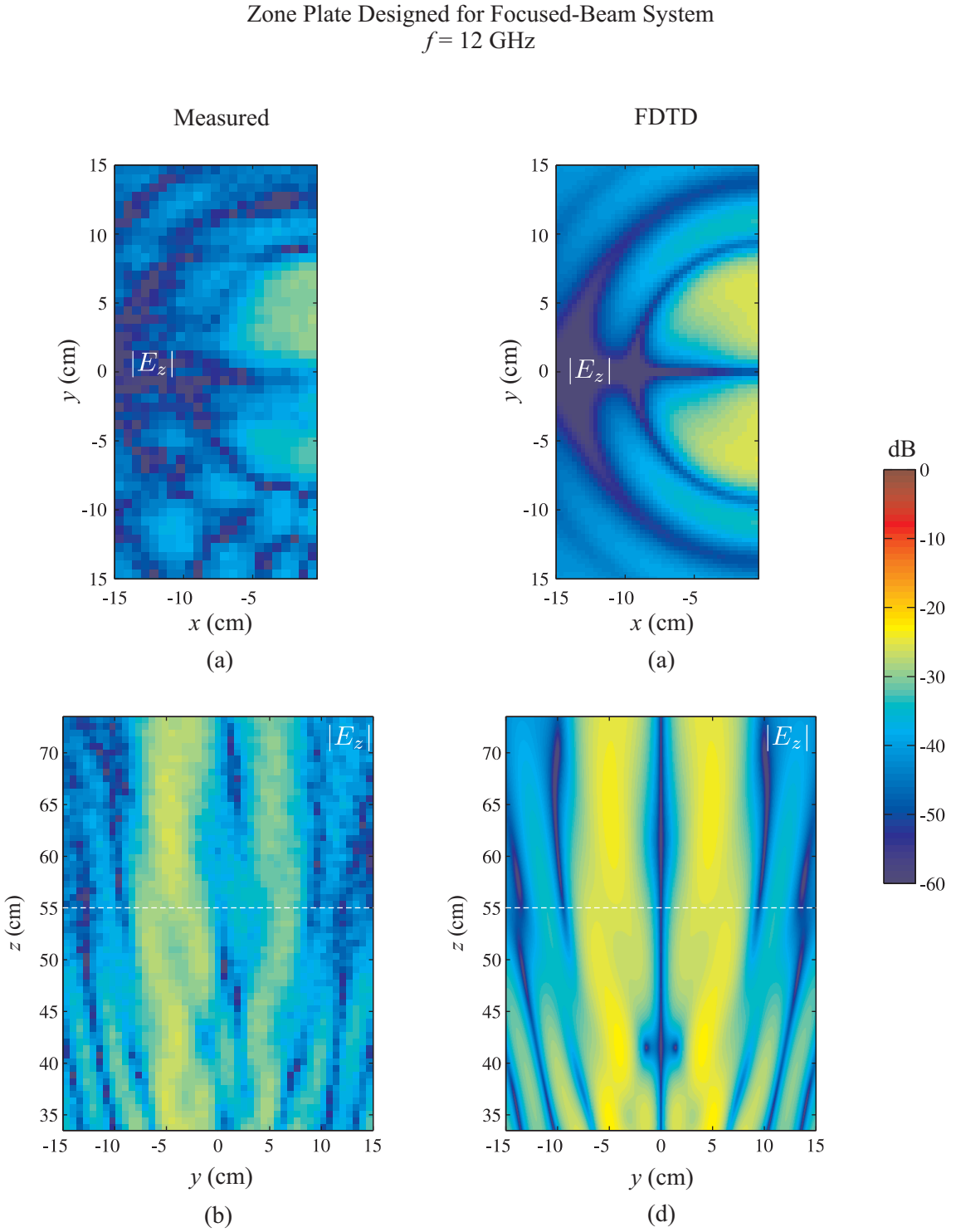

Figure A.16: Magnitude of E_z for (a) and (c) a vertical cut (xy-plane) through the designed focal plane of the zone plate and (b) and (d) a vertical cut (yz-plane) through the plane $x = -0.64\,\text{cm}$ when $f = 12\,\text{GHz}$. Figures (a) and (b) are for measurements and figures (c) and (d) are for FDTD simulations.

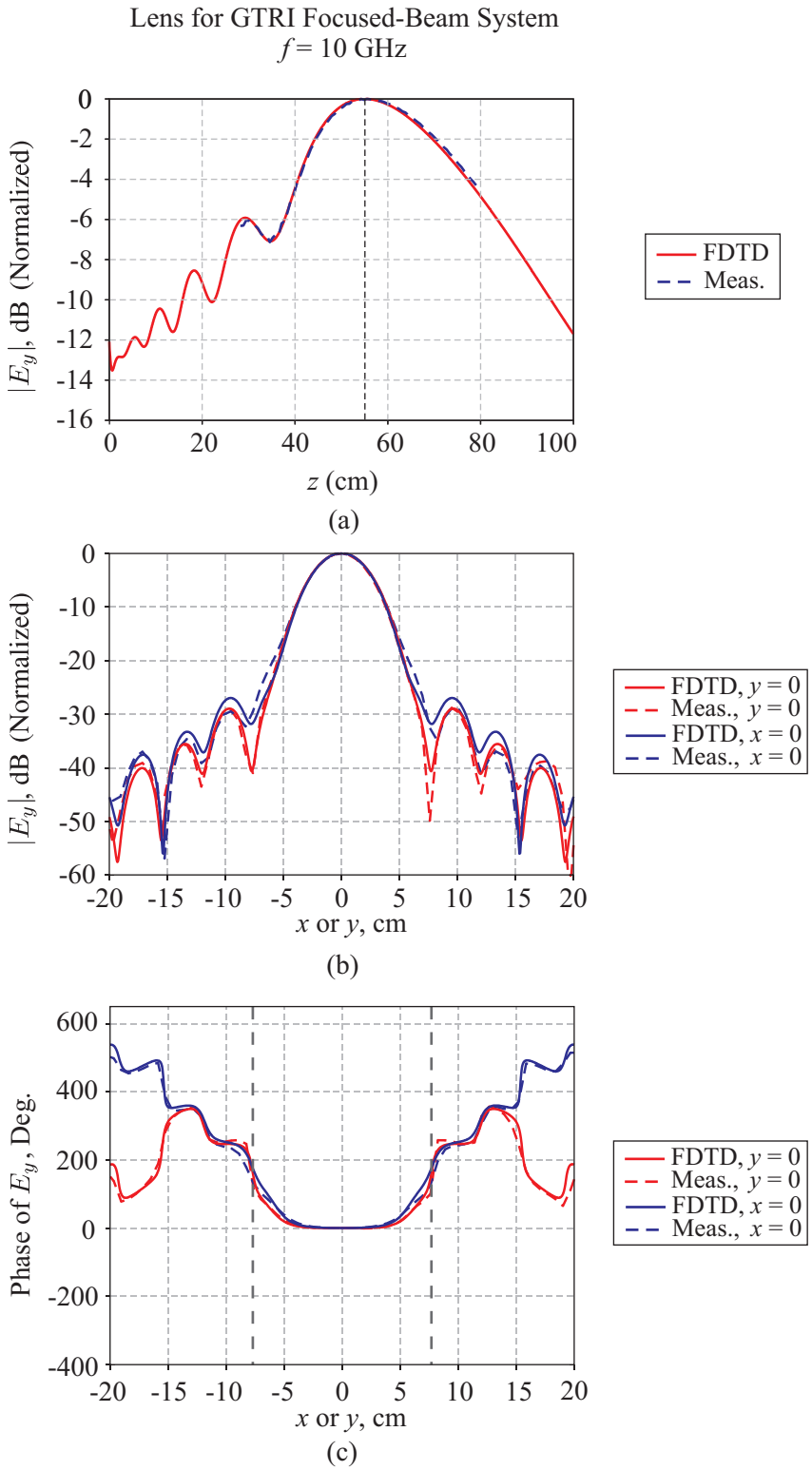

Figure A.17: Measured and simulated (FDTD) results for the electric field E_y of the lens when $f = 10\,\text{GHz}$. (a) $|E_y|$ along the z-axis, with $z = 0$ located at the output plane of the lens. The dashed back line indicates the designed focal length. (b) Magnitude and (c) phase of E_y on the designed focal plane ($z = 55\,\text{cm}$). The dashed black lines in (c) indicate the extent of the main beam.

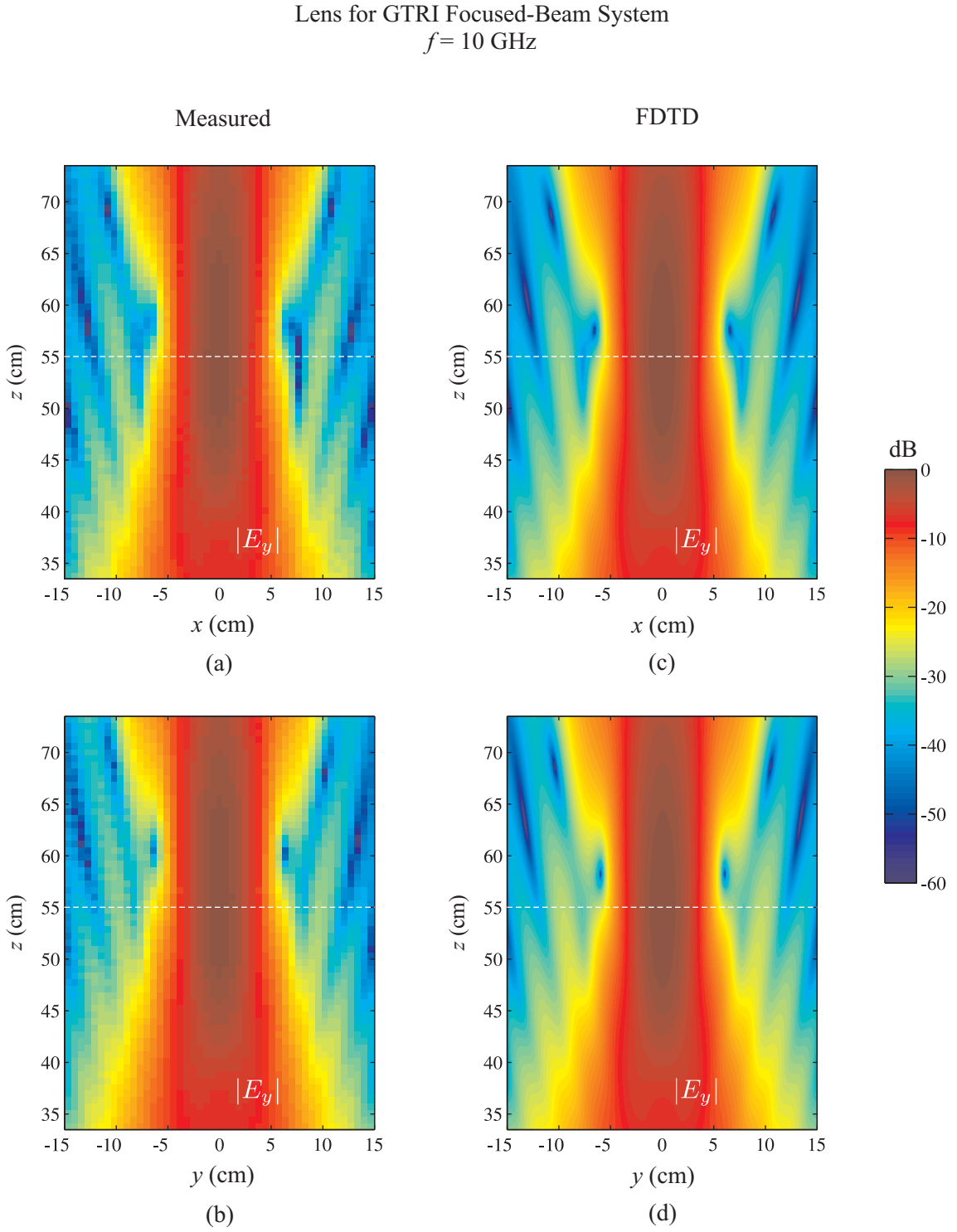

Figure A.18: Magnitude of E_y at $f = 10\,\text{GHz}$ for the lens for (a) and (c) a horizontal cut on the xz-plane and (b) and (d) a vertical cut on the yz-plane. Figures (a) and (b) are for measurements and figures (c) and (d) are for FDTD simulations. The dashed white line is the location of the designed focal point.

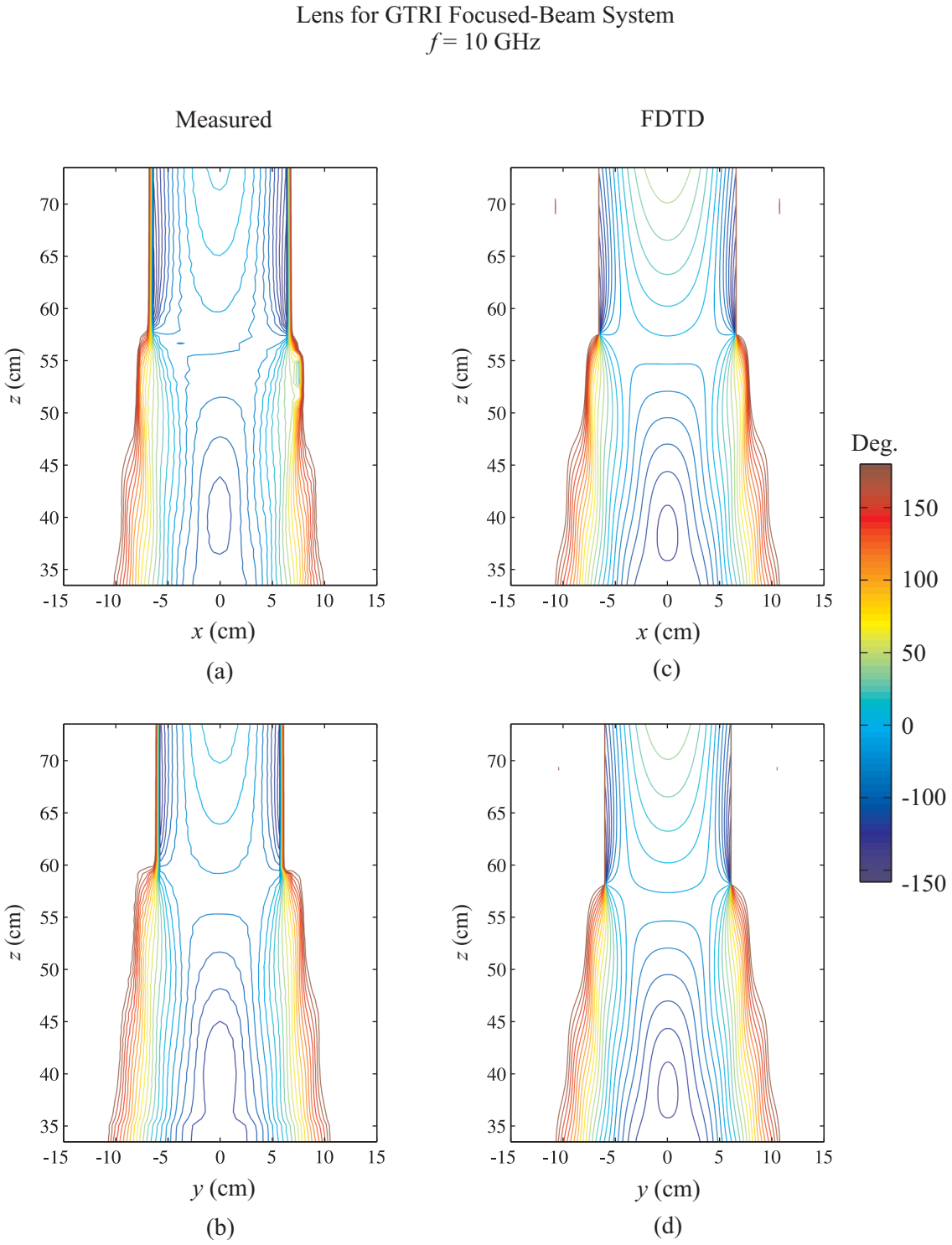

Figure A.19: Phase of E_y at $f = 10\,\text{GHz}$ for the lens for (a) and (c) a horizontal cut on the xz-plane and (b) and (d) a vertical cut on the yz-plane. Figures (a) and (b) are for measurements and figures (c) and (d) are for FDTD simulations.

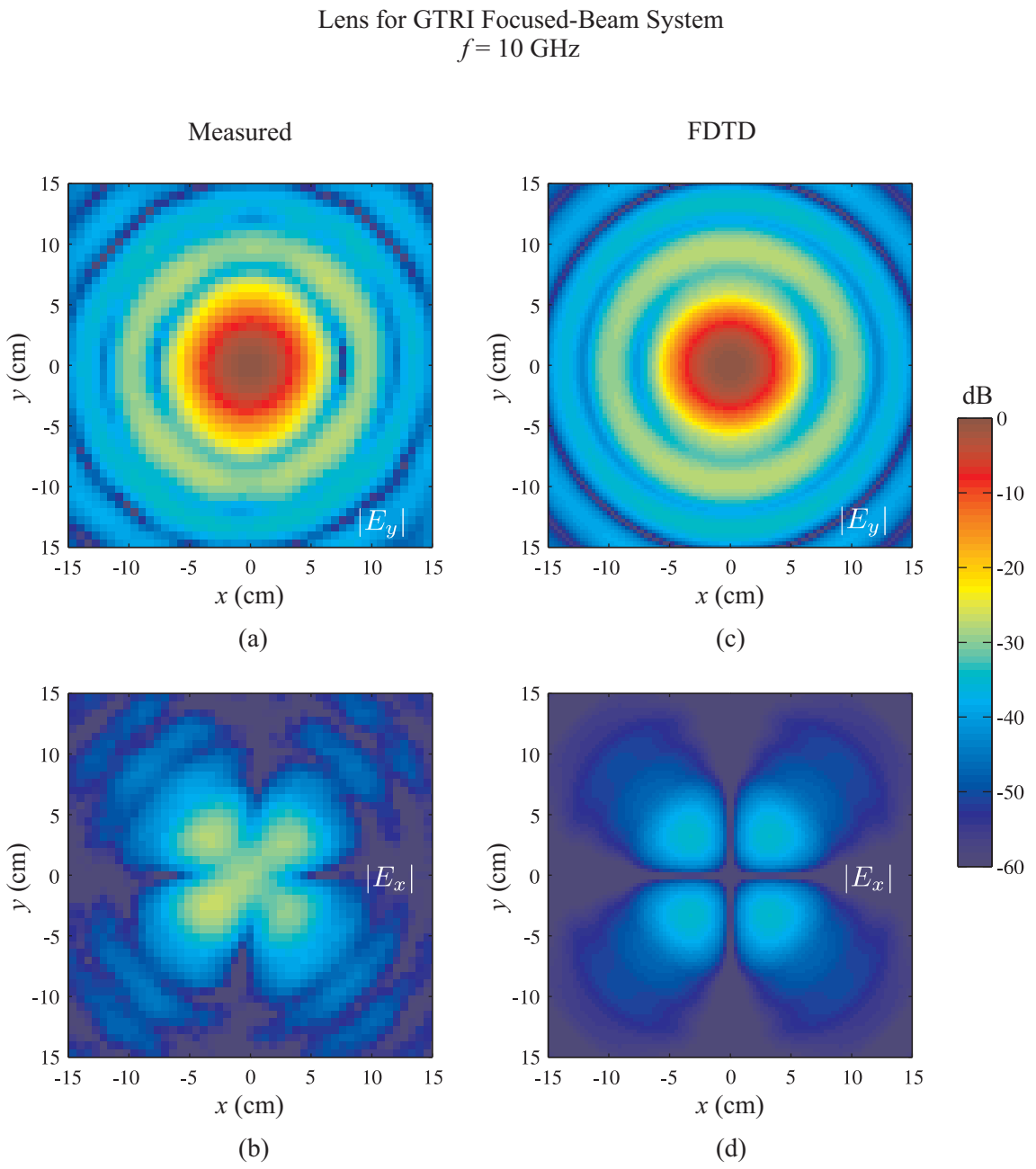

Figure A.20: Magnitude of (a) and (c) E_y and (b) and (d) E_x for a vertical cut (xy-plane) through the designed focal plane of the lens when $f = 10\,\text{GHz}$. Figures (a) and (b) are for measurements and figures (c) and (d) are for FDTD simulations.

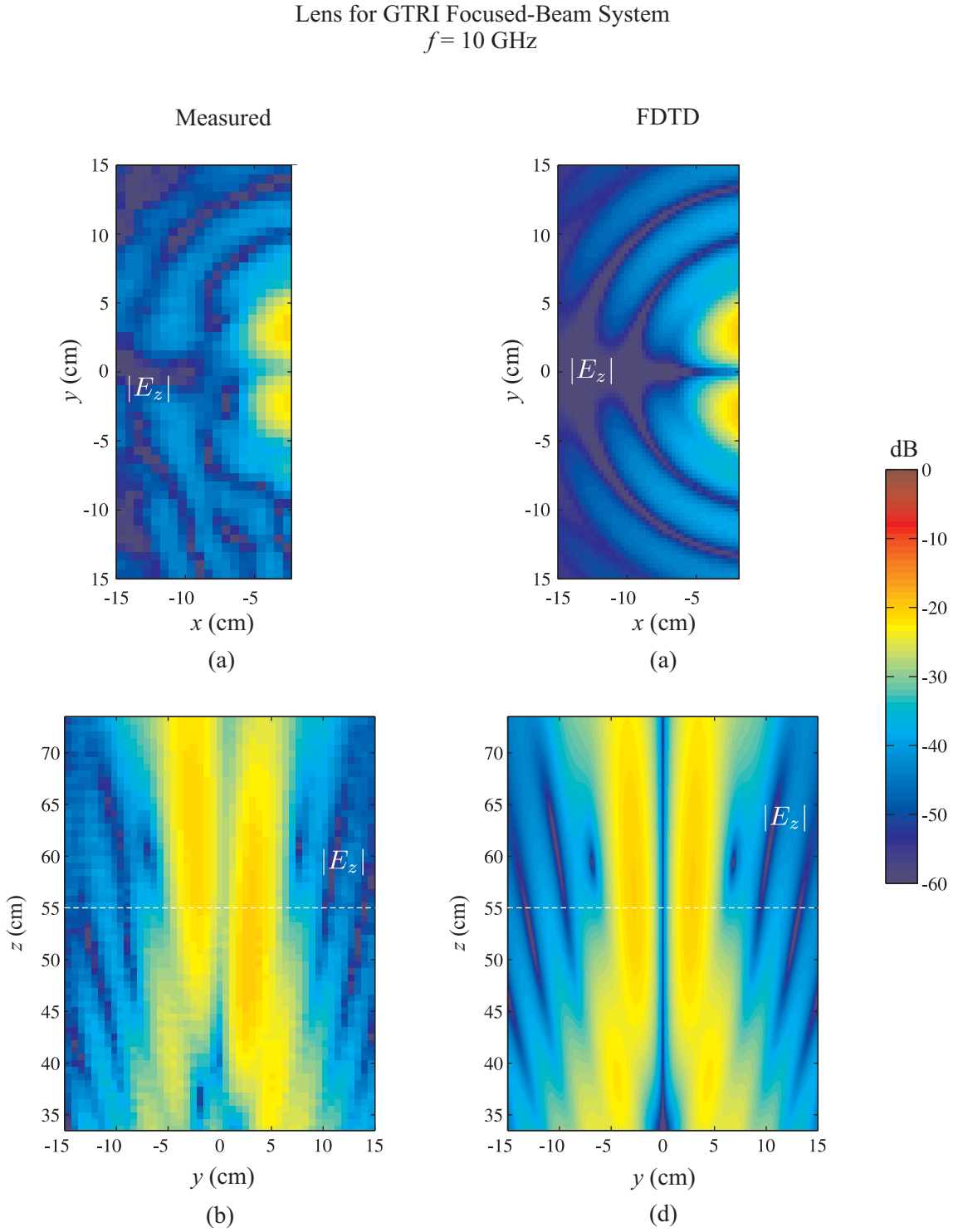

Figure A.21: Magnitude of E_z for (a) and (c) a vertical cut (xy-plane) through the designed focal plane of the lens and (b) and (d) a vertical cut (yz-plane) through the plane $x = -0.64\,\text{cm}$ when $f = 10\,\text{GHz}$. Figures (a) and (b) are for measurements and figures (c) and (d) are for FDTD simulations.

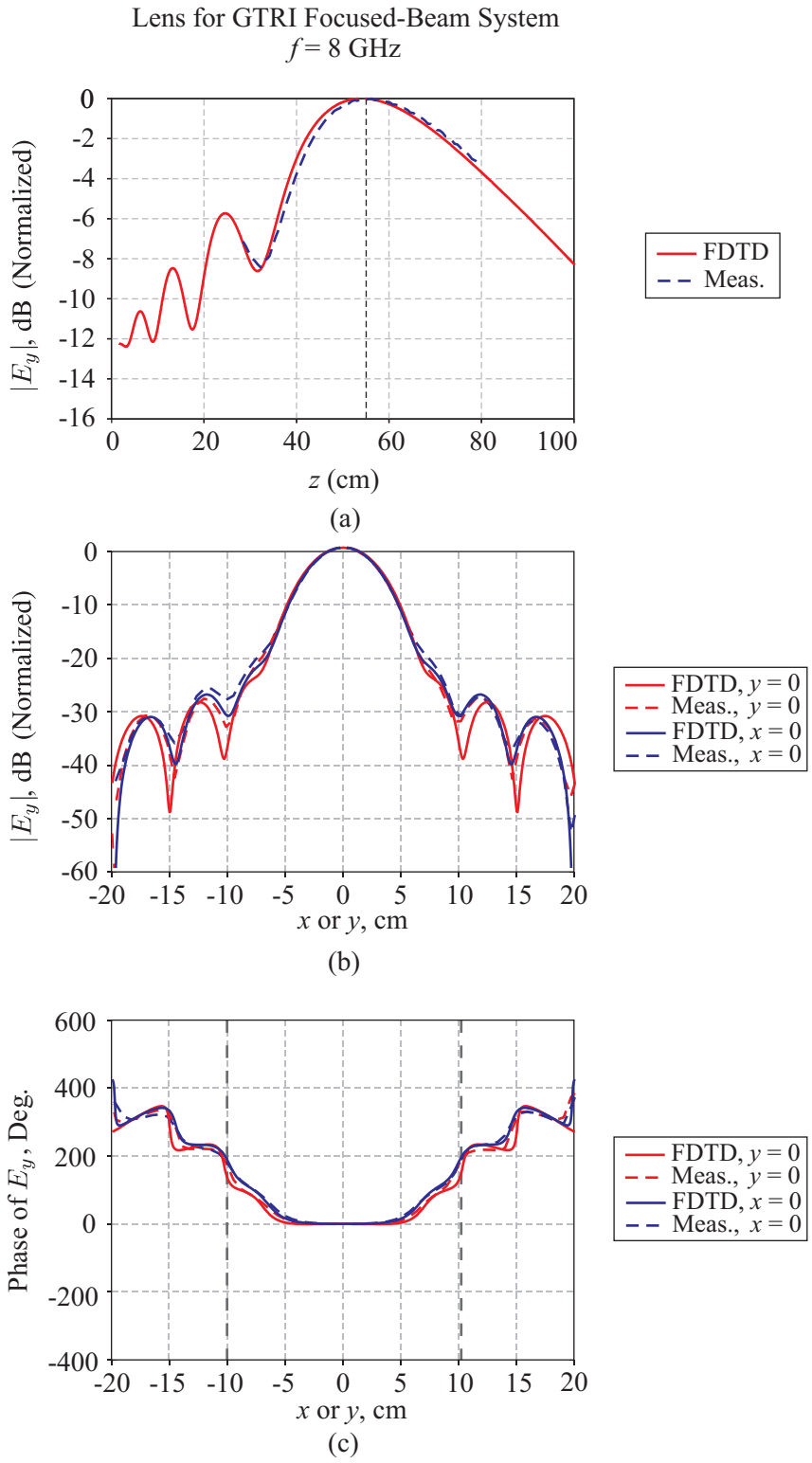

Figure A.22: Measured and simulated (FDTD) results for the electric field E_y of the lens when $f = 8\,\text{GHz}$. (a) $|E_y|$ along the z-axis, with $z = 0$ located at the output plane of the lens. The dashed back line indicates the designed focal length. (b) Magnitude and (c) phase of E_y on the designed focal plane ($z = 55\,\text{cm}$). The dashed black lines in (c) indicate the extent of the main beam.

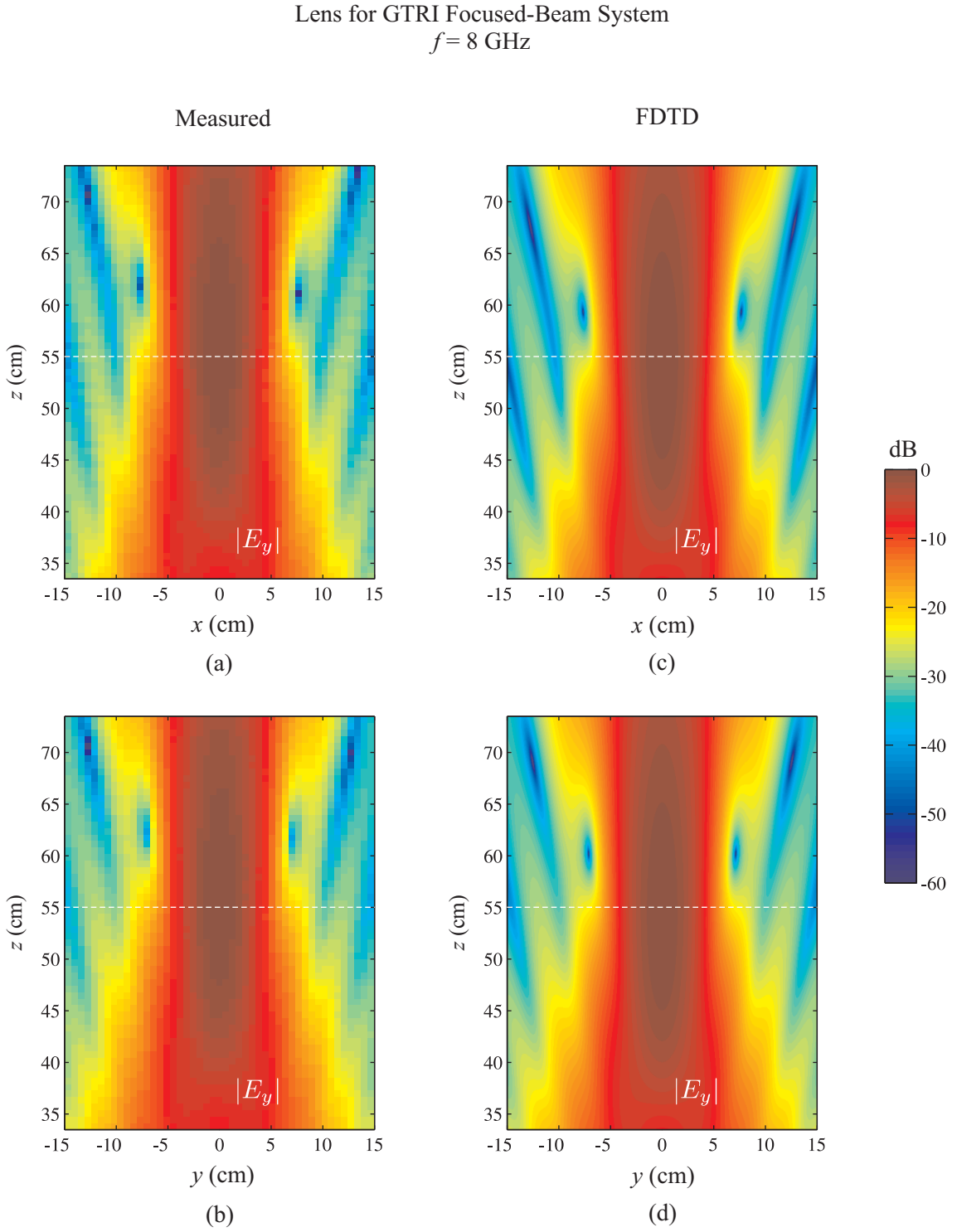

Figure A.23: Magnitude of E_y at $f = 8\,\text{GHz}$ for the lens for (a) and (c) a horizontal cut on the xz-plane and (b) and (d) a vertical cut on the yz-plane. Figures (a) and (b) are for measurements and figures (c) and (d) are for FDTD simulations. The dashed white line is the location of the designed focal point.

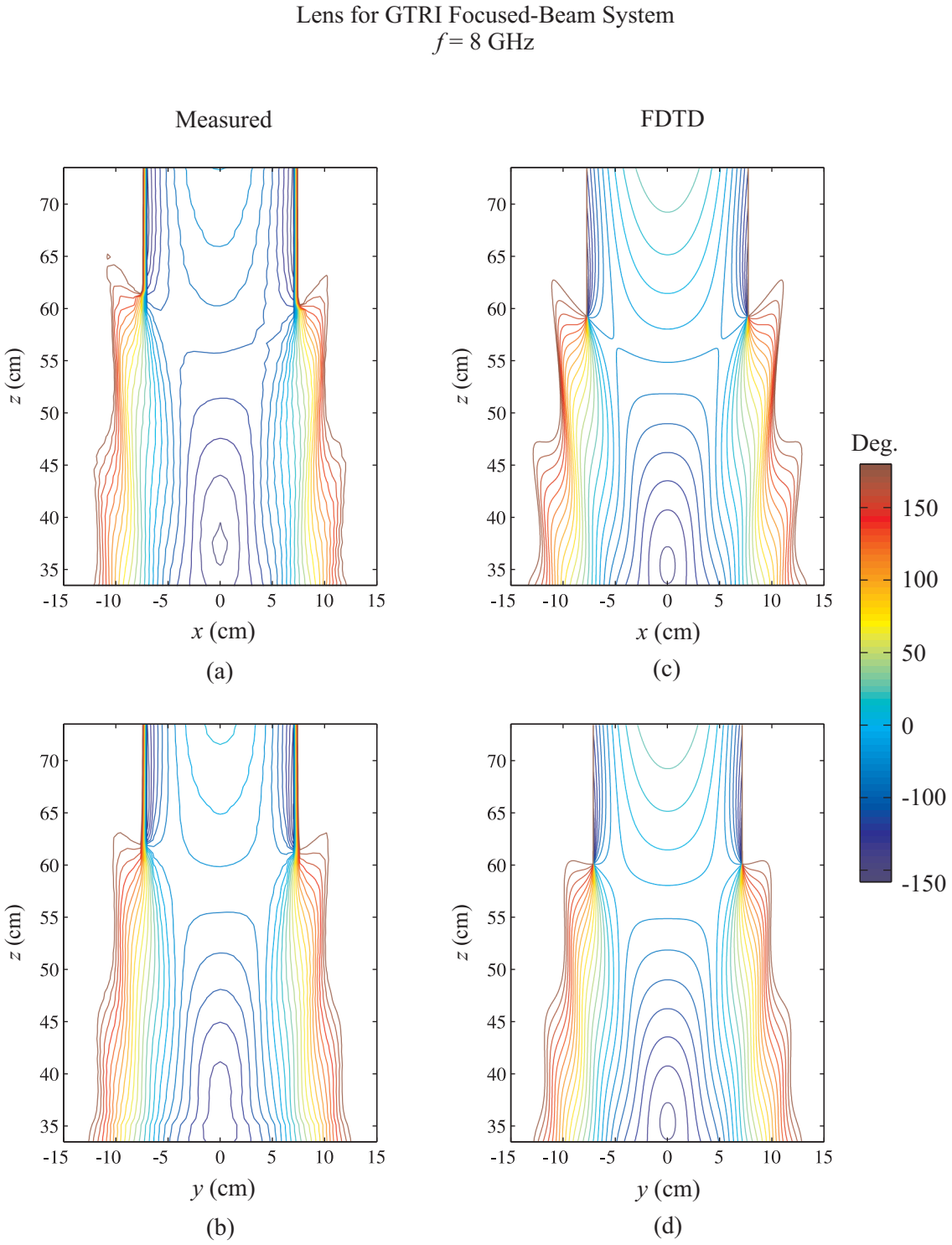

Figure A.24: Phase of E_y at $f = 8\,\text{GHz}$ for the lens for (a) and (c) a horizontal cut on the xz-plane and (b) and (d) a vertical cut on the yz-plane. Figures (a) and (b) are for measurements and figures (c) and (d) are for FDTD simulations.

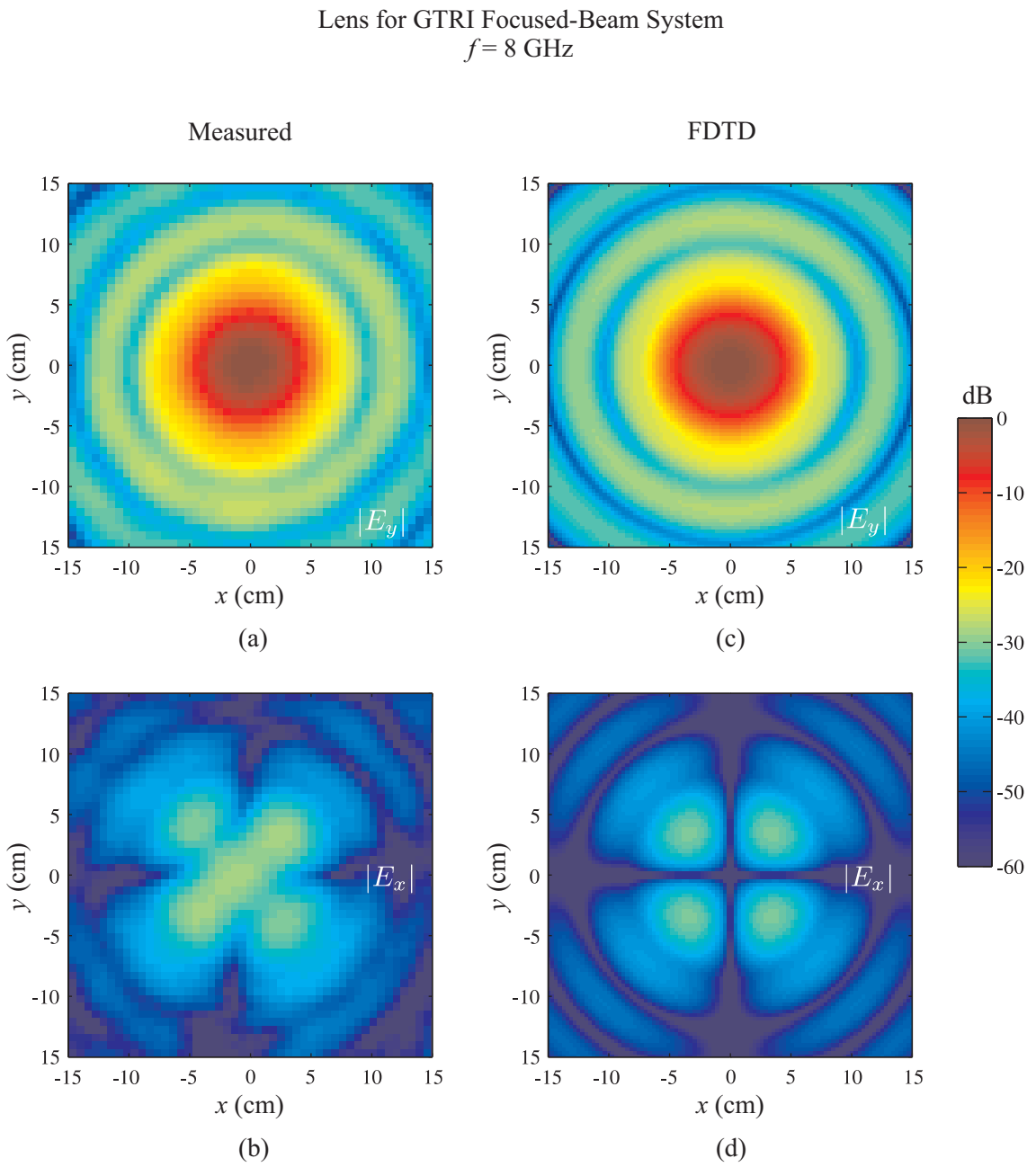

Figure A.25: Magnitude of (a) and (c) E_y and (b) and (d) E_x for a vertical cut (xy-plane) through the designed focal plane of the lens when $f = 8$ GHz. Figures (a) and (b) are for measurements and figures (c) and (d) are for FDTD simulations.

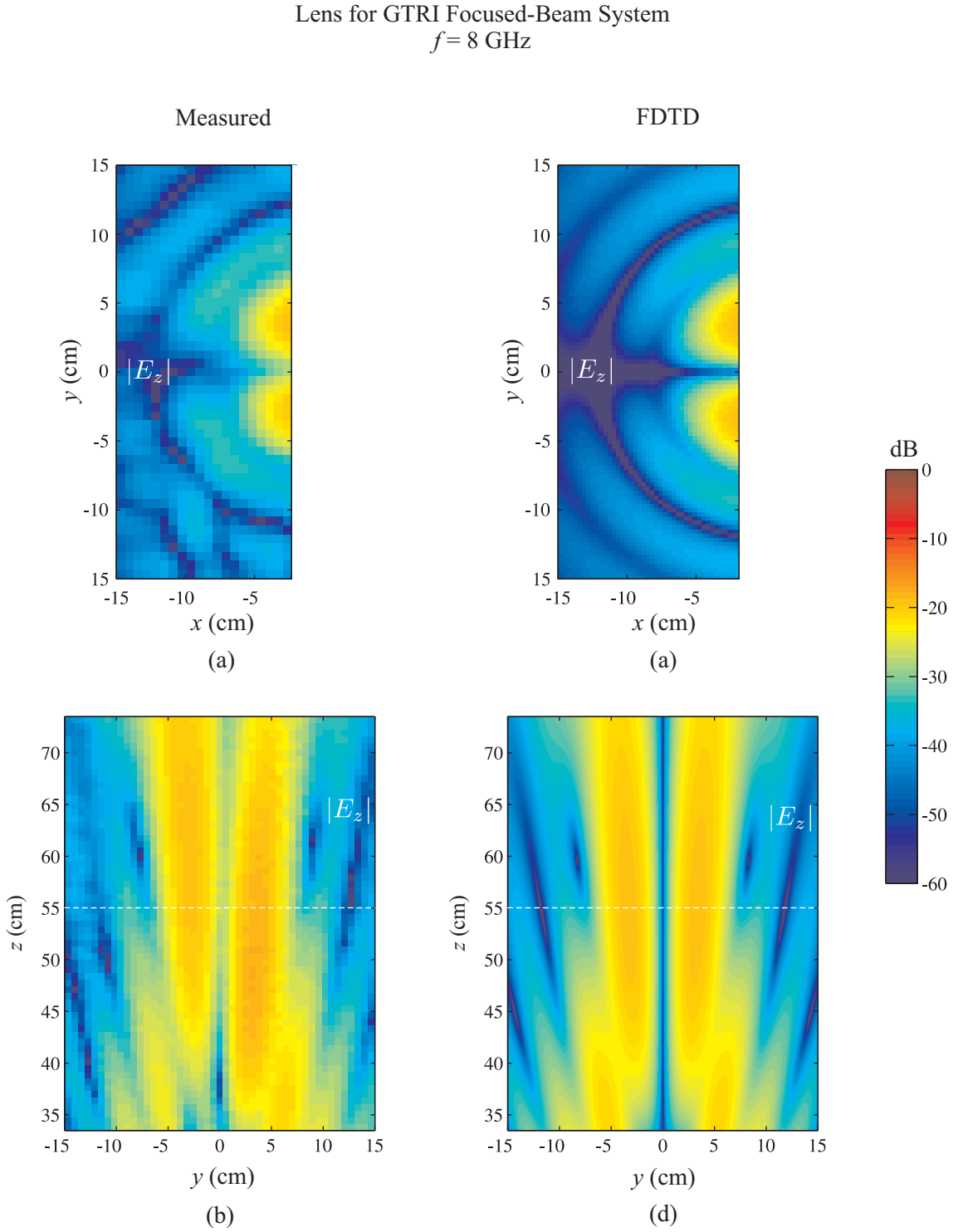

Figure A.26: Magnitude of E_z for (a) and (c) a vertical cut (xy-plane) through the designed focal plane of the lens and (b) and (d) a vertical cut (yz-plane) through the plane $x = -0.64\,\text{cm}$ when $f = 8\,\text{GHz}$. Figures (a) and (b) are for measurements and figures (c) and (d) are for FDTD simulations.

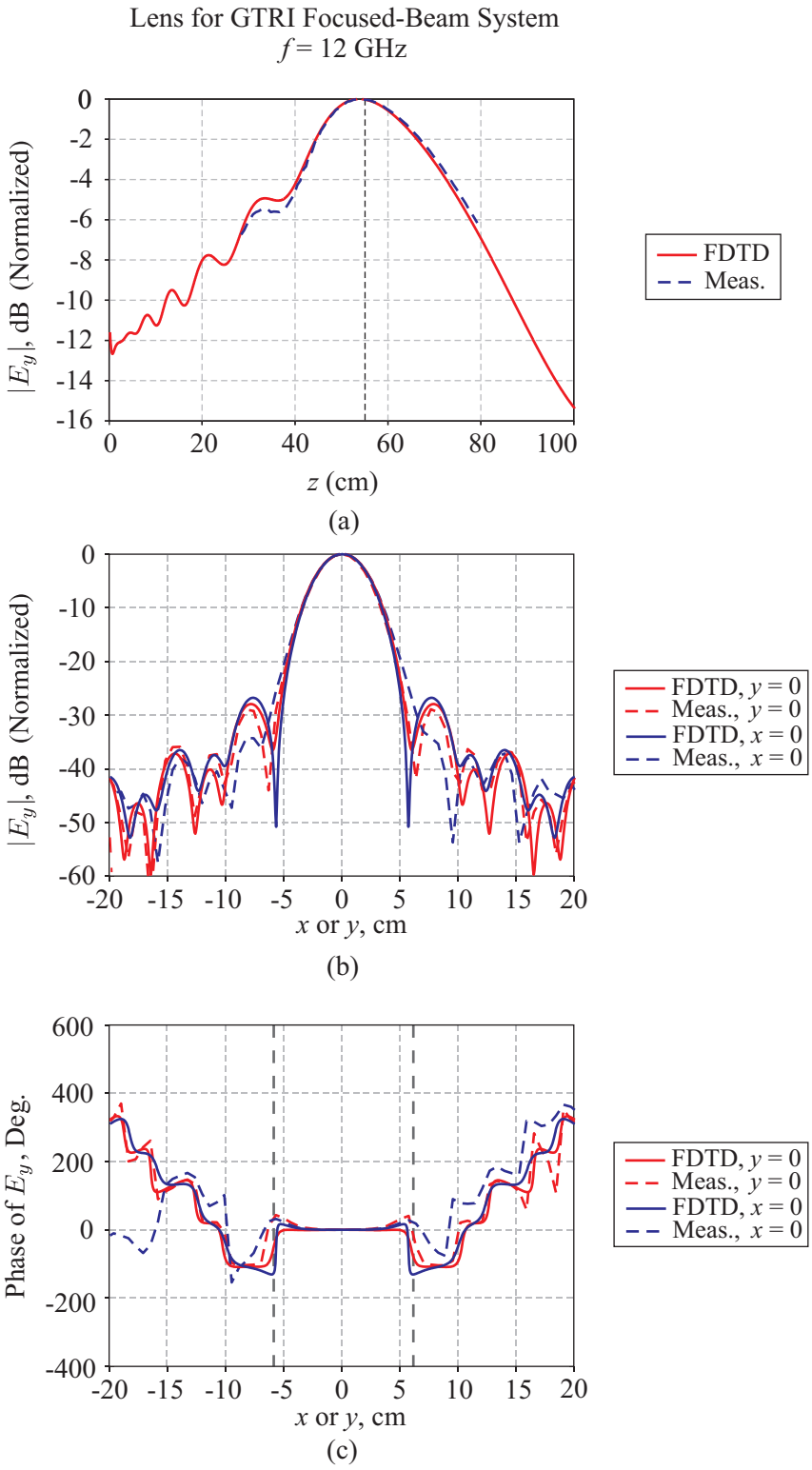

Figure A.27: Measured and simulated (FDTD) results for the electric field E_y of the lens when $f = 12\,\text{GHz}$. (a) $|E_y|$ along the z-axis, with $z = 0$ located at the output plane of the lens. The dashed back line indicates the designed focal length. (b) Magnitude and (c) phase of E_y on the designed focal plane ($z = 55\,\text{cm}$). The dashed black lines in (c) indicate the extent of the main beam.

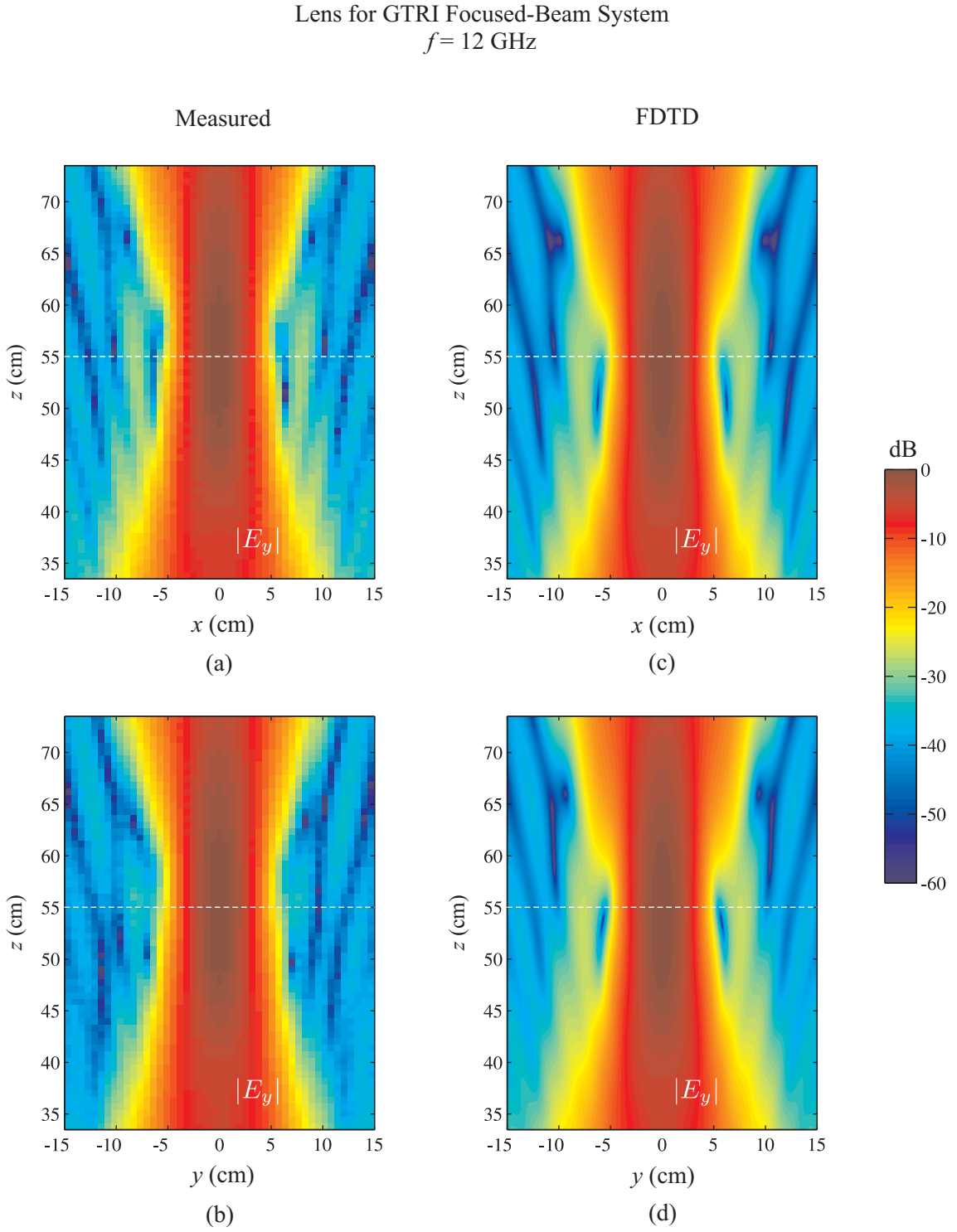

Figure A.28: Magnitude of E_y at $f = 12\,\text{GHz}$ for the lens for (a) and (c) a horizontal cut on the xz-plane and (b) and (d) a vertical cut on the yz-plane. Figures (a) and (b) are for measurements and figures (c) and (d) are for FDTD simulations. The dashed white line is the location of the designed focal point.

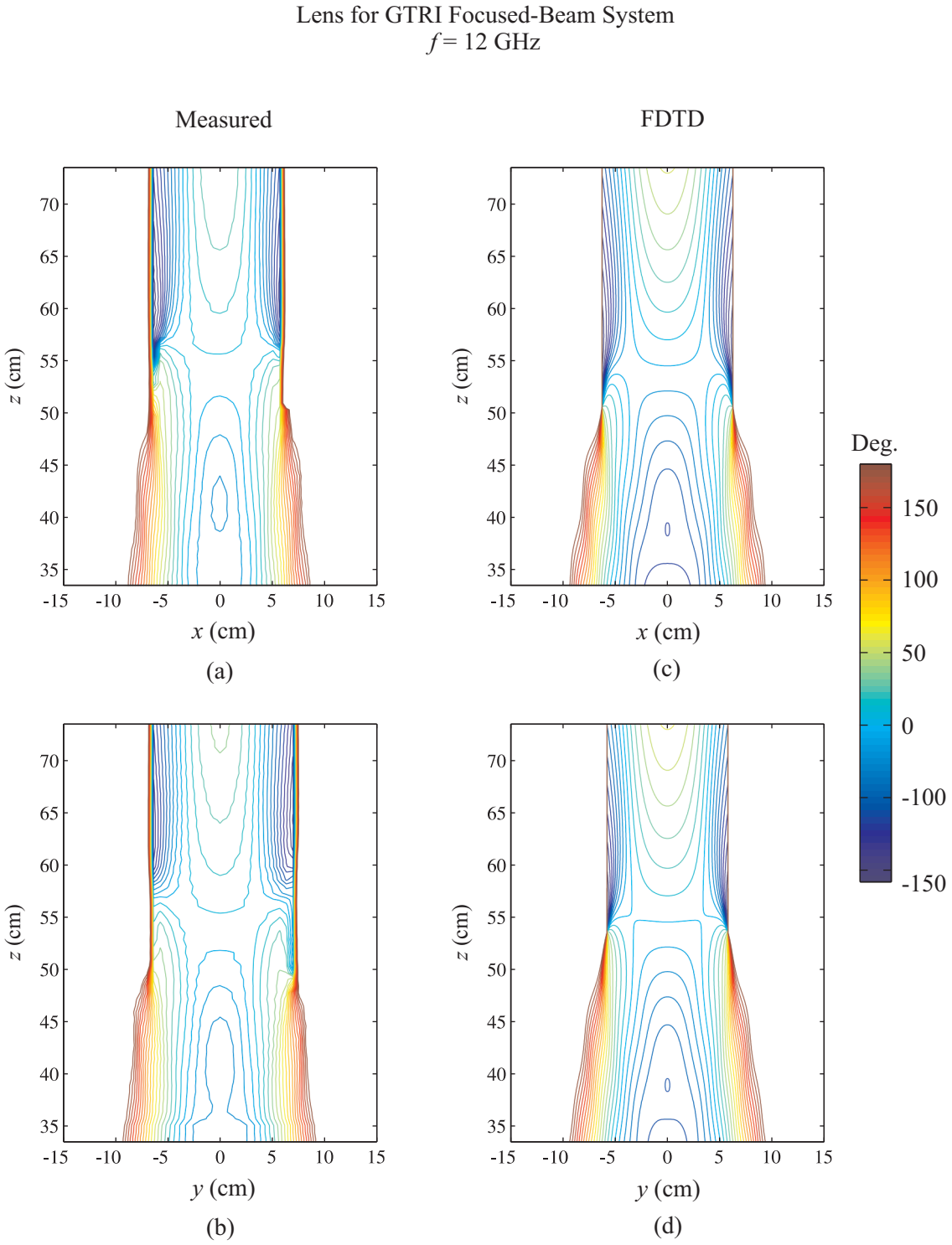

Figure A.29: Phase of E_y at $f = 12\,\text{GHz}$ for the lens for (a) and (c) a horizontal cut on the xz-plane and (b) and (d) a vertical cut on the yz-plane. Figures (a) and (b) are for measurements and figures (c) and (d) are for FDTD simulations.

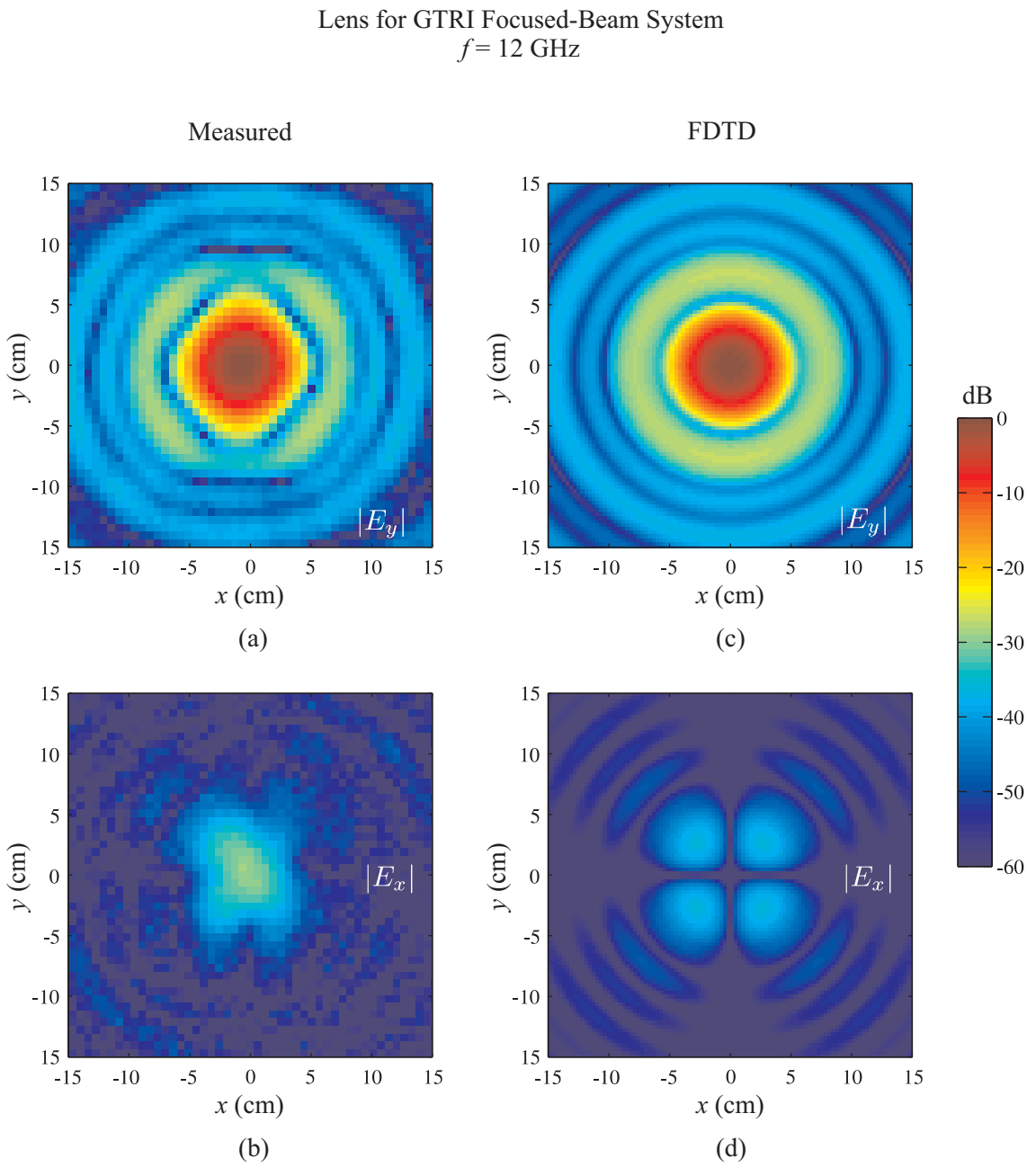

Figure A.30: Magnitude of (a) and (c) E_y and (b) and (d) E_x for a vertical cut (xy-plane) through the designed focal plane of the lens when $f = 12\,\text{GHz}$. Figures (a) and (b) are for measurements and figures (c) and (d) are for FDTD simulations.

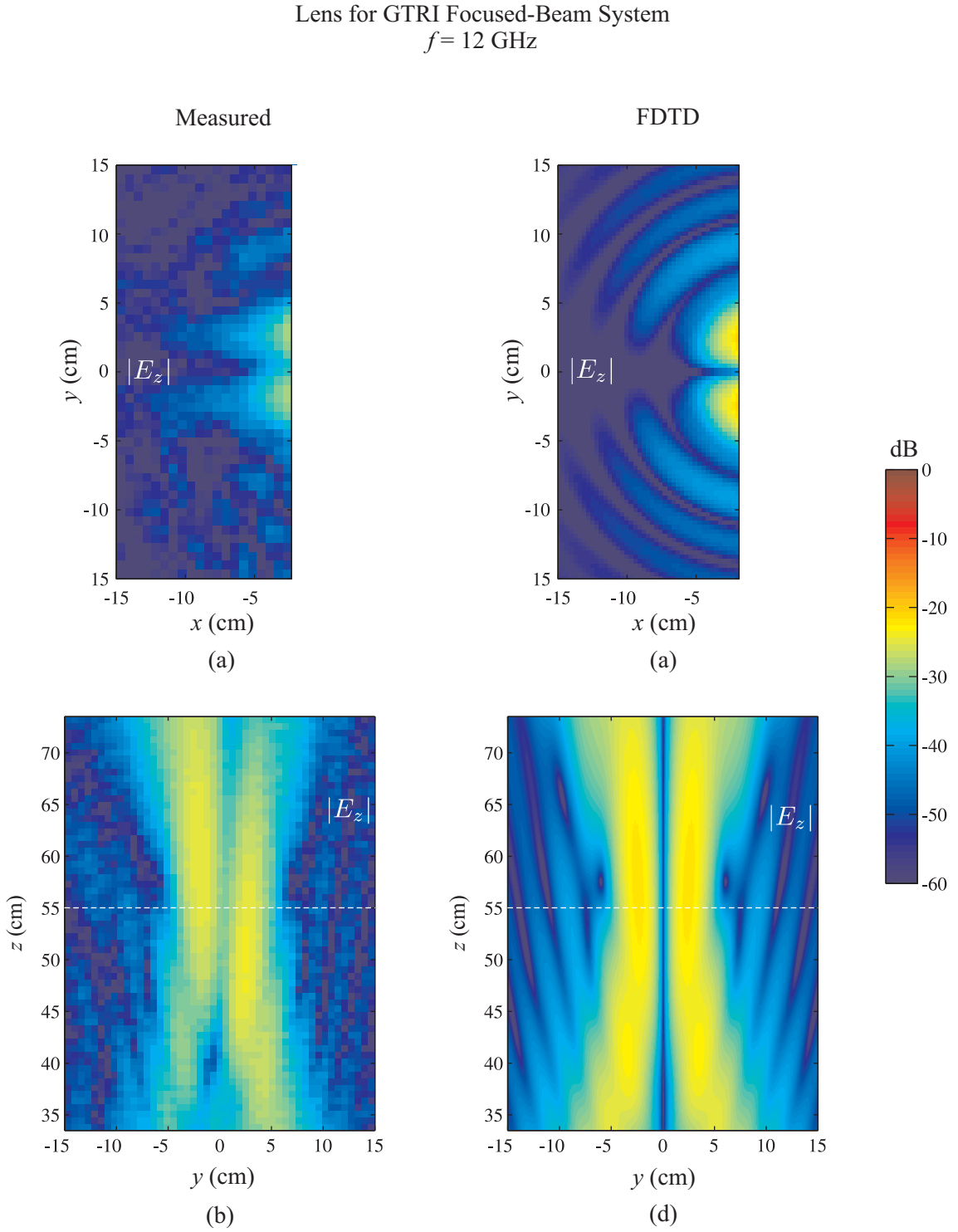

Figure A.31: Magnitude of E_z for (a) and (c) a vertical cut (xy-plane) through the designed focal plane of the lens and (b) and (d) a vertical cut (yz-plane) through the plane $x = -0.64\,\text{cm}$ when $f = 12\,\text{GHz}$. Figures (a) and (b) are for measurements and figures (c) and (d) are for FDTD simulations.

REFERENCES

[1] A. Fresnel, "Cacul de l'intensité de la lumière au centre se l'ombre d'un écran," in *Œuvres Completès d'Augustin Fresnel*, vol. 1, pp. 365-372 1866. Reprinted in *Selected Papers on Zone Plates*. J Ojeda-Castañeda and C. Gòmez-Reino, Eds. Bellingham, WA: SPIE, 1996, pp. 3-10.

[2] G. S. Smith, *An Introduction to Classical Electromagnetic Radiation*. Cambridge, United Kingdom: Cambridge University Press, 1997, ch. 4.

[3] J.-L. Soret, "Ueber die durch kreisgitter erzeugten diffractionsphänomene," *Ann. Phy. Chem.*, vol. 156, pp. 99–113, 1875. Reprinted in *Selected Papers on Zone Plates*. J Ojeda-Castañeda and C. Gòmez-Reino, Eds. Bellingham, WA: SPIE, 1996, pp. 11-25.

[4] R. W. Wood, *Physical Optics*, 3rd ed. New York: The Macmillan Co., 1934. Republication, Optical Society of America, Washington, DC, 1998.

[5] Lord Rayleigh, "Wave theory," in *The Encyclopædia Britannica*, 9th ed. New York: Henry G. Allen and Co., 1888, vol. 24, pp. 428–429.

[6] F. Sobel, F. L. Wentworth, and J. C. Wiltse, "Quasi-optical surface waveguide and other components for the 100- to 300-Gc region," *IRE Trans. Microwave Theory Tech.*, vol. MTT-9, pp. 512–518, Nov. 1961.

[7] L. F. V. Buskirk and C. R. Hendrix, "The zone plate as a radio-frequency focusing element," *IRE Trans. Antennas Propagat.*, vol. 9, pp. 319–320, May 1961. Also in U.S. Patent 3 189 907.

[8] Y. J. Guo and S. K. Barton, "Multilayer phase correcting Fresnel zone plate reflector antennas," *Int. J. of Satellite Comm.*, vol. 11, pp. 75–80, 1993.

[9] D. N. Black and J. C. Wiltse, "Millimeter-wave characteristics of phase-correcting Fresnel zone plates," *IEEE Trans. Microw. Theory Tech.*, vol. MTT-35, pp. 1122–1129, Dec. 1987.

[10] H. D. Hristov, *Fresnel Zones in Wireless Links, Zone Plate Lenses, and Antennas*. Boston: Artech House, 2000.

[11] J. C. Wiltse and J. E. Garrett, "The Fresnel zone plate antennas," *Microwave J.*, vol. 34, no. 1, pp. 101–114, Jan. 1991.

[12] G. F. Hull, Jr., "Microwave experiments and their optical analogs," *Am. J. Physics*, vol. 17, pp. 559–566, 1949.

[13] G. S. Sanyal and M. Singh, "Fresnel zone plate antenna," *J. of Inst. of Telecom. Eng. (India)*, vol. 14, pp. 265–281, 1968.

[14] G. E. Weibel and H. O. Dressel, "Propogation studies in millimeter-wave link systems," *Proc. IEEE*, no. 4, pp. 497–513, Apr. 1967.

[15] I. V. Minin and O. V. Minin, "Diffractional antenna-radomes for radar sensors: A review," *Proc. SPIE*, pp. 161–164, Jul. 2002.

[16] H. D. Hristov, L. P. Kamburov, J. R. Urumov, and R. Feick, "Focusing characteristics of curvilinear half-open Fresnel zone plate lenses: Plane wave illumination," *IEEE Trans. Antennas Propag.*, pp. 1912–1919, Jun. 2005.

[17] B. L. Ooi, H. D. Hristov, Y. Q. Zhang, Y. J. Fan, Y. Gao, G. Zhao, A. Lu, H. J. Lu, and M. S. Leong, "Development of conformal plane-conical binary Fresnel zone plate antenna for millimeter-waves," *10th IEEE Singapore Int. Conf. on Comm. Sys.*, Oct. 2006.

[18] H. D. Hristov, R. Feick, W. Grote, and P. Fernández, "Indoor signal focusing by means of Fresnel zone plate lens attached to building wall," *IEEE Trans. Antennas Propag.*, vol. 52, no. 4, pp. 933–940, Apr. 2004.

[19] T. M. B. Wright, "Focusing device for a microwave antenna," Canadian Patent 2 005 937, 1998.

[20] B. Khayatian and Y. Rahmat-Samii, "A novel antenna concept for future solar sails: Application of Fresnel antennas," *IEEE Antennas Propag. Mag.*, vol. 46, no. 2, pp. 50–63, Apr. 2004.

[21] Y. Ji and M. Fujita, "A cylindrical Fresnel zone antenna," *IEEE Trans. Antennas Propag.*, vol. 9, pp. 1301–1303, Sep. 1996.

[22] J.-J. Delmas, S. Toutain, G. Landrac, and P. Cousin, "TDF antenna for multisatellite reception using 3D Fresnel principle and multilayer structure," in *Proc. Antennas Propagat. Int. Symp.*, vol. 3, 1993, pp. 1647–1650.

[23] M. Gouker, "Studies of dipole antennas on finite thickness substrates with planar integrated focusing elements," Ph.D. Dissertation, Georgia Institute of Technology, May 1991.

[24] M. A. Gouker and G. S. Smith, "A millimeter-wave integrated-circuit antenna based on the Fresnel zone plate," *IEEE Trans. Microw. Theory Tech.*, vol. 40, no. 5, pp. 968–977, May 1992.

[25] B. Huder and W. Menzel, "Flat printed reflector antenna for mm-wave applications," *Electron Lett.*, vol. 24, no. 6, pp. 318–319, Mar. 1988.

[26] E. N. Glytsis, M. E. Harrigan, K. Hirayama, and T. K. Gaylord, "Collimating cylindrical diffractive lenses: Rigorous electromagnetic analysis and scalar approximation," *Appl. Optics*, no. 1, pp. 34–43, Jan. 1998.

[27] D. W. Prather, M. S. Mirotznik, and J. N. Mait, "Boundary integral methods applied to the analysis of diffractive optical elements," *J. Opt. Soc. Am. A*, vol. 14, no. 1, pp. 34–43, Jan. 1997.

[28] H. H. Chau, "Fourier-transform hologram by zone plate," *Optics Comm.*, no. 4, pp. 350–353, Dec. 1973.

[29] R. A. Hyde, "Large aperture Fresnel telescopes," Lawrence Livermore National Laboratory, Tech. Rep. UCRL-ID-131320, 1998.

[30] L. Koechlin, D. Serre, and P. Duchon, "High resolution imaging with Fresnel interferometric arrays: Suitability for exoplanet detection," *Astronomy and Astrophysics*, no. 2, pp. 709–720, Nov. 2005.

[31] L. D. Foo, "Objective lens system utilizing diffractive optical element," US Patent 5 880 879, 1997.

[32] "World's first revolutionary new optical element for a camera lens: Canon multi-layer diffractive optical element," Canon, Inc., Tech. Rep. 2001.6, 2006, translated from Japanese. [Online]. Available: http://www.canon.com/camera-museum/tech/report/200106/200106.html

[33] E. Renner, *Pinhole Photography: Rediscovering a Historic Technique*. Boston: Focal Press, 1995.

[34] G. Skinner, P. von Ballmoos, N. Gehrels, and J. Krizmanic, "Fresnel lenses for X-ray and gamma-ray astronomy," *Proc. SPIE*, pp. 459–470, 2004.

[35] *Application Note: Focusing X-rays With Zone Plates For Synchrotron Use*, Xradia, Inc., Concord, CA. [Online]. Available: http://xradia.com/Downloads/zp_focusing_notes.pdf

[36] O. V. Minin and I. V. Minin, *Diffractional Optics of Millimetre Waves*. Bristol, UK: Institute of Physics Publishing, 2004.

[37] I. V. Minin and O. V. Minin, *Basic Principles of Fresnel Antenna Arrays*. Springer, 2008.

[38] Y. J. Guo and S. K. Barton, *Fresnel Zone Antennas*. Kluwer Academic Publishers, Dordrecht, The Netherlands, 2002.

[39] G. S. Smith, *An Introduction to Classical Electromagnetic Radiation*. Cambridge, United Kingdom: Cambridge University Press, 1997, ch. 3.

[40] D. K. Ghodgaonkar, V. V. Varadan, and V. K. Varadan, "A free-space method for measurement of dielectric constants and loss tangents at microwave frequencies," *IEEE Trans. Instrum. Meas.*, vol. 37, no. 3, pp. 789–793, Jun. 1989.

[41] J. Musil and F. Žáček, *Microwave Measurements of Complex Permittivity by Free Space Methods and Their Applications*. Amstradam: Elsevier, 1986.

[42] L. E. R. Petersson and G. S. Smith, "An estimate of the error caused by the plane-wave approximation in free-space dielectric measurement systems," *IEEE Trans. Antennas Propag.*, vol. 50, no. 6, pp. 878–887, Jun. 2002.

[43] *Users Guide: Theory and Operation of the GTRI Focused Beam System*, Georgia Tech Research Institute, Feb. 2006.

[44] San Diego Plastics, Inc., Aug. 2008. [Online]. Available: http://www.sdplastics.com/rexolite.html

[45] J. E. Garrett and J. C. Wiltse, "Fresnel zone plate antennas at millimeter wavelengths," *Int. J. of Infrared and Millimeter Waves*, vol. 12, no. 3, pp. 195–220, Mar. 1991.

[46] K. W. Scanlon, "The new Point Loma lighthouse," *The Keeper's Log*, Winter 2002, U.S. Lighthouse Society.

[47] Y. Ji and M. Fujita, "Design and analysis of a folded Fresnel zone plate antenna," *Int. J. of Infrared and Millimeter Waves*, vol. 15, no. 8, pp. 1385–1406, Aug. 1994.

[48] L. Leyten and M. H. A. J. Herben, "Vectorial far-field analysis of the Fresnel-zone plate antenna: a comparison with the parabolic reflector antenna," *Microwave and Optical Tech. Letters*, vol. 5, no. 2, pp. 49–56, Feb. 1992.

[49] M. Born and E. Wolf, *Principles of Optics*, 7th ed. Cambridge: Cambridge University Press, 1999.

[50] D. Duan, Y. Rahmat-Samii, and J. P. Mahon, "Scattering from a circular disk: a comparative study of PTD and GTD techniques," *Proc. IEEE*, vol. 79, no. 10, pp. 1472–1480, 1991.

[51] J. M. van Houten and M. H. A. J. Herben, "Analysis of a phase-correcting Fresnel-zone plate antenna with dielectric/transparent zones," *J. Electromagn. Waves and Applicat.*, vol. 8, no. 7, pp. 847–858, 1994.

[52] L. C. J. Baggen and M. H. A. J. Herben, "Caclulating the radiation pattern of a Fresnel-zone plate antenna: A comparison between UTD/GTD and PO," *Electromagnetics*, vol. 15, no. 4, pp. 321–345, July-Aug 1995.

[53] J. M. van Houten and M. H. A. J. Herben, "Analysis of a phase-correcting Fresnel-zone plate antennas with dielectric/transparent zones," *J. Electro. Waves and Appl.*, vol. 8, no. 7, pp. 847–857, 1994.

[54] D. W. Prather and S. Shi, "Electromagnetic analaysis of axially symmetric diffractive lenses with the method of moments," *J. Opt. Soc. Am. A*, vol. 17, no. 4, pp. 729–739, Apr. 2000.

[55] ——, "Formulation and application of the finite-difference time-domain method for the analysis of axially symmetric diffractive optical elements," *J. Opt. Soc. Am. A*, vol. 16, no. 5, pp. 1131–1142, May 1999.

[56] W. B. Dou and C. Wan, "An analysis of diffractive lenses at millimeter wavelengths," *Microwave Opt. Technol. Let.*, vol. 31, no. 5, pp. 396–401, Dec. 2001.

[57] D. W. Prather, D. Pustai, and S. Shi, "Diffractive lens performance as a function of f-number," *Proc. SPIE Symp.*, vol. 3951, pp. 141–149, 2000.

[58] T. G. Jurgens, J. G. Blaschak, and G. W. Saewert, "Bodies of revolution," in *Computational Electrodynamics: The Finite-Difference Time-Domain Method*, 2nd ed., A. Taflove and S. C. Hagness, Eds. Boston: Artech House, 2000, ch. 12, pp. 529–568.

[59] D. B. Davidson and R. W. Ziolkowski, "Body-of-revolution finite-difference time-domain modeling of space-time focusing by a three-dimensional lens," *J. Opt. Soc. Am. A*, vol. 11, no. 4, pp. 1471–1490, Apr. 1994.

[60] A. Taflove and S. C. Hagness, *Computational Electrodynamics: The Finite-Difference Time-Domain Method*, 2nd ed. Boston: Artech House, 2000.

[61] J. G. Maloney, G. S. Smith, and W. R. Scott, "Accurate computation of the radiation from simple antennas using the finite-difference time-domain method," *IEEE Trans. Antennas Propag.*, no. 7, pp. 1059–1068, Jul. 1990.

[62] J. G. Maloney, G. S. Smith, E. T. Thiele, and O. P. Gandhi, "Modeling of antennas," in *Computational Electrodynamics: The Finite-Difference Time-Domain Method*, 2nd ed., A. Taflove and S. C. Hagness, Eds. Boston: Artech House, 2000, ch. 14, pp. 627–702.

[63] G. S. Smith, *An Introduction to Classical Electromagnetic Radiation.* Cambridge, United Kingdom: Cambridge University Press, 1997.

[64] V. Ronci, *The Nature of Light.* Harvard Univ. Pr., 1970. p. 251.

[65] I. R. Capoglu and G. S. Smith, "Application of new tools for the FDTD analysis of UWB antennas on dielectric substrates," *Microwave and Optical Tech. Letters*, vol. 50, no. 2, pp. 358–363, Feb. 2008.

[66] P. F. Goldsmith, *Quasioptical Systems: Gaussian Beam Quasioptical Propagation.* Piscataway, NJ: IEEE Press, 1998.

[67] M. Sussman, "Elementary diffraction theory of zone plates," *Am. J. Phys.*, vol. 28, pp. 394–398, 1960.

[68] J. C. Wiltse, "Analysis of the properties of large-angle zone plate antennas," in *Proc. Antennas Propagat. Int. Symp.*, vol. 1, Jul. 2001, pp. 284–287.

[69] A. Petosa, N. Gagnon, and A. Ittipiboon, "Effects of Fresnel lens thickness on aperture efficiency," in 10^{th} *Int. Symp. Antenna Tech. and Appl. EM and URSI conf.*, Jul. 2004, pp. 175–178.

[70] ——, "Optimization of dielectric Fresnel lens thickness for maximizing gain," in 12^{th} *Int. Symp. Antenna Tech. and Appl. EM and URSI conf.*, Jul. 2006, pp. 519–522.

[71] H. D. Hristov and M. H. A. J. Herben, "Millimeter-wave Fresnel-zone plate lens and antenna," *IEEE Trans. Microw. Theory Tech.*, vol. 43, no. 12, pp. 2779–2785, Dec. 1995.

[72] G. W. Farnell, "Measured phase distribution in the image space of a microwave lens," *Can. J. Phys.*, vol. 36, no. 7, pp. 935–943, Jul. 1958.

[73] J. C. Wiltse, "Zone plate designs for terahertz frequencies," *Proc. SPIE Symp.*, vol. 5790, pp. 167–179, 2005.

[74] ——, "The stepped conical zone plate antenna," *Proc. SPIE Symp.*, vol. 4386, pp. 85–92, 2001.

[75] A. I. Carswell, "Measurements of the longitudinal component of the electromagnetic field at the focus of coherent beam," *Phys. Review Letters*, vol. 15, no. 16, pp. 647–649, Oct. 1965. Reprinted in J. J. Stamnes, Ed. *Selected Papers on Electromagnetic Fields in the Focal Region.* Bellingham, WA: SPIE, 2001, pp. 391-393.

[76] A. Boivin and E. Wolf, "Electromagnetic field in the neighborhood of the focus of a coherent beam," *Phy. Review*, vol. 138, no. 6B, pp. B1561–B1565, Jun. 1965. Reprinted in J. J. Stamnes, Ed. *Selected Papers on Electromagnetic Fields in the Focal Region.* Bellingham, WA: SPIE, 2001, pp. 173-177.

[77] C-Lec Plastics Co., *Datasheet for Rexolite.* [Online]. Available: http://www.sdplastics.com/rexolite.html

[78] E. I. du Pont de Nemours and Company., *Datasheet for Delrin 100T.* [Online]. Available: http://www.dupont.com

[79] J. W. Schultz, E. J. Hopkins, and K. D. Rodkey, "An improved accuracy method for free space, electrimagnetic characterization of warped samples," Georgia Tech Research Institute, GTRI Internal Report.

[80] J. Baker-Jarvis, "Transmission / reflection and short-circuit line permittivity measurements," National Institution of Standards & Technology, Boulder, CO, Tech. Rep. NIST Tech. Note 1341, Jul. 1990.

[81] A. von Hipple, *Dielectric Materials and Applications.* Boston: Artech House, 1995, ch. 5.

[82] W. R. Humbert, "A new technique for measuring the electromagnetic properties of rotationally symmetric materials," Ph.D. Dissertation, Georgia Institute of Technology, Jun. 1997.

[83] "Standard reference material 2870: Relative permittivity and loss tangent 1422 cross-linked polystyrene," National Institution of Standards & Technology, Gaithersburg, MD, Certificate of Analysis, Oct. 2006.

[84] "Agilent basics of measuring the dielectric properties of materials," Agilent Technologies, Inc., Application Note 5989-2589EN, 2006.

[85] R. L. Haupt and S. Haupt, *Practical Genetic Algorithms.* New York: Wiley, 1998.

[86] R. L. Haupt and D. H. Werner, *Genetic Algorithms in Electromagnetics.* Hoboken, New Jersey: Wiley, 2007.

[87] S. M. Stout-Grandy, A. Petosa, I. V. Minin, O. V. Minin, and J. Wight, "A systematic study of varying reference phase in the design of circular fresnel zone plate antennas," *IEEE Trans. Antennas Propag.*, vol. 54, no. 12, pp. 3629–3637, Dec. 2006.

VITA

David R. Reid was born in Youngstown, Ohio, on February 12, 1980 and grew up in Defiance, Ohio. He received the B.S.E.E and M.S.E.C.E degrees from the Georgia Institute of Technology, Atlanta, in 2002 and 2005, respectively. From 2003 to 2008, he was employed as a graduate research assistant in the School of Electrical and Computer Engineering.